



HAL
open science

Modeling of solidification of TiAl alloys in centrifugal casting

Martín Cisternas Fernández

► **To cite this version:**

Martín Cisternas Fernández. Modeling of solidification of TiAl alloys in centrifugal casting. Materials. Université de Lorraine, 2019. English. NNT : 2019LORR0218 . tel-02528906

HAL Id: tel-02528906

<https://hal.univ-lorraine.fr/tel-02528906>

Submitted on 2 Apr 2020

HAL is a multi-disciplinary open access archive for the deposit and dissemination of scientific research documents, whether they are published or not. The documents may come from teaching and research institutions in France or abroad, or from public or private research centers.

L'archive ouverte pluridisciplinaire **HAL**, est destinée au dépôt et à la diffusion de documents scientifiques de niveau recherche, publiés ou non, émanant des établissements d'enseignement et de recherche français ou étrangers, des laboratoires publics ou privés.



AVERTISSEMENT

Ce document est le fruit d'un long travail approuvé par le jury de soutenance et mis à disposition de l'ensemble de la communauté universitaire élargie.

Il est soumis à la propriété intellectuelle de l'auteur. Ceci implique une obligation de citation et de référencement lors de l'utilisation de ce document.

D'autre part, toute contrefaçon, plagiat, reproduction illicite encourt une poursuite pénale.

Contact : ddoc-theses-contact@univ-lorraine.fr

LIENS

Code de la Propriété Intellectuelle. articles L 122. 4

Code de la Propriété Intellectuelle. articles L 335.2- L 335.10

http://www.cfcopies.com/V2/leg/leg_droi.php

<http://www.culture.gouv.fr/culture/infos-pratiques/droits/protection.htm>

Modeling of solidification of TiAl alloys in centrifugal casting

THÈSE

présentée et soutenue publiquement le 16 décembre 2019

pour l'obtention du titre de

Docteur de l'Université de Lorraine
(mention Science et ingénierie des matériaux et métallurgie)

par

Martín Matías CISTERNAS FERNÁNDEZ

Composition du jury

<i>Président :</i>	Charles-André GANDIN	Directeur de recherche CNRS, Cemef, Mines ParisTech
<i>Rapporteurs :</i>	Andreas LUDWIG Valéry BOTTON	Professeur, Montanuniversität Leoben Professeur, INSA Lyon
<i>Examineur :</i>	Nathalie BARDIN-MONNIER	Maître de conférences, Université de Lorraine
<i>Directeur de thèse :</i>	Hervé COMBEAU	Professeur, Université de Lorraine
<i>Co-directeur de thèse :</i>	Miha ZALOŽNIK	Chargé de recherche CNRS, IJL

*A mis padres,
Erica y Gabriel,
y a mi hermano Alfonso.*

Résumé étendu

Les alliages de titane et d'aluminium ont été étudiés au cours de ces 30 dernières années en raison de leur faible densité et de leur haute résistance à haute température, faisant d'eux de très bons candidats pour les applications automobiles et aérospatiales. Cependant, leur réactivité élevée à l'état liquide impose des coulées à des surchauffes très faibles et à des taux de remplissage rapides. La coulée centrifuge permet d'améliorer la vitesse de remplissage du moule en combinant l'effet de la gravité terrestre et de l'accélération centrifuge, empêchant les réactions indésirables et les défauts de porosité.

Malgré ces avantages, la coulée centrifuge peut augmenter l'amplitude de la convection thermosolutale liquide pendant la solidification et par conséquent augmenter la ségrégation des éléments d'alliage. Dans le cas des alliages TiAl, le contrôle de la macroségrégation des lingots centrifugés est important puisque la formation de microstructures est très sensible à la composition en aluminium [1]. La solidification pendant la centrifugation a été étudiée auparavant. Ramachandran et al. [2] a effectué des simulations numériques tentant de représenter la convection liquide thermo-entraînée qui a lieu dans une configuration de croissance cristalline Bridgman basée sur une centrifugeuse. Ses travaux signalent que l'accélération de Coriolis a joué un rôle stabilisateur dans les cas où l'accélération centrifuge était parallèle au gradient thermique. Des études expérimentales de solidification dans des centrifugeuses, comme celle de Rodot et al. [?] ou Müller et al. [3] concluent que les gradients d'accélération de Coriolis et d'accélération centrifuge peuvent jouer un rôle important sur la convection liquide. Bien que l'accélération de Coriolis soit connue pour avoir un impact sur la convection liquide pendant la solidification, son effet sur la macroségrégation n'a pas encore été étudié.

L'Agence spatiale européenne ("European Space Agency", ESA) a lancé le projet GRADECET ("GRAvity DEpendence of Columnar to Equiaxed Transition"), dont l'objectif principal est d'étudier l'influence de la gravité sur la transition colonnaire à équiaxe – *CET* – et sur la formation de microstructures dans les alliages péritectiques TiAl. Dans le cadre de ce projet, plusieurs expériences de solidification dirigée en hypergravité ont été réalisées sur la "Large Diameter Centrifuge" (LDC) de l'ESA. Ces expériences ont fourni des informations pertinentes sur la microstructure de solidification formée sous différents niveaux de gravité [1]. Pour bien comprendre les observations expérimentales, la caractérisation de la convection thermosolutale liquide pendant la solidification est nécessaire. Ce travail vise à soutenir la compréhension de la convection liquide et de la formation de macroségrégations au moyen de simulations numériques.

Ces essais de solidification dirigée ont été réalisés sur des échantillons cylindriques de TiAl (8 mm de diamètre et 165 mm de long) dans la centrifugeuse de grand diamètre ESA ("LDC"). Le four de solidification dirigée, conçu sur mesure, a été placé dans une nacelle fixée à l'extrémité du bras de la centrifugeuse, à 4 m de distance de l'axe de rotation. Sur la Figure RE-1, un schéma de la configuration du four monté dans la nacelle centrifuge est présenté. Plus de détails sur la configuration expérimentale sont rapportés dans la référence [1]. La nacelle était libre de s'incliner, de sorte que la gravité apparente totale (la somme de la gravité terrestre et de l'accélération centrifuge) était toujours alignée avec l'axe central de l'échantillon. Quatre

vitesse de centrifugation ont été utilisées, correspondant à des niveaux de gravité de $5g$, $10g$, $15g$ et $20g$ où g est l'accélération de la gravité terrestre. De plus, un cas avec $\vec{g}_{tot} = 1g$ a été réalisé sans centrifugation, sous gravité terrestre alignée avec la ligne médiane de l'échantillon. Tous ces résultats seront ensuite présentés dans le plan d'étude principal, formé par les vecteurs de vitesse de vol \vec{V}_{flight} et de la gravité apparente totale, \vec{g}_{tot} (voir Fig. RE-1).

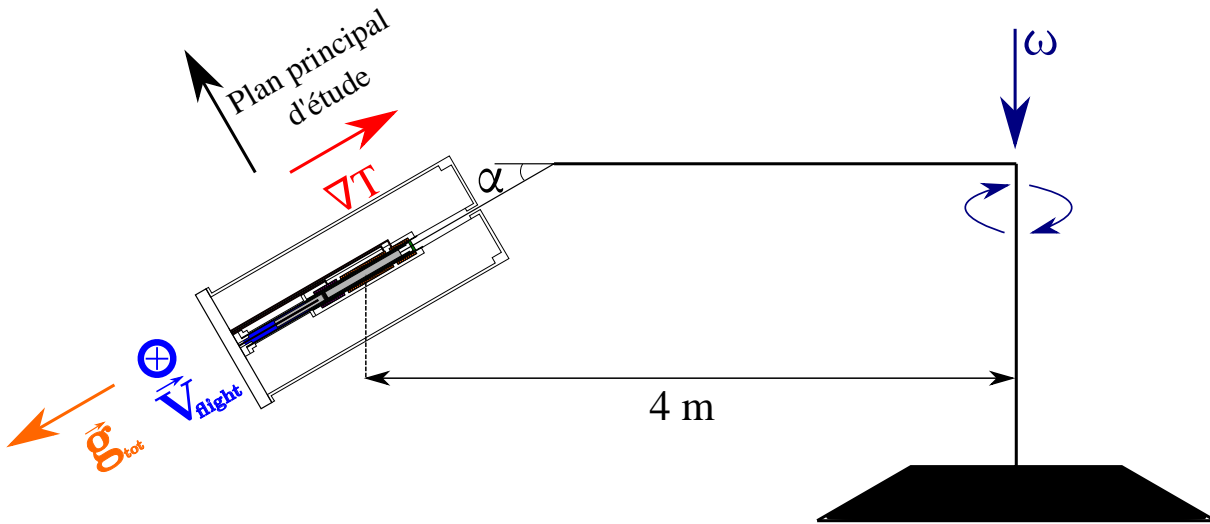


Figure RE-1 – Schéma du four et de l'échantillon de TiAl dans la centrifugeuse. L'échantillon est représenté en gris et les éléments chauffants en orange et jaune. L'angle d'inclinaison du four est indiqué par l'angle α , la vitesse de vol du four par \vec{V}_{flight} (en bleu), la gravité apparente totale par \vec{g}_{tot} (en orange) et le gradient de température principal de ∇T (en rouge). Le plan d'étude principal est défini comme celui formé par le vecteur de vitesse de vol \vec{V}_{flight} et la gravité apparente totale, \vec{g}_{tot} . Quatre gravités apparentes différentes ont été étudiées sous centrifugation: $\vec{g}_{tot} = 5g$, $10g$, $15g$ et $20g$.

Un nouvel outil numérique pour simuler la solidification à des échelles macroscopiques a été développé sur la base de la plate-forme open-source à volumes finis OpenFOAM. Ce nouvel outil numérique a été appelé *macroS3D*.

Convection thermosolutale liquide et macrosegragation dans un système centrifugé

Afin d'avoir un premier aperçu de l'effet de la centrifugation dans les expériences de solidification dirigée TiAl sous centrifugation, un modèle de solidification simplifié prenant compte les accélérations centrifuge et de Coriolis est utilisé pour simuler la convection thermosolutale liquide et la macroségragation de l'aluminium dans des conditions centrifuges. Ce modèle simplifié consiste à supposer une diffusion infiniment rapide du soluté aux échelles microscopiques dans les deux phases, *i.e.* la règle du bras de levier, pour un alliage binaire. Il s'agit du modèle de changement de phase le plus simple pouvant être utilisé dans la modélisation de la solidification macroscopique. D'autre part, la description des phénomènes macroscopiques a été simplifiée en supposant que la microstructure de la phase solide est entièrement colonnaire, de sorte que la

phase solide est fixée dans le domaine d'étude et donc immobile. Cette hypothèse simplifie le système global d'équations partielles différentielles. Malgré les simplifications, le modèle décrit le couplage complet entre l'enthalpie, la température, la concentration de soluté dans les deux phases, la croissance solide et les fractions de phase.

Le modèle de solidification simplifié est similaire à celui utilisé par Combeau et al. [4], dans lequel le transfert de chaleur, le transport de soluté, la convection thermosolutale et la solidification d'un alliage binaire sont pris en compte. La méthode de calcul de la moyenne des volumes [5, 6, 7] est utilisée pour formuler des équations de conservation pour la masse, l'élan, l'énergie et le soluté. Les équations sont formulées en termes de quantités moyennes, telles que la vitesse intrinsèque moyenne du liquide, $\langle \vec{v}_l \rangle^l$, l'enthalpie moyenne, $\langle h \rangle$, et la concentration moyenne de soluté, $\langle C \rangle$, respectivement. Les équations sont formulées pour un cadre référentiel non inertiel, donc l'équation de quantité de mouvement tient compte des accélérations centrifuges et de Coriolis. La relation Kozeny-Carman est utilisée pour calculer la perméabilité hydrodynamique, K , de la zone pâteuse et l'approximation de Boussinesq est utilisée pour prendre en compte le débit induit par la convection thermosolutale. Les densités solides et liquides sont considérées comme constantes et égales, $\rho_l = \rho_s = \bar{\rho}$, par conséquent, l'effet de retrait de solidification n'est pas inclus dans le modèle. La phase solide est considérée comme fixe dans le domaine, *i.e.* $\langle \vec{v}_s \rangle^s = 0$, car le modèle ne représente que la croissance en colonnes sans possibilité de fragmentation.

L'équation de conservation de l'énergie est formulée en termes d'enthalpie moyenne, $\langle h \rangle = c_p T \frac{g_l \rho_l L_f}{\bar{\rho}} = c_p T g_l L_f$ (note $\bar{\rho} = \rho_l$), où c_p est la chaleur spécifique, T la température, L_f la chaleur latente et g_l la fraction liquide. La chaleur spécifique est considérée comme constante et égale entre les phases, $c_{pl} = c_{ps} = c_p$. Le coefficient de conductivité thermique, k , est également considéré comme constant. La température locale est supposée égale dans les phases solide et liquide, $T = T_s = T_l$.

Enfin, le changement de phase solide-liquide est modélisé par un modèle d'équilibre qui suppose une diffusion infiniment rapide à l'échelle microscopique (règle du bras de levier). Ce modèle d'équilibre est pris en compte afin de simplifier le modèle global tout en permettant de représenter la convection thermosolutale liquide et le schéma de ségrégation des solutés. La diffusion à l'échelle macroscopique est négligée.

Les figures RE-2 et RE-3 présentent respectivement la fraction liquide et la vitesse du liquide pour les cas 1G ($\vec{g}_{tot} = g$) et 20G ($\vec{g}_{tot} = 20g$) dans la région entièrement liquide. Dans le cas 1G, pour $t = 50$ s le liquide s'écoule vers le front de solidification au centre du cylindre, tandis que, du côté du cylindre, il s'écoule antiparallèlement au vecteur de gravité apparent. À cet instant, le centre du cylindre est plus froid que les côtés. Le modèle d'écoulement est expliqué par la convection naturelle (thermique) qui est la force motrice dominante pour l'écoulement dans la région entièrement liquide. En effet, dans le cas 1G, le liquide enrichi en soluté ne peut pas s'échapper de la zone pâteuse et, par conséquent, il n'y a pas de gradients solutaux importants dans la région entièrement liquide. Pour les temps $t = 200$ s et $t = 400$ s le flux évolue avec le champ de température contrôlé par les conditions aux limites. Par exemple, à $t = 200$ s dans la zone $z > 60$ mm le liquide s'écoule antiparallèlement à la gravité apparente au centre du cylindre, alors qu'il s'écoule parallèlement sur les côtés du cylindre et pour $z < 60$ mm le flux

est inversé. Ce comportement s'explique par l'inversion radiale du gradient de température qui est imposé par le protocole thermique du four.

Dans le cas 20G, le liquide enrichi en aluminium qui s'échappe de la zone pâteuse en raison du fort effet de flottabilité solutal, est dévié par l'accélération de Coriolis vers le côté vitesse de vol du cylindre. Ce liquide avance tout le long de l'échantillon par le côté vitesse de vol et retourne à la zone pâteuse par le côté opposé au côté vitesse de vol formant une grande circulation dans le sens horaire (voir Fig. RE-3). Cette grande circulation est présente dans tous les cas étudiés avec centrifugation et rend le modèle d'écoulement de fluide entièrement non axisymétrique. En effet, l'impact de la flottabilité solutal le long du cylindre est plus important que l'effet thermique de stabilisation. Les gradients thermiques radiaux induits par le protocole thermique du four ne jouent pas de rôle dans la détermination du schéma d'écoulement du fluide comme ils le font dans le cas 1G. Dans le cas 20G, les caractéristiques d'écoulement du fluide sont principalement déterminées par le liquide enrichi en soluté qui s'échappe de la zone pâteuse anti-parallèle à la gravité apparente qui est ensuite poussé vers le côté vitesse de vol de l'échantillon par l'accélération de Coriolis.

Müller et al. [3] et plus tard Ramachandran et al. [2] ont décrit deux types de régime d'écoulement en cas de convection thermique dans des échantillons cylindriques soumis à la centrifugation. Les descriptions sont basées sur le modèle d'écoulement de fluide dans le plan perpendiculaire à l'axe de rotation. Le premier régime, ou régime de type I, consiste en une seule circulation dominante dont la rotation est à contre sens par rapport à la rotation de la centrifugeuse. De plus, ce type de régime présente des tourbillons dans les coins du conteneur qui provoquent un comportement instable du schéma d'écoulement. En revanche, le régime de type II consiste en une seule circulation dominante dont le sens de rotation est le même que celui de la centrifugeuse. Le deuxième type de régime est complètement dominé par l'influence de l'accélération de Coriolis. Les résultats numériques montrent que dans tous les cas avec centrifugation, le numéro de Rossby $Ro = \frac{U_{ref}}{2\omega L_{ref}} \ll 1$, ce qui signifie que l'accélération de Coriolis est très importante pour déterminer les caractéristiques d'écoulement du fluide. Selon les descriptions de Müller et al. et Ramachandran et al., le régime d'écoulement dans la région entièrement liquide correspond au type II dans tous les cas étudiés avec centrifugation.

La macroségrégation est l'hétérogénéité de la composition du soluté – en l'occurrence l'aluminium – à l'échelle macroscopique en raison du mouvement relatif des phases solide et liquide au cours d'un processus de solidification. On peut montrer que la concentration moyenne, $\langle C \rangle$, en tout point de la zone pâteuse varie comme $\frac{\partial \langle C \rangle}{\partial t} = -\frac{1}{m_l} g_l \langle \vec{v}_l \rangle^l \cdot \nabla T$. Il s'agit d'une relation utile pour comprendre les modèles de macroségrégation dus au mouvement du liquide en l'absence de variations de densité (retrait) et de déformations solides. Notez que $m_l < 0$.

La Figure RE-4 montre la ségrégation relative de l'aluminium dans le plan principal d'étude pour les différents cas en fin de solidification. Dans le cas 1G, la ségrégation relative globale est axisymétrique telle que la convection de liquide thermosolutal et sa magnitude maximale est d'environ 0,29%. Cette faible amplitude de ségrégation s'explique principalement par: (1) le grand coefficient de partage, $k_p = 0,885$, proche de l'unité, ce qui signifie que la concentration en aluminium dans les phases liquide et solide est similaire (rappel $\langle C_s \rangle^s = k_p \langle C_l \rangle^l$), et (2) la

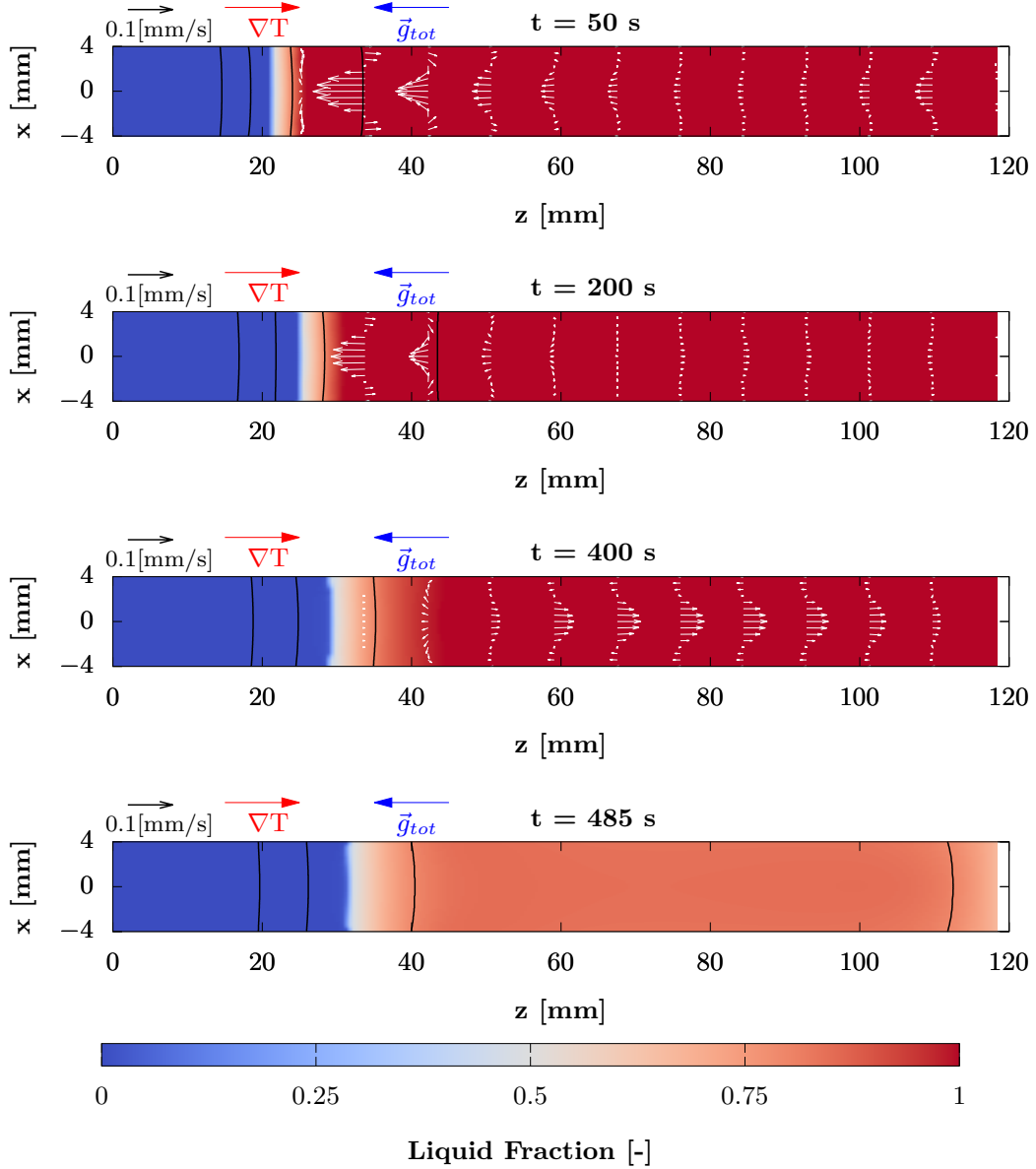


Figure RE-2 – Evolution du schéma de vitesse des liquides dans le plan d'étude principal dans la région entièrement liquide pour le cas 1G. Contours de température en noir: 1400, 1450, 1500 et 1550 °C.

faible convection liquide par rapport aux cas avec centrifugation. Le long de l'échantillon, trois schémas de ségrégation différents peuvent être facilement identifiés. Pour $20 \text{ mm} \leq z \leq 40 \text{ mm}$ une ségrégation négative est présente dans les côtés du cylindre tandis que positive dans l'axe du cylindre. Cette configuration s'explique par un écoulement parallèle du liquide au gradient de température principal ($\langle \vec{v}_l \rangle^l \cdot \nabla T > 0$) le long de l'échantillon dans l'axe du cylindre, amenant un liquide enrichi en soluté du plus profond de la zone pâteuse au front de solidification et anti-

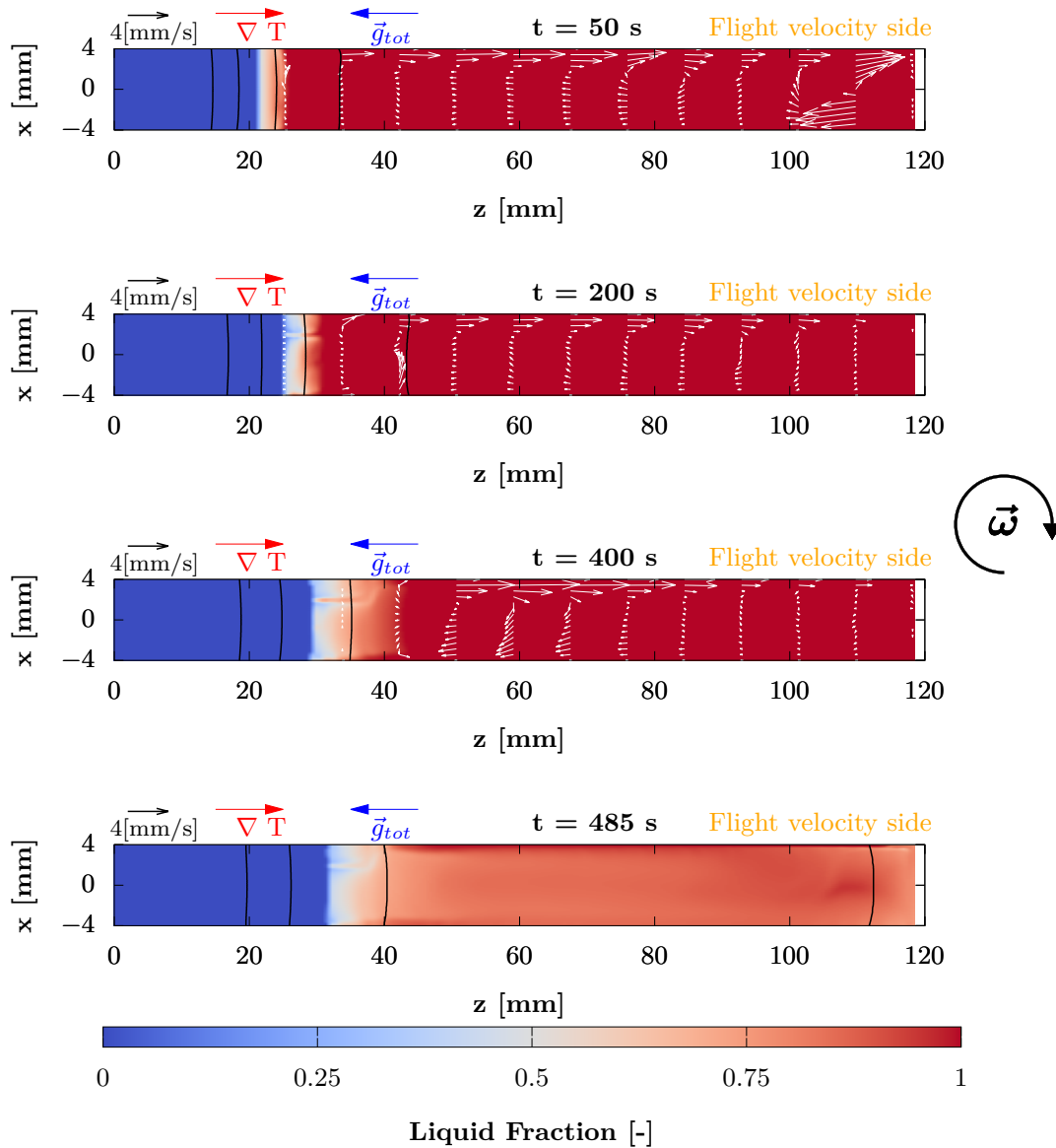


Figure RE-3 – Evolution du champ de vitesse du liquide dans le plan d'étude principal dans la région entièrement liquide pour le cas 20G. Contours de température en noir: 1400, 1450, 1500 et 1550 °C.

parallèle ($\langle \vec{v}_l \rangle^l \cdot \nabla T < 0$) sur les côtés du cylindre, en prenant un liquide pauvre en soluté du front de solidification au plus profond de la zone pâteuse. En revanche, pour $40 \text{ mm} \leq z \leq 95 \text{ mm}$, le modèle de ségrégation présente une configuration inverse: ségrégué positivement sur les côtés du cylindre et négativement au centre, ce qui s'explique par l'inversion de la direction du flux. Le même schéma d'écoulement de liquide est observé pour $z \geq 95 \text{ mm}$ cependant, un deuxième front de solidification se déplace de l'autre extrémité de l'échantillon parallèlement au vecteur

de gravité apparent (pour $t > 400$ s) enrichissant en soluté le centre du cylindre et épuisant ses côtés. Il est à noter que selon le protocole thermique du four, la zone $z > 40$ mm se solidifie très rapidement et à $t = 487$ s l'échantillon est entièrement éteint.

Dans les cas de centrifugation, nous observons que le modèle de ségrégation n'est pas axisymétrique en raison de l'effet de déviation de l'accélération de Coriolis sur la convection liquide. Comme dans le cas 1G, nous reconnaissons les trois mêmes zones, mais avec des différences importantes dans le modèle de ségrégation. La première zone entre $20 \text{ mm} \leq z \leq 40 \text{ mm}$ présente un modèle similaire au cas 1G, mais plus fortement séparé, non axisymétrique et avec l'occurrence des canaux de ségrégation (voir les cas 10G et 20G sur la Fig. RE-4). La deuxième zone $40 \text{ mm} \leq z \leq 95 \text{ mm}$ a une ségrégation positive du côté des cylindres, avec une zone plus fortement enrichie en aluminium du côté de la vitesse de vol. Cette caractéristique est due à l'effet de déviation de l'accélération de Coriolis. La troisième zone, $z > 95 \text{ mm}$ elle est presque entièrement séparée positivement (certaines petites zones négativement séparées peuvent être vues dans le cas 5G sur les côtés du cylindre) en raison de l'accumulation de liquide enrichi en aluminium léger .

Mouvement du grain équiaxe

Une interface colonnaire-équiaxe prédéfinie était prise en compte, de telle sorte que le domaine d'étude était divisé en deux régions: une région colonnaire, où les grains étaient immobiles, et une région équiaxe, où les grains équiaxes pouvaient bouger. De plus, un modèle globulaire à deux phases, qui considère une diffusion limitée du soluté dans les deux phases à des échelles microscopiques, a été pris en compte. Les mêmes conditions initiales et conditions aux limites que celle utilisées dans le cas d'une croissance colonnaire pure ont été considérées. En raison des limites de temps et du coût élevé du temps de calcul, seuls les cas 1G et 5G ($\vec{g}_{tot} = 5g$) ont été simulés.

Les simulations ont montré que, malgré la présence de grain équiaxes, un seul vortex se produit dans la zone de suspension des cas sous conditions centrifuges, en raison de l'accélération de Coriolis. Les simulations ont également montré que l'influence de la force de Coriolis sur le mouvement des grain équiaxes pour les cas étudiés est faible. En effet, leur mouvement est principalement régi par l'équilibre entre la force de traînée et le poids apparent.

Perspectives

Bien que les efforts déployés pour effectuer des simulations numériques toutes aussi semblables aux expériences protocole expérimental, des considérations particulières ont dû être prises en compte concernant la configuration des cas de simulation et le chemin de solidification de l'alliage. À cet égard, l'amélioration des conditions aux limites thermiques et la modélisation de l'alliage complet, considérant explicitement tout les composants, con des avancées pour mieux représenter la physique lors des expériences. Par la suite l'utilisation d'un modèle microscopique triphasé, actuellement disponible dans *macroS3D*, pourra permettre une meilleure description de la morphologie du grain, et donc une meilleure description du mouvement du grain équiaxe et de la

macroségrégation de l'aluminium. Cela n'a pas pu être fait dans le cadre de cette thèse en raison de contraintes de temps. Enfin, il convient de mentionner que *macroS3D* sera un élément fondamental d'un nouveau projet dirigé par notre équipe qui s'appelle OpenSOLID. Ce projet vise à apporter un logiciel de pointe pour la simulation de coulée à l'industrie métallurgique.

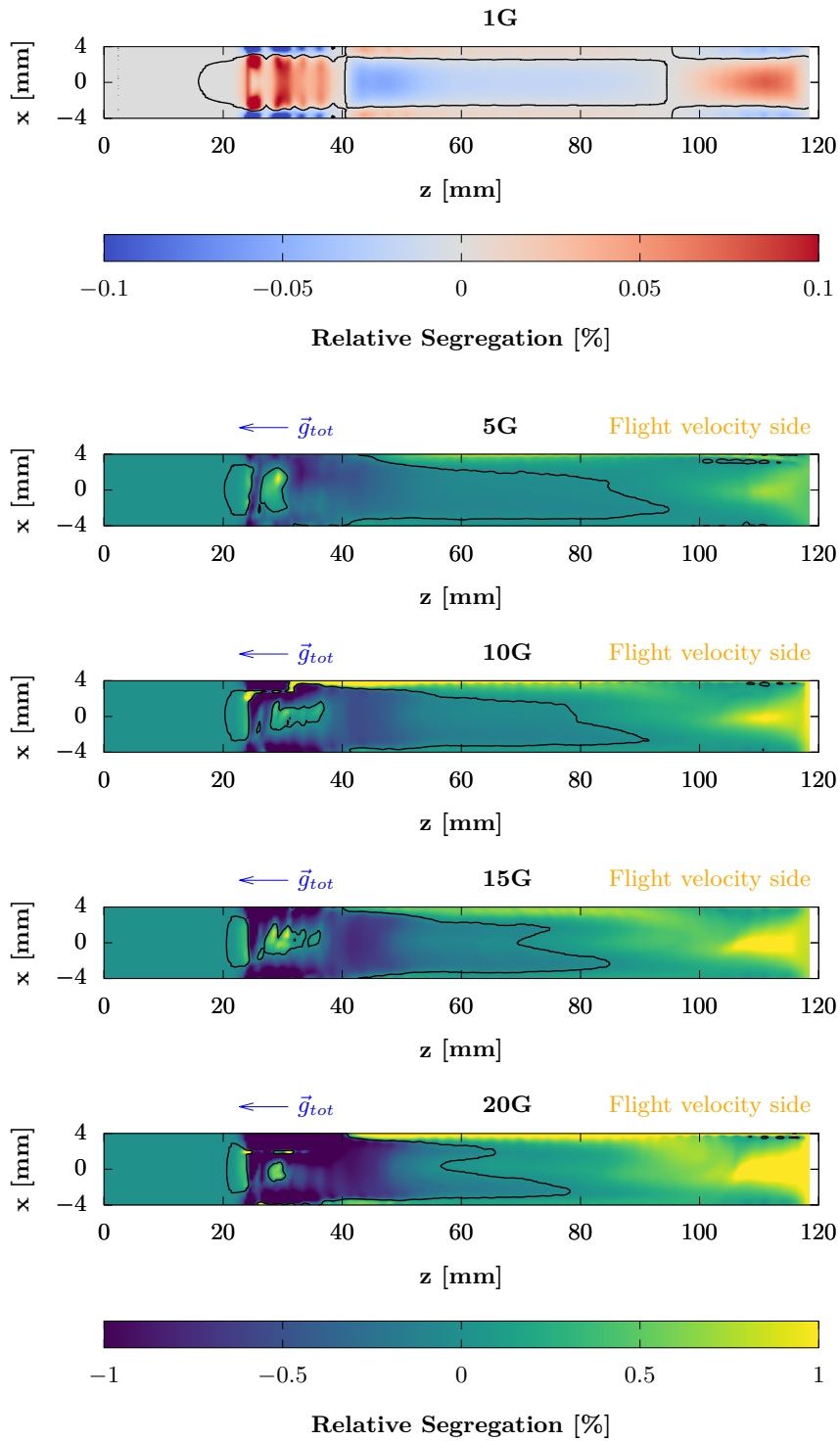


Figure RE-4 – Segregation relative de l'aluminium $\frac{\langle C \rangle - C_0}{C_0} \times 100\%$ dans le plan principal d'étude en fin de solidification pour différents niveaux de centrifugation. Contours à $\langle C \rangle = C_0$ (ligne noire).

Contents

Acknowledgments	1
Nomenclature	3
Introduction	7
Chapter 1 Literature review	13
1.1 Solidification and its macroscopic modeling	14
1.1.1 Macrosegregation	15
1.1.2 Volume averaging method	19
1.1.3 Microscopic modeling	21
1.1.4 Macroscopic modeling	24
1.1.5 Coupling micro/macro modeling: Operator-splitting method for the solution of the coupled equations	30
1.2 Rotating fluids and centrifugal casting	30
1.2.1 Solidification in centrifugal conditions	32
1.2.2 Rotating reference frame: Apparition of centrifugal and Coriolis	36
1.3 Objectives	38
1.4 Summary	40
Chapter 2 Solidification model for centrifugal casting	41
2.1 Eulerian derivation of Navier-Stokes equations in a rotating reference frame	42
2.2 Derivation of scalar conservation equation	48
2.3 Derivation of momentum conservation equations	50
2.4 Summary	54
Chapter 3 Thermosolutal buoyancy convection and macrosegregation during solidification in a centrifugated system	55
3.1 Simplified model for solidification modeling	56
3.1.1 Validation	59

3.2	Simulation of TiAl samples solidified in the “Large Diameter Centrifuge” (LDC)	65
3.2.1	Furnace thermal protocol	67
3.2.2	Solidification path and alloy phase diagram	68
3.2.3	Numerical setup	69
3.3	Results and discussion	71
3.3.1	Furnace thermal protocol: Temperature field and heat transfer	71
3.3.2	Liquid flow	73
3.3.3	Aluminum macrosegregation	80
3.3.4	Comparison with aluminum measurements	84
3.4	Summary	88
Chapter 4 Equiaxed grain motion and grain growth kinetics		91
4.1	Macroscopic conservation equations	93
4.1.1	Mass balance of phase k	93
4.1.2	On the coupling of enthalpy, temperature and solid fraction	95
4.1.3	Momentum conservation and mass conservation equations	95
4.1.4	Other macroscopic conservation equations	102
4.1.5	Validation of the transport model in <i>macroS3D</i>	103
4.2	Microscopic modeling in <i>macroS3D</i>	110
4.2.1	Grain growth kinetics	110
4.2.2	Grain nucleation and nuclei re-injection	114
4.2.3	Validation of the microscopic modeling in <i>macroS3D</i>	114
4.3	Coupling of macroscopic conservation equations with microscopic modeling	117
4.3.1	Validation of the multiscale modelling in <i>macroS3D</i> : The Hebditch and Hunt case	123
4.4	Simulations of the GRADECET experiments	129
4.4.1	Results and discussion	130
4.5	Summary	146
General conclusions and perspectives		149
4.6	Perspectives	151
Appendix		153
Appendix A Thermophysical properties		153
A.1	Validation	154
A.1.1	Thermophysical properties: Pb-18wt.%Sn alloy	154

A.1.2	Thermophysical properties: water/glycerol mixture for the rotating annulus case	154
A.1.3	Thermophysical properties: Sedimentation column and Hebditch-Hunt benchmark cases (Sn-5wt.%Pb)	156
A.1.4	Thermophysical properties: cases of solidification of an unitary control volume (Al-5wt.%Si)	157
	List of Tables	159
	List of Figures	161
	Bibliography	169

Acknowledgments

I would like to thank the members of the jury – Andreas Ludwig, Valéry Botton, Nathalie Bardin-Monnier and Chales-André Gandin – for their time to review and to comment this manuscript. Their questions and suggestions permitted to improve the final version of the manuscript and to expand the perspectives of this work. Special thanks to my mentors, Hervé Combeau and Miha Založnik, for supporting me during all my PhD. studies and for the trust that they placed on me.

This thesis was carried out within the framework of the ESA's GRADECET project. Thanks to the different research groups that participated in GRADECET for their scientific discussion. Special thanks to Dr. Ulrike Hecht and Can Huang, from Access Germany, for their support providing relevant information to carry out this work. In addition, I would like to acknowledge the trust and the support provided by Guillaume Martin and Nicolas Leriche from Safran Aircraft Engine.

Thanks as well to the research group “Solidification”: Dominique Daloz, Julien Zollinger, Bernard Rouat and Géraldine Georges, for their fruitful scientific discussions and for their willingness to help at all times. In addition, I would like to acknowledge all the support that I received from my colleagues: Marvin, Manoj, Edgar, Antonio, Savya, Jacob, Jaime, Kanika, Nicole, Yuze, Ilya, Rayan, Julien, Raphaël, Akash and so many others! Without them, this work could have been much more difficult.

Además, me gustaría agradecer a todos mis amigos de Chile por mantener siempre su apoyo a distancia. Mencion especial a todos aquellos que me vinieron a visitar y con los que me pude juntar en algún lugar del viejo continente. Agradecer al Prof. Olivier Skurtys (UTFSM-Chile), por sus enseñanzas durante mis estudios de magister y por impulsarme a seguir con mis estudios fuera de Chile. Sin ese empujon inicial nunca hubiese pensado en perseguir mayores estudios.

Pude realizar este trabajo principalmente por el apoyo que, desde un primer momento, me brindó mi familia en su conjunto y muy especialmente mis padres y hermano: Erica, Gabriel y Alfonso. Este trabajo va dedicado con mucho cariño para ustedes.

Finalmente, y no por eso menos importante, agradecer a Léa por apoyarme en todo sentido durante estos últimos años y por ser una gran compañera de ruta en este viaje. Agradecerle además por regalarme a (Gabriel)⁴ que ahora es mi mayor motivación para seguir adelante aún con más fuerzas.

This work was carried out as part of the GRADECET (GRAvity DEpendence of Columnar to Equiaxed Transition in TiAl Alloys) research project and was funded by the European Space Agency (contract 4000114221/15/NL/PG). The view expressed herein can in no way be taken to reflect the official opinion of the European Space Agency.

Nomenclature

Most of the variables are defined within the text. For clearance a nomenclature with all the variables is given below.

Latin symbols :

A_k	Surface of the phase k in an arbitrary representative elementary volume
C_0	Nominal concentration
C_{ref}	Reference concentration
C_{inv}	Pseudo-peritectic concentration
$\langle C \rangle$	Average solute concentration
$\langle C_l \rangle^l, \langle C_s \rangle^s$	Intrinsic solute concentration in liquid and in solid, respectively
$\langle C_l \rangle^{le}$	Intrinsic solute concentration in the extradendritic liquid
C_l^*, C_s^*	Equilibrium solute concentration in liquid and in solid, respectively
C_d	Drag coefficient
c_p	Specific heat
D_l, D_s	Diffusion coefficient in liquid and in solid, respectively
d_g	Grain diameter
g	Normal terrestrial gravity
\vec{g}_{tot}	Apparent gravity (sum of centrifugal acceleration and terrestrial gravity)
g_s, g_l	Solid and liquid volumetric fractions, respectively
g_e	Envelope fraction
g_i	Internal solid fraction
g_{le}, g_{li}	Extradendritic and intradendritic liquid fractions, respectively
g_e^{block}	Solid fraction packing limit (two-phase globular model) or envelope fraction packing limit (three-phase dendritic model)
g_{ep}^{max}	Maximum packing envelope/solid fraction.

$\mathbf{G}^{\vec{V}}$	Galilean transformation
$\langle h_l \rangle^l, \langle h_s \rangle^s$	Intrinsic averaged enthalpy of the liquid and solid phases, respectively
$\langle h \rangle$	Averaged specific enthalpy
k_p	Partition coefficient
k, k_l, k_s	Thermal conductivity, averaged, in liquid and in solid, respectively
K	Permeability
K_k	Kozeny constant
L_f	Latent heat
L_{ref}	Reference length
l_c	Characteristic length of porosity
m_l	Liquidus slope
$\vec{M}_k^d, \vec{M}_k^\Gamma, \vec{M}_k^\Phi$	Interfacial momentum exchange of the phase k due to drag, solid growth and nucleation, respectively
N	Volumetric density of nuclei
N_g	Volumetric density of grains
$Q_k, Q_k^\Gamma, Q_k^\Phi$	Interfacial energy exchange of the phase k due to diffusion, grain growth and grain nucleation
p	Pressure
$\mathbf{R}^{\vec{\omega}t}$	Rotational transformation
$\mathbf{R}(t, z)$	Radial contribution of heat diffusion
R	Averaged grain radius
R_{CD}	Ratio between the characteristic time of drag response and the characteristic time of rotation
Ro	Rossby number
R_{tip}	Tip radius
S_v	Specific surface area of spherical grains
S_v^E, S_v^S	Specific surface area for envelope and solid, respectively
T	Temperature
T_f	Melting temperature of a pure substance
ΔT_{nucl}	Nucleation undercooling
U_{rel}	Relative velocity between the phases
U_{ref}	Reference liquid velocity
T_{ref}	Reference temperature
V_c	Volume of an arbitrary representative elementary volume

V_0	Initial volume of a nucleated grain
V_g	Velocity of the solid-liquid interface in case of spherical shaped front
V_{tip}	Tip velocity
\vec{V}_{flight}	Centrifuge flight velocity vector
$\langle \vec{v}_l \rangle^l, \langle \vec{v}_s \rangle^s$	Averaged intrinsic velocity of the liquid and solid phases, respectively
\vec{w}	Velocity of the solid-liquid interface

Greek symbols :

α_t	Slurry/porous flow regime transition function
α	Coefficient for slurry/porous flow regime transition function
λ_2	Secondary arm spacing
β_T, β_C	Thermal and solutal expansion coefficients
Γ_s	Mass transfer rate from liquid to solid phase
Γ_e	Volumetric transfer rate to envelope phase
Φ_s	Mass transfer rate to the solid phase due to nucleation
Φ_e	Volumetric transfer rate to the envelope phase due to nucleation
δ_l, δ_s	Diffusion lengths for liquid and solid, respectively
μ_l, μ_s	Dynamic viscosities for the liquid and solid phases, respectively
ν_l	Liquid kinematic viscosity
ρ	Density
ρ_{ref}	Reference density
ρ_{ref}	Reference density
ρ_l, ρ_s	Liquid and solid densities, respectively
τ	Tortuosity
$\langle \tau_k \rangle^k$	Averaged intrinsic shear stress tensor of phase k
τ_V	Momentum response time
ω	Centrifuge rotation velocity

Introduction

This chapter aims to give a first insight about this work by answering several questions about its title (“Modeling of solidification of Ti-Al alloys in centrifugal casting”). The final purpose is to introduce the reader to the main objectives of this work.

Why Titanium aluminum alloys?

Titanium aluminum alloys have been studied for more than 20 years due to their low density, high oxidation resistance and good high temperature creep strength [8, 9, 10], making them a good candidate for automotive and aerospace applications. Indeed, they are used in the manufacture of turbocharger wheels and car engine valves [11, 12, 13, 14, 15, 16] and in the production of low-pressure turbine blades for the new-generation aircraft engines [10, 17]. Indeed, the GEnxTM, from General Electric, LEAPTM, from CFM International and PW1100GTM, from Pratt and Whitney are examples of aircraft engines in production that use TiAl alloys. Moreover, Rolls-Royce announced their intention to use TiAl alloys for their future new engines: AdvanceTM and UltraFanTM [10].

Two specific TiAl phases have attracted engineering and industrial attention: α_2 (Ti₃Al) and γ (TiAl). The interesting mixture of these two phases ($\alpha_2 + \gamma$) exists when the aluminum concentration is between 40 at.% and 48 at.% as shown in Fig. 1. In this range, the primary solidification phase is β which has a body centered cubic structure (eight Ti atoms on the vertices with one single atom in the center). Around 1764 K a peritectic transformation takes place in the solidification path. The phase α_2 grows from β and liquid, presenting a hexagonal close packed structure of Ti. The phase α_2 presents the same lattice structure than α but with the addition of Al to the lattice. The γ phase is a face centered cubic structure consisting of alternating planes of Ti and Al [18]. The mixture α_2 and γ presents a wide range of microstructures that can be achieved by different heat-treatments. Generally, these microstructures have been classified in four types: fully lamellar, nearly-lamellar, duplex and near-gamma. The fully lamellar microstructure is characterized by coarse grains (between 200 μm and 1000 μm), which in turn are formed by plates of α_2 and plates of γ . This microstructure presents an excellent creep and fatigue resistance but low ductility and strength. The duplex microstructure is formed by fully-lamellar colonies and gamma equiaxed grains, where the α_2/γ ratio is equal to 1, presenting a grain size of around 10 μm . This microstructure presents the best ductility and strength at room temperature, but its creep and fatigue resistance are very low. The nearly-lamellar

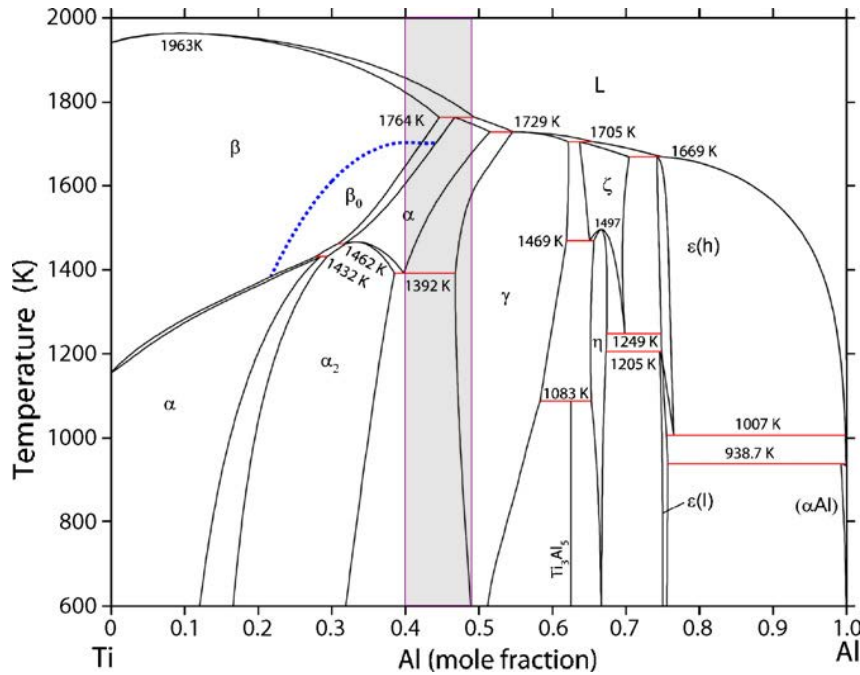


Figure 1 – Binary phase diagram Ti-Al [20] along with the range in which α_2 and γ phases coexist.

microstructure is produced when the α_2/γ ratio is greater than one, presenting mostly lamellar colonies along with gamma equiaxed grains, with grain sizes between 150 μm and 200 μm . The near-gamma microstructure is characterized by equiaxed gamma grains and α_2 precipitates. The interest has been put in the development of microstructures with properties between the duplex microstructure and the fully-lamellar microstructure [9]. Therefore, the control of the microstructure formation is an important key, since it enables to improve the mechanical properties of the alloy used in the final product. The most common alloying elements are Cr, Mn or V (< 4 at.%), which mainly improve the ductility of the duplex microstructure (α_2 and γ), Nb, W, Mo or Ta (< 10 at.%), which improve the oxidation resistance, and B, C or Si (< 1 at.%), which improve the mechanic resistance [19, 1].

Why centrifugal casting?

TiAl alloys present a high reactivity in liquid state [21]. Small traces of H, C, N and O can increase dramatically the embrittlement of single phase $\gamma(\text{TiAl})$ [19]. For these reasons, special considerations are required to melt and to cast TiAl alloys. Aguilar et al. [19] proposed an industrial process for the manufacture of TiAl low pressure turbine blades by means of centrifugal investment casting. In their process the melting of TiAl alloys is carried out in an “Induction Skull Melting” furnace under vacuum. This results in a very low oxygen pick-up during melting. Following, the liquid is poured in ceramic shell molds by means of centrifugal casting. Here, the centrifugation enables the use of a low superheated liquid, a fast mold filling and the prevention

of porosity defects.

The company “GfE” in Germany currently uses centrifugal casting to produce TiAl small sized slugs (100 mm in diameter and 750 mm length as maximum) [22]. These slugs are later machined to obtain the final part. In their manufacturing route, the alloy is melted by a “Vacuum Arc Remelting” (VAR) skull melting process and then poured by a funnel to permanent molds which are placed in a rotating wheel. The revert from the process is remelted again by an “Induction Skull Melting” process and then poured again in the rotating molds. In the last ten years, this manufacturing route has greatly reduced costs while increasing the production volume.

Lately, efforts are being put in the production of TiAl parts by means of additive manufacturing techniques, such as the “Selective Laser Melting” or “Selective electron beam melting”. In these techniques, the desired parts are built up layer after layer by melting metal powder using a laser or an electron beam. As the parts are built up layer after layer, the microstructure can be controlled by adjusting the processing parameters during the part production. Furthermore, as the metal powder is locally melted, a good chemical composition homogeneity at the product scale is achieved. Although the advantages, these techniques have shown aluminum loss through evaporation and residual microporosities [23, 24, 25].

The development of new generation of TiAl alloys (multi-phase β -solidifying) has enabled the manufacture of components with complex shapes and high dimensional precision by means of hot forging and machining [26]. Moreover, with these alloys, powder metallurgy processes such as spark plasma sintering, have been tested as a promising manufacture route [27].

Centrifugal casting is an established option to cast TiAl alloys since it improves the mold filling speed due to the combined effect of terrestrial gravity and centrifugal accelerations, which push the liquid inside the mold. This technique permits casting with a low superheated liquid and avoiding porosity or undesired chemical reactions. By counterpart, this technique may increase the magnitude of the liquid thermosolutal convection during solidification, which can lead to heterogeneities in chemical composition (macrosegregation) at the product scale.

Why modeling of solidification?

During solidification physical phenomena take place at different scales (from atomic scales to final product scale) and play a role in the final product quality. For example, in case of TiAl alloys, a small variation in the aluminum composition can dramatically change the grain morphology and the proportion of α_2 and γ phases in the final microstructure [9]. Moreover, the peritectic transformation enhances the dendrite fragmentation during solidification, adding nucleation sites for equiaxed grains in the liquid and promoting Columnar-to-Equiaxed Transition (*CET*) [28]. Therefore, to control the aluminum segregation during solidification is an important key to control the microstructure formation, and hence, the mechanical properties of the final product.

Numerical modeling is a powerful tool to improve the understanding of the different phenomena at the different scales. Detailed simulations of grain growth [29, 30], grain packing [31, 32] or segregation of constituent elements [33, 34, 35] are some examples of how numerical simulations

have contributed in the improvement of understanding of solidification. Particularly, software development to model solidification processes has taken place since the eighties in the “Solidification” group of the Institut Jean Lamour. Among the developments, SOLID[®] [36, 37, 38] can be remarked as one of the most complete packages in the prediction of macrosegregation and grain morphology. It has been used to simulate solidification of large steel ingots [38] or DC aluminum casting [39] among other applications. SOLID[®] was programmed in Fortran using a procedural style and is capable to resolve the coupled differential partial equations in two-dimensional geometries by means of the finite-volume method. Currently, SOLID[®] is commercialized by *Sciences Computers Consultants*.

Although, SOLID[®] software has advanced solidification models, it can not be directly used in cases of centrifugal casting. If a rotating reference frame is used to define the physical study domain, during centrifugation, the liquid and equiaxed grains are affected by the centrifugal and Coriolis accelerations. In particular, Coriolis acceleration adds important three-dimensional aspects to the problem that must be taken into account and can not be entirely depicted by 2D geometries. To overcome these limitations, a completely new implementation of solidification modeling is required. In this work, the OpenFOAM platform is chosen to that end.

The OpenFOAM platform is an open source finite-volume framework to resolve differential partial equations. It is written in C++ with a fully object-oriented style which makes it easy to modify or expand. It can handle complex 3D geometries and can be executed using distributed-memory parallel computation. In case of solidification modeling, OpenFOAM is a good alternative since it enables the resolution of conservation equations efficiently.

The GRADECET project

In order to improve the knowledge about peritectic TiAl alloys and their microstructure, the European Space Agency launched the GRADECET (“GRAvity DEpendance of Columnar to Equiaxed Transition”) project, whose main objective is to investigate the influence of gravity on Columnar to Equiaxed Transition (*CET*) and on microstructure formation in peritectic TiAl alloys. Within the framework of this project, several experiments of directional solidification in hypergravity were carried out in the ESA “Large Diameter Centrifuge” (LDC), covering a gravity range between 1g to 20g (where g is the normal terrestrial gravity). The experiments consisted in the remelting and subsequent directional solidification of cylindrical TiAl samples (8 mm diameter and 165 mm length) whose composition was Ti-32.96 wt.%Al-2.49 wt.%Cr-4.76 wt.%Nb. This alloy is also called “GE alloy”. The hypergravity is achieved in the centrifuge by combining the effect of the centrifugal and normal terrestrial gravity accelerations. Results of these experiments, along with, experimental set-up, analysis and characterization of the post-mortem microstructure, were reported in the PhD. thesis N. Reilly [1]. In addition, experiments of directional solidification, using the same thermal protocol as in the centrifugally solidified cases, were performed in the Maxus-9 sounding-rocket which provided twelve minutes of weightlessness (microgravity, 0g). The microgravity is achieved during the rocket free-fall after it reaches its maximum altitude. All these experiments gave relevant information on the solidification

microstructure of peritectic TiAl alloys formed under different gravity levels.

Several partners have been working in this project in the last years, performing experimental and modeling research from microscopic to macroscopic scales. The partners that have participated in this project, along with their role, are (as stated in [1]):

- **Safran Aircraft Engines (France):** The company supplied the TiAl material with which the experiments of directional solidification under centrifugal conditions were performed.
- **Institut Jean Lamour (France):** Experiments of peritectic solidification and analysis of the centrifugally solidified TiAl samples were conducted within the framework of N. Reilly PhD. thesis [1]. In addition, this work is also conducted in this institute.
- **European Space Agency:** To provide the “Large Diameter Centrifuge” (Noordwijk, Netherlands) in order to perform the experiments of directional solidification in hypergravity, as well as, the sounding rocket “Maxus 9” in order to perform experiments of directional solidification in microgravity.
- **Access e.V. (Germany):** To perform semi-industrial experiences of centrifugal casting in the framework of N. Reilly PhD. thesis. On the modeling side, to perform numerical analysis of the furnace thermal protocol which was used in the experiments of directional solidification, grain growth modeling in peritectic TiAl alloys and thermodynamic simulations of the system Ti-Al-Nb-Cr.
- **Slovak Academy of Sciences (Slovakia):** To conduct experiences of Bridgman directional solidification of TiAl alloys inoculated with carbon and boron.
- **Trinity College Dublin (Ireland):** To perform front tracking modeling on the experiences carried out by the Slovak Academy of Sciences (R. Mooney PhD. thesis [40]) and to study the conditions which drive Columnar-To-Equiaxed transition in case of directional solidification of peritectic TiAl alloys under hypergravity conditions (S. Battaglioli PhD. thesis [41]).
- **Wigner Research Center for Physics (Hungary):** To perform modeling on grain growth, grain movement and fluid flow at microscopic scales (L. Rátkai PhD. thesis).
- **Deutsches Zentrum für Luft-und Raumfahrt (Germany):** To perform diffusion experiments on TiAl alloys.

In particular, this work takes the mission of the macroscopic modeling (at the scale of the cylindrical TiAl samples) of solidification of the experiments carried out under centrifugal conditions.

General objectives

The microstructure characterization was conducted on post-mortem (after the end of solidification) TiAl centrifugally solidified samples. Only information about the thermal protocol is

available for its interpretation. To fully understand the experimental observations, characterization of the liquid thermosolutal convection and of equiaxed grains motion during solidification is needed. The general objective of this work is to study, by means of numerical simulations, the solidification process of the centrifugally solidified samples at the macroscopic scale and, in that way, to support the experimental analysis.

In case of centrifugal casting, as was previously mentioned, the Coriolis acceleration adds important three-dimensional aspects to the problem. For this reason and to meet the general objective, a new objective arise: to develop a new software, including the sophisticated solidification models present in SOLID[®] to enable the study of three-dimensional domains in rotating reference frames. As was mentioned before, the finite-volume framework OpenFOAM was chosen to be used in this new implementation.

Organization of the manuscript

This thesis is divided into four Chapters. Chapter 1 presents a literature review about macroscopic modeling of solidification and about solidification processes under centrifugal conditions. In Chapter 2 a macroscopic model for solidification is written in terms of a rotating coordinate system. In Chapter 3 a simplified solidification model is presented and then it is applied to the study cases of the GRADECET experiments. Chapter 4 presents a macroscopic solidification model that accounts for grain growth kinetics and equiaxed grain motion. This model is later applied to the study cases of the GRADECET experiments.

Chapter 1 : Literature review

Contents

1.1 Solidification and its macroscopic modeling	14
1.1.1 Macrosegregation	15
1.1.2 Volume averaging method	19
1.1.3 Microscopic modeling	21
1.1.4 Macroscopic modeling	24
1.1.5 Coupling micro/macro modeling: Operator-splitting method for the so- lution of the coupled equations	30
1.2 Rotating fluids and centrifugal casting	30
1.2.1 Solidification in centrifugal conditions	32
1.2.2 Rotating reference frame: Apparition of centrifugal and Coriolis	36
1.3 Objectives	38
1.4 Summary	40

1.1 Solidification and its macroscopic modeling

Solidification is the process by which a liquid substance changes its physical state to solid. This process can be observed in daily circumstances, such as making ice cubes at home or during winter when water freezes over cars. Solidification is a multiscale problem. Different physical phenomena take place simultaneously at different scales when solidification occurs. For example, at nano scales, atomic rearrangement takes place at the solid-liquid interface, while liquid and grain movement are present at macroscopic scales. Figure 1.1 exemplifies the scale separation of the different phenomena that take place during solidification. This thesis is focused on the solidification at macroscopic scales, which corresponds to the scale of the product. All these phenomena affect the solidification microstructure of the resulting solid, and hence, its mechanical properties. One particular case is solidification of metallic alloys which is present in many industrial applications. The control of solidification processes has enabled the production of new and improved quality alloys.

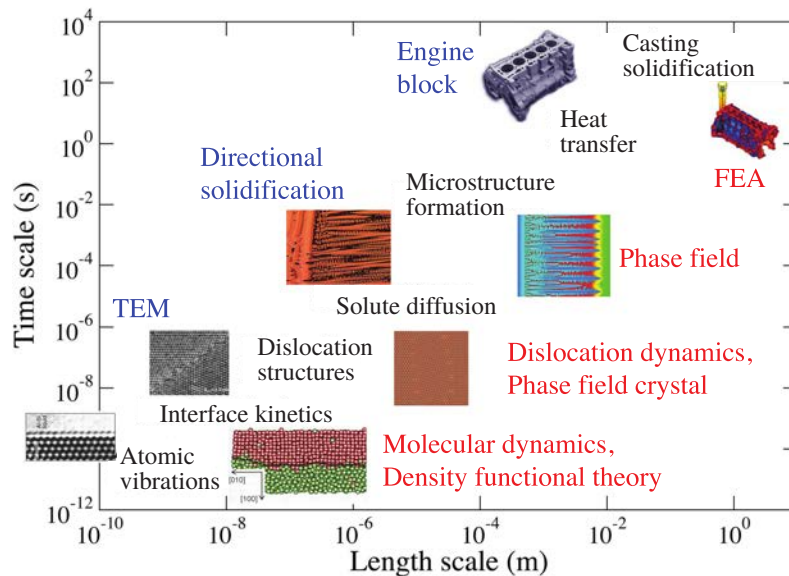


Figure 1.1 – Scales of solidification [42]

Macroscopic modeling of metallic alloys solidification involves the simultaneous representation of heat transfer, solute (alloying elements) transport, grain growth and motion of liquid and equiaxed grains. In case of heat transfer, it is necessary to consider that liquid and solid phase do not transport the same amount of energy. The liquid phase transports not only the sensible heat, but also the latent heat. Moreover, solid and liquid phases do not dissolve the same amount of solute at a given thermodynamic state. This entails solute incorporation or rejection by the growing solid during solidification, leading to gradients of solute composition in solid and liquid phases.

Thermal and solutal gradients trigger buoyancy forces, which drive thermosolutal convection of liquid. In addition to buoyancy forces, liquid convection can be dramatically affected by the motion of equiaxed grains, shrinkage due to density differences between solid and liquid, or

external forces, such as magnetic fields or centrifugation. Energy and solute are transported at the macroscopic throughout scale the solidification domain by liquid convection and equiaxed grain movement. The macroscopic heat, mass and solute transport affects the local conditions for the solid growth, which is mainly controlled by microscopic solute diffusion processes and the local thermodynamic state. The relative movement of the phases, with different compositions, produce heterogeneities of solute composition at the macroscopic scales. These heterogeneities are called *macrosegregation* and their causes will be discussed in Sec. 1.1.1. During solidification, the microscopic and macroscopic processes are strongly coupled and these couplings must be taken into account in macroscopic solidification modeling.

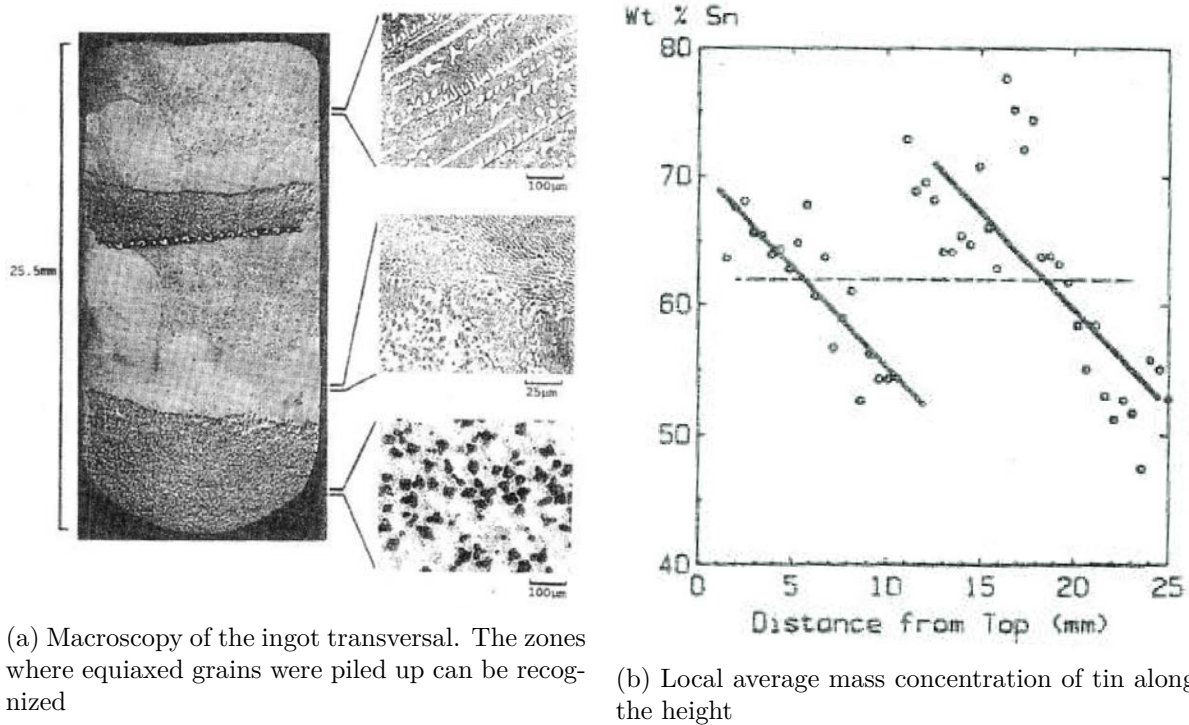
Macroscopic solidification modeling was initially conducted using a *multi region* or *multi domain* approach, in which each phase was circumscribed only in one domain while the solid/mushy zone/liquid interfacial interactions were implemented by means of boundary conditions [43, 44]. This kind of approach presents limitations when representing complicated or irregular shapes, thus, it was mainly used to model columnar growth. Bennon and Incropera [45] used the classical mixture theory to derive conservation equations that are valid in the whole domain (solid, mush and liquid), overcoming the limitations of the *multi domain* approach. In this approach, the microscopic interactions between the phases are represented by semi-empirical relationships, while the solid-liquid mixture macroscopic properties are assigned in a phenomenological manner [46]. This work will use the *Volume Averaging Method*, a formulation with which it is possible to derive macroscopic conservation equations for each phase (solid and liquid) from local (microscopic) equations. This makes it possible to naturally incorporate the effect of microscopic phenomena on macroscopic scales. This approach has been extensively used in the literature for solidification modeling, as it will be presented later on. In Section 1.1.2, a detailed description of the averaging process is given.

1.1.1 Macrosegregation

Macrosegregation is defined as the large-scale heterogeneities in chemical composition produced during solidification. These heterogeneities are not desired since they produce variations in the mechanical properties of the material, or in more severe cases, freckles (channels of segregation). Most of the time, macrosegregation can not be solved by means of homogenization treatments in solid state since the solute heterogeneities are present at the product scale.

The root cause of macrosegregation is the relative movement between the phases, as they do not transport the same amount of solute. This relative movement can be driven by equiaxed grain movement, liquid thermosolutal convection, liquid movement by solidification shrinkage or solid network deformation [47]. In this section, only the two firsts will be discussed since they are the most relevant for the future results interpretation.

- **Equiaxed grain movement:** If the local thermal and solute undercoolings are favorable for grain nucleation, equiaxed grains appear in the fully liquid region. These grains sediment, float or are entrained by liquid convection, depending on the surrounding hydrodynamic conditions.



(a) Macroscopy of the ingot transversal. The zones where equiaxed grains were piled up can be recognized

(b) Local average mass concentration of tin along the height

Figure 1.2 – Effect of the grain movement on macrosegregation in a case of Pb-Sn. A stainless steel mesh was placed at the half-height of the mold (de Groh [48]).

Along with grain movement, the equiaxed grains grow dendritically or globularly depending on the local solidification conditions. A more dendritic equiaxed grain presents a larger and more elongated primary arms with respect to a globulitic equiaxed grain. The grain morphology affects the way by which the grains move: a more dendritic grain will respond faster to changes in the liquid flow and will sediment slower than a globular one.

In the end of solidification, the grains can end up located far from the place where they nucleated, leading to heterogeneities in solute concentration.

The experimental work of de Groh [48] is a clear example of how grain motion creates macrosegregation. He solidified a small eutectic PbSn ingot in a mold with a permeable stainless steel mesh located at its half-height. A postmortem analysis revealed the presence of globular equiaxed grains in the lower zone of the ingot, as well as, just above the mesh as shown in Fig. 1.2a. As expected, in these zones, an impoverishment of solute with respect to the nominal concentration took place, as shown in Fig. 1.2. In this case, the main cause of macrosegregation was the sedimentation of grains lean in solute.

- **Liquid thermosolutal convection:** When the equiaxed grains are packed forming a consolidated porous medium or when they grow from cold walls in the form of columnar structures, the solid phase is fixed in the domain (motionless). In these cases, the

movement of liquid can transport solute throughout the solidification domain, leading to solute concentration heterogeneities. The thermal and solutal gradients produce spatial differences in the liquid density, leading to a thermosolutal buoyancy driven liquid convection. In this section, a Boussinesq approximation [49] will be used to model the relation between liquid density, temperature and solute concentration in the liquid:

$$\rho_l = \rho_{ref} [1 - \beta_T (T - T_{ref}) - \beta_C (C_l - C_{ref})] \quad (1.1)$$

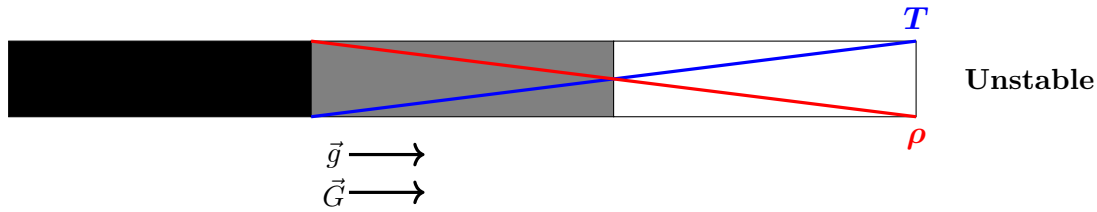
Where ρ_l is the liquid density, β_T the thermal expansion coefficient, β_C the solutal expansion coefficient, T the temperature, C_l the solute concentration in liquid and ρ_{ref} is the reference liquid density at a given reference temperature, T_{ref} , and at a given reference solute concentration in liquid, C_{ref} . Depending on the type of alloy, with an increase in solute concentration, the liquid density can increase or decrease ($\beta_C < 0$ or $\beta_C > 0$ respectively). On the other hand, an increase in temperature usually leads to a decrease in liquid density ($\beta_T > 0$). To illustrate the liquid movement, in a first instance, only thermal effects in a one-dimensional binary alloy solidification will be considered. Two configurations are shown in Fig. 1.3. In the first configuration, the temperature gradient is parallel (same direction) to the gravity acceleration, while in the second configuration, it is antiparallel. The first configuration is unstable since the liquid will tend to move from deep in the mushy zone towards the fully liquid region due to thermal buoyancy forces. On the other hand, in the second configuration the liquid will be motionless since it is hydrodynamically equilibrated.

When the solute effect is added in Eqn. 1.1 ($\beta_C \neq 0$), the previous analysis becomes more complex and a criterion of stability for liquid convection in the mushy zone can not be easily defined. Considering infinitely fast microscopic solute diffusion in both phases, the solute concentration in liquid and the temperature in the mushy zone, can be related by $T = T_f + m_l C_l$ in case of a binary alloy, where T_f is the melting temperature of the pure substance, m_l the *liquidus* slope from the phase diagram and C_l the solute concentration in the liquid. With this relation, Eqn. 1.1 can be re-written:

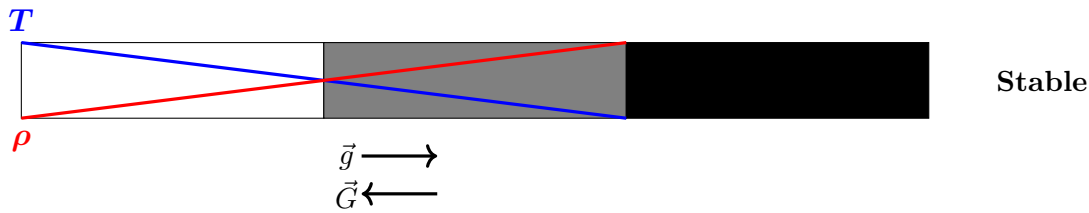
$$\rho_l = \rho_{ref} \left[1 + \beta_T T_{ref} + \beta_C C_{ref} + \frac{\beta_C T_f}{m_l} \right] - \rho_{ref} \left(\beta_T + \frac{\beta_C}{m_l} \right) T \quad (1.2)$$

The first term in the RHS of Eqn. 1.2 is constant and its value depends only on the type of alloy. The second term in the RHS depends on the temperature and on $\beta_T + \frac{\beta_C}{m_l}$ which is constant and also depends on the type of alloy. With this information, a stability criteria for liquid convection can be defined in the mushy zone:

- $\beta_T + \frac{\beta_C}{m_l} > 0$: In these alloys, liquid density in the mushy zone ρ_l decreases when the temperature increases, such as in the purely thermal case shown in Fig. 1.3. An unstable liquid convection will be produced when the thermal



(a) Thermal gradient and gravity acceleration are parallel oriented



(b) Thermal gradient and gravity acceleration are anti-parallel oriented

Figure 1.3 – Two 1D illustrative cases with different orientation between thermal gradient \vec{G} and gravity \vec{g} . Each case has a solid (black), mush (gray) and liquid (white) regions. No solutal buoyancy effects considered.

gradient \vec{G} and gravity \vec{g} are parallel.

- $\beta_T + \frac{\beta_C}{m_l} < 0$: In these alloys (e.g. Fe-C or Pb-Sn alloys), the liquid density in the mushy zone ρ_l increases when the temperature increases. An unstable configuration is produced when the thermal gradient \vec{G} and the gravity \vec{g} are anti-parallel. The focus of this work is put on the solidification of Titanium aluminum alloys that also belong to this category.

Indeed, liquid thermosolutal convection can generate macrosegregation since the liquid transport solute throughout the solidification domain. A one-dimensional case was characterized in order to illustrate the origin of liquid movement, however, a real solidification process has three-dimensional aspects, thus, gravity and thermal and solutal gradients are not necessarily aligned. This adds more complexity in the study of solidification. Liquid convection can become even more complex in the presence of volumetric external forces, such as magnetic fields or non-inertial forces.

Hebditch and Hunt [50] solidified two ingots – one of Sn-5wt.%Pb and the other of Pb-48 wt.%Sn – in a parallelepiped mold of 6 cm high, 10 cm long and 1.3 cm thick, that was completely thermally insulated, except for one narrow side face in which the ingots were cooled down. In a post-mortem analysis, it was verified that only columnar growth took place, therefore, the macrosegregation was entirely caused by liquid convection. Figure 1.4 presents the segregation map for both samples. In case of Sn-5 wt.%Pb, a lead rejection from the cold side (left) took place and therefore, an increase of the local liquid density just ahead the columnar front. This density change

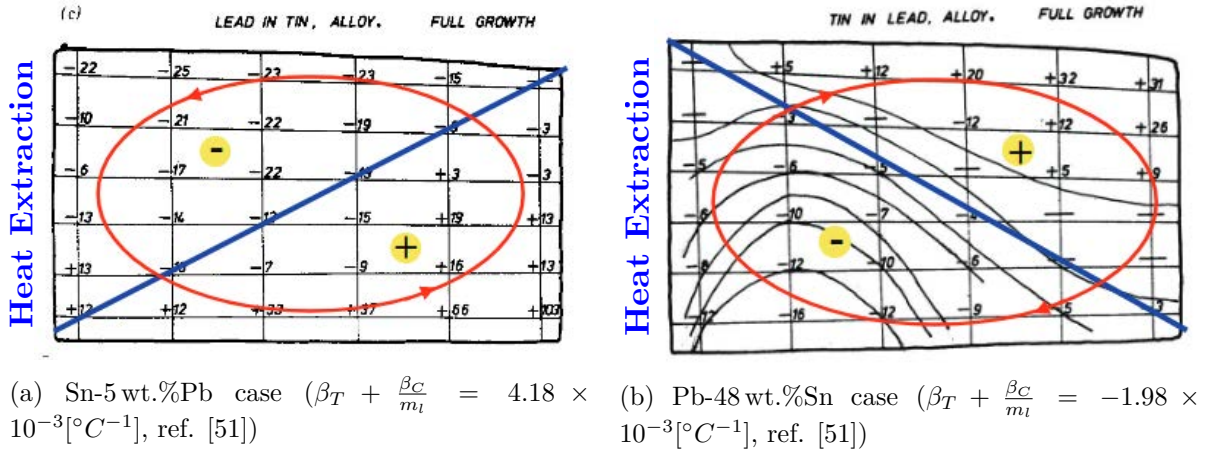


Figure 1.4 – Segregation maps reported by Hebditch and Hunt [50]. Red circle shows the main sense of the liquid flow.

drove an anti-clockwise liquid convection circulation (shown in red). In this case, the solutal effect was reinforced by the thermal effect. In case of Pb-48 wt.%Sn, the tin, that was rejected by the growing solid, made the liquid lighter ahead the columnar front, counteracting the thermal effect and leading to a liquid convection with a clockwise circulation. The final segregation showed that in case of Sn-5 wt.%Pb, the ingot lower-right zone was rich in lead while the upper-left was poor (as represented by the blue line), while in case of Pb-48 wt.%Sn, the final segregation map was in the other way around. This study is a clear example of how liquid thermosolutal convection can produce macrosegregation.

1.1.2 Volume averaging method

To address macroscopic solidification modeling, several authors have adopted the “Volume Averaging Method” which allows resolving averaged fields at the macroscopic scale, while the microscopic diffusion processes are accounted for by source terms which are figured in the macroscopic equations. Authors, like Drew [52] or Ishii and Hibiki [53], developed the averaging methodology in a general way to be applied on multiphase transport. Beckermann and Viskanta [5], Ganesan and Poirier [6], Ni and Beckermann [7] and Wang and Beckermann [54, 55, 56] introduced the averaging process in solidification modeling, accounting for solute diffusion and grain growth at microscopic scales, while momentum, energy and solute conservation at macroscopic scales. The objective of using macroscopic averaged equations is to represent the multiscale system on the macroscopic scale. For the volume averaging process to be valid, a scale separation between micro- and macro- scales is required.

The averaging of the equations is done over a “Representative Elementary Volume” (REV), as shown in Fig. 1.5. The REV should be small enough to account for averaged quantities as a continuum in the global system and large enough to achieve a good average of microscopic scales. Each phase k occupies a volume V_k that is delimited by an area A_k in the control volume

V_c where \vec{w}_k is the solid-liquid interface velocity. Using an averaging procedure, the description for columnar or equiaxed grain growth throughout the solidification domain can be adapted using different constitutive relations [54].

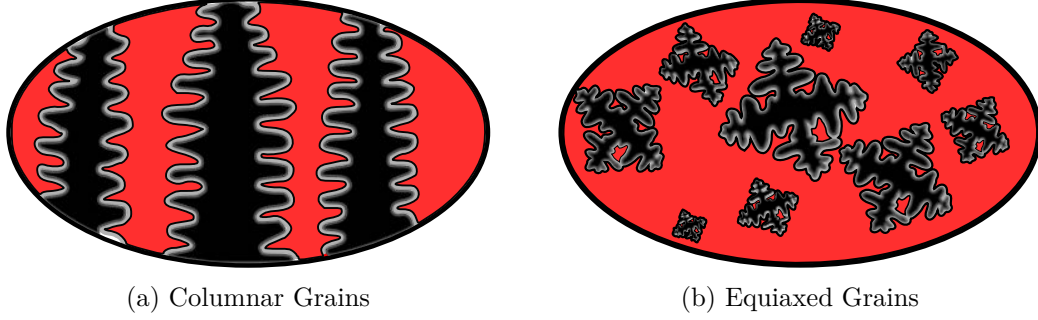


Figure 1.5 – Representative elementary volume (REV) for the representation of columnar and equiaxed grains (adapted from [7])

In the method, the definition of some averaged physical quantity ψ over the REV, in the phase k is defined as:

$$\langle \psi_k \rangle = \frac{1}{V_c} \int_{V_c} X_k \psi_k dV \quad (1.3)$$

where X_k is the phase function, which is equal to one inside the phase k and zero elsewhere. In the same way, the averaged physical quantity ψ , which is present in the phase k , is called the intrinsic average and can be written as:

$$\langle \psi_k \rangle^k = \frac{1}{V_k} \int_{V_k} X_k \psi_k dV \quad (1.4)$$

The averaged value $\langle \psi_k \rangle$ can be related to the intrinsic average $\langle \psi_k \rangle^k$ as:

$$\langle \psi_k \rangle = g_k \langle \psi_k \rangle^k \quad (1.5)$$

Where $g_k = \frac{V_k}{V_c}$ is the volume fraction of the phase k in the volume V_c . The sum of the volumetric fraction of all the phases in the representative elementary volume must be equal to unity: $\sum_k g_k = 1$. With these relations, three theorems can be written [7]:

$$\left\langle \frac{\partial \psi_k}{\partial t} \right\rangle = \frac{\partial \langle \psi_k \rangle}{\partial t} - \frac{1}{V_c} \int_{A_k} \psi_k \vec{w}_k \cdot \vec{n}_k dA \quad (1.6)$$

$$\langle \nabla \psi_k \rangle = \nabla \langle \psi_k \rangle + \frac{1}{V_c} \int_{A_k} \psi_k \vec{n}_k dA \quad (1.7)$$

$$\langle \nabla \psi_k \rangle = g_k \nabla \langle \psi_k \rangle^k + \frac{1}{V_c} \int_{A_k} \hat{\psi}_k \vec{n}_k dA \quad (1.8)$$

Where $\hat{\psi}_k = (\psi_k - \langle \psi_k \rangle^k) X_k$ is the fluctuation component of the quantity ψ_k , \vec{w}_k the velocity of the solid-liquid interface and \vec{n}_k the vector normal to the solid-liquid interface.

With the averaging process and Equations 1.6,1.7 and 1.8 it is possible to write averaged equations that are valid in the whole domain and for each phase k . Supplementary terms, which are related to the interfacial balances (between the different phases) and the fluctuating component, arise in these equations. The terms related to interfacial balances should be properly modeled, while terms related to the fluctuating component are usually considered equal to zero for simplicity. Depending on the study case, some terms can be neglected according to the physical description and the initial assumptions.

1.1.3 Microscopic modeling

Two types of microstructure can be formed during solidification of metallic alloys: (1) columnar structures, that grow from the mold walls following the thermal gradient and (2) equiaxed grains that can nucleate in the fully liquid region from columnar fragments, particles intentionally added or impurities. The growth of these structures is mainly governed by solute diffusion processes at the solid-liquid interface [57].

In macroscopic solidification modeling (product scale), the solid-liquid interface of the microstructures can not be solved explicitly. Instead, the microstructures and their growth are described in a volume-averaged way. In order to model the growth of equiaxed grains in macroscopic simulations, two approaches can be found in the literature:

- **Two-phase model:** Prakash [58, 59] proposed a model for binary solid-liquid phase change. Later, Ni and Beckermann [60] extended Prakash work and include it to describe growth kinetics of globular grains, in a model accounting for equiaxed grain movement and liquid thermosolutal convection by using the volume averaging method approach. Ludwig and Wu [33] also performed macroscopic simulations accounting for grain movement and liquid thermosolutal convection. In their work they assumed spherical morphology for the grains and that the grain growth rate was proportional to the solutal undercooling. Wu and Ludwig [61, 62] modeled the solute diffusion at microscopic scales using relations for the solid-liquid interface velocity for spherical and columnar grains. Once the solid-liquid interface velocity was known, the grain growth rate could be calculated. They also modeled the CET occurrence, equiaxed grain motion, liquid thermosolutal convection and columnar and equiaxed growth. Wu et al. [63] used a mass balance equation at microscopic scales along with a relation to calculate the solid-liquid interface velocity. This approach enabled the description of the grain growth rate in cases of solidification of ternary alloys. Combeau et al. [38] used a two-phase approach to understand the influence of the equiaxed grain morphology on the macrosegregation of large steel ingots. In their work, the equiaxed grains were surrounded by an envelope. The growth of the envelope was calculated by the Kurz-Giovanola-Trivedi (KGT) tip velocity model [64], whereas the phase change was controlled by solute diffusion in both phases. Although the use of the concept of “grain envelope”, this work uses a two-phase approach: the intradendritic liquid, which is present inside the envelopes, and extradendritic liquid, which is present out-

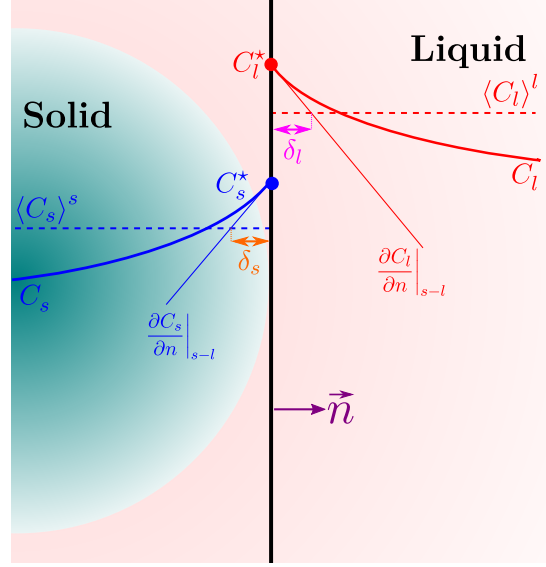


Figure 1.6 – Schematic of solute diffusion at solid-liquid interface in the two-phase approach for microscopic modeling.

side the envelopes, were not considered as separated phases. Založnik and Combeau [65] calculated the grain growth rate by means of a solute balance at the mobile solid-liquid interface. This approach was formulated for multicomponent alloys and has been adopted in SOLID[®] software. The solute balance in the solid-liquid interface is given by:

$$\Gamma_s (C_l^* - C_s^*) = \rho_s S_v D_s \left. \frac{\partial C_s}{\partial n} \right|_{s-l} - \rho_l S_v D_l \left. \frac{\partial C_l}{\partial n} \right|_{s-l} \quad (1.9)$$

Where $\Gamma_s = \frac{\partial}{\partial t} (\rho_s g_s)$ is the mass rate of solid growth (in $\frac{\text{kg}}{\text{s m}^3}$), C_s^* and C_l^* the equilibrium solute concentration at solid-liquid interface in the solid and liquid phases, respectively, D_s and D_l the solid and liquid diffusion coefficients, respectively, S_v the grain specific surface area and $\left. \frac{\partial C_s}{\partial n} \right|_{s-l}$ and $\left. \frac{\partial C_l}{\partial n} \right|_{s-l}$ the gradient of solute concentration in the solid and liquid sides, respectively. Figure 1.6 shows a schematic of the solute balance at the solid-liquid interface for a two-phase model (globular model).

The solute concentration gradients at the solid-liquid interface can be approximated as:

$$\left. \frac{\partial C_s}{\partial n} \right|_{s-l} = \frac{C_s^* - \langle C_s \rangle^s}{\delta_s} \quad (1.10)$$

$$\left. \frac{\partial C_l}{\partial n} \right|_{s-l} = \frac{\langle C_l \rangle^l - C_l^*}{\delta_l} \quad (1.11)$$

Where δ_s and δ_l are appropriate diffusion lengths.

- **Three-phase model (dendritic grains):** The two-phase model is usually used to depict globular grains or cylindrically shaped columnar structures. Rappaz and Thévoz

[66] proposed a solute diffusion model for equiaxed dendritic growth. For that, they introduce the concept “grain envelope”, which is a container of a solid skeleton filled by intradendritic liquid. The envelope, at the same time, is surrounded by extradendritic liquid. In this way, it is possible to improve the representation of the microscopic solute diffusion process by accounting for two types of liquid. This type of model assumes a predefined shape for the grain envelopes, *e.g.* spherical, octahedral, cylindrical, etc. An envelope grows according to a tip velocity model and their predefined morphology. On the other hand, the solid contained by an envelope grows according to the local energy balance and the solute diffusion at microscopic scales. This difference allows not only estimating grain size, but also grain morphology. The estimation is made by means of the internal solid fraction, which is the ratio between solid fraction and envelope fraction. A higher internal solid fraction indicates a more “globulitic” grain, whereas a lower internal fraction indicates a more “dendritic” one [67]. The mathematical expression for the internal solid fraction is:

$$g_i = \frac{g_s}{g_e} \quad (1.12)$$

where g_e is the envelope fraction. Wang and Beckermann [54], using a volume averaging approach, implemented this growth model in a macroscopic model accounting for nucleation, thermal and solute undercoolings and grain packing. Heyvaert et al. [39] also use the three-phase model to predict microstructure and macrosegregation in a direct chill cast Al-Cu billet. This grain growth kinetics model requires the resolution of the intradendritic liquid solute balance. Considering that the intradendritic liquid is perfectly mixed as proposed in ref. [66], the balance is given by:

$$\Gamma_s (C_l^* - C_s^*) - \rho_l g_{li} \frac{\partial C_l^*}{\partial t} = \rho_s S_v^S D_s \left. \frac{\partial C_s}{\partial n} \right|_{s-l_i} - \rho_l S_v^E D_l \left. \frac{\partial C_l}{\partial n} \right|_{l_i-l_e} \quad (1.13)$$

Where g_{li} is the intradendritic liquid fraction, S_v^E and S_v^S the envelope and solid specific surface area respectively and $\left. \frac{\partial C_s}{\partial n} \right|_{s-l_i}$ and $\left. \frac{\partial C_l}{\partial n} \right|_{l_i-l_e}$ the gradient of solute concentration at the solid - intradendritic liquid interface and at the intradendritic liquid - extradendritic liquid interface. Fig. 1.7 shows a schematic of the solute balance in the intradendritic liquid.

In Eqn. 1.13 the gradients of solute concentration can be approximated similarly to Eqns. 1.10 and 1.11. In order to obtain the solid growth rate, Eqn. 1.13 requires to be solved along with constitutive geometrical relations, models for both the diffusion lengths and the local energy balance. This leads to a non-linear system of equations. Furthermore, as mentioned before, this model also requires the resolution of a tip velocity model with which the envelope growth rate can be calculated. In literature, the hemispherical tip velocity model [68] and the paraboloidal tip velocity model [69, 70, 71] have been typically used. A detailed description of the formulation used in SOLID[®]

$\rho_l \neq \rho_s$ and $\rho_k = cte$. The buoyancy forces are modeled by means of a thermosolutal Boussinesq approximation.

Along with the solid and liquid momentum equations, the total mass conservation must be respected throughout the domain:

$$\frac{\partial}{\partial t} (g_s \rho_s + g_l \rho_l) + \nabla \cdot (g_s \rho_s \langle \vec{v}_s \rangle^{sf} + g_l \rho_l \langle \vec{v}_l \rangle^{lf}) = 0 \quad (1.15)$$

The mass conservation for the phase k can be written as:

$$\frac{\partial}{\partial t} (g_k) + \nabla \cdot (g_k \langle \vec{v}_k \rangle^{kf}) = \frac{1}{\rho} (\Gamma_k + \Phi_k) \quad (1.16)$$

Where Γ_k is the mass transfer rate to phase k due to phase transformation and Φ_k to grain nucleation.

In order to fully describe the physics behind the momentum conservation (Eqn. 1.14), additional constitutive models are needed to formulate the terms at the RHS of the equation:

- **Pressure term** ($\nabla \langle p_k \rangle^k$): Mechanical equilibrium is assumed, hence, the pressure in both phases is considered to be equal.

$$\langle p_l \rangle^l = \langle p_s \rangle^s = p \quad (1.17)$$

- **Stress term** ($\nabla \cdot (g_k \langle \tau_k \rangle^{kf})$): Ni and Beckermann [7, 60], performed an averaging procedure, modeled the shear stress as:

$$g_k \langle \tau_k \rangle^{kf} = \mu_k \left\{ \nabla \cdot (g_k \langle \vec{v}_k \rangle^{kf}) + \left[\nabla \cdot (g_k \langle \vec{v}_k \rangle^{kf}) \right]^t - \langle \vec{v}_s \rangle^{sf} \nabla g_k - \nabla g_k \langle \vec{v}_s \rangle^{sf} \right\} \quad (1.18)$$

Where μ_k is the dynamic viscosity of the phase k . Later, Wang and Beckermann [55] neglected the contributions of the phase fraction gradients ∇g_k in case of modeling liquid thermosolutal convection and equiaxed grain movement. In case of columnar growth, where $\langle \vec{v}_s \rangle^s = 0$, Bousquet-Melou et al. [46] justify that the intradendritic liquid is subjected to the strong effect of the interfacial drag, therefore, the viscous effects related to phase gradients are negligibly small. In this work, in a similar way to [55], the viscous dissipation in the phase k will be modeled as:

$$\nabla \cdot (g_k \langle \tau_k \rangle^{kf}) = \nabla \cdot (g_k \mu_k \nabla \langle \vec{v}_k \rangle^{kf}) \quad (1.19)$$

In case of the solid phase, the solid viscosity has been neglected for simplicity in several studies [65, 34, 75]. In this work, the expression derived by Ishii [76, 53] will be used:

$$\mu_s = \frac{\mu_l}{g_e} \left[\left(1 - \frac{g_e}{g_{ep}^{\max}} \right)^{-2.5 g_{ep}^{\max}} - (1 - g_e) \right] \quad (1.20)$$

Where g_{ep}^{\max} is the maximum envelope/solid fraction packing, usually considered equal to 0.6 as the maximum fraction of monodisperse spheres random packing. In all models described above, turbulent dissipation is not accounted for.

- **Gravitational term** ($\frac{g_k}{\rho_k} \rho_k^b \vec{g}^f$): This term represents the buoyancy force due to differences of temperature and solute concentrations. If a linear approximation is considered, ρ_k^b can be written as:

$$\rho_k^b = \rho_{ref} \left[1 - \beta_T (T - T_{ref}) - \beta_C (\langle C_l \rangle^l - C_{ref}) \right] \quad (1.21)$$

Where T_{ref} and C_{ref} are reference temperature and solute concentration respectively and β_T and β_C the thermal and solutal expansion coefficients respectively.

- **Interfacial drag term** (\vec{M}_k^{df}): During solidification two different convection regimes can take place. The first one is when equiaxed grains move freely in the liquid, so that, liquid and solid movement is represented by Eqn. 1.14. This convection regime is called *slurry flow* [7, 77]. The second one is called *porous flow* and occurs when grains are packed, forming a consolidated porous region, in which the liquid can flow through. In this regime, the solid velocity is equal to the velocity of its frame (in practice, the container or mold) while the liquid movement is represented by Eqn. 1.14. The transition between these two regimes has been modeled in several ways. For example, Založnik et al. [65] or Heyvaert et al. [39] used a sharp transition. Nguyen et al. [34] used a smooth transition due to discontinuities issues in the numerical implementation. In both cases, the transition depended on the solid packing fraction – in case of two-phase microscopic modeling – or the envelope packing fraction – in case of three-phase microscopic modeling. It is important to note that the packing fraction is a poorly known parameter for non-spherical grains. New insight was given by Olmedilla et al. [31, 32] who investigated the influence of grain morphology and of hydrodynamic conditions on the equiaxed grain packing phenomena.

Indeed, the interfacial drag force that arises due to the difference of solid and liquid velocities, strongly depends on the flow regime. In case of slurry flow regime, this term can be modeled as:

$$\vec{M}_s^{df} = -\vec{M}_l^{df} = \frac{3g_e \rho_l C_d}{4d_g} \left| \langle \vec{v}_l \rangle^{lf} - \langle \vec{v}_s \rangle^{sf} \right| \left(\langle \vec{v}_l \rangle^{lf} - \langle \vec{v}_s \rangle^{sf} \right) \quad (1.22)$$

Where d_g is the equivalent spherical diameter of grain envelope and C_d the drag coefficient which can be calculated as given by Ni and Beckermann [60]. The envelope fraction g_e , in Eqn. 1.22 can be replaced by solid fraction g_s in case of using a globular model.

On the other hand, in the porous flow regime, the interfacial drag depends on the permeability and the morphology of the porous media. The hydrodynamic permeability can be modeled by the Kozeny-Carman relation:

$$K = \frac{g_l^3}{(1 - g_l)^2} \frac{l_c^2}{\pi^2 K_k \tau^2} \quad (1.23)$$

where K_k is the Kozeny constant, l_c a characteristic length of porosity and τ the porous media tortuosity. Values for a packed bed of sphere are commonly used: $K_k = 5$ and $\tau = \frac{6}{\pi}$. Finally, following the Darcy's law, the interfacial drag force is given by:

$$\vec{M}_l^{df} = \frac{g_l^2 \mu_l}{K} [\langle \vec{v}_l \rangle^{lf} - \langle \vec{v}_s \rangle^{sf}] \quad (1.24)$$

In case of motionless frames (fixed molds or containers), $\langle \vec{v}_s \rangle^{sf} = 0$.

- **Phase change term** ($\vec{M}_k^{\Gamma f}$): This term accounts for the momentum exchange due to solid growth or solid remelting. The exact expression of this term, following the averaging methodology, is:

$$\vec{M}_k^{\Gamma f} = -\frac{1}{V_c} \int_{A_k} \rho_k \vec{v}_k (\vec{v}_k - \vec{w}_k) \cdot \vec{n}_k dA \quad (1.25)$$

Where \vec{v}_k is the velocity of the phase k , \vec{w}_k the solid-liquid interface velocity, A_k the close surface equivalent to the solid-liquid interface and \vec{n}_k the unitary vector normal to the moving interface. Considering that the average fluctuating solid velocity is negligibly small, this term can be modeled as:

$$\vec{M}_s^{\Gamma f} = -\vec{M}_l^{\Gamma f} = \langle \vec{v}_s \rangle^{sf} \Gamma_s \quad (1.26)$$

- **Grain nucleation term** ($\vec{M}^{\phi f}$): The contribution of nucleation of new grains to the momentum transfer between the solid and liquid phases is negligibly small, hence, it can be neglected in the momentum balance, thus:

$$\vec{M}^{\phi f} = 0 \quad (1.27)$$

1.1.4.2 Solute balance

Neglecting the solute diffusion at macroscopic scales, the solute balance equation in the phase k is given by:

$$\frac{\partial}{\partial t} (g_k \rho_k \langle C_k \rangle^k) + \nabla \cdot (g_k \rho_k \langle C_k \rangle^k \langle \vec{v}_k \rangle^{kf}) = (J_k^j + J_k^\Gamma + J_k^\Phi) \quad (1.28)$$

Where J_k^j , J_k^Γ and J_k^Φ are the interface solute exchange due to diffusion, grain growth and grain nucleation, respectively. Their exact expression, following the volume averaging method, and the way to model them is presented below. Note that the interfacial solutal exchanges, due to diffusion and growth, are given by the interfacial solute balance as presented in Sec. 1.1.3.

– **Solute diffusion**

$$J_k^j = -\frac{1}{V_c} \int_{A_k} \vec{j}_k^j \cdot \vec{n}_k dA \approx S_v D_k \rho_k \left. \frac{\partial C_k}{\partial n} \right|_{s-l} \approx S_v D_k \rho_k \frac{C_k^* - \langle C_k \rangle^k}{\delta_k} \quad (1.29)$$

where S_v is the grain specific surface area, which is defined as the surface of the solid-liquid interface per cubic meter, and δ_k is the diffusion length, which is used to approximate the solute gradient at the solid-liquid interface. Both quantities require to be represented by a proper model (for more details, see Sect. 4.2.1.1).

– **Solid growth**

$$J_k^\Gamma = -\frac{1}{V_c} \int_{A_k} \rho_k C_k (\vec{v}_k - \vec{w}_k) \cdot \vec{n}_k dA \approx \Gamma_k C_k^* \quad (1.30)$$

– **Grain nucleation**

$$J_s^\Phi = -J_l^\Phi \approx \Phi_s k_p \langle C_l \rangle^l \quad (1.31)$$

where Φ_s is the mass transformation rate from liquid to solid due to nucleation and k_p is the partition coefficient.

1.1.4.3 Energy balance

The energy balance for phase k , in terms of the averaged enthalpy, is given by:

$$\frac{\partial}{\partial t} (g_k \rho_k \langle h_k \rangle^k) + \nabla \cdot (g_k \rho_k \langle h_k \rangle^k \langle \vec{v}_k \rangle^k) = \nabla \cdot (g_k k_k \langle \nabla T_k \rangle^k) + (Q_k + Q_k^\Gamma + Q_k^\Phi) \quad (1.32)$$

Where $\langle h_k \rangle^k$ is the intrinsic averaged enthalpy of the phase k (in $\frac{J}{kg}$) and Q_k , Q_k^Γ and Q_k^Φ the interfacial energy exchange between the phases due to diffusion, grain growth and grain nucleation. As discussed by Dantzig and Rappaz [57], scaling analysis shows that the temperature of the different phases at the microstructure scale can be considered identical, $T_s = T_l = T$ for normal solidification times (minutes or hours). In addition, the sum of all the interfacial energy exchanges between the phases must be equal to zero due to energy conservation ($\sum_k (Q_k + Q_k^\Gamma + Q_k^\Phi) = 0$). Indeed, adding both, the solid and liquid averaged energy conservation equations, a simplified version of Eqn. 1.32 can be written:

$$\frac{\partial}{\partial t} (\bar{\rho} \langle h \rangle) + \nabla \cdot (g_s \rho_s \langle h_s \rangle^s \langle \vec{v}_s \rangle^s + g_l \rho_l \langle h_l \rangle^l \langle \vec{v}_l \rangle^l) = \nabla \cdot (k \nabla T) \quad (1.33)$$

Where $\langle h_l \rangle^l = c_p T + L_f$ is the intrinsic averaged liquid enthalpy, $\langle h_s \rangle^s = c_p T$ the intrinsic averaged solid enthalpy, L_f the latent heat, $k = g_l k_l + g_s k_s$ the averaged thermal conductivity, $\bar{\rho} = g_l \rho_l + g_s \rho_s$ the averaged density and $\langle h \rangle = c_p T + \frac{g_l \rho_l L_f}{\bar{\rho}}$ the averaged specific enthalpy.

In this model, the specific heat is considered constant and equal in solid and liquid phases:

$$c_{p_l} = c_{p_s} = c_p.$$

1.1.4.4 Volumetric grain and nuclei density and envelope conservation:

The grains can grow from a chill wall, in form of columns, or from nuclei in the fully liquid region, in form of equiaxed grains. A nucleus is a precursor or seed for the nucleation of a grain. The nuclei can be of different types depending on their origin (fragments of the columnar region, inoculated particles or impurities) and size, thus, their nucleation undercoolings can be different. Bedel et al. [78] investigated the impact of the nuclei movement on the microstructure and on macrosegregation in direct chill casting of aluminum alloys. For that, they considered that the nuclei were advected by the liquid phase, solving a nuclei population balance. This balance is given by:

$$\frac{\partial}{\partial t} N^i + \nabla \cdot (\langle \vec{v}_l \rangle^l N_{nuc}^i) = -\dot{N}_i \quad (1.34)$$

Where N is the nuclei density, which is defined as the number of nuclei per cubic meter and \dot{N} is the grain nucleation rate. The superscript i denotes each type of nuclei.

When nucleation occurs, equiaxed grains appear in the fully liquid region. In order to obtain geometrical information about the equiaxed grains, it is necessary to solve for the conservation of the volumetric grain density. For example, it is possible to relate the solid fraction to the averaged grain radius R by $g_s = \frac{4}{3} N_g \pi R^3$ (in case of two-phase globular model), where N_g is the volumetric grain density. The volumetric grain density is advected by the solid phase and its conservation equation is given by a population balance:

$$\frac{\partial}{\partial t} N_g + \nabla \cdot (\langle \vec{v}_s \rangle^s N_g) = \sum_{i=1}^m \dot{N}_i \quad (1.35)$$

The RHS of Eqn. 1.35 is a sum of source terms where \dot{N}_i represents the nucleation rate of nuclei type i .

Only for a three-phase microscopic model, in addition to solve the volumetric grain density and volumetric nuclei density conservation equations, it is required to solve for the envelope balance. By doing this, information about the intradendritic liquid, g_{li} , and extradendritic liquid, g_{le} , fractions can be obtained. The envelope fraction, g_e , balance is given by:

$$\frac{\partial g_e}{\partial t} + \nabla \cdot (g_e \langle \vec{v}_s \rangle^s) = (\Gamma_e + \Phi_e) \quad (1.36)$$

Where Γ_e is the volumetric envelope growth rate and Φ_e the instantaneous volumetric contribution to the envelope fraction due to nucleation.

1.1.5 Coupling micro/macro modeling: Operator-splitting method for the solution of the coupled equations

The solidification model previously presented leads to a complex system of coupled partial differential equations. This system must be solved consistently to ensure precision and numerical stability on all computed fields. In literature, it is usually mentioned that iterative methods are used to couple the system of equations without further explanation. Založnik and Combeau [65, 79] proposed an operator-splitting scheme for the solution of the coupled system which basically consists in the scale separation (micro/macro) at the solution level.

They proposed a temporal scheme that, in a first stage, solves all the advective contributions to the different conservation equations, neglecting all the interfacial exchanges due to grain growth. Next, in a second stage, all interfacial exchange terms are computed by means of a proper grain growth kinetics model. Finally, both contributions, advection and interfacial exchanges, are added as shown in Figures 1.8 and 4.11. For a quantity ϕ , the temporal splitting scheme is given by:

$$\frac{\partial \phi}{\partial t} = A\phi^{tr} + B\phi^{gr} \quad (1.37)$$

Where A and B are the operators describing the advection and grain growth contributions respectively. These contributions are calculated as follows:

$$A\phi^{tr} = \frac{\partial \phi^{tr}}{\partial t} \quad , \quad \phi^{tr}(t_0) = \phi_0 \text{ on } [t_0, t_0 + \Delta t] \quad (1.38)$$

$$B\phi^{gr} = \frac{\partial \phi^{gr}}{\partial t} \quad , \quad \phi^{gr}(t_0) = \phi^{tr}(t_0 + \Delta t) \text{ on } [t_0, t_0 + \Delta t] \quad (1.39)$$

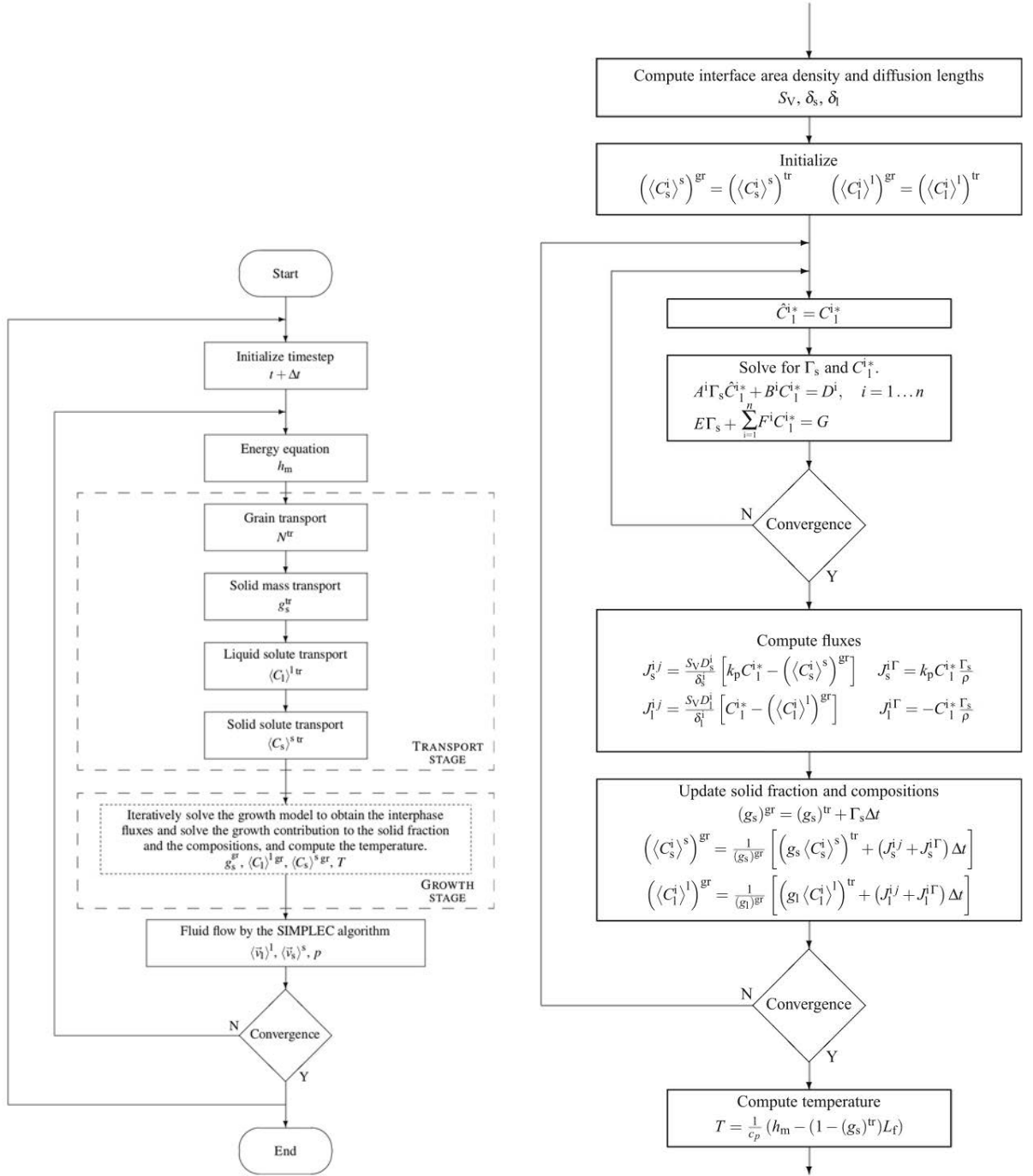
Equations 1.38 and 1.39 introduce a mathematical error that should be small in order to apply the scheme. The authors presented a physical explanation through a scaling analysis where they demonstrated that the error made, using the operator-splitting scheme, is small in case of solidification. The main relation that should be satisfied to probe the viability of the method is:

$$\left(\left| \frac{\partial \phi}{\partial t} \right| \sim |A\phi^{tr}| \right) \gg |B\phi^{gr}| \quad (1.40)$$

Several authors [34, 75, 39] have adopted the operator splitting scheme in solidification modeling. Some of them have modified the transport/growth scheme adding a grain nucleation stage to account for the interfacial exchanges produced when new equiaxed grains appear in the liquid.

1.2 Rotating fluids and centrifugal casting

Various applications of rotating fluids can be found in engineering *e.g.*, turbomachinery development, food processing or centrifugal filtration among others. Moreover, in the last years, this



(a) Global algorithm for solidification modeling using the operator-splitting scheme

(b) Growth stage in the operator-splitting algorithm

Figure 1.8 – Complete algorithm proposed by Založnik and Combeau [65] for solidification modeling. Note that the numerical time integration of the respective operators is separated.

topic has acquired special attention due to its application on geophysical modeling for prediction of climate behavior. On bigger scales, oceans and the atmosphere are good examples of fluids

in rotating systems (considering Earth as their container). Particularly, in the field of materials processing, centrifugation has been experimentally studied to stabilize liquid melt convection during crystal solidification for the production of semiconductors [80, 3]. These studies were mainly conducted in the nineties when numerical methods for multi-scale solidification modeling were still in development. Numerical modeling was only used for the explanation of thermal buoyancy liquid convection without taking into account the effect of solidification.

In order to model numerically fluids in rotating systems, a rotating reference frame is largely used since it allows solving fluid models within a domain which is fixed in space with respect to the observer, avoiding complexities of accounting for the domain rotational movement. When a rotating reference frame is used, the numerical model must be transformed adequately into the new moving coordinate system.

This section, is divided in two parts. In the first part (Sec. 1.2.1), a literature review is conducted about applications that centrifugation has had in materials processing. In the second part (Sec. 1.2.2), the rotating reference frame, for rotating fluids modeling, is presented in order to show the apparition of centrifugal and Coriolis non-inertial accelerations.

1.2.1 Solidification in centrifugal conditions

1.2.1.1 Model alloys with columnar mushy zone

The use of modified gravity forces in solidification to improve the product final quality is not new. Sample and Hellawell [81, 82] conducted solidification experiments of ammonium chloride-water and lead-tin systems, in which cylindrical (80 mm diameter) and slab shaped (140 mm wide and 16 mm thick) containers rotated axially at rates from 0 to 10 rpm about an inclined rotation axis, from 0° to 30° to the vertical. They noticed that it is possible to prevent the formation of segregation channels by changing the direction of the effective gravity with respect to the mold during solidification. The authors explained this effect by the impact that the effective gravity direction has on the liquid thermosolutal convection.

1.2.1.2 Solidification with a planar front in semiconductor processing (no mushy zone)

Directional solidification experiments under centrifugal conditions were conducted by Rodot et al. [80] using a PbTe and PbSnTe alloys which were doped with Ag atoms. Centrifugation was used to reduce the damaging effect of small lateral temperature gradients that occur due to imperfect thermal control of the crucible. In the study case, the axial temperature gradient (along the ampoule) was antiparallel to the centrifugation induced gravity (perpendicular to the rotation axis). Their results showed that increasing the level of centrifugation, the magnitude of Ag macrosegregation also increased due to liquid convection. However, they also reported that in cases with $N = 5g$; $r = 18$ m and $N = 2g$; $r = 5.5$ m (where N is the centrifugal acceleration and r the centrifuge arm size), the segregation profile was similar to the one observed in samples solidified in microgravity. Moreover, an improvement on the surface quality and on crystalline structure was noticed. In their work, they could not explain completely these results, but they

indicate that a “convectionless regime” can be achieved combining properly centrifugation level (centrifuge rotation rate) and centrifuge arm size. In their cases, the “convectionless regime” was produced when $\frac{N}{r} \approx 3$. This study was the first one found that relates the segregation of alloying elements to centrifugation level.

Growth of Te-doped InSb cylindrically-shaped crystals were performed by Müller et al. [3] by using a Bridgman apparatus mounted in a centrifuge. The axial temperature gradient (along the cylinder centerline) was anti-parallel to the total apparent gravity \vec{g}_{tot} , sum of centrifugal and normal terrestrial gravity accelerations, in such a way, that “vertical” Bridgman growth, under variable gravity levels, could be performed. Temperature fluctuations in the thermocouples and striations in the resulting crystal appeared when $1.65g < \vec{g}_{tot} < 2.5g$. Increasing even more the total gravity, $\vec{g}_{tot} > 2.7g$, all temperature fluctuations and crystal striations disappeared. The authors pointed out that a flow regime transition took place in the melt convection when the total apparent gravity was increased. In order to have a better insight of the transition process, several numerical simulations of liquid convection were performed. In the simulations, the cylinder aspect ratio was maintained constant while the temperature gradient and centrifuge rotation speed were varied. All the analysis was given in function of the dimensionless Rayleigh number $Ra = \frac{\vec{g}_{tot}\beta_T\Delta Th^3}{\nu\alpha}$, where β_T is the thermal expansion coefficient, α the thermal diffusivity, ν the viscosity and ΔT the difference across the cylinder length h . The Rayleigh number is defined as the ratio between the time scale for thermal transport via diffusion and the time scale for thermal transport via convection. Two types of flow regime were found and characterized in the numerical study. The regime type I was characterized by a main circulation in the perpendicular plane to the rotation axis with small eddy currents in the corners. The circulation had a rotation sense opposite to the centrifuge. The authors conclude that this regime is quasi-stable since it had a small stability range when different parameters were varied. On the other hand, the regime type II was characterized by a main circulation in the perpendicular plane to the rotation axis and presented the same rotation sense to the centrifuge. This regime had a wide stability range and a much stronger convection compared to the regime type I. Both regimes could be achieved with the same set of Rayleigh, Prandtl, Taylor and aspect ratio. This work was the first one to describe the flow transition in cylinders mounted along centrifuge arms, in solidification cases. Although the importance of this work, the authors did not relate the regime transition with the dimensionless Rossby number, $Ro = \frac{U_{ref}}{2\omega L_{ref}}$ (where U_{ref} is the reference velocity, L_{ref} the reference length scale and ω the centrifuge angular velocity), which quantifies the Coriolis effect. This study demonstrated that the Rayleigh number is insufficient to fully characterize the different types of flow regimes.

1.2.1.3 Natural convection

Ramachandran et al. [2] studied the natural convection during crystal growth in a centrifuge by means of scaling analysis and numerical simulations. From the scaling analysis, the authors recognized that contrary to inertia or centrifugation terms, in Navier-Stokes equations, the Coriolis contribution is independent to geometric scales and varies linearly to the system rotation speed. The Rossby number gives an estimation of the Coriolis effect in the system. A dominant

Coriolis effect takes place when $Ro < 1$, which means that the system time scale, $\frac{L_{ref}}{U_{ref}}$, is larger than the rotation period. In their simulations, an ampoule (cylinder) placed along the centrifuge arm was considered, in such a way, that the centrifugal acceleration was aligned with the cylinder centerline. Two thermal configurations were investigated: (1) top heated and (2) bottom heated with respect to the centrifugal acceleration. They reported that in case of the *configuration 1*, the centrifugal acceleration reduces the magnitude of natural convection within the melt. Moreover, quasi-steady thermal diffusion conditions can be achieved under some circumstances. On the other hand, in *configuration 2*, the authors reported that Coriolis acceleration has a stabilizing effect on the liquid movement by delaying the onset of unsteady convection. This work is important since studies liquid buoyancy driven convection, in similar conditions and geometry, to real processes of crystal growth or metallic alloys solidification.

1.2.1.4 Columnar and equiaxed grain growth

Solidification experiments in a centrifuge using the transparent model alloy Neopentylglycol-(D)Camphor were recently conducted by Zimmermann et al. [83]. Images and videos of the in-situ solidification process were reported. The experiments consisted in directional solidification of a parallelepiped cavity of 10 mm high, 13 mm width and only 3 mm depth. The total apparent gravity (\vec{g}_{tot}) was along the height of the cavity and the flight velocity vector along the sample width. A linear temperature gradient was adjusted anti-parallel to the total apparent gravity, which was ranged from $1g$ (out of centrifuge) to $10g$. The resulting melt flow during solidification could not be characterized due to its complex time dependent 3D structure. However, close to the solidification front, the flow is qualitatively comparable in the different gravity levels studied. Increasing the gravity level, it could be observed that stronger liquid convection took place, the equiaxed grain settling velocity augmented and the CET was produced faster. Moreover, smaller final equiaxed grain microstructure was obtained, since, as the grain settling velocity augmented, the grains did not have sufficient time to grow before they packed ahead the columnar front. In spite of the good experimental characterization, no explanation about the asymmetric equiaxed grain packing front and no further analysis on the liquid thermosolutal convection was given.

Well controlled experiments of directional solidification were conducted within the framework of the GRADECET project, as part of N. Reilly PhD. thesis [1]. Four experiments, with different total apparent gravity (5g,10g,15g and 20g), were carried out in the ESA's "Large Diameter Centrifuge". Additionally, one control experiment was conducted out of the centrifuge accounting only for the normal terrestrial gravity. All experiments consisted in the partial remelting and posterior controlled directional solidification of TiAl cylindrically-shaped samples by using the "power down" technique. The samples were 8 mm in diameter and 165 mm length. The total apparent gravity was antiparallel to the axial temperature gradient since the furnace was free to tilt. Three heaters, located along the cylinder sides, were the responsible for the special furnace protocol. Detailed schematic figures of the furnace and the heaters (see Fig. 3.10 and Fig. 3.8, respectively) along with explanations of the furnace thermal protocol are presented in Chapt. 3. Moreover, the final microstructure of the centrifugally solidified sample is presented in Fig. 4.1 of Chap. 4.

The main conclusions of centrifugal directional solidification can be summarized as:

- The samples centrifugally solidified presented three main zones: first solidified liquid, columnar growth and equiaxed growth.
- The samples solidified under normal terrestrial gravity did not present a CET.
- All the centrifugally solidified samples presented a CET. The position of the CET seems to be independent to the apparent gravity level.
- The size of the equiaxed grains decreases as the level of apparent gravity increases.
- Probably, the Coriolis force has an effect on the motion of equiaxed grains. This hypothesis came up since the radial distribution of equiaxed grains is not homogeneous.
- The equiaxed grains appear in the liquid from fragments of the columnar grains. The fragmentation is due to the remelting of secondary arms of the columnar grains.
- The equiaxed grain motion results from a competition between the apparent gravity, that pushes the grains, which are heavier than the liquid ($\rho_s > \rho_l$), towards the columnar front, and the liquid convection, that entrains the grains away from the columnar front. At high gravity level, $g_{tot} > 5g$, the centrifugal acceleration controls the equiaxed grain motion.

In addition to the well controlled directional solidification experiments, semi-industrial centrifugal casting of TiAl cylindrical ingots was conducted (180 mm long and between 50 mm and 57 mm in diameter). In these trials, the axis of the ingot was aligned to the centrifugal acceleration and the solid grew both, axially and radially. The investigated centrifugal accelerations were around 30g and 24g. It was found that the radial growth had a “seagull wing” shape for low aluminum content, as shown in Fig. 1.9. The probable reason of this particular radial growth shape is believed to be the liquid thermosolutal convection.

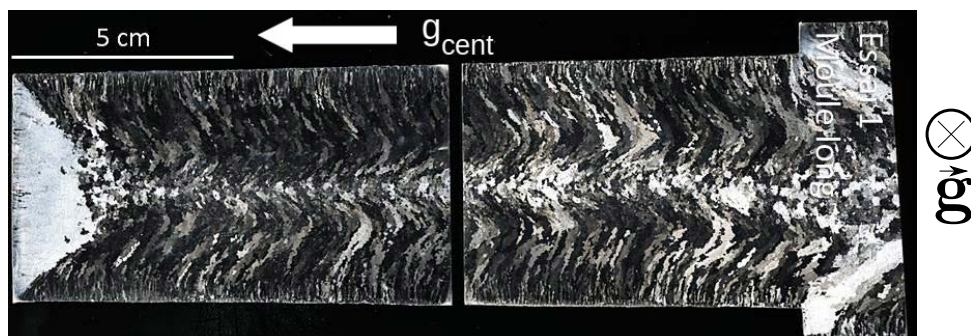


Figure 1.9 – Example of semi-industrial centrifugal casting of TiAl cylindrical ingots. Note the “seagull wing” shape of the radial columnar growth. g_{cent} denotes the direction of the centrifugal acceleration. Vector \vec{g} denotes the direction of the normal terrestrial gravity.

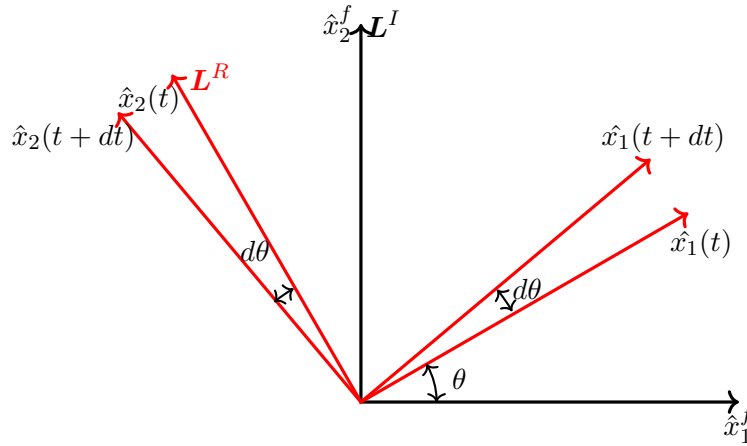


Figure 1.10 – Fixed reference frame (black) and rotating reference frame (red) which is dependent in time. The center of rotation in the fixed coordinate system is $(0,0)$

1.2.1.5 Other processing defects

In a recent study, Yang et al. [84] performed numerical simulations and experiments of centrifugal investment casting of high Nb TiAl low pressure turbine blades of 10 cm long, 4 cm wide and 2 cm thick, approximately. They used the commercial software ProCAST to estimate the shrinkage porosity, defects in mould filling and crack formation due to mechanical stresses. The numerical results and the experiments showed a good agreement in spite of the lack of mathematical rigorousness in the liquid metal model, which neglected the Coriolis acceleration. The main conclusion of this study was that the centrifugation helps to reduce the shrinkage porosity, to improve the mold filling and to reduce the crack occurrence.

1.2.2 Rotating reference frame: Apparition of centrifugal and Coriolis

In order to introduce the rotating reference frame, consider two reference systems which share the same origin. One of them, rotates at constant angular velocity $\vec{\omega}$ with respect the other, as shown in Figure 1.10. The fixed reference frame is an inertial one, in which all Newtonian laws of linear momentum conservation are fully respected. On the other hand, the rotating reference frame is not an inertial one, therefore, any conservation equation must be properly re-written on the new rotating coordinate system.

Note: Hereafter, three types of notation will be used for the same physical magnitude. The superscript $'$ means that the magnitude is observed from a reference frame that is in rectilinear motion at constant velocity with respect to the fixed reference frame. The superscript f denotes a physical magnitude observed from the fixed reference frame. Finally, no superscript will be used when the magnitude is observed from a rotational reference system.

In the literature, with respect to fluid dynamics models, several authors [85, 86, 87] have adopted a Lagrangian approach to transform the Navier-Stokes equations to a rotating reference frame. The Lagrangian approach can be described as follows. Consider an arbitrary vectorial magnitude \vec{m}^f which is written using the coordinate system of a fixed reference frame (L^I).

Using the coordinate system of the rotating reference frame (\mathbf{L}^R), this vector is *written* as $\vec{m} = \mathbf{R}^{\vec{\omega}t} \vec{m}^f$. Then, the vector \vec{m} total derivative is:

$$\frac{d\vec{m}}{dt} = \frac{d}{dt} \left[\mathbf{R}^{\vec{\omega}t} \vec{m}^f \right] = \mathbf{R}^{\vec{\omega}t} \frac{d\vec{m}^f}{dt} + \frac{d\mathbf{R}^{\vec{\omega}t}}{dt} \vec{m}^f \quad (1.41)$$

Where $\mathbf{R}^{\vec{\omega}t}$ is a rotational transformation:

$$\mathbf{R}^{\vec{\omega}t} = \begin{bmatrix} \cos(\omega t) & \sin(\omega t) & 0 \\ -\sin(\omega t) & \cos(\omega t) & 0 \\ 0 & 0 & 1 \end{bmatrix} \quad (1.42)$$

It can be proven that $\frac{d\mathbf{R}^{\vec{\omega}t}}{dt} \vec{m}^f = -\vec{\omega} \times \left[\mathbf{R}^{\vec{\omega}t} \vec{m}^f \right]$, thus, it is obtained:

$$\frac{d\mathbf{R}^{\vec{\omega}t} \vec{m}^f}{dt} = \mathbf{R}^{\vec{\omega}t} \frac{d\vec{m}^f}{dt} - \vec{\omega} \times \left[\mathbf{R}^{\vec{\omega}t} \vec{m}^f \right] \quad (1.43)$$

In case of the velocity, in Lagrangian approach, a fluid particle or *fluid parcel* is followed within the domain, hence, the “observer” is mounted on it. Consider a fluid parcel which velocity is written in terms of the fixed reference frame: \vec{u}^f . The same velocity, written in the coordinate system of the rotating reference frame is given by $\vec{u} = \mathbf{R}^{\vec{\omega}t} \left\{ \vec{u}^f - \vec{\omega} \times \vec{x}^f \right\}$, since the rotating reference frame is moving with respect to the fluid parcel with a velocity of $\vec{\omega} \times \vec{x}^f$. The acceleration of the fluid parcel, written in the coordinate system of the rotating reference frame, is given by $\frac{d\vec{u}}{dt}$:

$$\begin{aligned} \frac{d\vec{u}}{dt} &= \frac{d}{dt} \left[\mathbf{R}^{\vec{\omega}t} \left\{ \vec{u}^f - \vec{\omega} \times \vec{x}^f \right\} \right] \\ &= \frac{d}{dt} \left[\mathbf{R}^{\vec{\omega}t} \vec{u}^f \right] - \frac{d}{dt} \left[\mathbf{R}^{\vec{\omega}t} \left\{ \vec{\omega} \times \vec{x}^f \right\} \right] \\ &= \left\{ \mathbf{R}^{\vec{\omega}t} \frac{d\vec{u}^f}{dt} - \vec{\omega} \times \left[\mathbf{R}^{\vec{\omega}t} \vec{u}^f \right] \right\} - \vec{\omega} \times \frac{d}{dt} \left[\mathbf{R}^{\vec{\omega}t} \vec{x}^f \right] \\ &= \left\{ \mathbf{R}^{\vec{\omega}t} \frac{d\vec{u}^f}{dt} - \vec{\omega} \times \left[\vec{u} + \vec{\omega} \times \vec{x} \right] \right\} - \vec{\omega} \times \left\{ \mathbf{R}^{\vec{\omega}t} \frac{d\vec{x}^f}{dt} - \vec{\omega} \times \left[\mathbf{R}^{\vec{\omega}t} \vec{x}^f \right] \right\} \\ &= \left\{ \mathbf{R}^{\vec{\omega}t} \frac{d\vec{u}^f}{dt} - \vec{\omega} \times \vec{u} - \vec{\omega} \times \left(\vec{\omega} \times \vec{x} \right) \right\} - \vec{\omega} \times \left\{ \left[\vec{u} + \vec{\omega} \times \vec{x} \right] - \vec{\omega} \times \vec{x} \right\} \\ &= \mathbf{R}^{\vec{\omega}t} \frac{d\vec{u}^f}{dt} - 2 \left(\vec{\omega} \times \vec{u} \right) - \vec{\omega} \times \left(\vec{\omega} \times \vec{x} \right) \end{aligned} \quad (1.44)$$

Where $\frac{d\vec{x}}{dt} = \vec{u}$ is the fluid parcel velocity written in the rotating reference frame coordinate system. The equation 1.44 shows an important result: in the process of calculating the fluid parcel acceleration, in coordinates of the rotating reference frame, two non-inertial accelerations appear: the Coriolis ($2(\vec{\omega} \times \vec{u})$) and centrifugal ($\vec{\omega} \times (\vec{\omega} \times \vec{x})$) accelerations.

The total temporal derivative of the fluid parcel velocity, $\frac{d\vec{u}^f}{dt}$, is its net acceleration in the fixed reference frame. According to the second law of Newton, the net acceleration, can be interpreted as the specific net force acting over the fluid parcel. In other words:

$$m \frac{d\vec{u}^f}{dt} = \vec{F}_s + \vec{F}_b \quad (1.45)$$

Where \vec{F}_s and \vec{F}_b are the surface and body forces acting over the fluid parcel respectively and m the mass of the fluid parcel. Using the material derivative definition ($\frac{d\star}{dt} = \frac{\partial\star}{\partial t} + \vec{u} \cdot \nabla\star$) with Equation 1.44 and 1.45, the Navier-Stokes equations, for a Newtonian and incompressible fluid, can be written in an Eulerian frame as:

$$\mathbf{R}^{\vec{\omega}t} \left\{ \frac{d\vec{u}^f}{dt} \right\} = \frac{\partial\vec{u}}{\partial t} + (\vec{u} \cdot \nabla) \vec{u} + 2(\vec{\omega} \times \vec{u}) + \vec{\omega} \times (\vec{\omega} \times \vec{x}) = -\frac{1}{\rho} \nabla p + \nu \nabla^2 \vec{u} + \vec{g} \quad (1.46)$$

Where ν is the kinematic viscosity and p the pressure.

Kageyama and Hyodo [88] used an Eulerian approach to transform the Navier-Stokes equations to a rotating reference frame, in case of incompressible flow. The main difference between an Eulerian and Lagrangian approach is that in the first, the velocity is described in a fixed point or control volume instead of following a fluid parcel as is done in the second. Combrinck et al. [89] extended the work Kageyama and Hyodo to be applied in compressible flows, however, a mistake on their mathematical development was noticed, leaving unanswered the question of how generic momentum conservation equations can be properly written in coordinates of a rotating reference frame.

In the next chapter (Chapt. 2), the methodology proposed in [88] will be used to write the complete solidification model in the rotating reference frame.

1.3 Objectives

The literature review shows that the liquid convection and equiaxed grain motion during solidification can have an important impact on the mechanical properties of the final product. For that reason, the interest on numerical modeling of solidification has greatly increased in the recent years as the computational resources and numerical models have improved. It was shown that the “volume averaging method” has been adopted by several authors to formulate macroscopic solidification models. These models have been successfully applied in the prediction of macrosegregation in large steel ingots and in the prediction of grain morphology. Among of these models, the one used by Heyvaert et al. [39] was reviewed in detail. This model enables the description of liquid thermosolutal convection, equiaxed grain motion, grain growth kinetics and grain morphology. In spite of the advances on macroscopic modeling of solidification, the literature review also revealed that the effect of centrifugation on solidification has been poorly investigated. Moreover, the solidification models have not been adapted to include the effect of centrifugation.

The first objective of this work is to formulate a macroscopic solidification model in terms of a rotating reference system and therefore to include the effect of the centrifugal and Coriolis accelerations. It is known that the Coriolis acceleration adds important three-dimensional aspects to the liquid convection. Because of this, the use of SOLID[®] to study the effect of centrifugation on solidification is not possible. SOLID[®] is able to handle only two-dimensional study cases. These circumstances lead to the next objective of this work which is the development of a new numerical tool based on the open-source OpenFOAM platform. This tool must enable the three-dimensional modeling of solidification accounting for the centrifugal and Coriolis accelerations.

The final and most important objective is to support the understanding of the effect of the centrifugation on the microstructure of the GRADECET experiments by means of numerical simulations. The numerical simulations should be performed using the new numerical tool. Particularly, a description of the liquid thermosolutal convection and equiaxed grain motion during solidification is required.

1.4 Summary

The main points of this literature review can be summarized as follows:

- Solidification is a multi scale process. Atomic re-arrangement at the solid-liquid interface (nano scale) occurs simultaneously to equiaxed grain movement or liquid thermosolutal convection in macroscopic scales, to give an example. This work takes the mission of solidification modeling at macroscopic scales in centrifugal conditions.
- Macrosegregation is the defect related to heterogeneities in solute composition at the product scale that can be observed at the end of solidification. It can not be solved by homogenization treatments in solid state due to its presence at the product scale. The root cause of macrosegregation is the relative movement between the solid and liquid phases. The results of this work will be mainly focused in macrosegregation due to liquid thermosolutal convection and equiaxed grain movement.
- The “Volume averaging method” was presented. By using this method it is possible to write a solidification model in terms of macroscopic conservation equations while microscopic scale effects are represented by proper models and included in the macroscopic equations through source terms.
- A macroscopic model for solidification was presented. The model included liquid thermosolutal convection, equiaxed grain movement and conservation of energy and solute. In addition, a review of the main grain growth kinetics models, used for macroscopic solidification modeling, was conducted. A lack of literature with respect to the solidification modeling in centrifugal casting was realized.
- A review of material processing in centrifugal conditions was conducted. Several experiments of directional solidification in centrifuges were discussed. Even though it is well known that the Coriolis acceleration has a large impact determining liquid flow pattern and equiaxed grain movement during solidification, its effect, as well as centrifugal acceleration effect, has not been completely characterized.
- Finally, in order to solve the solidification model under centrifugal conditions, the rotating reference frame was presented. As an example, the Navier-Stokes equations of a Newtonian and incompressible flow were transformed to the rotating reference frame by means of a Lagrangian approach. A lack of literature was noticed with respect to the transformation of complex flow models to the rotating reference frame.

Chapter 2 : Solidification model for centrifugal casting

Contents

2.1	Eulerian derivation of Navier-Stokes equations in a rotating reference frame	42
2.2	Derivation of scalar conservation equation	48
2.3	Derivation of momentum conservation equations	50
2.4	Summary	54

In the previous chapter, a complete macroscopic solidification model was presented, which included scalar and vectorial conservation equations written in a reference frame fixed in space. Additionally, a rotating reference frame was introduced, in order to write fluid-dynamics models without considering explicitly the rotational movement of the study domain. The use of a rotating reference system requires that the physical model, written initially in fixed coordinates, be rewritten in terms of rotating coordinates.

This chapter is devoted to rewrite the solidification model into the rotating reference frame in a mathematically rigorous way. For that, in a first place, the methodology proposed by Kageyama and Hyodo [88] will be presented, in order to, in a second place, apply it to the transformation of scalar and vectorial conservation equations.

2.1 Eulerian derivation of Navier-Stokes equations in a rotating reference frame

Kageyama and Hyodo [88] used an Eulerian approach to show the derivation of the Coriolis force in a rotating reference frame. Contrarily to a Lagrangian approach, in an Eulerian approach, the velocity is described in a point which is fixed in space instead of following a fluid parcel. According to the authors, there are three advantages of using an Eulerian approach: (1) it is general, since it can be used in the transformation of any vector field (e.g. Maxwell's equations in rotating reference frame), (2) the physical meaning of the Eulerian derivation is clear and (3) it is mathematically rigorous. Although the authors clearly presented the methodology, it was only used in the transformation of incompressible Navier-Stokes equations, not reviewing its application in cases of scalar conservation equation or more complex models, such as, multi-phase flows models. In this section, the methodology used in [88] will be presented, detailing all the intermediate steps that were omitted in the original publication. In the following sections the methodology will be applied to derive averaged scalar conservation equations and averaged momentum conservation equations for macroscopic modeling of solidification.

Consider an arbitrary velocity vector \vec{u}^f and a reference frame in constant rectilinear movement with a \vec{V}^f velocity. The moving reference frame will be denoted as \mathbf{L}' , as shown in Fig. 2.1.

Note that vector \vec{u}^f , observed from \mathbf{L}' is $\vec{u}' = \vec{u}^f - \vec{V}^f$ since both reference frames are in relative movement. A Galilean transformation for velocity can be defined in order to relate how the same vector is *observed from* the different reference frames:

$$\vec{u}'(\vec{x}', t) = \mathbf{G}^{\vec{V}} \left\{ \vec{u}^f(\vec{x}^f, t) \right\} = \vec{u}^f(\vec{x}^f, t) - \vec{V}^f \quad (2.1)$$

Consider now a fixed reference frame and a rotating reference frame (\mathbf{L}^I and \mathbf{L}^R , respectively) that share the same origin. The relative velocity between both frames is $\vec{V}^f = \vec{\omega} \times \vec{x}^f$, therefore, an arbitrary velocity observed from the rotational reference frame is $\vec{u}(\vec{x}, t) = \mathbf{G}^{\vec{\omega} \times \vec{x}^f} \left\{ \vec{u}^f(\vec{x}^f, t) \right\} = \vec{u}^f(\vec{x}^f, t) - \vec{\omega} \times \vec{x}^f$, as shown in Fig. 2.2. However, this relation is only valid when the axes of both frames are aligned (*i.e.* $\hat{x}_1^f = \hat{x}_1$ and $\hat{x}_2^f = \hat{x}_2$, where $\hat{\cdot}$ denotes a basis

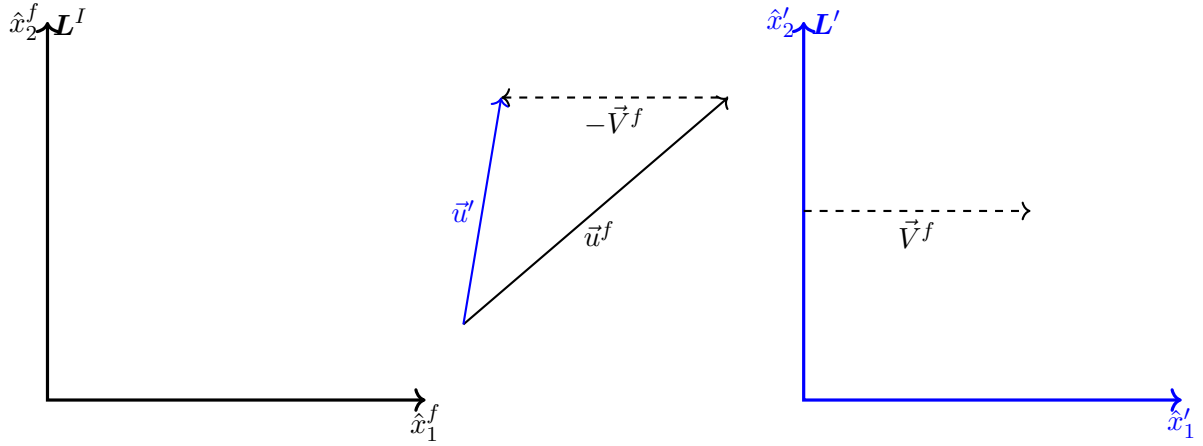


Figure 2.1 – Fixed reference frame (black) and a moving reference frame (blue) at constant velocity \vec{V}^f . The axes of both reference frames are aligned.

vector of a reference frame). Therefore a rotational transformation, $\mathbf{R}^{\vec{\omega}t}$, must be applied to write the resulting vector from the Galilean transformation in terms of the rotating coordinates frame:

$$\vec{u}(\vec{x}, t) = \mathbf{R}^{\vec{\omega}t} \mathbf{G}^{\vec{\omega} \times \vec{x}^f} \left\{ \vec{u}^f(\vec{x}^f, t) \right\} = \mathbf{R}^{\vec{\omega}t} \left\{ \vec{u}^f(\vec{x}^f, t) - \vec{\omega} \times \vec{x}^f \right\} \quad (2.2)$$

Note that the angular velocity, *observed from* the fixed reference frame $\vec{\omega}^f$ and *observed from* the rotating reference frame $\vec{\omega}$, is exactly the same. In order to relate an arbitrary position vector between a fixed and a rotating reference frames, the following analysis is proposed: imagine an arbitrary point with a position vector \vec{x}^f *observed from* the rotating reference frame \mathbf{L}^R . It may be noted that the point moves over a circumferential path of radius $|\vec{x}^f|$ centered in the origin of the reference frame. However, the point has always been in the same fixed position, which is only observable from the fixed reference frame \mathbf{L}^I . In that way, a fixed position in space, *observed from* the rotating reference frame, depends on time since the rotating frame is in motion. An arbitrary position vector, \vec{x}^f , expressed in terms of the rotating coordinates, \vec{x} , is equivalent to:

$$\vec{x}^f = \mathbf{R}^{-\vec{\omega}t} \left\{ \vec{x}(\vec{x}^f, t) \right\} \quad (2.3)$$

In addition, as both reference frames share the same origin, it can be written:

$$\mathbf{R}^{\vec{\omega}t} \left\{ \vec{\omega} \times \vec{x}^f \right\} = \vec{\omega} \times \vec{x} \quad (2.4)$$

Finally, applying the inverse rotational transformation $\mathbf{R}^{-\vec{\omega}t}$ to Eqn. 2.2 and using the relation of Eqn. 2.4, an arbitrary velocity vector *observed from* the fixed reference frame can be written as:

$$\vec{u}^f(\vec{x}^f, t) = \mathbf{R}^{-\vec{\omega}t} \left\{ \vec{u}(\vec{x}, t) + \vec{\omega} \times \vec{x} \right\} \quad (2.5)$$

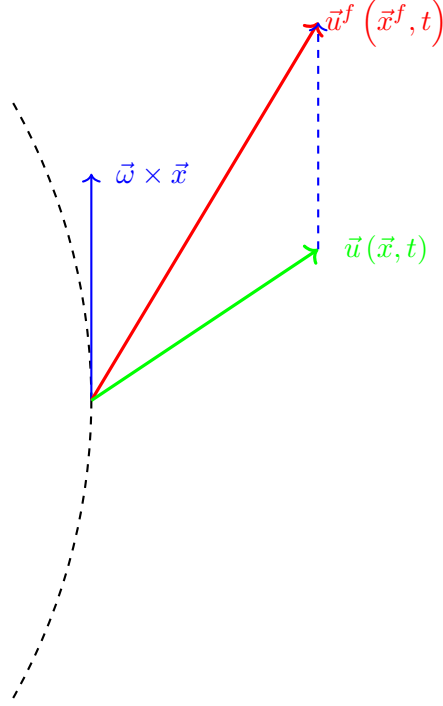


Figure 2.2 – Schematic representation of how the same velocity vector is *observed from* a fixed reference frame $\vec{u}^f(\vec{x}^f, t)$ and a rotating reference frame $\vec{u}(\vec{x}, t)$

With the Galilean \mathbf{G}^V and rotational $\mathbf{R}^{\vec{\omega}t}$ transformations, along with Eqns. 2.2 and 2.5, it is possible to rewrite the incompressible Navier-Stokes equations in terms of rotating coordinates. Following, the temporal term $\frac{\partial \vec{u}^f}{\partial t}$ and advective term $(\vec{u}^f \cdot \nabla) \vec{u}^f$ of those equations will be discussed.

– **Temporal term:**

Consider the partial temporal derivative of an arbitrary velocity vector \vec{a} in the rotating reference frame \mathbf{L}^R , at the position \vec{x} :

$$\frac{\partial \vec{a}(\vec{x}, t)}{\partial t} = \lim_{\Delta t \rightarrow 0} \frac{\vec{a}(\vec{x}, t + \Delta t) - \vec{a}(\vec{x}, t)}{\Delta t} \quad (2.6)$$

Where the vectors $\vec{a}(\vec{x}, t + \Delta t)$ and $\vec{a}(\vec{x}, t)$ can be written as a function of the same vector, but in the fixed reference frame:

$$\vec{a}(\vec{x}, t + \Delta t) = \mathbf{R}^{\vec{\omega}(t+\Delta t)} \mathbf{G}^{\vec{\omega} \times \vec{x}_{t+\Delta t}^f} \left\{ \vec{a}^f(\vec{x}_{t+\Delta t}^f, t + \Delta t) \right\} \quad (2.7)$$

$$\vec{a}(\vec{x}, t) = \mathbf{R}^{\vec{\omega}t} \mathbf{G}^{\vec{\omega} \times \vec{x}_t^f} \left\{ \vec{a}^f(\vec{x}_t^f, t) \right\} \quad (2.8)$$

Where $\vec{x}_t^f = \vec{x}^f(t)$ and $\vec{x}_{t+\Delta t}^f = \vec{x}^f(t + \Delta t)$. If the right hand side of Eqn. 2.7 is written in terms of the time t , we obtain:

$$\vec{a}^f(\vec{x}_{t+\Delta t}^f, t + \Delta t) = \vec{a}^f(\vec{x}_t^f + \Delta t(\vec{\omega} \times \vec{x}_t^f), t + \Delta t) \quad (2.9)$$

Eqn. 2.9 can be expanded around the position \vec{x}_t^f and time t , using a Taylor series, up to first order, as:

$$\begin{aligned} \vec{a}^f(\vec{x}_{t+\Delta t}^f, t + \Delta t) &= \vec{a}^f(\vec{x}_t^f, t) + [(\vec{x}_t^f + \Delta t(\vec{\omega} \times \vec{x}_t^f) - \vec{x}_t^f) \cdot \nabla] \vec{a}^f(\vec{x}_t^f, t) + (t + \Delta t - t) \frac{\partial}{\partial t} [\vec{a}^f(\vec{x}_t^f, t)] \\ &= \vec{a}^f(\vec{x}_t^f, t) + [\Delta t(\vec{\omega} \times \vec{x}_t^f) \cdot \nabla] \vec{a}^f(\vec{x}_t^f, t) + \Delta t \frac{\partial}{\partial t} [\vec{a}^f(\vec{x}_t^f, t)] \end{aligned} \quad (2.10)$$

Applying the corresponding Galilean transformation $\mathbf{G}^{\vec{\omega} \times \vec{x}_{t+\Delta t}}$ to Eqn. 2.10, we obtain:

$$\begin{aligned} &\mathbf{G}^{\vec{\omega} \times \vec{x}_{t+\Delta t}} \left\{ \vec{a}^f(\vec{x}_{t+\Delta t}^f, t + \Delta t) \right\} \\ &= \vec{a}^f(\vec{x}_t^f, t) + [\Delta t(\vec{\omega} \times \vec{x}_t^f) \cdot \nabla] \vec{a}^f(\vec{x}_t^f, t) + \Delta t \frac{\partial \vec{a}^f(\vec{x}_t^f, t)}{\partial t} - \vec{\omega} \times \vec{x}_{t+\Delta t}^f \\ &= \vec{a}^f(\vec{x}_t^f, t) + [\Delta t(\vec{\omega} \times \vec{x}_t^f) \cdot \nabla] \vec{a}^f(\vec{x}_t^f, t) + \Delta t \frac{\partial \vec{a}^f(\vec{x}_t^f, t)}{\partial t} - \vec{\omega} \times (\vec{x}_t^f + \Delta t(\vec{\omega} \times \vec{x}_t^f)) \\ &= \vec{a}^f(\vec{x}_t^f, t) + [\Delta t(\vec{\omega} \times \vec{x}_t^f) \cdot \nabla] \vec{a}^f(\vec{x}_t^f, t) + \Delta t \frac{\partial \vec{a}^f(\vec{x}_t^f, t)}{\partial t} - \vec{\omega} \times \vec{x}_t^f - \Delta t(\vec{\omega} \times (\vec{\omega} \times \vec{x}_t^f)) \end{aligned} \quad (2.11)$$

Coming back to Eqn. 2.8, the Galilean transformation is given by:

$$\mathbf{G}^{\vec{\omega} \times \vec{x}_t} \left\{ \vec{a}^f(\vec{x}_t^f, t) \right\} = \vec{a}^f(\vec{x}_t^f, t) - \vec{\omega} \times \vec{x}_t^f \quad (2.12)$$

Finally, the limit that defines the temporal term (Eqn. 2.6) can be rewritten in function of $\vec{a}(\vec{x}_t^f, t)$ and the rotational transformation, by using Eqns. 2.11 and 2.12:

$$\begin{aligned} &\lim_{\Delta t \rightarrow 0} \frac{\mathbf{R}^{\vec{\omega}(t+\Delta t)} \left\{ \vec{a}^f(\vec{x}_t^f, t) + [\Delta t(\vec{\omega} \times \vec{x}_t^f) \cdot \nabla] \vec{a}^f(\vec{x}_t^f, t) + \Delta t \frac{\partial \vec{a}^f(\vec{x}_t^f, t)}{\partial t} - \vec{\omega} \times \vec{x}_t^f - \Delta t \vec{\omega} \times (\vec{\omega} \times \vec{x}_t^f) \right\}}{\Delta t} \\ &- \lim_{\Delta t \rightarrow 0} \frac{\mathbf{R}^{\vec{\omega}t} \left\{ \vec{a}^f(\vec{x}_t^f, t) - \vec{\omega} \times \vec{x}_t^f \right\}}{\Delta t} \end{aligned} \quad (2.13)$$

Where the Eqn. 2.13 can be separated in three simpler limits:

1. The first one:

$$\lim_{\Delta t \rightarrow 0} \frac{\mathbf{R}^{\vec{\omega}(t+\Delta t)} \left\{ \left[\Delta t (\vec{\omega} \times \vec{x}_t^f) \cdot \nabla \right] \vec{a}^f(\vec{x}_t^f, t) \right\}}{\Delta t} = \mathbf{R}^{\vec{\omega}t} \left\{ \left[(\vec{\omega} \times \vec{x}_t^f) \cdot \nabla \right] \vec{a}^f(\vec{x}_t, t) \right\} \quad (2.14)$$

2. The second one:

$$\lim_{\Delta t \rightarrow 0} \frac{\mathbf{R}^{\vec{\omega}(t+\Delta t)} \left\{ \Delta t \frac{\partial \vec{a}^f(\vec{x}_t^f, t)}{\partial t} \right\}}{\Delta t} = \mathbf{R}^{\vec{\omega}t} \left\{ \frac{\partial \vec{a}^f(\vec{x}_t^f, t)}{\partial t} \right\} \quad (2.15)$$

3. And the third one:

$$\lim_{\Delta t \rightarrow 0} \frac{\mathbf{R}^{\vec{\omega}(t+\Delta t)} \left\{ \left[\vec{a}^f(\vec{x}_t^f, t) - \vec{\omega} \times \vec{x}_t^f - \Delta t \vec{\omega} \times (\vec{\omega} \times \vec{x}_t^f) \right] - \mathbf{R}^{\vec{\omega}t} \left[\vec{a}^f(\vec{x}_t^f, t) - \vec{\omega} \times \vec{x}_t^f \right] \right\}}{\Delta t} \quad (2.16)$$

In the same way, this limit can be separated in other three simpler limits:

(a)

$$\begin{aligned} & \lim_{\Delta t \rightarrow 0} \frac{\mathbf{R}^{\vec{\omega}(t+\Delta t)} \left\{ \vec{a}^f(\vec{x}_t^f, t) \right\} - \mathbf{R}^{\vec{\omega}t} \left\{ \vec{a}^f(\vec{x}_t^f, t) \right\}}{\Delta t} \quad (2.17) \\ &= \lim_{\Delta t \rightarrow 0} \frac{\mathbf{R}^{\vec{\omega}\Delta t} \mathbf{R}^{\vec{\omega}t} \left\{ \vec{a}^f(\vec{x}_t^f, t) \right\} - \mathbf{R}^{\vec{\omega}t} \left\{ \vec{a}^f(\vec{x}_t^f, t) \right\}}{\Delta t} \\ &= -\mathbf{R}^{\vec{\omega}t} \left\{ (\vec{\omega} \times \vec{a}^f(\vec{x}_t^f, t)) \right\} \end{aligned}$$

To solve the limit of Eqn. 2.17, the following relation was used:

$$\lim_{\Delta t \rightarrow 0} \frac{\mathbf{R}^{\vec{\omega}\Delta t} \{ \vec{m} \} - \vec{m}}{\Delta t} = -(\vec{\omega} \times \vec{m}) \quad (2.18)$$

Where \vec{m} is an arbitrary vector which, in this case, $\vec{m} = \mathbf{R}^{\vec{\omega}t} \left\{ \vec{a}^f(\vec{x}_t^f, t) \right\}$.

(b)

$$\lim_{\Delta t \rightarrow 0} \frac{\mathbf{R}^{\vec{\omega}t} \left\{ \vec{\omega} \times \vec{x}_t^f \right\} - \mathbf{R}^{\vec{\omega}(t+\Delta t)} \left\{ \vec{\omega} \times \vec{x}_t^f \right\}}{\Delta t} = \mathbf{R}^{\vec{\omega}t} \left\{ \vec{\omega} \times (\vec{\omega} \times \vec{x}_t^f) \right\} \quad (2.19)$$

Where the relation of Eqn. 2.18 was used, with $\vec{m} = \mathbf{R}^{\vec{\omega}t} \left\{ \vec{\omega} \times \vec{x}_t^f \right\}$.

(c)

$$-\lim_{\Delta t \rightarrow 0} \frac{\mathbf{R}^{\vec{\omega}(t+\Delta t)} \left\{ \Delta t (\vec{\omega} \times (\vec{\omega} \times \vec{x}_t^f)) \right\}}{\Delta t} = -\mathbf{R}^{\vec{\omega}t} \left\{ \vec{\omega} \times (\vec{\omega} \times \vec{x}_t^f) \right\} \quad (2.20)$$

Then, the limit from Eqn. 2.16 is the sum of Eqns. 2.17, 2.19 and 2.20:

$$- \mathbf{R}^{\bar{\omega}t} \left\{ \bar{\omega} \times \bar{a}^f \left(\bar{x}_t^f, t \right) \right\} \quad (2.21)$$

The temporal derivative $\frac{\partial a(\bar{x}, t)}{\partial t}$ of Eqn. 2.6 is the sum of Eqns. 2.14, 2.15 and 2.21:

$$\frac{\partial \bar{a}(\bar{x}, t)}{\partial t} = \mathbf{R}^{\bar{\omega}t} \left\{ \left[\frac{\partial}{\partial t} + \left(\bar{\omega} \times \bar{x}_t^f \right) \cdot \nabla - \bar{\omega} \times \right] \bar{a}^f \right\} \quad (2.22)$$

With the relation of Eqn. 2.22, the temporal derivative $\frac{\partial \bar{u}}{\partial t}$ can be written in the rotating reference frame as:

$$\frac{\partial \bar{u}(x, t)}{\partial t} = \mathbf{R}^{\bar{\omega}t} \left\{ \left[\frac{\partial}{\partial t} + \left(\bar{\omega} \times \bar{x}_t^f \right) \cdot \nabla - \bar{\omega} \times \right] \bar{u}^f \right\} \quad (2.23)$$

– **Advective term:**

The advective term $(\bar{u} \cdot \nabla) \bar{u}$ can be developed as:

$$\begin{aligned} (\bar{u} \cdot \nabla) \bar{u} &= \mathbf{R}^{\bar{\omega}t} \left\{ \left[(\bar{u}^f - \bar{\omega} \times \bar{x}^f) \cdot \nabla \right] (\bar{u}^f - \bar{\omega} \times \bar{x}^f) \right\} \\ &= \mathbf{R}^{\bar{\omega}t} \left\{ (\bar{u}^f \cdot \nabla) \bar{u}^f - \bar{u}^f \cdot \nabla (\bar{\omega} \times \bar{x}^f) - (\bar{\omega} \times \bar{x}^f) \cdot \nabla \bar{u}^f + (\bar{\omega} \times \bar{x}^f) \cdot \nabla (\bar{\omega} \times \bar{x}^f) \right\} \\ &= \mathbf{R}^{\bar{\omega}t} \left\{ (\bar{u}^f \cdot \nabla) \bar{u}^f - \bar{\omega} \times \bar{u}^f - (\bar{\omega} \times \bar{x}^f) \cdot \nabla \bar{u}^f + \bar{\omega} \times (\bar{\omega} \times \bar{x}^f) \right\} \end{aligned} \quad (2.24)$$

The sum of temporal and advective terms of the incompressible Navier-Stokes equations can be written in the rotating reference frame using the relations of Eqns. 2.23 and 2.24:

$$\begin{aligned} \frac{\partial \bar{u}}{\partial t} + (\bar{u} \cdot \nabla) \bar{u} &= \mathbf{R}^{\bar{\omega}t} \left\{ \frac{\partial \bar{u}^f}{\partial t} + (\bar{\omega} \times \bar{x}^f) \cdot \nabla \bar{u}^f - \bar{\omega} \times \bar{u}^f + (\bar{u}^f \cdot \nabla) \bar{u}^f - \bar{\omega} \times \bar{u}^f - (\bar{\omega} \times \bar{x}^f) \cdot \nabla \bar{u}^f + \bar{\omega} \times (\bar{\omega} \times \bar{x}^f) \right\} \\ &= \mathbf{R}^{\bar{\omega}t} \left\{ \frac{\partial \bar{u}^f}{\partial t} + (\bar{u}^f \cdot \nabla) \bar{u}^f - 2\bar{\omega} \times \bar{u}^f + \bar{\omega} \times (\bar{\omega} \times \bar{x}^f) \right\} \end{aligned} \quad (2.25)$$

The rotational transformation of the last two terms, recalling Eqn. 2.5 ($\mathbf{R}^{\bar{\omega}t} \left\{ \bar{u}^f \left(\bar{x}^f, t \right) \right\} = \bar{u}(\bar{x}, t) + \bar{\omega} \times \bar{x}$), is given by:

$$\begin{aligned} \mathbf{R}^{\bar{\omega}t} \left\{ -2\bar{\omega} \times \bar{u}^f + \bar{\omega} \times (\bar{\omega} \times \bar{x}^f) \right\} &= -2\bar{\omega} \times \mathbf{R}^{\bar{\omega}t} \left\{ \bar{u}^f \right\} + \bar{\omega} \times \left(\bar{\omega} \times \mathbf{R}^{\bar{\omega}t} \left\{ \bar{x}^f \right\} \right) \\ &= -2\bar{\omega} \times (\bar{u} + \bar{\omega} \times \bar{x}) + \bar{\omega} \times (\bar{\omega} \times \bar{x}) \\ &= -2(\bar{\omega} \times \bar{u}) - 2\bar{\omega} \times (\bar{\omega} \times \bar{x}) - \bar{\omega} \times (\bar{\omega} \times \bar{x}) \\ &= -2(\bar{\omega} \times \bar{u}) - \bar{\omega} \times (\bar{\omega} \times \bar{x}) \end{aligned} \quad (2.26)$$

Finally, simplifying Eqn. 2.25, using Eqn. 2.26, we obtain:

$$\mathbf{R}^{\bar{\omega}t} \left\{ \frac{\partial \bar{u}^f}{\partial t} + (\bar{u}^f \cdot \nabla) \bar{u}^f \right\} = \frac{\partial \bar{u}}{\partial t} + (\bar{u} \cdot \nabla) \bar{u} + 2(\bar{\omega} \times \bar{u}) + \bar{\omega} \times (\bar{\omega} \times \bar{x}) \quad (2.27)$$

As expected, the final expression of transformed incompressible Navier-Stokes equations, using the Kageyama and Hyodo methodology, is equivalent to the one presented in Sec. 1.2.2.

2.2 Derivation of scalar conservation equation

The macroscopic solidification model requires the resolution of several scalar conservation equations, which must be rewritten in terms of the rotating coordinate system. In this section, the Eulerian methodology will be used in order to derive a conservation equation of an arbitrary scalar in a rotating reference frame.

Consider the arbitrary scalar conservation equation:

$$\frac{\partial}{\partial t} [\Phi(\vec{x}^f, t)] + \nabla \cdot [\Phi(\vec{x}^f, t) \vec{v}^f(\vec{x}^f, t)] = S_t(\vec{x}^f, t) \quad (2.28)$$

Where $\Phi(\vec{x}^f, t)$ is the arbitrary scalar field, \vec{x}^f the position vector *observed from* the fixed reference frame, t the time, $\vec{v}^f(\vec{x}^f, t)$ the velocity field which advects the scalar magnitude Φ and S_t arbitrary sources terms. An analysis term by term of Eqn.2.28 is required, in order to rewrite the equation in rotating coordinates:

– Temporal term:

By definition, the temporal term of Eq. 2.28 is equivalent to:

$$\frac{\partial}{\partial t} [\Phi(\vec{x}^f, t)] = \lim_{\Delta t \rightarrow 0} \frac{\Phi(\vec{x}^f, t + \Delta t) - \Phi(\vec{x}^f, t)}{\Delta t} \quad (2.29)$$

Using the relation given in the Eqn. 2.3 and rewriting the Eqn. 2.29 it is obtained:

$$\frac{\partial}{\partial t} [\Phi(\vec{x}^f, t)] = \lim_{\Delta t \rightarrow 0} \frac{\Phi(\mathbf{R}^{-\vec{\omega}(t+\Delta t)} \{ \vec{x}(\vec{x}^f, t + \Delta t) \}, t + \Delta t) - \Phi(\mathbf{R}^{-\vec{\omega}t} \{ \vec{x}(\vec{x}^f, t) \}, t)}{\Delta t} \quad (2.30)$$

The first term in the numerator (Eqn. 2.30) can be expanded around the position $\mathbf{R}^{-\vec{\omega}(t+\Delta t)} \{ \vec{x}(\vec{x}^f, t) \}$ and time t :

$$\begin{aligned} & \Phi(\mathbf{R}^{\vec{\omega}(t+\Delta t)} \{ \vec{x}(\vec{x}^f, t + \Delta t) \}, t + \Delta t) \\ &= \Phi(\mathbf{R}^{-\vec{\omega}(t+\Delta t)} \{ \vec{x}(\vec{x}^f, t) - \Delta t \vec{\omega} \times \vec{x} \}, t + \Delta t) \\ &= \Phi(\mathbf{R}^{-\vec{\omega}(t+\Delta t)} \{ \vec{x}(\vec{x}^f, t) \}, t) - \mathbf{R}^{-\vec{\omega}(t+\Delta t)} \{ \Delta t \vec{\omega} \times \vec{x}(\vec{x}^f, t) \} \cdot \nabla \Phi(\mathbf{R}^{-\vec{\omega}(t+\Delta t)} \{ \vec{x}(\vec{x}^f, t) \}, t) \\ & \quad + \Delta t \frac{\partial}{\partial t} [\Phi(\mathbf{R}^{-\vec{\omega}(t+\Delta t)} \{ \vec{x}(\vec{x}^f, t) \}, t)] \end{aligned} \quad (2.31)$$

With Eqn. 2.31, the limit of Eqn. 2.30 can be separated in three simpler limits:

$$1. \quad \lim_{\Delta t \rightarrow 0} \frac{\Phi \left(\mathbf{R}^{-\vec{\omega}(t+\Delta t)} \left\{ \vec{x} \left(\vec{x}^f, t \right) \right\}, t \right) - \Phi \left(\mathbf{R}^{-\vec{\omega}t} \left\{ \vec{x} \left(\vec{x}^f, t \right) \right\}, t \right)}{\Delta t} = 0 \quad (2.32)$$

Where the first term of the numerator can be interpreted as the scalar magnitude in the point $\mathbf{R}^{-\vec{\omega}t} \vec{x} = \vec{x}^f$, *observed from* the rotating reference frame in the time $t + \Delta t$. The scalar magnitude does not depend on the reference frame from which it is observed, so that, the limit is equal to zero.

$$2. \quad \lim_{\Delta t \rightarrow 0} - \frac{\mathbf{R}^{-\vec{\omega}(t+\Delta t)} \left\{ \Delta t \vec{\omega} \times \vec{x} \left(\vec{x}^f, t \right) \right\} \cdot \nabla \Phi \left(\mathbf{R}^{-\vec{\omega}(t+\Delta t)} \left\{ \vec{x} \left(\vec{x}^f, t \right) \right\}, t \right)}{\Delta t} \quad (2.33)$$

$$=$$

$$- \mathbf{R}^{-\vec{\omega}t} \left\{ \vec{\omega} \times \vec{x} \left(\vec{x}^f, t \right) \right\} \cdot \nabla \Phi \left(\mathbf{R}^{-\vec{\omega}t} \left\{ \vec{x} \left(\vec{x}^f, t \right) \right\}, t \right)$$

$$3. \quad \lim_{\Delta t \rightarrow 0} \frac{\Delta t \frac{\partial}{\partial t} \left[\Phi \left(\mathbf{R}^{-\vec{\omega}(t+\Delta t)} \left\{ \vec{x} \left(\vec{x}^f, t \right) \right\}, t \right) \right]}{\Delta t} = \frac{\partial}{\partial t} \Phi \left(\mathbf{R}^{-\vec{\omega}t} \left\{ \vec{x} \left(\vec{x}^f, t \right) \right\}, t \right) \quad (2.34)$$

To simplify the notation, it will be considered from this point:

$$\Phi \left(\mathbf{R}^{-\vec{\omega}t} \left\{ \vec{x} \left(\vec{x}^f, t \right) \right\}, t \right) = \mathbf{R}^{-\vec{\omega}t} \left\{ \Phi \left(\vec{x}, t \right) \right\} \quad (2.35)$$

Finally, the temporal derivative is equivalent to:

$$\frac{\partial}{\partial t} \left[\Phi \left(\vec{x}^f, t \right) \right] = \mathbf{R}^{-\vec{\omega}t} \left\{ \frac{\partial}{\partial t} \left[\Phi \left(\vec{x}, t \right) \right] - \left(\vec{\omega} \times \vec{x} \right) \cdot \nabla \Phi \left(\vec{x}, t \right) \right\} \quad (2.36)$$

– **Advective term:**

The advective term depends on the scalar field, which is observed by the rotating reference frame as $\Phi \left(\mathbf{R}^{-\vec{\omega}t} \left\{ \vec{x} \left(\vec{x}^f, t \right) \right\}, t \right) = \mathbf{R}^{-\vec{\omega}t} \left\{ \Phi \left(\vec{x}, t \right) \right\}$, and the velocity field, which can be written as $\vec{v}^f \left(\vec{x}^f, t \right) = \mathbf{R}^{-\vec{\omega}t} \left\{ \vec{v} \left(\vec{x}, t \right) + \vec{\omega} \times \vec{x} \right\}$ according Eqn. 2.5.

Using property $\nabla \cdot \left(\vec{\omega} \times \vec{x} \right) = 0$, the advective term can be rewritten as:

$$\begin{aligned} & \nabla \cdot \left(\Phi \left(\vec{x}^f, t \right) \vec{v}^f \left(\vec{x}^f, t \right) \right) \quad (2.37) \\ &= \nabla \cdot \left[\mathbf{R}^{-\vec{\omega}t} \left\{ \Phi \left(\vec{x}^f, t \right) \right\} \mathbf{R}^{-\vec{\omega}t} \left\{ \vec{v}^f \left(\vec{x}^f, t \right) + \vec{\omega} \times \vec{x}^f \right\} \right] \\ &= \mathbf{R}^{-\vec{\omega}t} \left\{ \nabla \cdot \left[\Phi \left(\vec{x}, t \right) \vec{v} \left(\vec{x}, t \right) \right] + \left(\vec{\omega} \times \vec{x} \right) \cdot \nabla \Phi \left(\vec{x}, t \right) \right\} \end{aligned}$$

– **Source terms:**

The source terms can be written as:

$$S_t(\vec{x}^f, t) = S_t(\mathbf{R}^{-\vec{\omega}t} \{\vec{x}\}, t) = \mathbf{R}^{-\vec{\omega}t} \{S_t(x, t)\} \quad (2.38)$$

Adding both, temporal and advective terms, and taking out the rotational transformation, an arbitrary scalar conservation equation, written in terms of the rotating coordinates, is:

$$\frac{\partial}{\partial t} [\Phi(\vec{x}, t)] + \nabla \cdot [\Phi(\vec{x}, t) \vec{v}(\vec{x}, t)] = S_t(\vec{x}, t) \quad (2.39)$$

Table 2.1 summarise the scalar conservation equations that must be solved in the solidification model. It is noted that the equations are identical in both, fixed and rotating reference frames.

Table 2.1 – Scalar conservation equations for solidification modeling written in terms of the rotating reference frame.

Total mass conservation	$\frac{\partial}{\partial t} (g_s \rho_s + g_l \rho_l) + \nabla \cdot (g_s \rho_s \langle \vec{v}_s \rangle^s + g_l \rho_l \langle \vec{v}_l \rangle^l) = 0$
Phase balance	$\frac{\partial}{\partial t} (g_k) + \nabla \cdot (g_k \langle \vec{v}_k \rangle^k) = \frac{1}{\rho} (\Gamma_k + \Phi_k)$
Energy conservation	$\frac{\partial \bar{\rho} \langle h \rangle}{\partial t} + \nabla \cdot (g_s \rho_s \langle h_s \rangle^s \langle \vec{v}_s \rangle^s + g_l \rho_l \langle h_l \rangle^l \langle \vec{v}_l \rangle^l) = \nabla \cdot (\lambda \nabla T)$
Grain envelope balance	$\frac{\partial g_e}{\partial t} + \nabla \cdot (g_e \langle \vec{v}_s \rangle^s) = (\Gamma_e + \Phi_e)$
Solute mass balance (no macroscopic diffusion)	$\frac{\partial}{\partial t} (g_k \langle C_k^i \rangle^k) + \nabla \cdot (g_k \langle C_k^i \rangle^k \langle \vec{v}_k \rangle^k) = \frac{1}{\rho_k} (J_k^{ij} + J_k^{i\Gamma} + J_k^{i\Phi})$
Grain population balance	$\frac{\partial}{\partial t} N_g + \nabla \cdot (\langle \vec{v}_s \rangle^s N_g) = \sum_{i=1}^m \Phi_i$
Nuclei density balance	$\frac{\partial}{\partial t} N_{nuc}^i + \nabla \cdot (\langle \vec{v}_l \rangle^l N_{nuc}^i) = -\Phi_i$

2.3 Derivation of momentum conservation equations

This section is devoted to rewrite the phase- k momentum equation in terms of the rotating reference frame. In order to perform the derivation, Eqn. 1.14 is recalled:

$$\frac{\partial}{\partial t} (g_k \langle \vec{v}_k \rangle^{kf}) + \nabla \cdot (g_k \langle \vec{v}_k \rangle^{kf} \langle \vec{v}_k \rangle^{kf}) = -\frac{g_k}{\rho_k} \nabla p_k + \frac{1}{\rho_k} \nabla \cdot (g_k \langle \tau_k \rangle^{kf}) + \frac{g_k}{\rho_k} \rho_k^b \vec{g}^f + \frac{1}{\rho_k} (\vec{M}_k^{df} + \vec{M}_k^{\Gamma f} + \vec{M}_k^{\phi f}) \quad (2.40)$$

An analysis term-to-term is conducted below:

Temporal term:

$$\begin{aligned}
\frac{\partial}{\partial t} \left(g_k \langle \vec{v}_k \rangle^k \right) &= \langle \vec{v}_k \rangle^{kf} \frac{\partial g_k}{\partial t} + g_k \frac{\partial \langle \vec{v}_k \rangle^{kf}}{\partial t} \\
&= \mathbf{R}^{-\vec{\omega}t} \left\{ \left[\frac{\partial g_k}{\partial t} - (\vec{\omega} \times \vec{x}) \cdot \nabla g_k \right] \left(\langle \vec{v}_k \rangle^k + \vec{\omega} \times \vec{x} \right) + g_k \left[\frac{\partial \langle \vec{v}_k \rangle^k}{\partial t} - (\vec{\omega} \times \vec{x}) \cdot \nabla \langle \vec{v}_k \rangle^k + \vec{\omega} \times \langle \vec{v}_k \rangle^k \right] \right\} \\
&= \mathbf{R}^{-\vec{\omega}t} \left\{ \langle \vec{v}_k \rangle^k \frac{\partial g_k}{\partial t} + (\vec{\omega} \times \vec{x}) \frac{\partial g_k}{\partial t} - \langle \vec{v}_k \rangle^k (\vec{\omega} \times \vec{x}) \cdot \nabla g_k - (\vec{\omega} \times \vec{x}) [(\vec{\omega} \times \vec{x}) \cdot \nabla g_k] \right. \\
&\quad \left. + g_k \frac{\partial \langle \vec{v}_k \rangle^k}{\partial t} - g_k (\vec{\omega} \times \vec{x}) \cdot \nabla \langle \vec{v}_k \rangle^k + g_k \vec{\omega} \times \langle \vec{v}_k \rangle^k \right\} \\
&= \mathbf{R}^{-\vec{\omega}t} \left\{ \frac{\partial g_k \langle \vec{v}_k \rangle^k}{\partial t} + (\vec{\omega} \times \vec{x}) \frac{\partial g_k}{\partial t} - \langle \vec{v}_k \rangle^k [(\vec{\omega} \times \vec{x}) \cdot \nabla g_k] - (\vec{\omega} \times \vec{x}) [(\vec{\omega} \times \vec{x}) \cdot \nabla g_k] \right. \\
&\quad \left. - g_k (\vec{\omega} \times \vec{x}) \cdot \nabla \langle \vec{v}_k \rangle^k + g_k \vec{\omega} \times \langle \vec{v}_k \rangle^k \right\}
\end{aligned} \tag{2.41}$$

Convective term:

$$\begin{aligned}
\nabla \left(g_k \langle \vec{v}_k \rangle^{kf} \langle \vec{v}_k \rangle^{kf} \right) &= \langle \vec{v}_k \rangle^{kf} \nabla \cdot \left[g_k \langle \vec{v}_k \rangle^{kf} \right] + g_k \langle \vec{v}_k \rangle^{kf} \cdot \nabla \langle \vec{v}_k \rangle^{kf} \\
&= \mathbf{R}^{-\vec{\omega}t} \left\{ \left(\langle \vec{v}_k \rangle^k + \vec{\omega} \times \vec{x} \right) \nabla \cdot \left[g_k \left(\langle \vec{v}_k \rangle^k + \vec{\omega} \times \vec{x} \right) \right] + g_k \left(\langle \vec{v}_k \rangle^k + \vec{\omega} \times \vec{x} \right) \cdot \nabla \left(\langle \vec{v}_k \rangle^k + \vec{\omega} \times \vec{x} \right) \right\} \\
&= \mathbf{R}^{-\vec{\omega}t} \left\{ \langle \vec{v}_k \rangle^k \nabla \cdot \left[g_k \langle \vec{v}_k \rangle^k \right] + \langle \vec{v}_k \rangle^k \nabla \cdot \left[g_k (\vec{\omega} \times \vec{x}) \right] + (\vec{\omega} \times \vec{x}) \nabla \cdot \left[g_k \langle \vec{v}_k \rangle^k \right] \right. \\
&\quad \left. + (\vec{\omega} \times \vec{x}) \nabla \cdot \left[g_k (\vec{\omega} \times \vec{x}) \right] + g_k \langle \vec{v}_k \rangle^k \cdot \nabla \langle \vec{v}_k \rangle^k + g_k \langle \vec{v}_k \rangle^k \cdot \nabla (\vec{\omega} \times \vec{x}) \right. \\
&\quad \left. + g_k (\vec{\omega} \times \vec{x}) \cdot \nabla \langle \vec{v}_k \rangle^k + g_k (\vec{\omega} \times \vec{x}) \right\} \\
&= \mathbf{R}^{-\vec{\omega}t} \left\{ \nabla \cdot \left(g_k \langle \vec{v}_k \rangle^k \langle \vec{v}_k \rangle^k \right) + \langle \vec{v}_k \rangle^k [(\vec{\omega} \times \vec{x}) \cdot \nabla g_k] + (\vec{\omega} \times \vec{x}) \nabla \left[g_k \langle \vec{v}_k \rangle^k \right] \right. \\
&\quad \left. + (\vec{\omega} \times \vec{x}) [(\vec{\omega} \times \vec{x}) \cdot \nabla g_k] + g_k \vec{\omega} \times \langle \vec{v}_k \rangle^k + g_k (\vec{\omega} \times \vec{x}) \cdot \nabla \langle \vec{v}_k \rangle^k + g_k (\vec{\omega} \times (\vec{\omega} \times \vec{x})) \right\}
\end{aligned} \tag{2.42}$$

The sum of **temporal** and **convective** terms is given by:

$$\begin{aligned}
& \frac{\partial}{\partial t} \left(g_k \langle \vec{v}_k \rangle^{kf} \right) + \nabla \cdot \left(g_k \langle \vec{v}_k \rangle^{kf} \langle \vec{v}_k \rangle^{kf} \right) \tag{2.43} \\
& = \mathbf{R}^{-\vec{\omega}t} \left\{ \frac{\partial}{\partial t} \left(g_k \langle \vec{v}_k \rangle^k \right) + (\vec{\omega} \times \vec{x}) \frac{\partial g_k}{\partial t} - \langle \vec{v}_k \rangle^k [(\vec{\omega} \times \vec{x}) \cdot \nabla g_k] - (\vec{\omega} \times \vec{x}) [(\vec{\omega} \times \vec{x}) \cdot \nabla g_k] \right. \\
& \quad - g_k (\vec{\omega} \times \vec{x}) \cdot \nabla \langle \vec{v}_k \rangle^k + g_k \vec{\omega} \times \langle \vec{v}_k \rangle^k + \nabla \cdot \left(g_k \langle \vec{v}_k \rangle^k \langle \vec{v}_k \rangle^k \right) + \langle \vec{v}_k \rangle^k [(\vec{\omega} \times \vec{x}) \cdot \nabla g_k] \\
& \quad \left. + (\vec{\omega} \times \vec{x}) \nabla \cdot \left[g_k \langle \vec{v}_k \rangle^k \right] + (\vec{\omega} \times \vec{x}) [(\vec{\omega} \times \vec{x}) \cdot \nabla g_k] + g_k \vec{\omega} \times \langle \vec{v}_k \rangle^k + g_k (\vec{\omega} \times \vec{x}) \cdot \nabla \langle \vec{v}_k \rangle^k \right. \\
& \quad \left. + g_k (\vec{\omega} \times (\vec{\omega} \times \vec{x})) \right\} \\
& = \mathbf{R}^{-\vec{\omega}t} \left\{ \frac{\partial}{\partial t} \left(g_k \langle \vec{v}_k \rangle^k \right) + \nabla \cdot \left(g_k \langle \vec{v}_k \rangle^k \langle \vec{v}_k \rangle^k \right) + 2g_k \vec{\omega} \times \langle \vec{v}_k \rangle^k + g_k (\vec{\omega} \times (\vec{\omega} \times \vec{x})) \right. \\
& \quad \left. + (\vec{\omega} \times \vec{x}) \frac{\partial g_k}{\partial t} + (\vec{\omega} \times \vec{x}) \nabla \cdot \left[g_k \langle \vec{v}_k \rangle^k \right] \right\}
\end{aligned}$$

Where $2g_k (\vec{\omega} \times \langle \vec{v}_k \rangle^k)$ and $g_k [\vec{\omega} \times (\vec{\omega} \times \vec{x})]$ correspond to the Coriolis and centrifugal accelerations.

Pressure term:

∇p_k is an invariant Galilean vector since if it is observed from the fixed reference frame, as well as, the rotating reference frame, its value is exactly the same.

Stress term:

The averaged shear stress $\langle \tau_k \rangle^k$ is function of the **relative** velocity, so that, it can be expressed in the same as in the fixed reference frame:

$$\frac{1}{\rho_k} \nabla \cdot \left(g_k \mu_k \nabla \left(\langle \vec{v}_k \rangle^k \right) \right) \tag{2.44}$$

Gravitational term:

The gravity vector does not depend on the reference frame, thus:

$$\frac{g_k}{\rho_k} \rho_k^b \vec{g} \tag{2.45}$$

It is worth to mention that, as the centrifugal acceleration can be much bigger than the terrestrial gravity acceleration, the Boussinesq assumption will also be applied to the centrifugal term.

Interfacial drag term \vec{M}_k^{df} :

In case of slurry flow regime, the interfacial drag term is transformed to the rotating reference frame as:

$$\begin{aligned}
& \frac{3g_e\rho_l C_d}{4d_g} \left| \langle \vec{v}_l \rangle^{lf} - \langle \vec{v}_s \rangle^{sf} \right| \left(\langle \vec{v}_l \rangle^{lf} - \langle \vec{v}_s \rangle^{sf} \right) \\
&= \mathbf{R}^{-\vec{\omega}t} \left\{ \frac{3g_e\rho_l C_d}{4d_g} \left| \left(\langle \vec{v}_l \rangle^l + \vec{\omega} \times \vec{x} \right) - \left(\langle \vec{v}_s \rangle^s + \vec{\omega} \times \vec{x} \right) \right| \left(\left(\langle \vec{v}_l \rangle^l + \vec{\omega} \times \vec{x} \right) - \left(\langle \vec{v}_s \rangle^s + \vec{\omega} \times \vec{x} \right) \right) \right\} \\
&= \mathbf{R}^{-\vec{\omega}t} \left\{ \frac{3g_e\rho_l C_d}{4d_g} \left| \langle \vec{v}_l \rangle^l - \langle \vec{v}_s \rangle^s \right| \left(\langle \vec{v}_l \rangle^l - \langle \vec{v}_s \rangle^s \right) \right\}
\end{aligned} \tag{2.46}$$

On the other hand, in the porous flow regime, the solid velocity in the rotating reference frame is zero $\langle \vec{v}_s \rangle^s = 0$, which means that in the fixed reference frame it is equal to $\langle \vec{v}_s \rangle^{sf} = \vec{\omega} \times \vec{x}^f$. In that way, in case of porous flow regime, the interfacial drag term is given by:

$$\begin{aligned}
& \frac{g_l^2 \mu_l}{K} \left[\langle \vec{v}_l \rangle^{lf} - \langle \vec{v}_s \rangle^{sf} \right] \\
& \mathbf{R}^{-\vec{\omega}t} \left\{ \frac{g_l^2 \mu_l}{K} \left[\left(\langle \vec{v}_l \rangle^l + \vec{\omega} \times \vec{x} \right) - \left(\langle \vec{v}_s \rangle^s + \vec{\omega} \times \vec{x} \right) \right] \right\} \\
& \mathbf{R}^{-\vec{\omega}t} \left\{ \frac{g_l^2 \mu_l}{K} \langle \vec{v}_l \rangle^l \right\}
\end{aligned} \tag{2.47}$$

Phase Change Term $\vec{M}_k^{\Gamma f}$:

Rewriting the velocity vector in rotating coordinates, the phase change term can be rewritten as:

$$\begin{aligned}
\langle \vec{v}_k \rangle^{kf} \Gamma^k &= \mathbf{R}^{-\vec{\omega}t} \left\{ \left(\langle \vec{v}_k \rangle^k + \vec{\omega} \times \vec{x} \right) \Gamma^k \right\} \\
&= \mathbf{R}^{-\vec{\omega}t} \left\{ \langle \vec{v}_k \rangle^k \Gamma^k + (\vec{\omega} \times \vec{x}) \Gamma^k \right\}
\end{aligned} \tag{2.48}$$

Grain nucleation term:

The contribution of the grain nucleation in the momentum balance is negligibly small, so that it will be not be considered in the model.

Writing all the terms together and performing the rotational transformation $\mathbf{R}^{\vec{\omega}t}$ on the equation, the momentum conservation equation, written in the rotating reference frame, is obtained:

$$\frac{\partial}{\partial t} \left(g_k \langle \vec{v}_k \rangle^k \right) + \nabla \cdot \left(g_k \langle \vec{v}_k \rangle^k \langle \vec{v}_k \rangle^k \right) + 2g_k \vec{\omega} \times \langle \vec{v}_k \rangle^k + g_k (\vec{\omega} \times (\vec{\omega} \times \vec{x})) \quad (2.49)$$

$$+ (\vec{\omega} \times \vec{x}) \frac{\partial g_k}{\partial t} + (\vec{\omega} \times \vec{x}) \nabla \cdot \left[g_k \langle \vec{v}_k \rangle^k \right] - \frac{1}{\rho_k} (\vec{\omega} \times \vec{x}) \Gamma_k$$

0 (D)

$$=$$

$$- \frac{g_k}{\rho_k} \nabla p + \frac{1}{\rho_k} \nabla \cdot \left(g_k \mu_k \nabla \left(\langle \vec{v}_k \rangle^k \right) \right) + \frac{1}{\rho_k} \vec{M}_k^{df} + \frac{1}{\rho_k} \langle \vec{v}_k \rangle^k \Gamma_k + \frac{g_k}{\rho_k} \rho_k^b \vec{g}$$

Where, by using the phase balance equation $\frac{\partial g_k}{\partial t} + \nabla \cdot (g_k \langle \vec{v}_k \rangle) = \frac{\Gamma}{\rho_k}$ (neglecting the nucleation term), the cancellation in (D) is performed. The final equation for the momentum conservation for the phase k , in a rotational reference frame, is:

$$\frac{\partial}{\partial t} \left(g_k \langle \vec{v}_k \rangle^k \right) + \nabla \cdot \left(g_k \langle \vec{v}_k \rangle^k \langle \vec{v}_k \rangle^k \right) + 2g_k \vec{\omega} \times \langle \vec{v}_k \rangle^k + g_k (\vec{\omega} \times (\vec{\omega} \times \vec{x})) \quad (2.50)$$

$$=$$

$$- \frac{g_k}{\rho_k} \nabla p + \frac{1}{\rho_k} \nabla \cdot \left(g_k \mu_k \nabla \left(\langle \vec{v}_k \rangle^k \right) \right) + \frac{1}{\rho_k} \vec{M}_k^{df} + \frac{1}{\rho_k} \langle \vec{v}_k \rangle^k \Gamma_k + \frac{g_k}{\rho_k} \rho_k^b \vec{g}$$

2.4 Summary

The main concepts of this chapter can be resumed as follow:

- The Galilean transformation $\mathbf{G}^{\vec{V}}$ was presented in order to write the velocity in terms of a reference frame in relative movement. In case of the rotating reference frame $\vec{V} = \vec{\omega} \times \vec{x}^f$.
- The Eulerian methodology proposed by Kageyama and Hyodo [88] to derive conservation equation into rotating reference frame was presented.
- The scalar and momentum conservation equations for solidification modeling were rewritten in the rotating reference frame. In case of momentum equations, the Coriolis and centrifugal non-inertial accelerations appeared.

Chapter 3 : Thermosolutal buoyancy convection and macrosegregation during solidification in a centrifugated system

Contents

3.1	Simplified model for solidification modeling	56
3.1.1	Validation	59
3.2	Simulation of TiAl samples solidified in the “Large Diameter Centrifuge” (LDC)	65
3.2.1	Furnace thermal protocol	67
3.2.2	Solidification path and alloy phase diagram	68
3.2.3	Numerical setup	69
3.3	Results and discussion	71
3.3.1	Furnace thermal protocol: Temperature field and heat transfer	71
3.3.2	Liquid flow	73
3.3.3	Aluminum macrosegregation	80
3.3.4	Comparison with aluminum measurements	84
3.4	Summary	88

The previous chapter showed that in rotating systems two non-inertial accelerations – centrifugal and Coriolis – appear in the momentum conservation equations due to the use of a rotating coordinate system. These accelerations add three-dimensional aspects to the movement of liquid and grains that cannot be depicted by axisymmetric solvers in two-dimensional geometries. For example, the centrifugal acceleration is not homogeneous within the domain of study since it depends on the normal distance to the axis of rotation of an arbitrary point in the domain. Moreover, the Coriolis acceleration breaks any convection axisymmetry in an axisymmetric geometry. Furthermore, the literature review revealed that the impact of these accelerations on solidification has been poorly investigated.

This chapter is devoted to understand the combined effect of the centrifugal and Coriolis accelerations on the liquid thermosolutal convection and on the aluminum macrosegregation in the GRADECET experiments of TiAl directional solidification under centrifugal conditions. For that, a simplified solidification model that accounts for infinitely fast solute diffusion at microscopic scales and only columnar growth (no equiaxed grain growth nor equiaxed grain motion) was implemented in the open-source finite-volume OpenFOAM platform. This simplified solidification model is then used to perform numerical simulations of the GRADECET experiments.

The OpenFOAM platform was chosen due to its advantages on code customization, syntax of differential partial equations, unstructured polyhedral mesh handling and parallelization with respect to other commercial and open-source alternatives. In addition, OpenFOAM includes various pre- and post- processing tools that enable three-dimensional mesh generation and data visualization, among others tasks. It is important to outline that OpenFOAM does not have any license cost and is openly available under the “GNU General Public License” (GPL) [90].

This chapter is divided in three main sections. The first section presents the simplified solidification model along with validations of the numerical implementation. The validations were carried out to corroborate the prediction of macrosegregation and the simulation of natural convection in rotating systems. In the second section, the experimental protocol of the centrifugally solidified TiAl samples is presented along with the simulations numerical setup. Finally, in the third section, numerical simulations results about the liquid thermosolutal convection and aluminum macrosegregation are presented.

3.1 Simplified model for solidification modeling

In order to have a first insight about the effect of centrifugation in the TiAl directional solidification experiments under centrifugation, the model presented in Chap. 2 is simplified to a degree where the effect of the non-inertial accelerations on solidification can be realized. At microscopic scales, the model simplification consists of assuming infinitely fast solute diffusion at microscopic scales in both phases, *i.e.* lever rule, for a binary alloy. This is the simplest phase change model that can be used in macroscopic solidification modeling. For its part, the description of the macroscopic phenomena can be simplified assuming that the microstructure of the solid phase is entirely columnar, such that the solid phase is fixed in the domain of study, *i.e.*

it is motionless. This assumption simplifies the overall system of differential partial equations. Despite the simplifications, the model describes the full coupling between enthalpy, temperature, solute concentration in both phases, solid growth and phase fractions.

The simplified solidification model is similar to the one used by Combeau et al. [4], in which heat transfer, solute transport, buoyancy driven liquid flow, and solidification of a binary alloy are taken into account. The volume-averaging method [5, 6, 7] is used to formulate conservation equations for mass, momentum, energy and solute. The equations are formulated in terms of averaged quantities, such as averaged intrinsic liquid velocity, $\langle \vec{v}_l \rangle^l$, averaged enthalpy, $\langle h \rangle$, and averaged solute concentration, $\langle C \rangle$, respectively. The equations are formulated for a non-inertial reference frame, therefore the momentum equation accounts for the centrifugal and Coriolis accelerations. The Kozeny-Carman relation is used to calculate the hydrodynamic permeability, K , of the mushy zone and the Boussinesq approximation is employed to take into account the thermosolutal buoyancy driven flow. The solid and liquid densities are considered to be constant and equal, $\rho_l = \rho_s = \bar{\rho}$, therefore, the solidification shrinkage effect is not included in the model. The solid phase is considered to be fixed in the domain, *i.e.* $\langle \vec{v}_s \rangle^s = 0$, since the model only represents columnar growth with no fragmentation possibility.

The energy conservation equation is formulated in terms of the averaged enthalpy, $\langle h \rangle = c_p T + \frac{g_l \rho_l L_f}{\bar{\rho}} = c_p T + g_l L_f$ (note that $\bar{\rho} = \rho_l$), where c_p is the specific heat, T the temperature, L_f the latent heat, and g_l the liquid fraction. The specific heat is considered constant and equal between the phases, $c_{pl} = c_{ps} = c_p$. The thermal conductivity coefficient, k , is also considered to be constant. The local temperature is assumed to be equal in the solid and liquid phases, $T = T_s = T_l$.

Finally, the solid-liquid phase change is modeled by an equilibrium model that assumes infinitely fast diffusion at the microscopic scale (lever rule). This equilibrium model is taken into account in order to simplify the overall model and still be able to depict the liquid thermosolutal convection and the solute segregation pattern. The diffusion at the macroscopic scale is neglected. The full description of the volume-averaged solidification model is presented below.

- *Mass conservation:* Only the liquid movement is considered.

$$\nabla \cdot (g_l \langle \vec{v}_l \rangle^l) = 0 \quad (3.1)$$

- *Liquid momentum conservation:*

$$\begin{aligned} \frac{\partial}{\partial t} (g_l \langle \vec{v}_l \rangle^l) + \nabla \cdot (g_l \langle \vec{v}_l \rangle^l \langle \vec{v}_l \rangle^l) + 2g_l (\vec{\omega} \times \langle \vec{v}_l \rangle^l) = \\ - \frac{g_l}{\rho} \nabla p + \nabla \cdot (g_l \nu_l \nabla \langle \vec{v}_l \rangle^l) - \frac{\nu_l g_l^2}{K} \langle \vec{v}_l \rangle^l + \frac{g_l \rho_l^b}{\rho} [\vec{g} - \vec{\omega} \times (\vec{\omega} \times \vec{x}_c)] \end{aligned} \quad (3.2)$$

Where $\rho_l^b = \rho_l (1 - \beta_T (T - T_{ref}) - \beta_C (\langle C_l \rangle^l - C_{ref}))$ and $K = \frac{\lambda_2^2 g_l^3}{180(1-g_l)^2}$, with λ_2 the secondary arm spacing which is considered as the characteristic length for permeability of the mushy zone.

– *Energy conservation:*

$$\frac{\partial \langle h \rangle}{\partial t} + \nabla \cdot (g_l \langle \vec{v}_l \rangle^l \langle h_l \rangle^l) - \frac{1}{\rho} \nabla \cdot (k \nabla T) = 0 \quad (3.3)$$

Where $\langle h \rangle = c_p T + g_l L_f$ and $\langle h_l \rangle^l = c_p T + L_f$.

– *Solute conservation:* Macroscopic solute diffusion is neglected.

$$\frac{\partial \langle C \rangle}{\partial t} + \nabla \cdot (g_l \langle \vec{v}_l \rangle^l \langle C_l \rangle^l) = 0 \quad (3.4)$$

– *Liquid fraction:* The local state is obtained by comparing the averaged enthalpy to the enthalpy based phase diagram. An invariant point at the temperature $T_{per} = T_f + m_l C_{inv}$ is considered. Then, the liquid fraction is calculated as:

$$g_l = \begin{cases} 1.0 & \text{if } \langle h \rangle > h_{liq} ; \text{ Fully liquid} \\ 0.0 & \text{if } \langle h \rangle < h_{sol} ; \text{ Fully solid} \\ \frac{\langle h \rangle - c_p T_{per}}{L_f} & \text{if } c_p T_{per} < \langle h \rangle < h_{per} ; \text{ Pseudo-peritectic} \\ \frac{-B + \sqrt{(B^2 - 4A \cdot V)}}{2A} & \text{otherwise ; Primary Solidification} \end{cases} \quad (3.5)$$

Where, $h_{liq} = c_p \max(T_f + m_l \langle C \rangle, T_{per}) + L_f$ is the *liquidus* enthalpy, $h_{sol} = c_p \max(T_f + \frac{m_l}{k_p} \langle C \rangle, T_{per})$ the *solidus* enthalpy and $h_{per} = c_p T_{per} + \frac{L_f (\langle C \rangle - k_p C_{inv})}{(1 - k_p) C_{inv}}$ the enthalpy in which the pseudo-peritectic transformation starts taking place, where k_p is the partition coefficient. In case of primary solidification, the liquid fraction is calculated from a second order equation which is obtained by combining the equations for average solute concentration (Eqn. 3.6), the solid-liquid equilibrium relations (Eqns. 3.7 and 3.8) and the average enthalpy relation ($\langle h \rangle = c_p T + g_l L_f$). The parameters for the primary solidification case in Eqn. 3.5 are given by:

$$A = \frac{L_f (k_p - 1)}{c_p m_l} = \text{cte.}$$

$$B = \frac{\langle h \rangle (1 - k_p) - k_p L_f}{c_p m_l} + \frac{T_f (k_p - 1)}{m_l} = B(\langle h \rangle)$$

$$V = \frac{k_p \langle h \rangle}{c_p m_l} - \frac{k_p T_f}{m_l} - \langle C \rangle = V(\langle h \rangle, \langle C \rangle)$$

– *Supplementary relations:*

- Averaged solute concentration:

$$\langle C \rangle = g_l \langle C_l \rangle^l + (1 - g_l) \langle C_s \rangle^s \quad (3.6)$$

- Solid - liquid equilibrium relations:

$$T = T_f + m_l \langle C_l \rangle^l \quad (3.7)$$

$$\langle C_s \rangle^s = k_p \langle C_l \rangle^l \quad (3.8)$$

This simplified model was implemented using OpenFOAM high-level syntax to take advantage of automatic parallelization. The new numerical solver was called *macroS3D* and uses an iterative procedure to couple the averaged enthalpy, the liquid averaged concentration, liquid fraction and temperature on each time step.

3.1.1 Validation

As all new numerical implementations, *macroS3D* required to be validated. Unfortunately, a well documented case involving liquid thermosolutal convection during centrifugal solidification was not found in the literature. For this reason, solidification and buoyancy driven liquid convection in rotating systems were validated separately. With regard to solidification cases, *macroS3D* was validated for the prediction of macrosegregation by simulating the benchmark case proposed by Bellet et al. [51]. This validation case is presented in Sect. 3.1.1.1. On the other hand, the buoyancy driven liquid convection under centrifugal conditions was validated using a well documented rotating annulus case. This validation case is presented in Sect. 3.1.1.2.

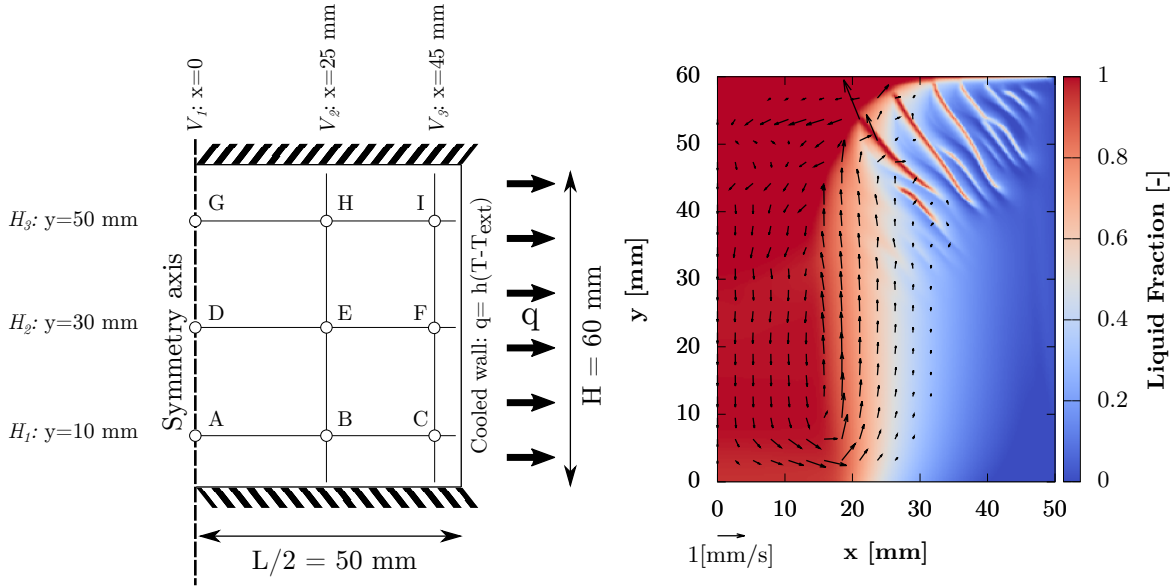
3.1.1.1 Prediction of macrosegregation

macroS3D was validated for solidification cases using the Pb-18wt%Sn benchmark solidification case proposed by Bellet et al. [51]. This benchmark case was well documented by Combeau et al. [4], who reported results obtained with various numerical implementations. The case consists of the solidification of a two-dimensional cavity (50 mm wide and 60 mm high), which is cooled from the right side, whereas the left side is a symmetry plane and the upper and lower sides are thermally insulated. Figure 3.1a presents a schematic of the solidification domain and its boundary conditions.

In order to perform the numerical simulation, a quadrilateral mesh containing 200 cells along the width and 240 along the height was created using the OpenFOAM standard tool *blockMesh*. The first order *upwind* interpolation scheme was used for all advective terms and a linear interpolation scheme for all diffusion terms. The alloy thermophysical properties used to simulate this case are reported in Appendix A.1.1.

In this case, from a purely thermal point of view, the main circulation sense of the liquid convection should be clockwise since cold liquid tends to flow downwards by the right boundary and upwards by the symmetry plane. However, once solidification starts, tin is rejected from

growing solid, making the colder liquid in the mushy zone lighter. Particularly in this case, the solutal buoyancy effect completely counteracts the thermal buoyancy effect, leading to a counterclockwise circulation sense of the liquid convection. The enriched liquid finds its way through the mushy zone in zones where the permeability is high, forming segregation channels. Figure 3.1b shows the instantaneous intrinsic liquid velocity along with the liquid fraction obtained with *macroS3D* after 120 s of solidification. The figure shows the formation of segregation channels in the top-right of the domain and a counterclockwise liquid circulation sense.



(a) Schematic of the solidification domain. Chill heat transfer parameters: $h = 400 \text{ W}/(\text{m}^2\text{K})$ and $T_{ext} = 25^\circ\text{C}$.

(b) Liquid fraction and liquid velocity after 120 s of solidification. Result obtained with *macroS3D*

Figure 3.1 – Schematic and instantaneous result of the Pb-18wt%Sn solidification case proposed by Bellet et al. [51]

Combeau et al. [4] reported results obtained with different numerical solvers for this benchmark case. “castFoam” is one of those solvers and was also implemented using the OpenFOAM platform. Although both, “castFoam” and *macroS3D*, are based in the OpenFOAM platform, they use entirely different algorithms for the coupling of heat transfer, solute transport, flow and phase change. For example, “castFoam” uses a temperature based approach to solve the energy conservation equation whereas *macroS3D* solves for the averaged enthalpy. In spite of the differences on their numerical implementations, results obtained with “castFoam” and *macroS3D* are comparable since both solve very similar solidification models. Following, a comparison between “castFoam” and *macroS3D* is carried out in order to validate the new implementation. Here, the solution obtained by “castFoam” is considered as reference since it was already compared with other well-validated numerical implementations (see ref. [4]).

Figure 3.2 presents a comparison for the intrinsic liquid velocity and the liquid fraction along the H_2 horizontal line (see Fig. 3.1a) after 120 s of solidification. The figure shows that the liquid velocity magnitude decreases dramatically as the liquid fraction decreases due to the

low permeability of the mushy zone that imposes a high restriction to the intradendritic liquid flow. Indeed, the instantaneous maximum liquid velocity is found near the columnar front and is around $0.7 \text{ mm} \cdot \text{s}^{-1}$. A local minimum velocity ($\sim 0.1 \text{ mm} \cdot \text{s}^{-1}$) is found at $x \sim 15 \text{ mm}$ (where x is the distance to the symmetry axis) since there is located the center of the liquid convection cell. Additionally, small local liquid velocity peaks are observed around $x \sim 30 \text{ mm}$ due to the formation of segregation channels. These local peaks are noticed in the solution of both numerical implementations but with a slight difference on their localization. With regard to the liquid fraction, both solvers give very similar solutions that are difficult to differentiate to the naked eye.

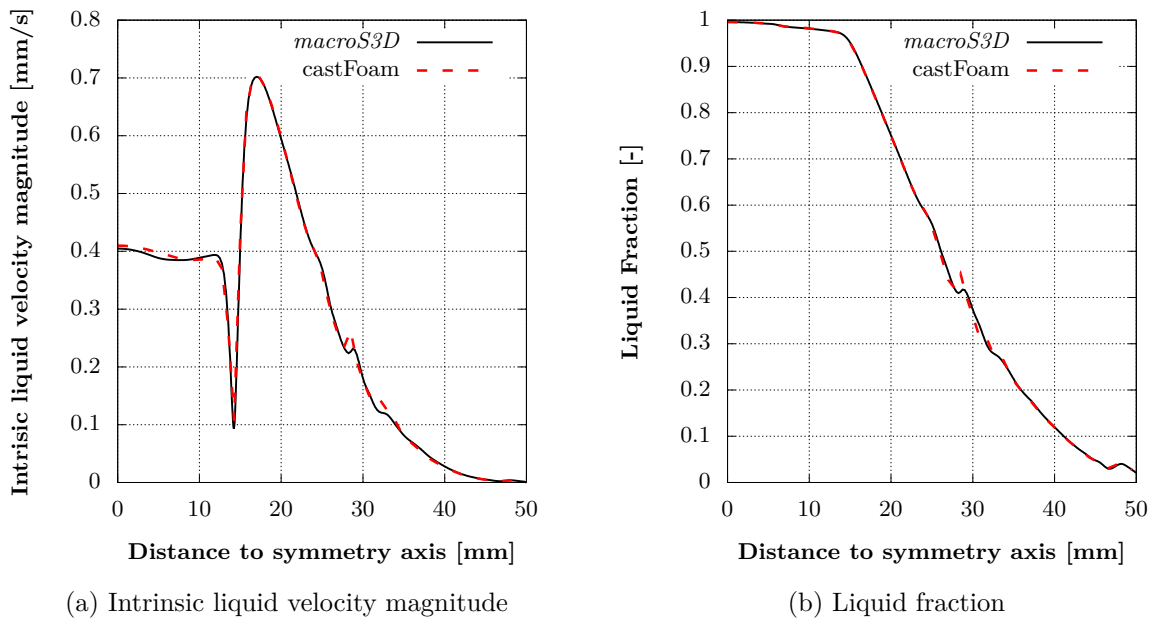


Figure 3.2 – Comparison between “castFoam” and *macroS3D*: Instantaneous intrinsic liquid velocity magnitude and liquid fraction at $t = 120 \text{ s}$ along the H_2 line (see Fig. 3.1a)

Figure 3.3 presents a comparison for the tin concentration at the end of solidification in the horizontal H_1 and H_2 lines (see Fig. 3.1a). The figure shows that the solute concentration follows a similar pattern along both lines: it approaches to the nominal concentration near the chill face, it is impoverished by the center of the domain and enriched by the symmetry line. This pattern is explained due to the interdendritic flow that takes place during solidification within the mushy zone. Thus, following the solute profile in H_1 and H_2 lines, the solute impoverishment located at $x > 10 \text{ mm}$, approximately, is produced since (along with the advance of solidification front from left to right) solute enriched liquid flows towards the top of the domain within the mushy zone, depleting the bottom of the domain in solute. Indeed, H_1 line is quantitatively more tin impoverished than H_2 line (H_2 is located above H_1). Simultaneously, the solute enriched liquid flow retards the solidification of the top of the domain since a solute enrichment takes place there. Moreover, solute enriched liquid from the mushy zone is able to enter the fully liquid region by the top of the domain, as shown in Fig. 3.1b. The solute enrichment observed

for $x < 10$ mm close to the symmetry plane, is produced since the last liquid, which is solute enriched, solidifies there. In case of the line H_1 , the solution of both solvers are superimposed as showed in Fig. 3.3a and no difference is noticed. On the other hand, in case of the line H_2 , slight differences near $x \sim 28$ mm are noticed. Here the line crosses two mild segregation channels and the prediction of both solvers is similar with respect to their magnitude but small differences of their position are noticed.

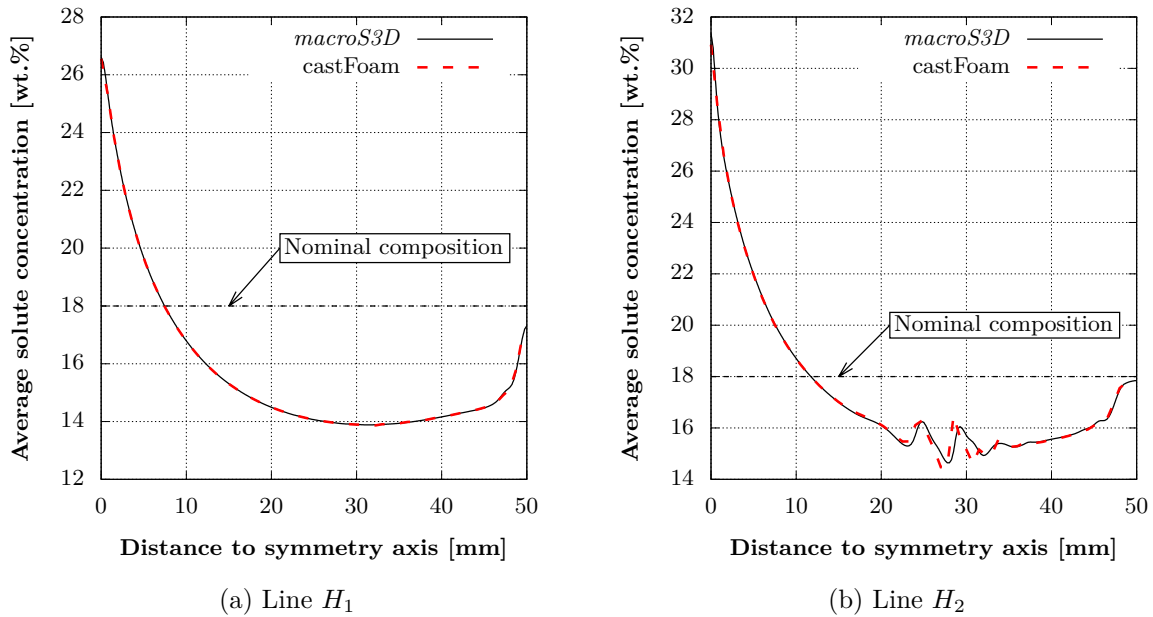


Figure 3.3 – Comparison between “castFoam” and *macroS3D*: Averaged solute concentration of tin at the end of solidification in H_1 and H_2 lines (See Fig. 3.1a)

Figure 3.4 shows a comparison of the tin segregation in the entire domain at the end of solidification. Three main features about the segregation map can be pointed out. The first is a zone depleted in tin in the bottom of the domain due to liquid intradendritic flow during solidification. The second feature is an enriched zone located in the top-left corner because the last liquid, that is solute enriched, solidifies there. The third feature are segregation channels that take place by the top-left corner due to liquid intradendritic flow and the entrapment of solute rich liquid in the mushy zone during solidification. Combeau et al. [4] pointed out that the predicted shape, position and intensity of solute enrichment of the segregation channels are very sensitive to the numerical method and to the spatial and time discretization schemes used to solve the model constituted by the coupled system of differential partial equations.

In spite of the small differences found in the solution of *macroS3D* and “castFoam”, it is concluded that both solvers give similar qualitative and quantitative results. The only noticeable differences are the position, shape and intensity of the segregation channels.

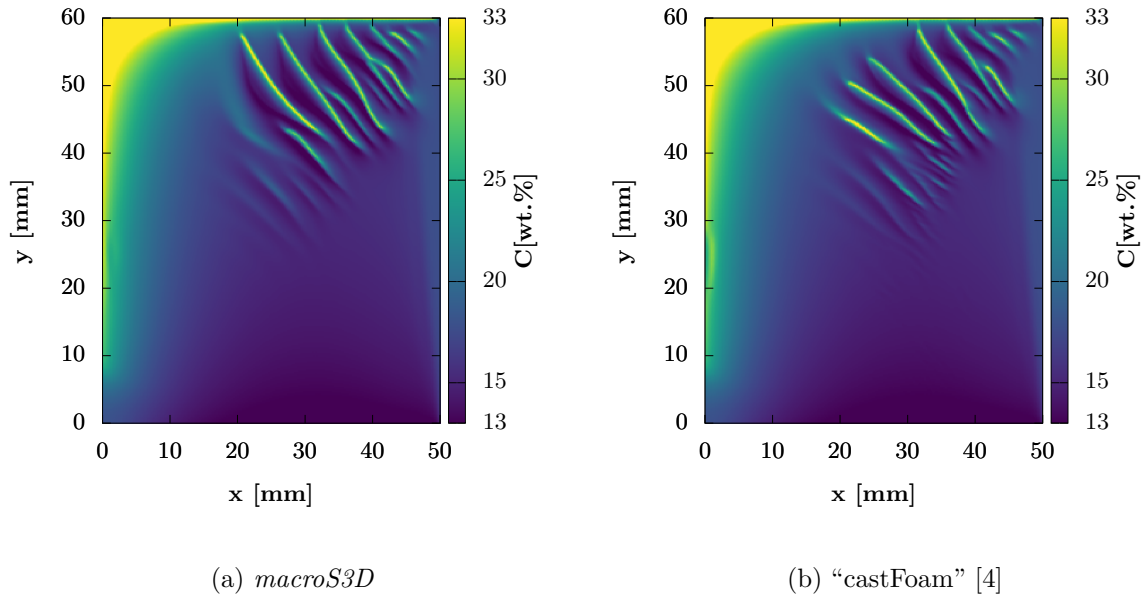


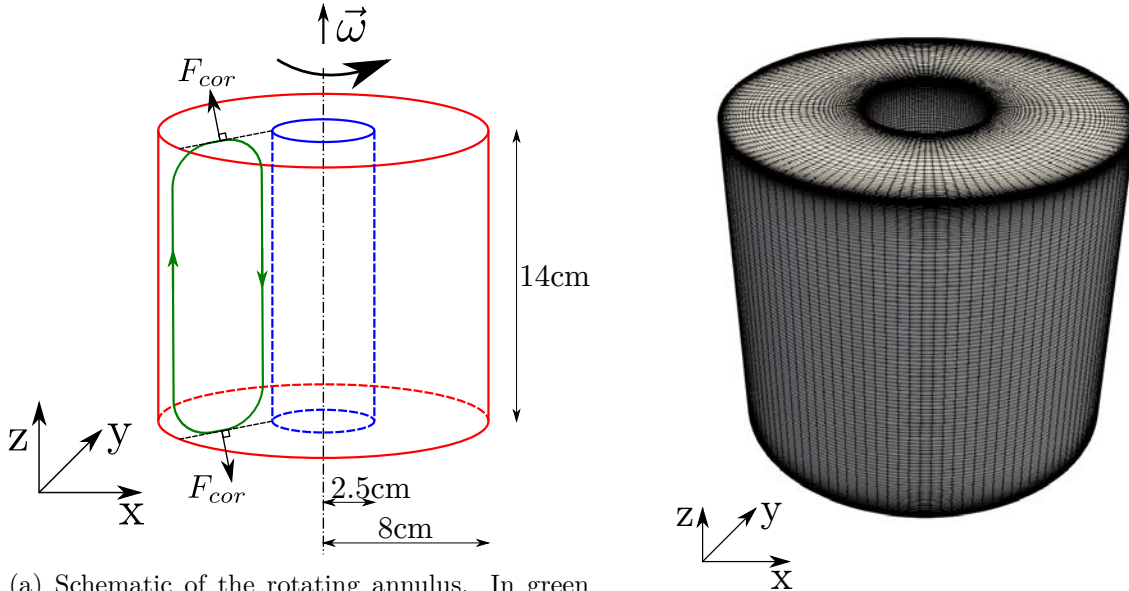
Figure 3.4 – Tin segregation map at the end of solidification. Comparison between *macroS3D* and “castFoam” [4] (re-plotted).

3.1.1.2 Natural convection in a rotating annulus

Along with the validation for the prediction of macrosegregation, *macroS3D* was validated on the description of natural convection in rotating systems. For that, a case of natural convection in a thermally-driven rotating annulus was selected since it was well reported, both numerically and experimentally, by Hignett et al. [91] and Young et al. [92]. The case consists of an annulus $d = 14$ cm high, with an inner radius equal to $r_{in} = 2.5$ cm and an outer radius equal to $r_{out} = 8$ cm as shown in Fig. 3.5a. The annulus rotates at a constant angular velocity of $\vec{\omega} = 1 \text{ rad} \cdot \text{s}^{-1}$ and the axis of rotation coincides with the axis of the annulus. The annulus inner side is 4°C colder than the annulus outer side. This induces a convection cell: the liquid flows downwards by the cold side and upwards by the hot side. The base and the top of annulus are thermally insulated and the working fluid is a mixture of water and glycerol. This case does not consider solidification. The dimensionless numbers that characterize the effect of rotation in this case are the Taylor number and the thermal Rossby number. The Taylor number, which is the ratio between the forces due to rotation and the viscous forces, is defined in this case as $Ta = \frac{4\omega^2(r_{out}-r_{in})^5}{\nu^2 d} = 5.21 \times 10^6$. On the other hand, the thermal Rossby number, which is the ratio between buoyancy/inertial forces and Coriolis forces is defined as $Ro_T = \frac{g\beta_T(T_h-T_c)d}{\omega^2(r_{in}-r_{out})^2} = 0.52$, where $T_h = 22^\circ\text{C}$ is the temperature of the outer side and $T_c = 18^\circ\text{C}$ the one of the inner side [92]. The Prandtl number of the fluid used in the experiments is $Pr = 13.07$. The Rayleigh number can be calculated as $Ra = \frac{\rho c_p g \beta_T (T_h - T_c) d}{k \nu} = 1.45 \times 10^7$, where k is the thermal conductivity coefficient.

Initially, in the base of the annulus, the liquid flows radially from the cold side towards the hot side, whereas, in the top, the flow is in the other way around, as shown in Fig. 3.5a.

This radial flows are deflected in the base and in the top in opposite directions by the Coriolis acceleration. Over time, the Coriolis acceleration destabilizes the axisymmetric convection cell, driving the formation of baroclinic waves. The objective of this section is to compare the results obtained by means of *macroS3D* to the experimentally measured liquid velocity from references [92, 91], rather than doing a physical analysis of the baroclinic waves phenomenon.



(a) Schematic of the rotating annulus. In green the shape of the convection cell before being deflected by the Coriolis acceleration (F_{cor}). Inner side represented in blue and outer side in red.

(b) Three-dimensional mesh used to spatially discretize the annulus domain.

Figure 3.5 – Schematic of the rotating annulus case along with the three-dimensional mesh used to perform the numerical simulations.

Small modifications to the *macroS3D* code were introduced in order to simulate this case. The objective of these modifications is the improvement of the representation of the fluid properties (thermal diffusivity, viscosity and buoyant liquid density) since they present a high temperature dependency. More details on the fluid properties are reported in Appendix A.1.2. The mesh was created using *blockMesh* and was constituted by 8.64×10^5 hexahedral cells. Mesh refinements were applied normal to the boundaries as shown in Fig. 3.5b. The second order *van Leer* interpolation scheme was used for all advective terms and a linear interpolation for all diffusion terms. The PISO algorithm with two correctors was used for the velocity-pressure coupling, with two non-orthogonal iterations.

A null liquid velocity and an uniform temperature of $\frac{T_h+T_c}{2} = 20^\circ\text{C}$ were imposed as initial conditions. In the simulations, the liquid convection developed transiently until reaching a stabilized regime. In order to calculate the mean velocity field, the instantaneous velocity field was sampled during the stabilized regime until the convergence of the mean velocity field.

Figure 3.6 presents a comparison for the velocity between results obtained with *macroS3D* and experimental measurements reported in reference [92] in a horizontal plane located 12.4 cm from the annulus base. In this plane, three structures with a counterclockwise circulation are

identified. These structures change their position over time following a circular path when they are observed from the rotating reference frame. The Coriolis acceleration produces these structures by deflecting the liquid flow in opposite directions in the top and the base of the annulus as schematized in Fig. 3.5a. The solution given by *macroS3D* is very similar to the experimental measurements reported in [92] and no differences are observable to the naked eye.

Figure 3.7 presents a comparison between *macroS3D* and numerical and experimental results reported by Hignett et al. [91] for the mean azimuthal velocity (time averaged) in different horizontal lines. The results show that the mean azimuthal velocity near the top and the bottom (see Figs. 3.7a and 3.7e, respectively) presents similar shape but different direction, which makes evident the effect of the Coriolis acceleration acting in opposite directions. Moreover, the azimuthal velocity in the horizontal line at 7.0 cm (half height of the domain) from the annulus base (Fig. 3.7c) presents the lowest magnitude since the Coriolis effects in the top and bottom are mutually counteracted there. This comparison of the mean velocity profiles shows a good agreement between the *macroS3D* and the numerical and experimental results reported in ref. [91]. This validates *macroS3D* to be used in cases of natural convection in rotating systems.

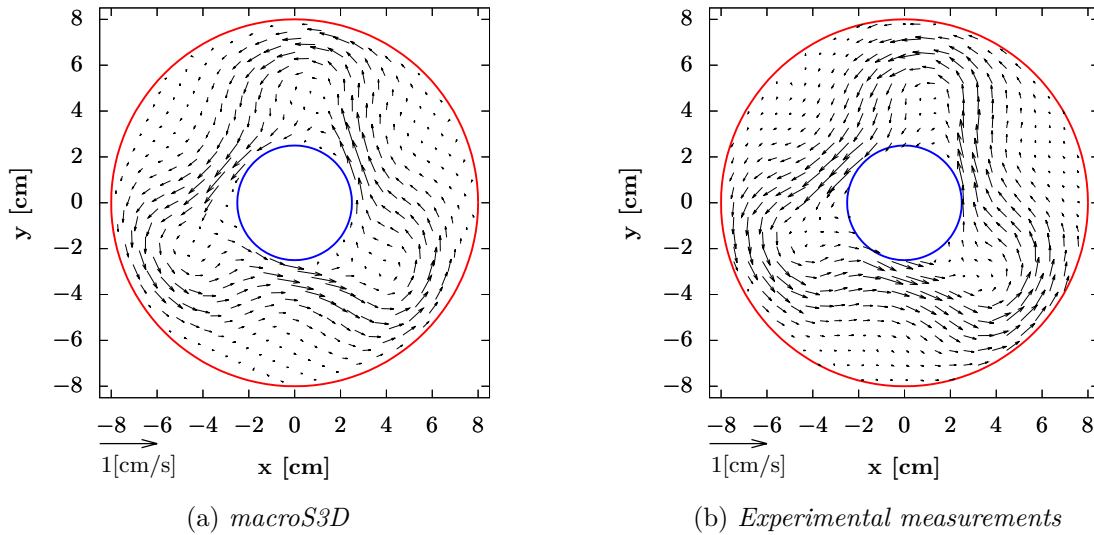


Figure 3.6 – Instantaneous liquid velocity fields projected into the corresponding horizontal plane of height 12.4 cm. Comparison between results obtained with *macroS3D* and experimental measurements. The inner side (blue line) is 4 °C colder than the outer side (red line).

3.2 Simulation of TiAl samples solidified in the “Large Diameter Centrifuge” (LDC)

Once *macroS3D* was validated on the prediction of macrosegregation and on the simulation of liquid buoyancy convection in rotating systems, it was used to simulate the experiments of TiAl directional solidification under centrifugal conditions carried out by N. Reilly [1] within the framework of the GRADECET project. The experiments consisted of the directional solidifica-

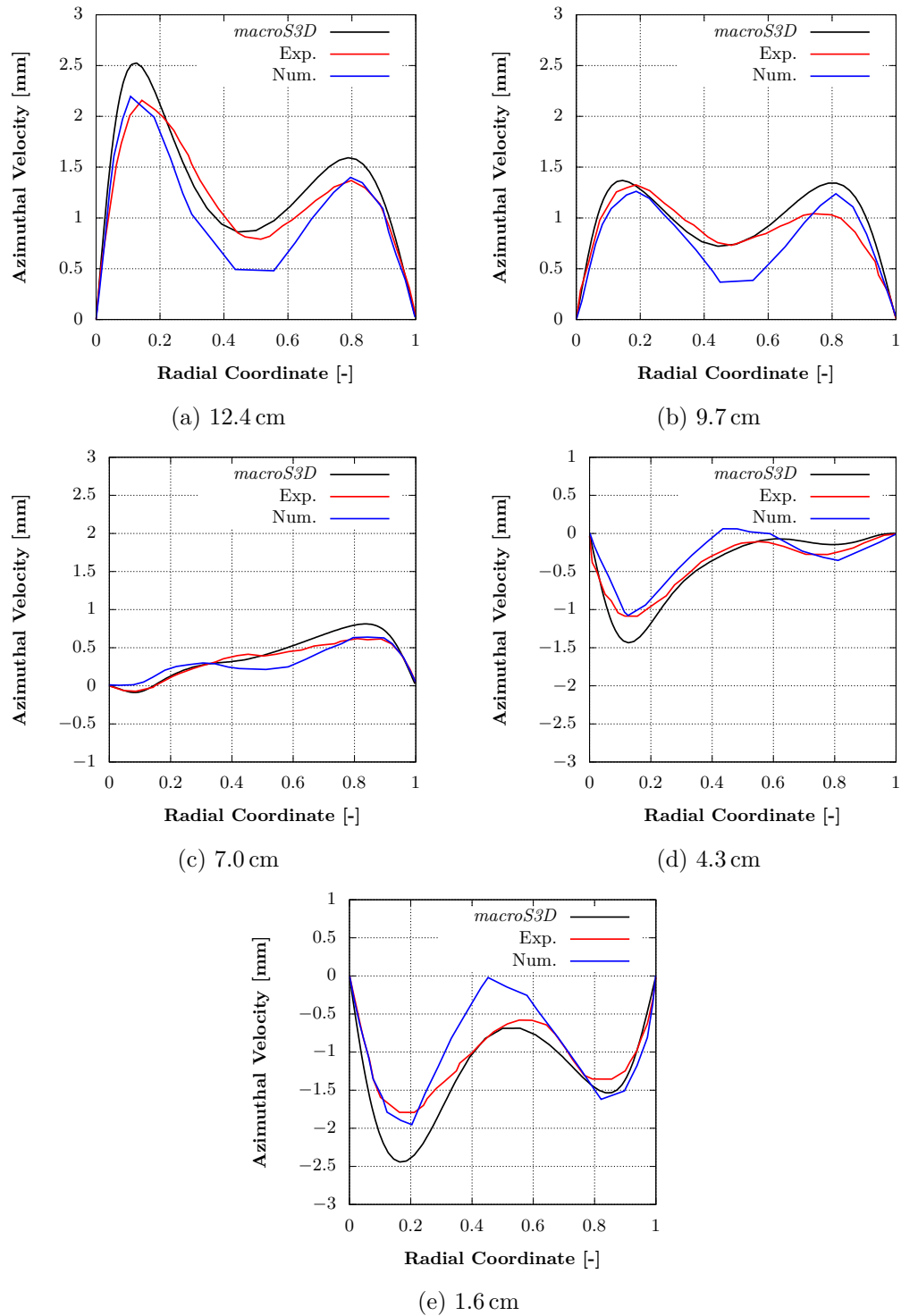


Figure 3.7 – Comparison between *macroS3D* numerical results, experimental measurements and numerical results from [91]: Mean azimuthal velocity vs radial position for horizontal lines at 12.4, 9.7, 7.0, 4.3 and 1.6 cm from the annulus base

tion of cylindrical TiAl samples (8 mm diameter and 165 mm long) in the ESA Large Diameter Centrifuge (“LDC”). The custom designed directional solidification furnace was placed in a gondola fixed at the end of the arm of the centrifuge, at a distance of 4 m from the rotation axis. The gondola was free to tilt, such that the total apparent gravity (the sum of the terrestrial gravity and centrifugal acceleration) was always aligned with the sample centerline. Four centrifugation speeds were used, corresponding to gravity levels of $5g$, $10g$, $15g$, and $20g$, where g is the terrestrial gravity acceleration. Additionally, a case in which $\vec{g}_{tot} = 1g$ was performed without centrifugation, under terrestrial gravity aligned with the sample centerline.

3.2.1 Furnace thermal protocol

The thermal protocol consisted of three stages: remelting of the initially solid sample, holding and solidification. It was driven by three temperature controlled heaters placed around the crucible, as shown in Fig. 3.8. During the solidification stage the thermal protocol was adjusted in order to induce a temperature field that would promote a columnar-to-equiaxed transition. The remelting stage starts with a fully solid sample and the heaters increase their temperature until the sample is partially melted. Following, in the holding stage, all the heaters maintain their temperature for five minutes in order to stabilize the thermal profile within the sample. The solidification and last stage is divided in two sub-stages. In the first solidification sub-stage, the heater “H3” decreases its temperature at a cooling rate of $0.3 \text{ K} \cdot \text{s}^{-1}$ for 120 s while heaters “H1” and “H2” maintain their temperature. In the second solidification sub-step, the heater “H3” decreases its cooling rate to $0.1 \text{ K} \cdot \text{s}^{-1}$ while “H1” and “H2” increase it to $0.4 \text{ K} \cdot \text{s}^{-1}$. This second-substage lasts 367 s implying that the total duration of the solidification stage is 487 s. At the end of the solidification stage, the sample is quenched, solidifying any remaining liquid. Time is defined as $t = 0$ at the beginning of the solidification stage. The temperature was sampled throughout each experiment by three thermocouples located in each heater and one located in the part of the sample that was not melted (Fig. 3.8). Figure 3.9 shows the temperature measured by the thermocouples over time, along with the corresponding protocol stages. In Figure 3.10 a schematic of the furnace configuration mounted in the centrifuge gondola is presented. More details on the experimental configuration are reported in reference [1].

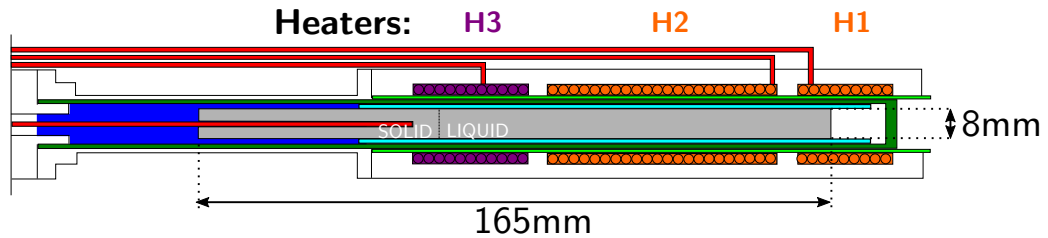


Figure 3.8 – Schematic of the sample, heaters and thermocouples. The thermocouples are represented by the red wires and the heaters by purple (“H3”) and orange (“H1” and “H2”) circles. At $t = 0$, the heaters temperatures are $T_{H1} = 1623 \text{ }^\circ\text{C}$, $T_{H2} = 1623 \text{ }^\circ\text{C}$ and $T_{H3} = 1543 \text{ }^\circ\text{C}$.

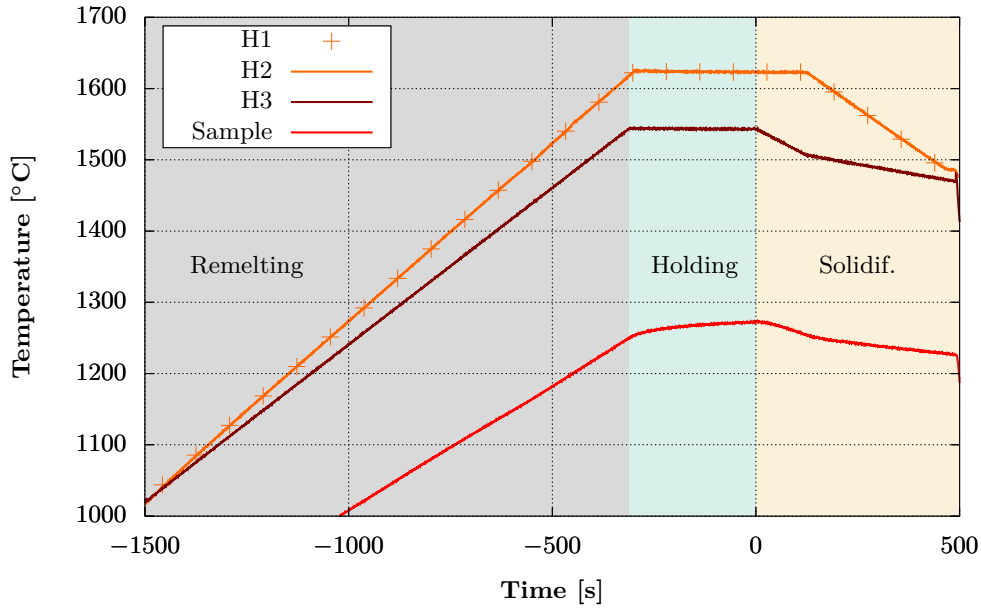


Figure 3.9 – Temperature measured by the thermocouples in the three stages of the furnace protocol. Time $t = 0$ is adjusted the beginning of the solidification stage.

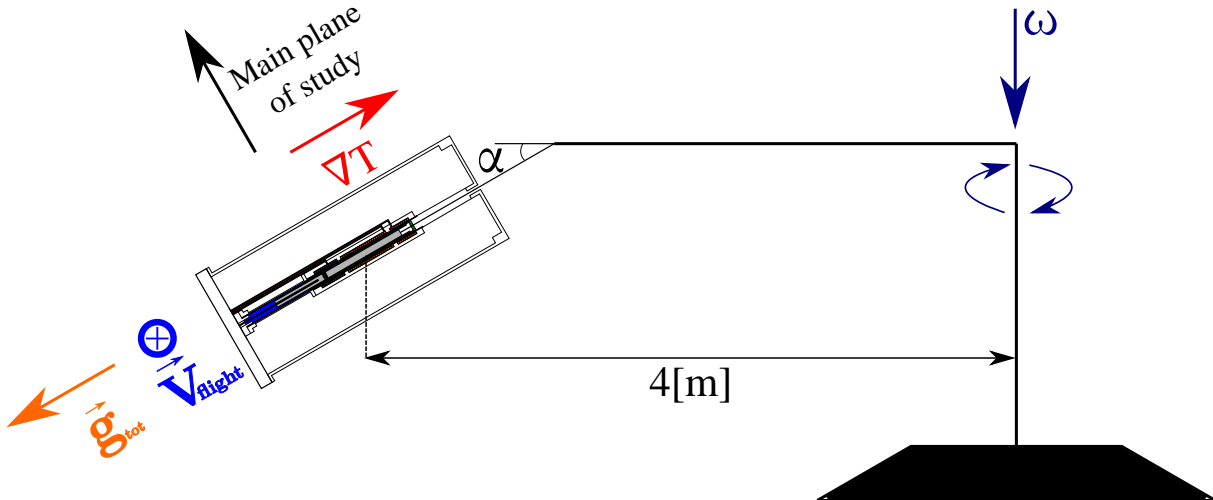
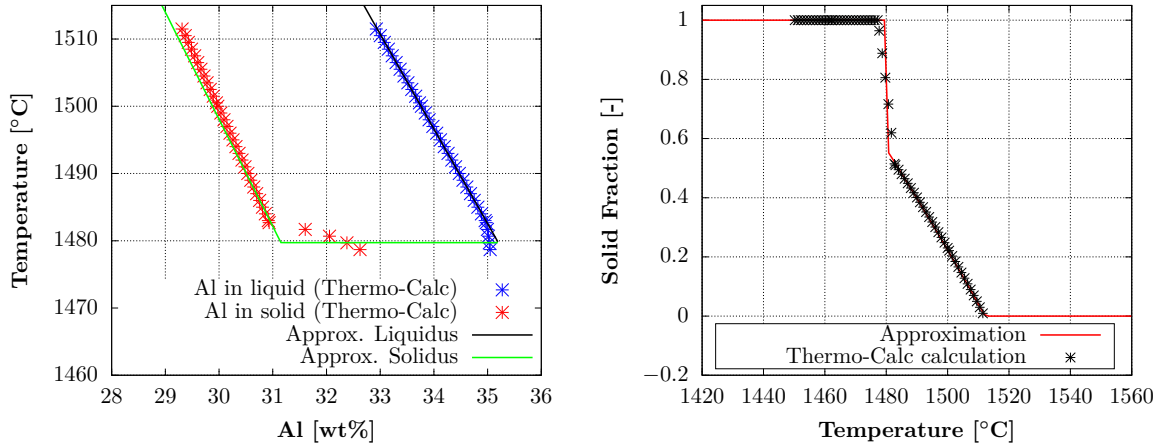


Figure 3.10 – Schematic of the furnace and the TiAl sample in the centrifuge. The sample is represented in grey and the heaters in orange and yellow. The furnace tilting angle is denoted by α , the furnace flight velocity by \vec{V}_{flight} (in blue), the total apparent gravity by \vec{g}_{tot} (in orange) and the main temperature gradient by ∇T (in red). The main plane of study is defined as the one formed by the flight velocity vector, \vec{V}_{flight} and the total apparent gravity, \vec{g}_{tot} . Four different apparent gravities were investigated under centrifugation: $\vec{g}_{tot} = 5g, 10g, 15g$ and $20g$.

3.2.2 Solidification path and alloy phase diagram

The alloy composition was Ti-32.96wt%Al-2.49wt%Cr-4.76wt%Nb (Ti-47.46at%Al-1.86at%Cr-1.99at%Nb in atomic percent). This alloy is also known as “GE alloy”. This alloy undergoes a



(a) Averaged equilibrium concentration of aluminum in solid and liquid phases vs temperature.

(b) Solidification path

Figure 3.11 – Results of the solidification path simulation using Thermo-Calc Software along with the approximations used in this work.

peritectic transformation in its solidification path near 1480 °C. In order to account for this transformation, a simulation of the solidification path was performed using Thermo-Calc Software considering full equilibrium between the phases. The multicomponent alloy was approximated by a pseudo-binary approximation (Ti-32.96wt.%Al) that fits the full alloy in terms of solidification path, solute partitioning and evolution of the liquid density in the mushy zone. This approximation was performed considering the multi-component equilibrium composition along the solidification path obtained with Thermo-Calc Software and calculating the corresponding liquid density at a given temperature and aluminum composition. Figure 3.11a presents the averaged aluminum concentration in solid and liquid phases obtained with Thermo-Calc and the approximation for the *liquidus* and *solidus* lines used in this work. Figure 3.11b presents the corresponding solidification path that assumes thermodynamic equilibrium between all phases along with the approximation of the solidification path used in this work. The simplified solidification path considers an invariant point – pseudo-peritectic – at $T_{per} = 1479.7^{\circ}\text{C}$. This simplification on the solidification path is valid under hypo-peritectic solidification. Yet, it can also be used as an approximation under hyper-peritectic solidification, in the neighborhood of the peritectic point, if a low peritectic phase formation is assumed. The nominal alloy composition used in this work is slightly hypo-peritectic and it is assumed that the formation of peritectic phase does not have a large impact on the solute segregation.

3.2.3 Numerical setup

The domain of study was a cylinder 8 mm in diameter and 118 mm long since in the experiments the samples were not fully remelted. The domain was discretized in a structured hexahedral mesh using the standard OpenFOAM tool *blockMesh*, as presented in the schematic of Fig. 3.12. The mesh is constituted by 5×10^5 cells, that are distributed following an *O-H grid* (see

Fig. 3.12b), with 250 cells along the cylinder length and 45 cells along the cylinder diameter (in average, $\sim \sqrt{(5 \times 10^5)/250}$). The maximum mesh non-orthogonality angle is 37.8 (the maximum recommended is $\ll 70$) and the maximum skewness is 0.56, which means that the generated mesh has a good quality and can be used for numerical simulations. Only the solidification stage of the thermal protocol was simulated. The furnace was not included in the model.

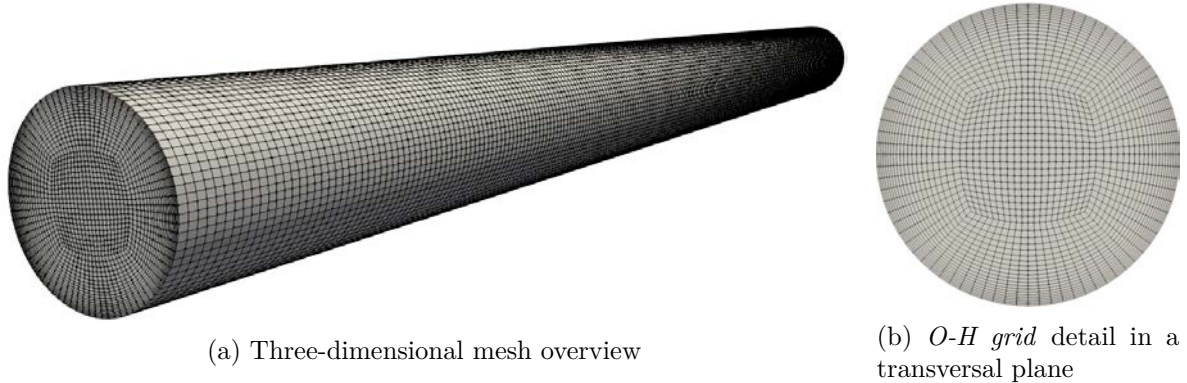


Figure 3.12 – Schematic of the three-dimensional mesh

Due to the complex design of the furnace, the heater temperatures can not be directly used as boundary conditions on the sample furnace. Moreover, *macroS3D* does not have a conjugate heat transfer facility to simulate the conducting/insulating walls of the furnace. For that reason, numerical heat transfer simulations of the full furnace using a dedicated furnace model were performed and calibrated with temperature measurements to obtain realistic boundary conditions. In these simulations, the latent heat release due to phase change was included. From these simulations, the evolution of the temperature profile along the sample over time was extracted. The temperature information was imposed as a Dirichlet boundary condition on the surface of the TiAl sample in the solidification simulations. Figure 3.13 shows the temperature boundary conditions on the cylinder surface at different times. The initial temperature in the cylinder was assumed to be independent of the radius and to follow the temperature profile at $t = 0$. The initial solid fraction was determined from the temperature using the solidification path (see Fig. 3.11b). In addition, throughout the domain, at $t = 0$, the liquid intrinsic velocity was assumed to be null (it is assumed that a permanent regime is reached in the experiments), and the aluminum concentration to be equal to the nominal concentration ($\langle C \rangle = 32.96$ wt.%). The characteristic length for the mushy zone permeability is assumed to be the secondary dendrite arm spacing (SDAS), which was measured by means of post-mortem grain morphology characterizations of the GRADECET experiments [1]. Table 3.1 presents the thermophysical properties that were used in the numerical simulations.

The finite-volume method was used to solve all transport equations (Eqns. 3.1-3.4). The *van Leer* interpolation scheme was used for the discretization of all advective terms and a linear interpolation scheme for all diffusion terms in the system of differential partial equations. For the discretization of the temporal terms, an implicit Euler scheme was used. The PISO algorithm with two correctors was used for the velocity-pressure coupling with two non-orthogonal

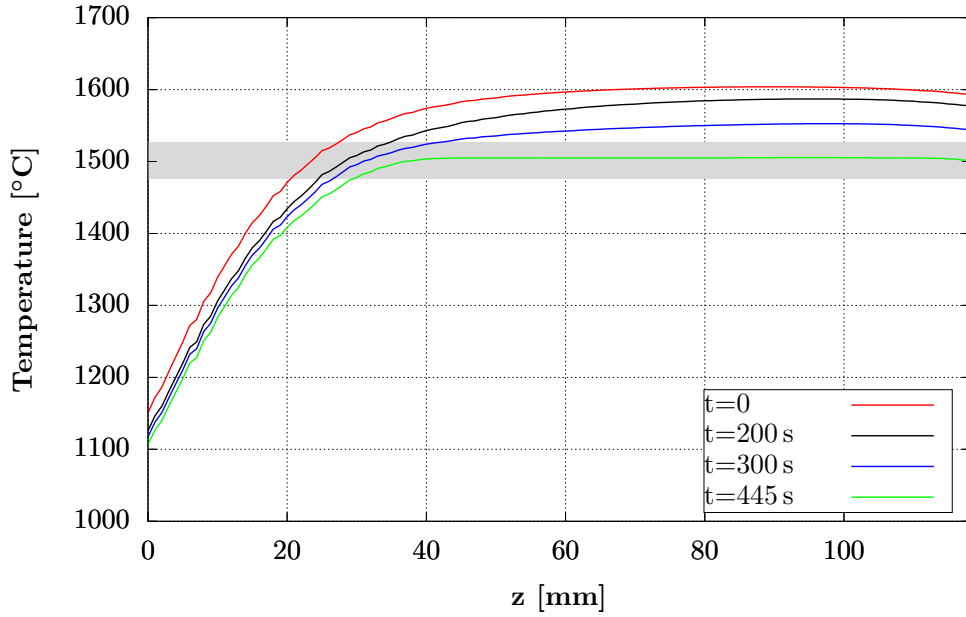


Figure 3.13 – Temperature boundary condition imposed along the cylindrical sample for four different times. These temperature profiles are the result of the dedicated thermal furnace model. The thermal protocol does not depend on the apparent gravity level. The gray shaded area represents the alloy solidification range.

iterations. The numerical solver, *macroS3D*, uses an iterative procedure to couple the averaged enthalpy, the liquid averaged concentration and liquid fraction at each time step.

3.3 Results and discussion

3.3.1 Furnace thermal protocol: Temperature field and heat transfer

The buoyancy driven flow is induced by temperature and concentration gradients in the liquid. In the directional solidification furnace the thermal configuration is essentially hydrodynamically stable in the axial direction, *i.e.* the temperature gradient along the sample axis (z direction) does not trigger natural convection. However, convection is triggered by solute concentration gradients built up in the mushy zone due to solidification. In the TiAl alloys, the liquid in the mushy zone is progressively enriched in aluminum with decreasing temperature. The increase in Al concentration causes a decrease of the liquid density. A hydrodynamically unstable configuration in the axial direction is created if the solutal effect dominates over the thermal effect. Furthermore, convection is triggered by lateral temperature gradients due to heat transfer in the radial direction. The lateral temperature gradients are essential for the understanding of the flow structure in the sample, as will be seen in the simulation results later on.

To facilitate the analysis of the simulations, we will first examine the heat transfer in the sample. The objective is to explain how the lateral temperature gradients are established and how they vary with time and with position along the sample. Consider the heat equation (Eqn.

Table 3.1 – Thermophysical properties used in the simulations.

Property	Symbol	Units	Value
Nominal aluminum concentration	C_0	[wt%]	32.96
Partition coefficient	k_p	[–]	0.885
Melting point of the pure substance	T_f	[°C]	1975.66
Liquidus slope	m_l	[K/wt%]	-14.089
Pseudo-peritectic concentration	C_{inv}	[wt%]	35.2
Reference liquid density	ρ_l	[kg/m ³]	3877.8
Kinematic viscosity	ν_l	[m ² /s]	1.65×10^{-6}
Thermal conductivity	k	[W/mK]	19.9
Solutal expansion coeff.	β_C	[wt% ⁻¹]	8.465×10^{-3}
Thermal expansion coeff.	β_T	[°C ⁻¹]	1.1785×10^{-4}
Reference temperature	T_{ref}	[°C]	1511.29
Reference concentration	C_{ref}	[wt%]	32.96
Latent heat	L_f	[J/kg]	3.62×10^5
Specific heat capacity	c_p	[J/(kgK)]	1100
Characteristic length for permeability	λ_2	[m]	6.50×10^{-5}

3.3) written in terms of the temperature, in a cylindrical coordinate system and neglecting any advective contribution. Axisymmetric conditions are assumed ($\frac{\partial T}{\partial \theta} = 0$ and $\frac{\partial T}{\partial r} \Big|_{r=0} = 0$):

$$\left(1 + \frac{L_f}{c_p} \frac{\partial g_l}{\partial T}\right) \frac{\partial T}{\partial t} = \frac{k}{\rho c_p} \frac{\partial^2 T}{\partial z^2} + \frac{k}{\rho c_p} \frac{1}{r} \frac{\partial}{\partial r} \left(r \frac{\partial T}{\partial r} \right) \quad (3.9)$$

This equation shows that the temperature evolution at any point in the sample is affected by a contribution (variation of conduction heat flux) in the radial direction (r direction) and a contribution in the axial direction (z direction). Now consider that the temperature profile along the sample and over time is known, such that the axial and temporal contributions of Eqn. 3.9 can be explicitly calculated: $\mathbf{R}(t, z) = \left(1 + \frac{L_f}{c_p} \frac{\partial g_l}{\partial T}\right) \frac{\partial T}{\partial t} - \frac{k}{\rho c_p} \frac{\partial^2 T}{\partial z^2}$. It is assumed that $\mathbf{R}(t, z)$ only weakly depends on r . This gives the following expression for the radial contribution:

$$\frac{k}{\rho c_p} \left(\frac{1}{r} \frac{\partial}{\partial r} r \frac{\partial T}{\partial r} \right) = \mathbf{R}(t, z) \quad (3.10)$$

The solution of Eqn. 3.10 is given by:

$$T(r, t, z) = \frac{\rho c_p}{4k} \mathbf{R}(t, z) r^2 + T(r = 0) \quad (3.11)$$

The relation of Eqn. 3.11 approximates the temperature profile in the radial direction. When $\mathbf{R}(t, z) > 0$ the cylinder centerline is colder than the cylinder sides, which means that the heat diffusion along the cylinder occurs faster than the change of temperature in the boundaries, and when $\mathbf{R}(t, z) < 0$, it is in the other way around. The value of $\mathbf{R}(t, z)$ can be approximated assuming that the cylinder centerline ($r = 0$) follows a temperature profile similar to that imposed by the boundary conditions with only a small delay. This is realistic, since the heat diffusion time in the sample thickness $d^2 / (4k / (\rho c_p))$, where d is the sample diameter, is of the order of 3 s *i.e.* much smaller than the solidification time of the sample. Furthermore, this assumption is confirmed by the detailed study of heat transfer in the sample by Battaglioli et al. [93]. Figure 3.14 shows the value of $\mathbf{R}(t, z)$ along the sample for different times, which was approximated by calculating the derivatives with a first order finite differencing scheme using the information of the boundary conditions. For $t = 50$ s, $\mathbf{R}(t, z) > 0$ throughout all the zone of interest (in and close to the mushy zone), meaning that the cylinder centerline cools down faster than the cylinder sides. On the other hand, for $t = 200$ s and $t = 400$ s there is a transition around $z = 50$ mm in which the cooling rate at the sides of the cylinder is faster than the heat diffusion along the sample, making the cylinder sides colder than the cylinder centerline. This behaviour is explained by the change of the cooling rate of the furnace thermal protocol during the solidification stage. The fully coupled numerical simulations of solidification, including aluminum segregation and full equilibrium, predict that the temperature radial inversion occurs around $z = 51$ mm at $t = 200$ s and $z = 38$ mm at $t = 400$ s.

3.3.2 Liquid flow

The case study presents a thermally stable configuration along the cylindrical sample, which means that the axial gradients of temperature will not trigger any liquid convection (the main temperature gradient is anti-parallel to the total apparent gravity). However, inside the mushy zone, the solutal buoyancy effect competes with the thermal buoyancy effect, since there is aluminum enriched liquid, which is lighter than the one at nominal concentration. As was shown in Sect. 1.1.1, by combining the buoyancy term of Eqn. 3.2 and the link between the temperature and the liquid concentration in the solid-liquid region (Eqn. 3.7), it can be shown that if $\beta_T + \frac{\beta_C}{m_l} < 0$ and the main temperature gradient is anti-parallel to the total apparent gravity, the destabilizing solutal effect dominates over the stabilizing thermal effect, resulting in thermosolutal liquid convection. In case of the TiAl alloy studied here, $\beta_T + \frac{\beta_C}{m_l} = -4.83 \times 10^{-4}$. Indeed, the aluminum enriched liquid in the mushy zone will tend to flow in an anti-parallel direction to the total apparent gravity due to the dominant solutal buoyancy effect, finding its way through the porous media that forms the mushy zone. A flow along the apparent gravity direction will be strongly affected by the Coriolis acceleration. The Coriolis acceleration pushes the fluid flow to the flight velocity or opposite to flight velocity sides of the sample if its direction is anti-parallel or parallel to the total apparent gravity, respectively. The flight velocity side is

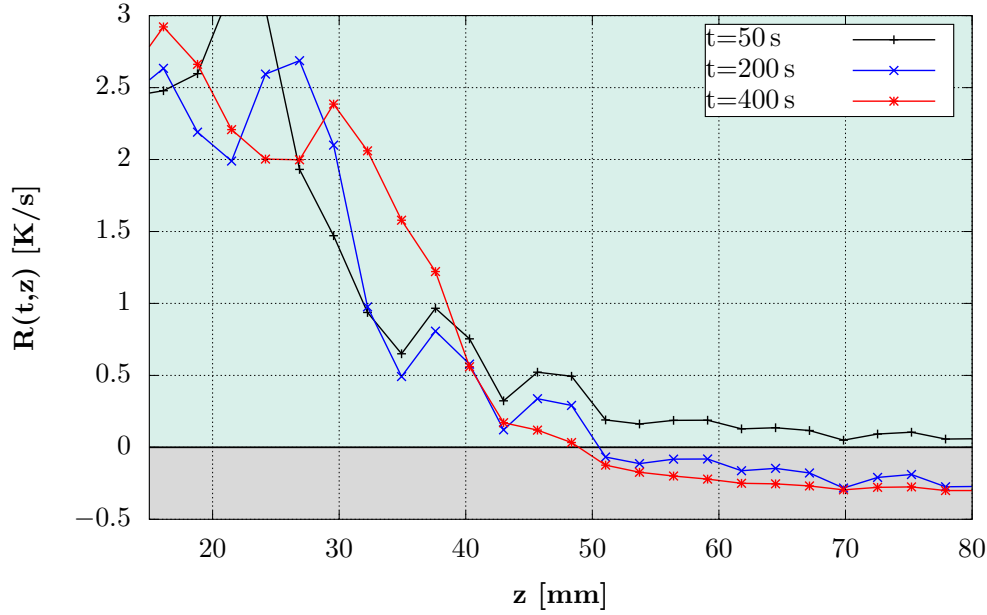


Figure 3.14 – Contribution of radial heat diffusion, $\mathbf{R}(t, z) = \frac{k}{\rho c_p} \left(\frac{1}{r} \frac{\partial}{\partial r} r \frac{\partial T}{\partial r} \right)$, calculated using information of the boundary conditions. The mushy zone is located between 21 mm and 26 mm at $t = 50$ s between 24 mm and 31 mm at $t = 200$ s and between 28 mm and 45 mm at $t = 400$ s approximately.

defined as the side which is pointed by the furnace flight velocity vector in the main plane of study (see Fig. 3.10). In order to make more evident the effect of the Coriolis acceleration, all the results are presented in the plane formed by the flight velocity vector, \vec{V}_{flight} , and the total apparent gravity vector, \vec{g}_{tot} (see Fig. 3.10). We define this plane as the main plane of study.

3.3.2.1 Liquid flow in the mushy zone

Figures 3.15 and 3.16 present the liquid density, in terms of the ratio ρ_l^b/ρ_l , inside the mushy zone in the main plane of study for the cases 1G and 20G, respectively. Both figures show that the liquid density in the mushy zone is lower than in the fully liquid region. Moreover, they show that there are radial gradients of liquid density. This distribution is due to the aluminum enrichment in the liquid, driven by solidification.

As it was previously demonstrated, if $\mathbf{R}(t, z) > 0$, the cylinder center is colder than the cylinder sides, implying that in the radial direction solidification occurs first in the cylinder center. Along with solidification, aluminum is rejected to the liquid by the growing solid, decreasing the liquid density. Indeed, in the case 1G, at $t = 50$ s and $t = 200$ s the liquid density is lower in the cylinder center than in the cylinder sides. However, at $t = 400$ s the inversion of radial temperature gradient leads to a change of the liquid density configuration: for $z > 38$ mm where $\mathbf{R}(t, z) < 0$, the lowest liquid density is located at the cylinder sides, whereas for $z < 38$ mm where $\mathbf{R}(t, z) > 0$, the density is lower in the center. The case 20G (see Fig. 3.16) presents the same features as the case 1G, but with the apparition of a segregation

channel, where the liquid density is lower.

Figures 3.17 and 3.18 show the liquid velocity field inside the mushy zone in the main plane of study for the cases 1G and 20G, respectively. In case 1G, for $t = 50$ s the liquid flows along the cylinder centerline, from the fully solid region towards the fully liquid region. Before arriving to the fully liquid region, the liquid flow is deflected towards the cylinder sides where it flows returning to the fully solid region, forming a ring of three dimensional toroidal circulation. This axisymmetric flow pattern is explained due to the difference of liquid density between the center and the sides of the cylinder. A buoyancy driven flow, antiparallel to the apparent gravity, is triggered in the cylinder center due to solidification and the decrease in liquid density. This interdendritic flow, in the cylinder center, is deflected towards the cylinder sides by the action of the liquid flow in the fully liquid region, which is parallel to the apparent gravity in the cylinder center and antiparallel in the cylinder sides (see Fig. 3.19). The same kind of flow pattern is also observed for $t = 200$ s but with a notable decrease of its magnitude because it is affected by the flow in the fully liquid region, which attempts to enter the mushy zone by the cylinder center. For $t = 400$ s a completely different liquid flow behaviour is observed: liquid flows towards the fully solid region in the cylinder center, while on the cylinder sides, it flows towards the fully liquid region. This change of circulation is due to the inversion of the radial temperature gradient.

On the other hand, in the case 20G, for $t = 50$ s solute enriched liquid flows antiparallel to the apparent gravity towards the fully liquid region in the cylinder center (see Fig. 3.18a). The buoyancy forces, which are controlled by solutal gradients, are strong enough to make solute enriched liquid escape from the mushy zone and enter the fully liquid region. This flow current of solute enriched liquid is deflected towards the flight velocity side of the cylinder due to the Coriolis acceleration effect. Simultaneously, liquid enters the mushy zone by the cylinder sides to compensate the liquid that escapes from it by the cylinder center. At $t = 200$ s the solute enriched liquid flow has created a channel in the mushy zone. The channel is an elongated region where the solid fraction is lower than in the surrounding mushy zone [94]. Due to a higher permeability, the channel is a self-reinforcing preferential path for the flow. At $t = 400$ s the channel is extinct. A flow pattern similar to the one observed in the case 1G is present, however not axisymmetric due to the deflecting effect of the Coriolis acceleration.

3.3.2.2 Liquid flow in the fully liquid region

Figures 3.19 and 3.20 present the liquid fraction and the liquid velocity for cases 1G and 20G in the fully liquid region, respectively. In case 1G, for $t = 50$ s liquid flows towards the solidification front in the cylinder center, whereas, in the cylinder sides, it flows antiparallel to the apparent gravity vector. At this instant, the cylinder center is colder than the sides. The flow pattern is explained by thermal buoyancy which is the dominant driving force for the flow in the fully liquid region. This is because in case 1G, solute enriched liquid is not able to escape from the mushy zone and therefore, there are no important solutal gradients in the fully liquid region. For $t = 200$ s and $t = 400$ s the flow evolves with the temperature field controlled by the boundary conditions. For example, at $t = 200$ s in the zone $z > 60$ mm the liquid flows antiparallel to the

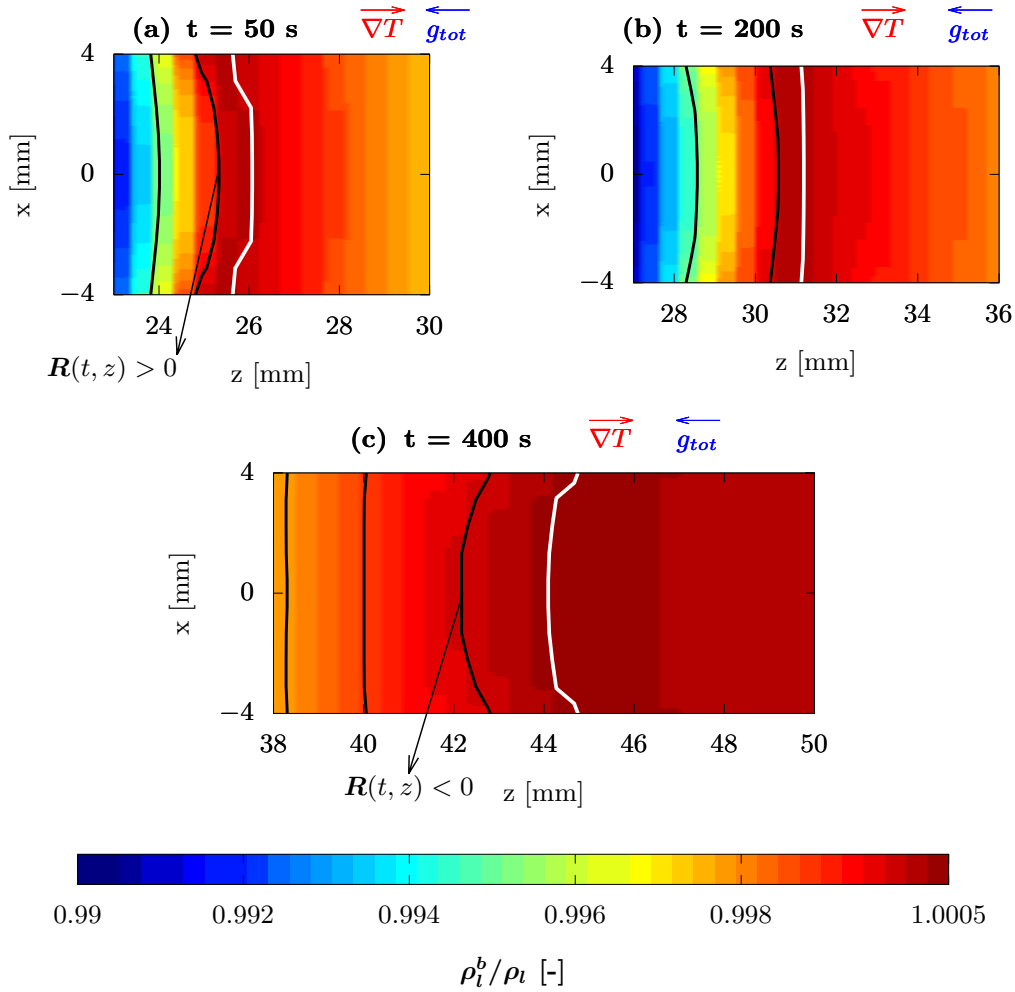


Figure 3.15 – Evolution of the liquid density, in terms of ρ_l^b / ρ_l in the main plane of study inside the mushy zone for the case 1G. White contours delimit the mushy zone ($g_l = 0.01$, $g_l = 0.99$). For (a) and (b), temperature contours in black: 1500, 1510 °C. For (c) temperature contours 1506, 1508 and 1510 °C. It is shown the sign of coefficient $R(t, z)$ depending on the shape of the temperature contours.

apparent gravity in the cylinder center, whereas, it flows parallel in the cylinder sides and for $z < 60 \text{ mm}$ the flow is in the other way around. This behaviour is explained due to the radial inversion of the temperature gradient (recall the analysis of the furnace thermal protocol and temperature field).

In case 20G, the aluminum enriched liquid that escapes from the mushy zone due to the strong solutal buoyancy effect, is deflected by the Coriolis acceleration to the flight velocity side of the cylinder. This liquid advances all along the sample by the flight velocity side and returns to the mushy zone by the opposite to flight velocity side forming a large clockwise circulation (see Fig. 3.20). This large circulation is present in all the studied cases with centrifugation and makes the fluid flow pattern entirely non-axisymmetric. Indeed, the solutal buoyancy effect along the cylinder is stronger than the stabilizing thermal effect and the radial thermal gradients

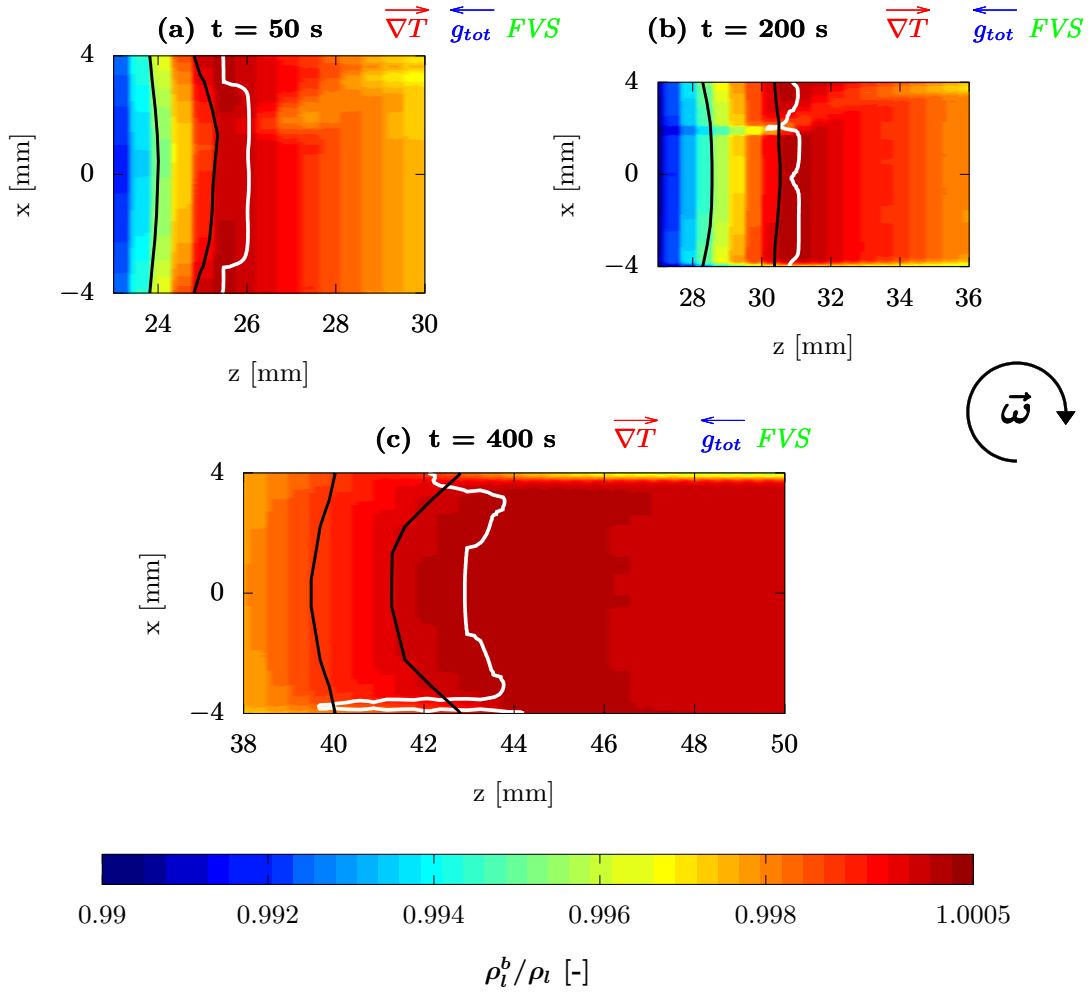


Figure 3.16 – Evolution of the liquid velocity and liquid fraction in the main plane of study inside the mushy zone for the case 20G. FVS denotes the flight velocity side of the sample. White contours delimit the mushy zone ($g_l = 0.01$, $g_l = 0.99$). For (a) and (b), temperature contours in black: 1500 and 1510 °C. For (c) temperature contours 1508 and 1510 °C.

induced by the furnace thermal protocol do not play a role in determining the fluid flow pattern as they do in case 1G. In case 20G, the fluid flow features are mainly determined by the solute enriched liquid that escapes from the mushy zone anti-parallel to the apparent gravity and then is pushed towards the flight velocity side of the sample by the Coriolis acceleration.

To distinguish the thermal and solutal effects on the liquid convection in the fully liquid region, Figures 3.21 and 3.22 present the liquid density, in terms of ρ_l^b / ρ_l , along with the temperature and the average solute concentration in the liquid at $t = 200$ s for the cases 1G and 20G, respectively. We should keep in mind that the temperature fields in both cases are virtually identical (see Fig. 3.21a and 3.22a) because they are mainly controlled by the boundary conditions. In case 1G, the solute enriched liquid is retained in the mushy zone by the liquid flow in the fully liquid region. As a result, there are no significant concentration gradients in the fully liquid zone. The liquid density in the fully liquid zone is controlled only by the thermal effect,

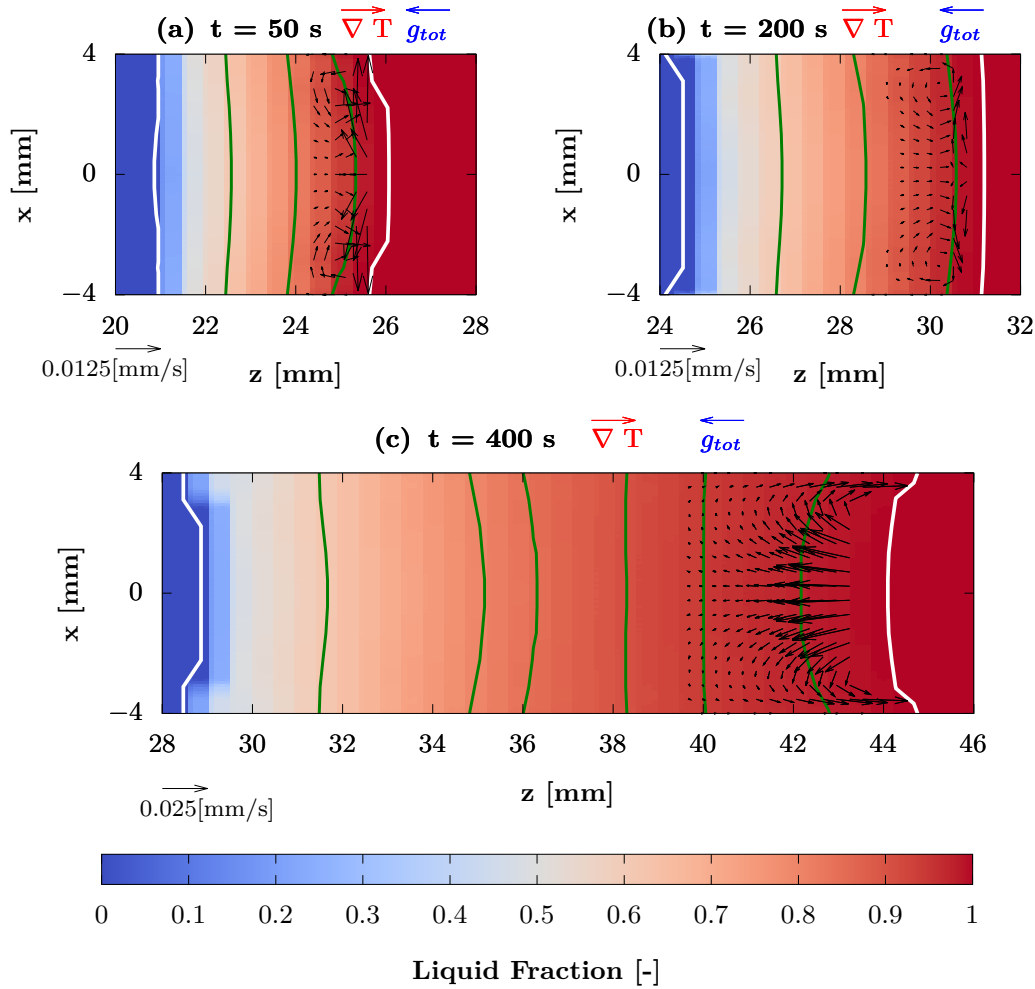


Figure 3.17 – Evolution of the liquid velocity and liquid fraction in the main plane of study inside the mushy zone for the case 1G. White contours delimit the mushy zone ($g_l = 0.01$, $g_l = 0.99$). For (a) and (b), temperature contours in green: 1490, 1500 and 1510 °C. For (c) temperature contours 1490,1500,1503,1506,1508 and 1510 °C.

leading to a stable configuration. The convection in this zone is therefore driven exclusively by radial temperature gradients. On the other hand, in the 20G case, solute enriched liquid escapes from the mushy zone, in a stream that is anti-parallel to the apparent gravity and is therefore pushed to the flight velocity side by the Coriolis acceleration (see Fig. 3.22b). The liquid density map clearly shows that the lightest liquid is located along the flight velocity side. It is concluded that the convection in fully liquid zone is driven by solutal buoyancy forces in the 20G case and by thermal buoyancy forces in the 1G case.

Müller et al. [3] and later Ramachandran et al. [2] described two types of flow regime in cases of thermally driven convection within cylindrical samples submitted to centrifugation. The descriptions are based on the fluid flow pattern in the plane perpendicular to the rotation axis. The first regime, or regime type I, consists of a single dominant circulation whose rotation is counter sense with respect to the rotation of the centrifuge. In addition, this type of regime

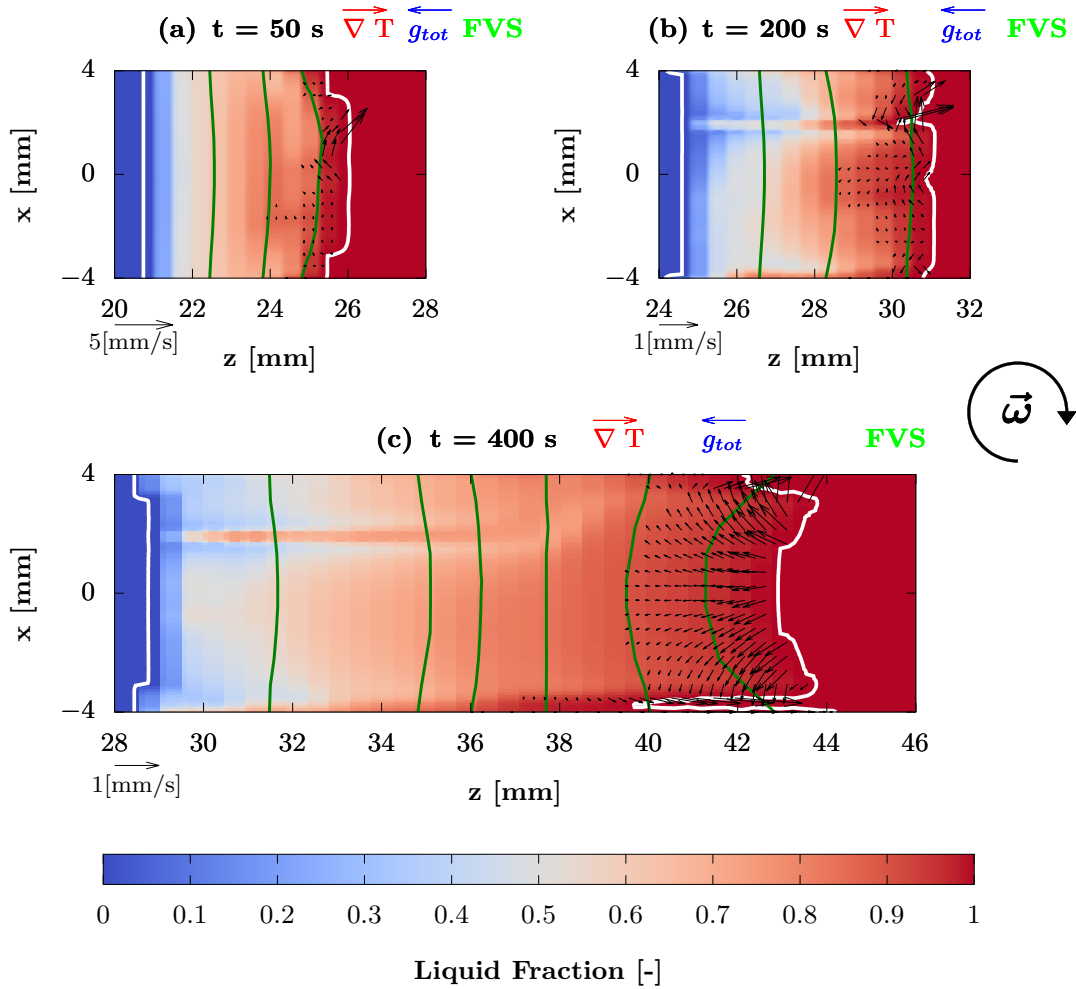


Figure 3.18 – Evolution of the liquid velocity and liquid fraction in the main plane of study in the mushy zone for the case 20G. *FVS* denotes the flight velocity side of the sample. White contours delimit the mushy zone ($g_l = 0.01$, $g_l = 0.99$). For (a) and (b), temperature contours in green: 1490, 1500 and 1510 °C. For (c) temperature contours 1490, 1500, 1503, 1505.2, 1508 and 1510 °C.

presents eddy currents in the corners of the container that cause an unsteady behaviour of the flow pattern. On the other hand, the regime type II consists in a single dominant circulation whose rotation sense is the same than the one of the centrifuge. The second type of regime is completely dominated by the influence of the Coriolis acceleration.

In order to establish the impact of the Coriolis acceleration on the determination of the fluid flow features, we investigated the Rossby dimensionless number. The Rossby number is the ratio between the inertia and the Coriolis accelerations and can be defined as $Ro = \frac{U_{ref}}{2\omega L}$, where U_{ref} is a reference velocity, ω the magnitude of the centrifuge angular velocity and L a characteristic length. The reference velocity U_{ref} was considered as the average of the maximum velocity at the instants $t = 50 \text{ s}$, $t = 200 \text{ s}$ and $t = 400 \text{ s}$ in the main plane of study and in the fully liquid region. The characteristic length was considered to be $L \sim 100 \text{ mm}$ which is the approximate

Table 3.2 – Total apparent gravity (g is the normal terrestrial gravity), centrifuge angular velocity, ω , reference velocity, U_{ref} and Rossby number, $Ro = \frac{U_{ref}}{2\omega L}$ for all the studied cases. The reference velocity is considered to be the average of the maximum velocity in the main plane of study at the instants $t = 50$ s $t = 200$ s and $t = 400$ s.

Case	g-level	ω [rad/s]	U_{ref} [mm/s]	Ro [-]
1G	1g	0.00	0.13	∞
5G	5g	3.47	2.13	3.06×10^{-3}
10G	10g	4.94	3.58	3.62×10^{-3}
15G	15g	6.06	4.77	3.94×10^{-3}
20G	20g	7.00	7.67	5.48×10^{-3}

length of the fully liquid region at $t = 50$ s. Table 3.2 presents the reference velocity, U_{ref} , the centrifuge angular velocity, ω , and the Rossby number, Ro , for each one of the investigated cases. The numerical results shows that in all the cases with centrifugation, $Ro \ll 1$, which means that the Coriolis acceleration is very important in determining the fluid flow features. According to the descriptions of Müller et al. and Ramachandran et al., the flow regime in the fully liquid region corresponds to type II in all the studied cases with centrifugation.

Figure 3.23 shows three-dimensional views of the domain during solidification at $t = 150$ s for the relative solute segregation and axial velocity magnitude in the case 20G. It can be seen that in the fully liquid region, solute enriched liquid is located in the flight velocity side of the sample due to the combined effect of the centrifugal and Coriolis accelerations. The unique large liquid circulation and the non-axisymmetric liquid flow is clearly noticeable.

3.3.3 Aluminum macrosegregation

Macroseggregation is the heterogeneity in solute composition – in this case aluminum – at the macroscopic scale due to the relative movement of the solid and liquid phases during a solidification process. By combining Eqns. 3.4 and 3.7 it can be shown that the average concentration, $\langle C \rangle$, in any point in the mushy zone varies as $\frac{\partial \langle C \rangle}{\partial t} = -\frac{1}{m_l} g_l \langle \vec{v}_l \rangle^l \cdot \nabla T$. This is a useful relation to understand the macrosegregation patterns due to liquid movement in the absence of density variations (shrinkage) and solid deformations. Note that $m_l < 0$.

Figure 3.24 shows the aluminum relative segregation in the main plane of study for the different cases at the end of solidification. In case 1G, the overall relative segregation is axisymmetric such as the thermosolutal liquid convection and its maximum magnitude is around 0.29%. This weak magnitude of segregation can be explained mainly by: (1) the large partition coefficient, $k_p = 0.885$, close to unity, meaning that the aluminum concentration in liquid and solid phases is similar (recall $\langle C_s \rangle^s = k_p \langle C_l \rangle^l$), and (2) the weak liquid convection with respect to the cases with centrifugation. Along the sample, three different segregation patterns can be

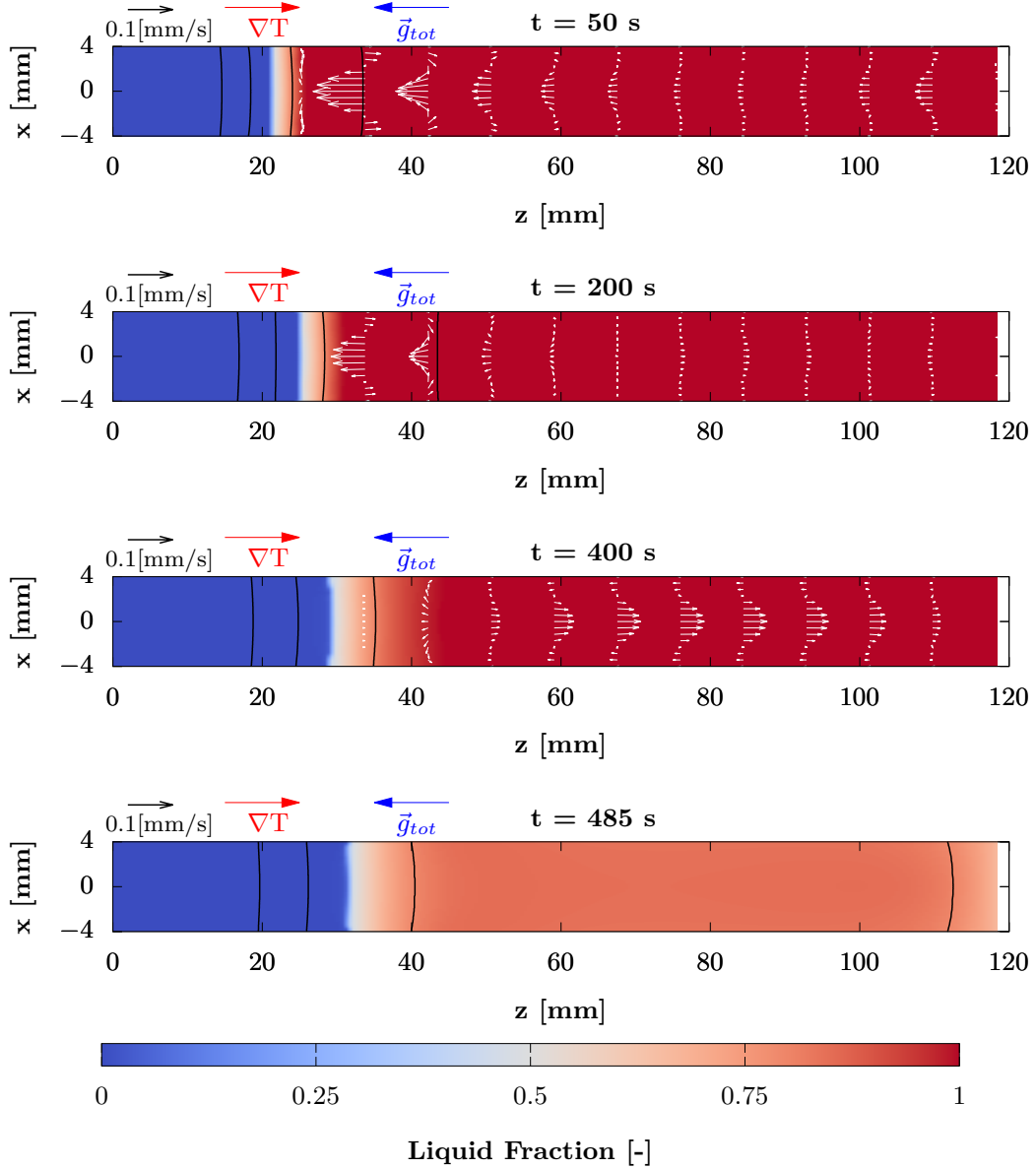


Figure 3.19 – Evolution of the liquid velocity pattern in the main plane of study in the fully liquid region for the 1G case. Temperature contours in black: 1400, 1450, 1500, and 1550 °C.

easily identified. For $20 \text{ mm} \leq z \leq 40 \text{ mm}$ a negative segregation is present in the cylinder sides whereas positive in the cylinder centerline. This pattern is explained since the liquid flow is parallel to the main temperature gradient ($\langle \vec{v}_l \rangle^l \cdot \nabla T > 0$) along the sample in the cylinder centerline, bringing solute enriched liquid from deep in the mushy zone to the solidification front, and anti-parallel ($\langle \vec{v}_l \rangle^l \cdot \nabla T < 0$) in the cylinder sides, taking poor liquid in solute from the solidification front to deep in the mushy zone (see Fig. 3.17[a,b]). On the other hand, for $40 \text{ mm} \leq z \leq 95 \text{ mm}$ the segregation pattern is in the other way around: positively segregated

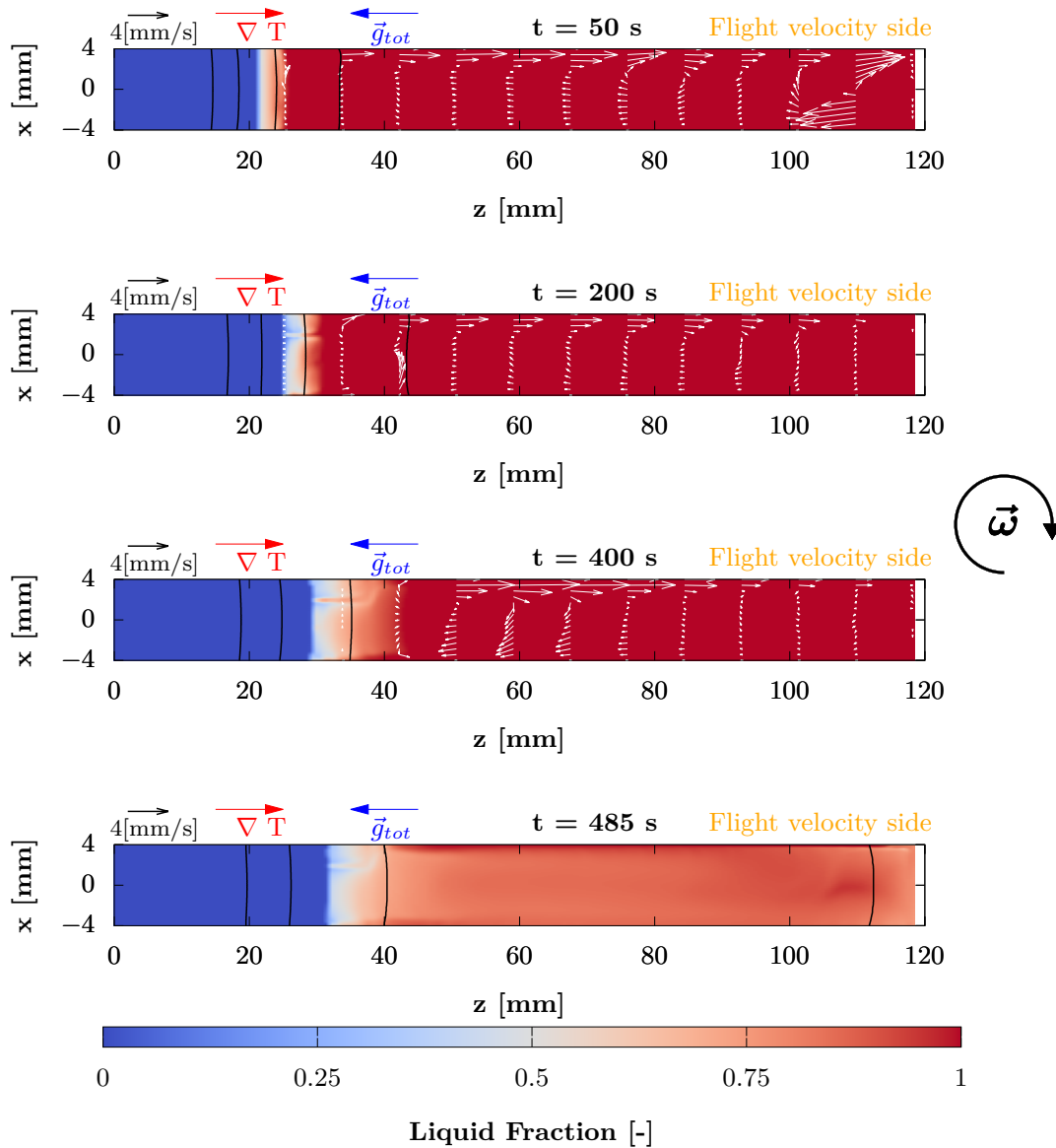


Figure 3.20 – Evolution of the liquid velocity pattern in the main plane of study in the fully liquid region for the 20G case. Temperature contours in black: 1400, 1450, 1500, and 1550 °C.

in the cylinder sides, whereas negatively in the cylinder center. This pattern is explained by the inversion of the flow direction (see Fig. 3.17c). The same liquid flow pattern is observed for $z \geq 95$ mm however, there is a second solidification front moving from the other end of the sample parallel to the apparent gravity vector (for $t > 400$ s) enriching in solute the center of the cylinder and depleting its sides. It is worth to mention that according to the furnace thermal protocol, the zone $z > 40$ mm solidifies very fast and at $t = 487$ s the sample is fully quenched.

In cases with centrifugation, we observe that the segregation pattern is not axisymmetric due

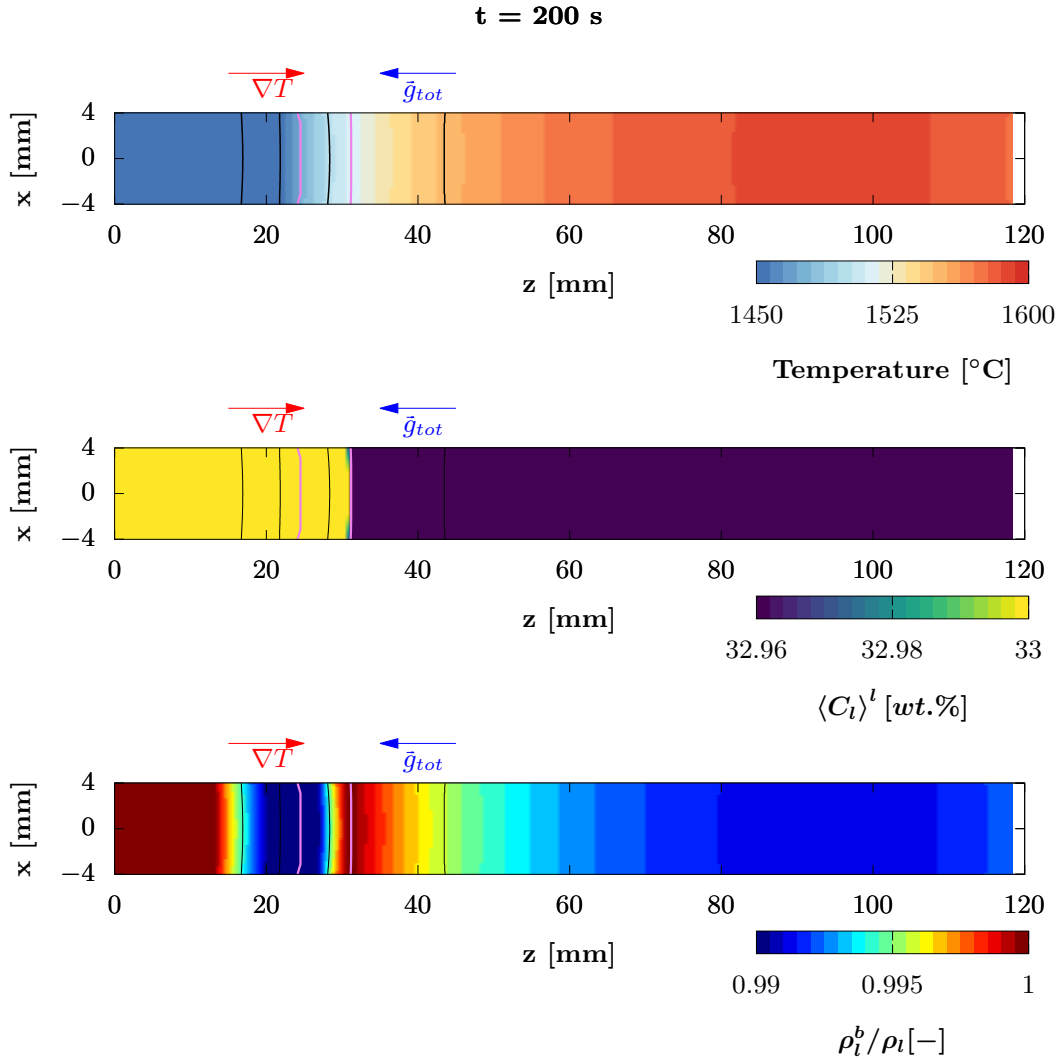


Figure 3.21 – Temperature, average concentration in the liquid and liquid density (in terms of ρ_i^b / ρ_l) in the main plane of study at $t = 200$ s for the case 1G. Violet contours delimit the mushy zone. Temperature contours in black: 1400, 1450, 1500, and 1550 °C.

to the deflecting effect of the Coriolis acceleration on the liquid convection. Such as in the case 1G, we recognize the same three zones, however with important differences in the segregation pattern. The first zone between $20 \text{ mm} \leq z \leq 40 \text{ mm}$ presents a similar pattern to the case 1G, but more strongly segregated, non-axisymmetric and with the occurrence of segregation channels (see 10G and 20G cases in Fig. 3.24). The second zone $40 \text{ mm} \leq z \leq 95 \text{ mm}$ has a positive segregation in the cylinder sides, with a more strongly aluminum enriched zone in the flight velocity side. This feature is due to the deflecting effect of the Coriolis acceleration. The third zone, $z > 95 \text{ mm}$ it is almost fully positively segregated (some small negatively segregated zones can be seen in the 5G case at the cylinder sides) because of the accumulation of light aluminum enriched liquid.

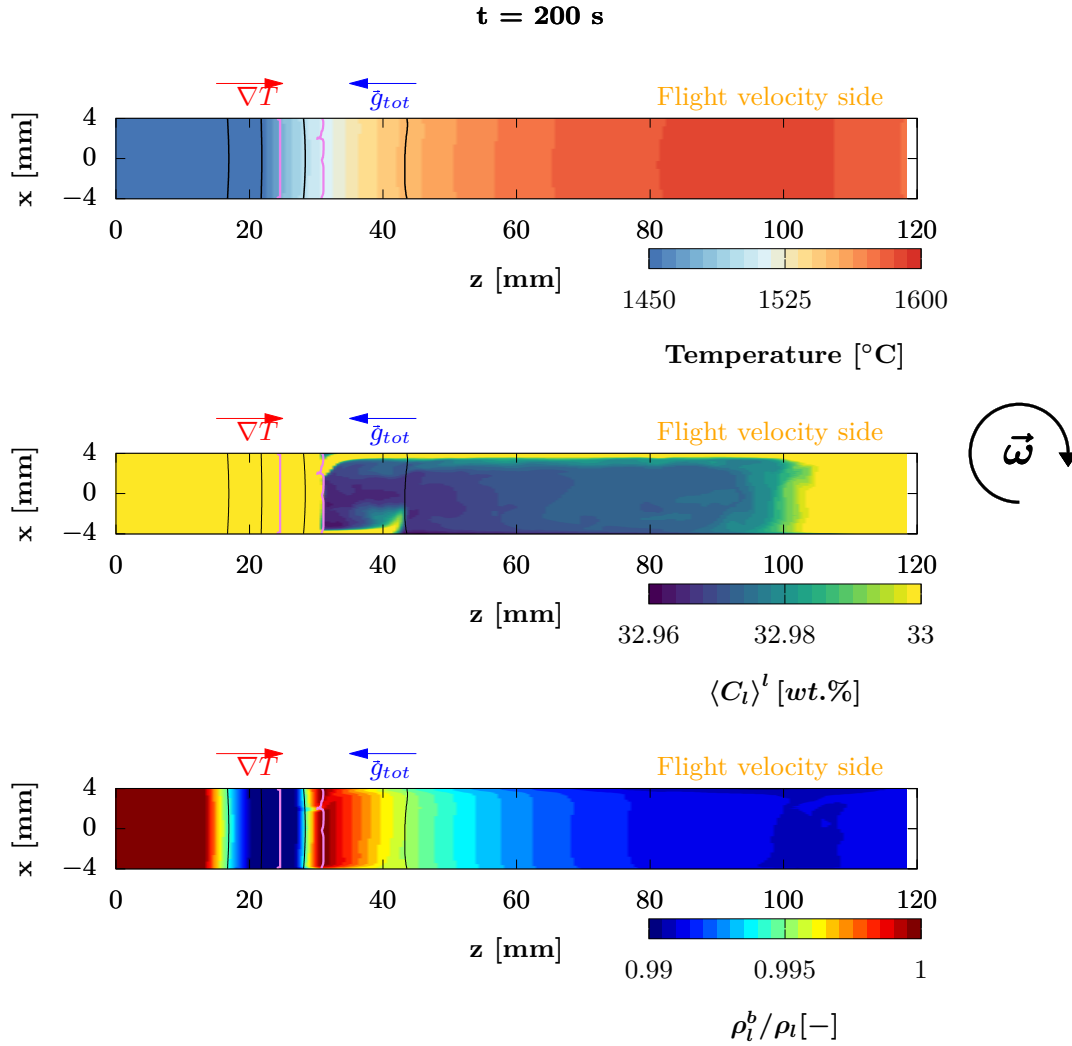


Figure 3.22 – Temperature, average concentration in the liquid and liquid density (in terms of ρ_l^b / ρ_l) in the main plane of study at $t = 200 \text{ s}$ for the case 20G. Violet contours delimit the mushy zone. Temperature contours in black: 1400, 1450, 1500, and 1550 $^{\circ}\text{C}$.

Figure 3.25 presents the relative aluminum segregation in three transversal planes for the 15G case. We can notice positive segregation in spots distributed around the sample circumference. They are a consequence of instabilities at the cylinder sides that do not evolve into fully developed channels. These instabilities appear in the cylinder in the beginning of the temperature radial inversion that has been described previously.

3.3.4 Comparison with aluminum measurements

In order to validate our observations with respect to the one-vortex fluid flow pattern which develops in the cases with centrifugation, measurements of aluminum concentration were made in the sample solidified with an apparent gravity of $\vec{g}_{tot} = 15g$ (15G case). Three lines along

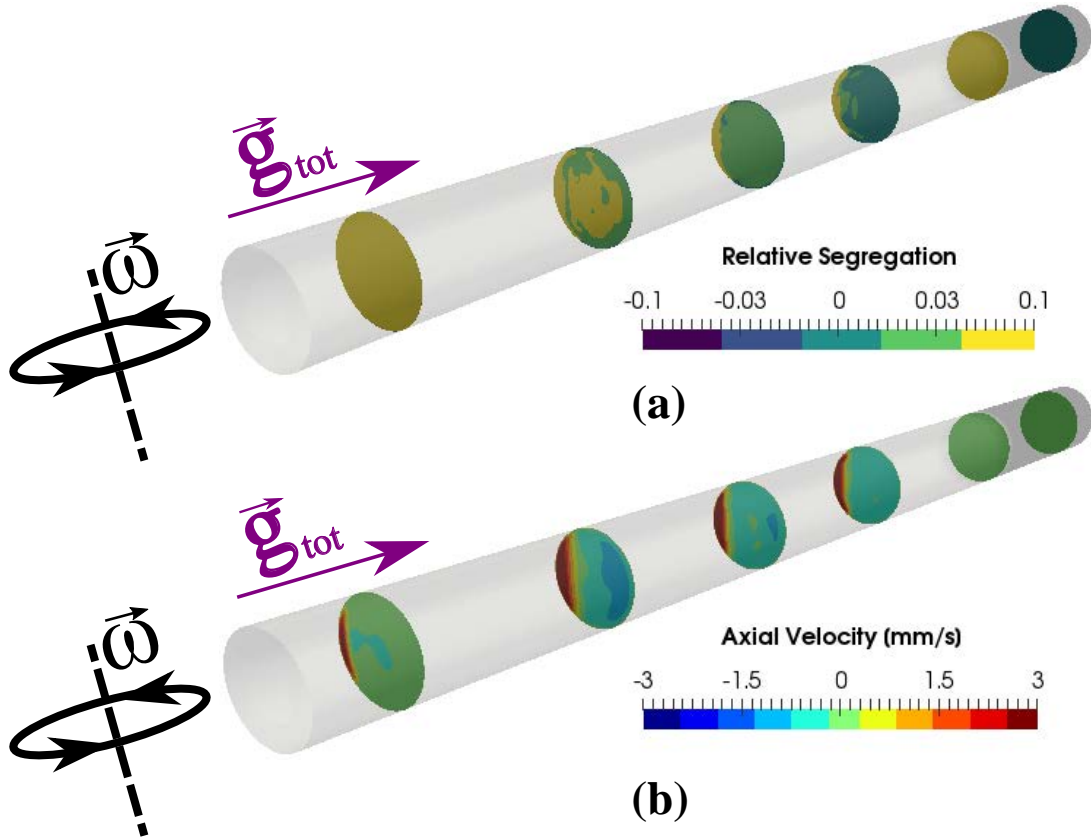


Figure 3.23 – 3D views of the domain at $t = 150\text{s}$ for the case 20G. (a) Relative segregation $\frac{\langle C \rangle - C_0}{C_0} \times 100\%$. (b) Axial intrinsic liquid velocity magnitude (negative magnitude in the direction parallel to the apparent gravity).

the cylindrical sample, in the main plane of study, were selected to conduct the measurements: One line in the cylinder centerline and two in the periphery (flight direction side and opposite to flight direction side). Each measurement line started at $z = 21\text{ mm}$ covering a length of 40 mm (in total 81 EDX measurement were performed).

Figure 3.26 presents the comparison between the results of the aluminum composition obtained by means of numerical simulations and experimental measurements. A three-point moving average smoothing of the experimental profiles was used to improve the visualization and interpretation of the measurements. Additionally, it is worth to mention that in the centrifugally solidified sample, the columnar-to-equiaxed transition was present around $z = 35\text{ mm}$. Any interpretation comparing the numerical results with the measurements for $z \geq 35\text{ mm}$ should be done considering that the model is only valid for motionless solid (columnar growth or after packing of all equiaxed grains). Fig. 3.26 also presents dashed lines that were sampled 0.5 mm and -0.5 mm displaced along the y -axis direction (normal to the main plane of study) from numerical simulation results. This allow us to realize how much can change the aluminum composition slightly displacing the sampling line position in an unstable mushy zone. Figure 3.25 presents the aluminum segregation pattern in three transversal planes. Several high concentra-

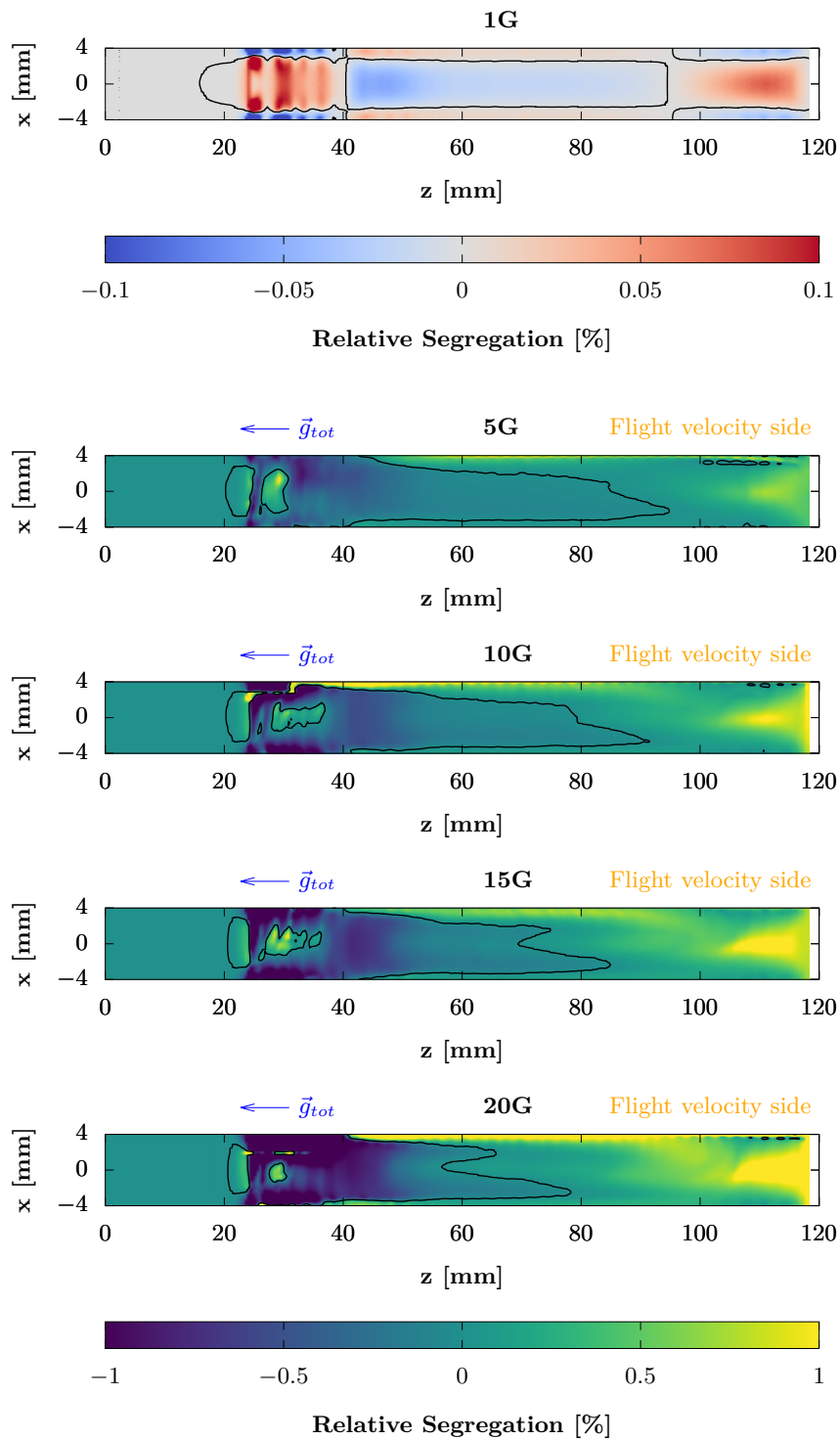


Figure 3.24 – Relative aluminum segregation $\frac{\langle C \rangle - C_0}{C_0} \times 100\%$ in the main plane of study at the end of solidification for different centrifugation levels. Contours at $\langle C \rangle = C_0$ (black line).

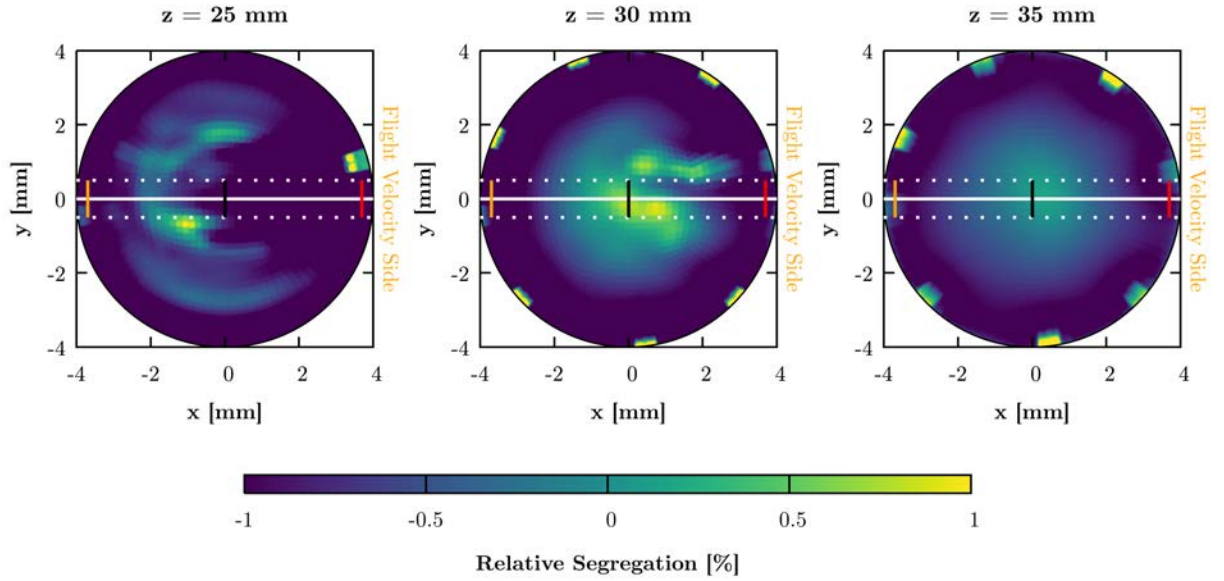


Figure 3.25 – Relative segregation $\frac{\langle C \rangle - C_0}{C_0} \times 100\%$ for the case 15G in transversal planes at the end of solidification.

tion spots appear in the edges of the transversal planes for $z = 30$ mm and for $z = 35$ mm. These are consequence of the instabilities of the liquid convection in the mushy zone as the inversion of the radial temperature gradient takes place. The segregation intensity, number and position of the spots may depend on numerical parameters such as numerical schemes and time and spatial discretization. The figure also schematizes with a solid white line the main plane of study, with dashed white lines the planes displaced ± 0.5 mm along the y -axis direction and with orange (opposite to flight direction side), black (cylinder centerline) and red (flight direction side) lines the localization of numerical sampling points in transversal planes.

The numerical simulation is able to depict the segregation of aluminum in the axial direction and gives a good qualitative match to the measurements in the centerline and in the opposite to flight velocity side. However, the flight velocity side presents a strong positive segregation throughout all the investigated length, feature that was underestimated by the numerical model.

The numerical model could depict the entirely non-axisymmetric thermosolutal liquid convection with the unique large circulation (type II according the descriptions of Müller et al. [3]). This can be confirmed since the flight velocity side of the sample is notoriously more enriched in aluminum than the opposite to flight velocity side due to the deflecting effect of the Coriolis acceleration. In spite of the good agreement in depicting the fluid flow convection pattern, the numerical model could not quantitatively predict the magnitude of aluminum segregation. The quantitative prediction of flow and segregation could be very sensitive to the used microscopic grain growth kinetics model, the assumed microstructure, the assumed pseudo-binary alloy and the temperature field, especially in the radial direction. This aspect of modeling of the experiment should be refined, to achieve quantitative simulations.

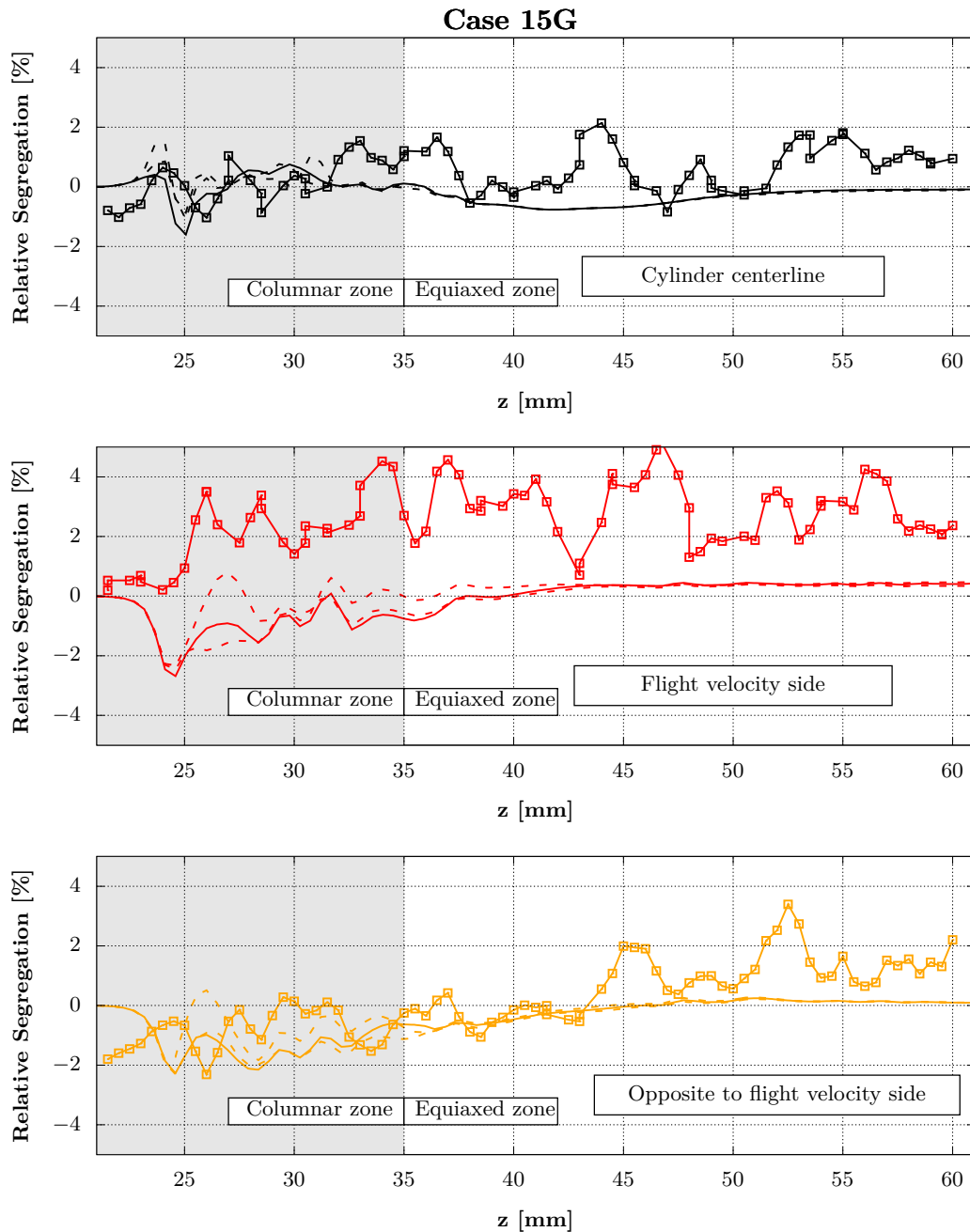


Figure 3.26 – Comparison of aluminum concentration between EDX measurements and numerical simulations in the Case 15G. Line-point: Measurements (3-point moving averaging). Solid Line: Numerical results. Dashed line: Numerical results displaced 0.5 mm and -0.5 mm in the y -axis direction (normal to the main plane of study).

3.4 Summary

In this work the application of a numerical model to predict liquid thermosolutal convection and aluminum macrosegregation during centrifugal casting of TiAl alloy was performed. The results

allows us to understand in a better way the deflecting effect of the Coriolis acceleration in the GRADECET experiments, where the temperature and solute gradients play an important role in the buoyancy driven convection. The general remarks can be summarized as follows:

- In spite of the thermally stable configuration, where the main temperature gradient is anti-parallel to the apparent gravity, TiAl alloys present an unstable mushy zone since the solutal effect counteracts the thermal effect.
- The temperature field behaviour was characterized. Special attention was paid to the radial temperature inversion imposed by the furnace thermal protocol.
- The furnace protocol could have an impact in the liquid thermosolutal convection and aluminum macrosegregation in the 1G case. The fluid flow pattern was mainly dependent on the ratio between the thermal diffusion along the sample and the cooling rate from the sides. In cases with centrifugation, the solutal effect on the buoyancy driven flow was much stronger than the thermal effect imposed by the radial temperature gradients.
- The Rossby number for all the studied cases with centrifugation was much smaller than unity. For these cases, the Coriolis effect determines completely the fluid flow pattern.
- The Coriolis effect pushes the lighter liquid, that flows antiparallel to the apparent gravity, to the flight velocity of the sample, generating one large circulation throughout the fully liquid region. This is in agreement with previous observations (Müller et al. [3] and Ramachandran [2]).
- A comparison between aluminum concentration measurements and simulation results on the case 15G was performed. The numerical model could depict qualitatively the aluminum segregation pattern and the fluid flow features. However, a quantitative prediction of the aluminum segregation magnitude could not be achieved.
- A higher aluminum concentration is present in the flight velocity side with respect to the opposite to flight velocity side of the samples centrifugally solidified. This is due to the thermosolutal convection that is modified by the deflecting effect of the Coriolis acceleration.

Chapter 4 : Equiaxed grain motion and grain growth kinetics

Contents

4.1	Macroscopic conservation equations	93
4.1.1	Mass balance of phase k	93
4.1.2	On the coupling of enthalpy, temperature and solid fraction	95
4.1.3	Momentum conservation and mass conservation equations	95
4.1.4	Other macroscopic conservation equations	102
4.1.5	Validation of the transport model in <i>macroS3D</i>	103
4.2	Microscopic modeling in <i>macroS3D</i>	110
4.2.1	Grain growth kinetics	110
4.2.2	Grain nucleation and nuclei re-injection	114
4.2.3	Validation of the microscopic modeling in <i>macroS3D</i>	114
4.3	Coupling of macroscopic conservation equations with microscopic modeling	117
4.3.1	Validation of the multiscale modelling in <i>macroS3D</i> : The Hebditch and Hunt case	123
4.4	Simulations of the GRADECET experiments	129
4.4.1	Results and discussion	130
4.5	Summary	146
4.6	Perspectives	151

The liquid thermosolutal convection and aluminum macrosegregation were characterized in the GRADECET experiments in the previous chapter using a simplified solidification model. The main drawbacks encountered in the model were the use of lever rule for the description of solid growth and the assumption about the solid phase was fixed in the domain.

As an example, figure 4.1 shows the microstructure of the samples of the GRADECET experiments for different levels of total apparent gravity. The columnar zone, the CET, the equiaxed zone and the quenched liquid are recognized. Another relevant feature observed in cases with centrifugation, is the tilted packing front of equiaxed grains. This feature is attributed to the effect of the Coriolis acceleration on the way that equiaxed grains move, however this has not been fully understood [1]. In order to improve the understanding of these features, a multiscale model that depicts simultaneously liquid convection, grain motion and grain growth kinetics can allow for better explanations.

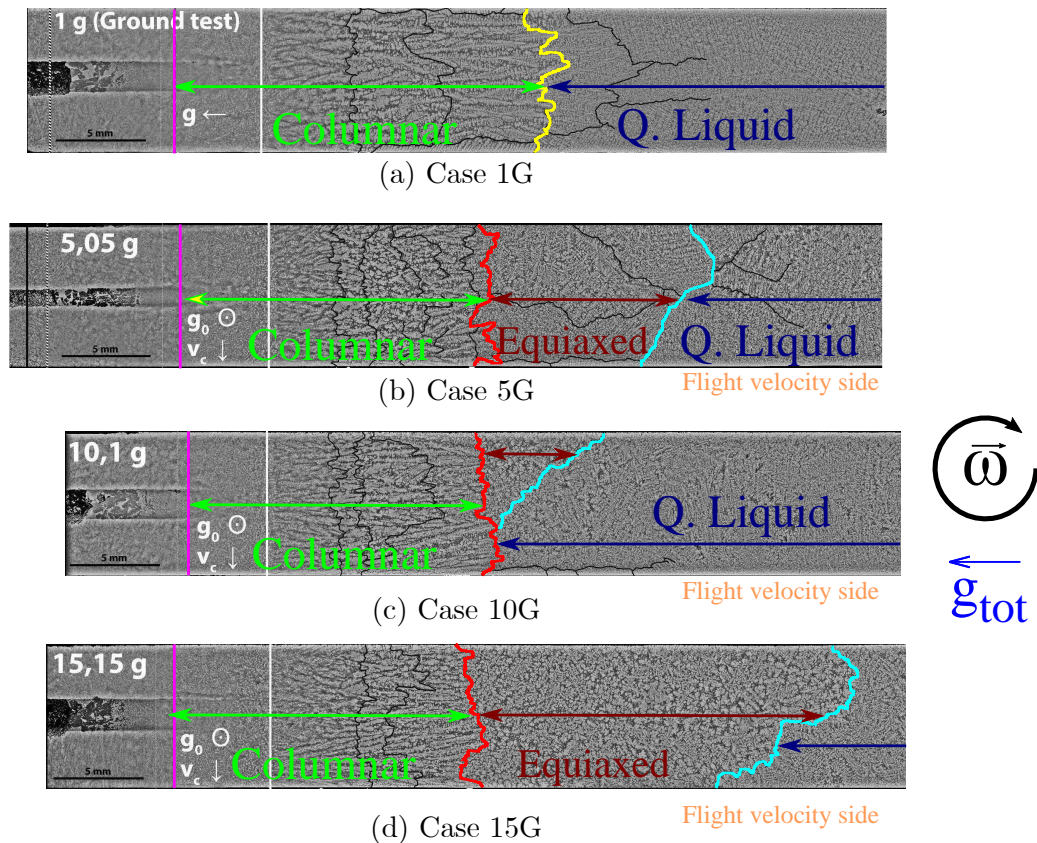


Figure 4.1 – Microstructure of the experiments of directional solidification under centrifugal conditions carried out within the framework of the GRADECET project. The full analysis of the microstructure is reported in ref. [1]. The violet line is the melting front at $t = 0$. The white line is the onset of columnar growth. The red line delimits the columnar region to the equiaxed region. The black lines are recognizable differences in the microstructure. The light blue line delimits the equiaxed region to the quenched liquid region. In Case 1G, the yellow line delimits the columnar region to the quenched liquid region (there is no CET).

For this reason, two main new developments were carried out in *macroS3D*. The first one

is the implementation of a model for the representation of liquid thermosolutal convection and equiaxed grain motion using a multiphase Euler-Euler approach. The second one is the implementation of advanced grain growth kinetics models that accounts for the limited solute diffusion at microscopic scales, and therefore describes the link between the undercooling of the liquid and the grain growth rate. The macroscopic equations implemented in *macroS3D* are described in Sect. 4.1, along with the corresponding verification and validation. Following, in Sect. 4.2, the implemented grain growth kinetics models are described and validated. Finally, the application of these models to the GRADECET experiments and its results are reported in Sect. 4.4.

4.1 Macroscopic conservation equations

In Chapter 1 a literature review of the macroscopic modeling of solidification was made. In Chapter 2 scalar conservation equations and momentum conservation equations were written for a rotating reference system in order to be applied on the simulation of the GRADECET experiments. In this section, the solidification model implemented in *macroS3D* will be presented, recalling some of the equations and phenomena that were already presented.

The improved *macroS3D* model uses an Euler-Euler approach to represent the solid and liquid phases. The model considers heat transfer, liquid thermosolutal convection, equiaxed grain motion, equiaxed grain nucleation, equiaxed grain packing and solidification of a binary alloy controlled by the limited solute diffusion at microscopic scales. Below, the set of macroscopic conservation equations (partial differential equations) included in the model is presented, along with explanations about their numerical implementation.

4.1.1 Mass balance of phase k

The mass balance equation of the phase k is written as:

$$\frac{\partial}{\partial t} (\rho_k g_k) + \nabla \cdot (\rho_k g_k \langle \vec{v}_k \rangle^k) = \Gamma_k + \Phi_k \quad (4.1)$$

Where Γ_k and Φ_k are the mass transformation rate of phase k due to growth and nucleation, respectively.

The model implemented in *macroS3D* uses a Boussinesq approximation, which means that solid and liquid densities are considered to be constant in all conservation equations, except in the gravity term – which includes the centrifugal acceleration – in the momentum equations. In addition, *macroS3D* uses the operator splitting-algorithm [65] to couple the resolution of macro/micro scales. This implies that Eqn. 4.1 is solved in two stages. In a first stage (transport stage in the algorithm), only the macroscopic operators (advection term in Eqn. 4.1) are integrated. In a second stage the growth and nucleation contributions are integrated, using the solution from the transport stage as initial condition.

Particularly, *macroS3D* solves Eqn. 4.1 only for the transported solid fraction, g_s^{tr} , whereas the liquid fraction, g_l^{tr} , is calculated as the complement to ensure mass conservation: $g_l^{tr} = 1 - g_s^{tr}$. In consequence, the equations implemented in *macroS3D* are:

$$\frac{\partial g_s^{tr}}{\partial t} + \nabla \cdot (g_s^{tr} \langle \vec{v}_s \rangle^s) = 0 \quad (4.2)$$

$$\frac{\partial g_s^{nucl+gr}}{\partial t} = \Phi_s + \Gamma_s \quad (4.3)$$

Where the superscript tr denotes the transport stage, $^{nucl+gr}$ the nucleation and growth stages. The resolution of Eqn. 4.2 may seem trivial, however, it presents an important numerical challenge: the physical quantity g_s^{tr} is bounded between 0 and 1. The boundedness of g_s^{tr} is a critical feature to maintain mass conservation and for convergence of the overall algorithm. There are several causes that can lead to an unbounded solution for g_s^{tr} :

- Due to the iterative nature of the algorithm used by *macroS3D*, the solid intrinsic velocity, $\langle \vec{v}_s \rangle^s$, may not be fully converged in the initial iterations, leading to scenarios where the solution of Eqn. 4.2 gives ill values of g_s^{tr} .
- In collocated grids, such as the used by OpenFOAM and consequently by *macroS3D*, the value $\langle \vec{v}_s \rangle^s$ needs to be interpolated from the cell centers to the cell faces. This interpolation may produce loss of information and may lead to solid fluxes inconsistent with the boundedness of g_s^{tr} .
- The use of high order schemes for the interpolation of the advective terms can introduce spurious oscillations in the g_s^{tr} field that can be unbounded values. This aspect can be overcome using the “Total Variation Diminishing” [95] or “Normalized Variable” [96] methods. These methods remove the spurious oscillations while using high-order schemes, however, they do not solve the other problems encountered to guarantee a bounded solution for g_s^{tr} .
- First order schemes avoid unboundedness, but suffer from “numerical diffusion”.

This problematic has been addressed by Boris and Book [97], who introduced the “Flux Corrected Transport” (FCT) technique, and by Zalesak et al. [98] who improved the FCT technique. The main objective of this approach is to guarantee bounded solutions for hyperbolic problems. In the OpenFOAM library an improved implementation of the FCT technique is available, which is called *MULES* (Multidimensional Universal Limiter with Explicit Solution) algorithm. This algorithm allows the use of “sub-cycles”, by which the *phase-k* conservation equation is solved using a smaller time-step than the one for other conservation equations and re-distribution of *phase-k* fraction (or an arbitrary scalar), when it reaches a predefined maximum value (*e.g.* grain packing limit), among other features. *macroS3D* uses this algorithm due to its advantages for solving the solid mass balance (Eqn. 4.2) and for obtaining bounded solutions for g_s^{tr} . A full explanation of the *MULES* algorithm is far from the scope of this work and more details can be found in reference [99].

4.1.2 On the coupling of enthalpy, temperature and solid fraction

In order to solve the energy balance (Eqn. 1.33), the solid enthalpy, h_s , the liquid enthalpy, h_l , and the temperature, T , are re-written in terms of the averaged enthalpy, $\langle h \rangle$, as the leading variable. The equation that *macroS3D* solves for is:

$$\begin{aligned} \frac{\partial}{\partial t} (\bar{\rho} \langle h \rangle) + \nabla \cdot \left((g_s \rho_s \langle \vec{v}_s \rangle^s c_p \xi \bar{\rho} + g_l \rho_l \langle \vec{v}_l \rangle^l c_p \xi \bar{\rho}) \langle h \rangle \right) \\ + \nabla \cdot \left(g_l \rho_l \langle \vec{v}_l \rangle^l L_f - g_s \rho_s \langle \vec{v}_s \rangle^s c_p \xi_2 - g_l \rho_l \langle \vec{v}_l \rangle^l c_p \xi_2 \right) \\ = \\ \nabla \cdot (k \langle h \rangle \nabla (\xi \bar{\rho})) + \nabla \cdot (\xi k \bar{\rho} \nabla \langle h \rangle) - \nabla \cdot (k \nabla \xi_2) \end{aligned} \quad (4.4)$$

Where $\xi = \frac{1}{c_p \bar{\rho}}$ and $\xi_2 = g_l \rho_l L_f \xi$ are auxiliary variables and $\bar{\rho} = g_l \rho_l + g_s \rho_s$ the averaged density. The term $\nabla \cdot (k \langle h \rangle \nabla (\xi \bar{\rho}))$ is explicitly considered in order to use the built-in OpenFOAM operators and thus, simplify the implementation. Note that by assuming $\rho_l = \rho_s$, the averaged density is identical to the solid and liquid densities, $\bar{\rho} = \rho_l = \rho_s$. The specific heat is considered equal and constant in both phases: $c_{pl} = c_{ps} = c_p$.

Equation 4.4 is solved for $\langle h \rangle$. Each time when Eqn. 4.4 is solved, the temperature is updated with the new solution of averaged enthalpy.

$$T = \bar{\rho} \xi \langle h \rangle - \xi_2 \quad (4.5)$$

This temperature update is required because the thermal boundary conditions are typically given in terms of the temperature rather than the enthalpy. Once the temperature is updated by Eqn. 4.5, the boundary conditions for the enthalpy equation (Eqn. 4.4) are also updated. Equations 4.4 and 4.5 are solved iteratively until the enthalpy and the temperature fields converge. The iterations are required here to account for the updates in the thermal boundary conditions and the explicit term in Eqn. 4.4.

4.1.3 Momentum conservation and mass conservation equations

4.1.3.1 Model

Here, the non-inertial accelerations that appear in a rotating reference frame – Coriolis and centrifugal – are included in the momentum equations as derived in Chapter 2. In addition, as mentioned before, a Boussinesq approximation is used, that is, any induced flow due to solidification shrinkage is neglected in the model ($\rho_l = \rho_s = \rho$). Although the momentum conservation equations have already been written previously, they are re-called in this section putting the focus on the formulation used by *macroS3D* and their numerical implementation.

The two convection regimes that take place during solidification are:

- **Slurry flow regime:** In this regime, the equiaxed grains are able to move being affected by the liquid drag, the apparent gravity, their inertia and the collisions between

each other. The liquid phase movement is strongly coupled to the solid phase movement. In this regime, the momentum exchange between the phases is dominated by the drag force. The momentum equations for liquid and solid, respectively, are:

$$\begin{aligned} \frac{\partial}{\partial t} (g_l \rho_l \langle \vec{v}_l \rangle^l) + \nabla \cdot (g_l \rho_l \langle \vec{v}_l \rangle^l \langle \vec{v}_l \rangle^l) + 2g_l \rho_l \vec{\omega} \times \langle \vec{v}_l \rangle^l \\ = -g_l \nabla p + \nabla \cdot (g_l \mu_l \nabla \langle \vec{v}_l \rangle^l) - K_d^s (\langle \vec{v}_l \rangle^l - \langle \vec{v}_s \rangle^s) \\ - \langle \vec{v}_s \rangle^s \Gamma_s + g_l \rho_l^b (\vec{g} - \vec{\omega} \times (\vec{\omega} \times \vec{x})) \end{aligned} \quad (4.6)$$

$$\begin{aligned} \frac{\partial}{\partial t} (g_s \rho_s \langle \vec{v}_s \rangle^s) + \nabla \cdot (g_s \rho_s \langle \vec{v}_s \rangle^s \langle \vec{v}_s \rangle^s) + 2g_s \rho_s \vec{\omega} \times \langle \vec{v}_s \rangle^s \\ = -g_s \nabla p + \nabla \cdot (g_s \mu_s \nabla \langle \vec{v}_s \rangle^s) + K_d^s (\langle \vec{v}_l \rangle^l - \langle \vec{v}_s \rangle^s) \\ + \langle \vec{v}_s \rangle^s \Gamma_s + g_s \rho_s^{ref} (\vec{g} - \vec{\omega} \times (\vec{\omega} \times \vec{x})) \end{aligned} \quad (4.7)$$

Where μ_s is the solid dynamic viscosity, which is modeled as proposed by Ishii [76, 53] (Eqn. 1.20) and $K_d^s (\langle \vec{v}_l \rangle^l - \langle \vec{v}_s \rangle^s)$ the interfacial momentum exchange due to drag that arises due to the phases relative movement. This term is written as a function of K_d^s , which is a convenient formulation for both the slurry and porous flow regimes, as it will be seen later on (the superscript s denotes the slurry flow regime). K_d^s is given by:

$$K_d^s = \frac{3g_e \rho_l C_d}{4d_g} |\langle \vec{v}_l \rangle^l - \langle \vec{v}_s \rangle^s| \quad (4.8)$$

Where d_g is the equivalent spherical diameter of grain envelope, g_e the envelope fraction and C_d is the drag coefficient. In case of using a two-phase globular model, the envelope fraction, g_e , is equivalent to solid fraction, g_s , *i.e.* $g_e = g_s$. Hereinafter, the equations are written in the most generic case, which is when $g_e \neq g_s$. In *macroS3D*, the drag coefficient is modeled as proposed by Ni and Beckermann [60], following the model of Agarwal and O'Neill [100]:

$$C_d = \frac{48C_{ke}g_s}{Re} + C_{ie} \quad (4.9)$$

$$C_{ke} = \begin{cases} 25/6 & \text{if } g_e > 0.5 \\ \frac{1}{2} \frac{(1-g_e)^3}{g_e} \frac{1+4.7g_e}{1-1.83g_e} & \text{if } g_e \leq 0.5 \end{cases} \quad (4.10)$$

$$C_{ie} = \begin{cases} 7/3 & \text{if } g_e > 0.5 \\ \frac{24(10^E - 1)}{Re \left[1 - 0.9(0.75 - g_e)^{1/3} g_e^{2/3} \right]^3} & \text{if } g_e \leq 0.5 \end{cases} \quad (4.11)$$

$$E = 0.261Re^{0.369} - 0.105Re^{0.431} - \frac{0.124}{1 + (\log_{10} Re)^2} \quad (4.12)$$

$$Re = \frac{d_g (1 - g_e) \left| \langle \vec{v}_s \rangle^s - \langle \vec{v}_l \rangle^l \right|}{\nu_l} \quad (4.13)$$

The drag coefficient, in the model proposed by Ni and Beckermann [60], reduces to the one for a single sphere in the limit $g_e \rightarrow 0$. Moreover, if $g_e \rightarrow 0$ and $Re \rightarrow 0$ the drag coefficient reduces to the one given by the Stokes law, $C_d = 24/Re$.

- **Porous flow regime:** The porous flow regime takes place when the equiaxed grains are packed, such that they are immobile in the domain, *i.e.* $\langle \vec{v}_s \rangle^s = 0$. The momentum equations that describe this flow regime are:

$$\begin{aligned} \frac{\partial}{\partial t} (g_l \rho_l \langle \vec{v}_l \rangle^l) + \nabla \cdot (g_l \rho_l \langle \vec{v}_l \rangle^l \langle \vec{v} \rangle^l) + 2g_l \rho_l \vec{\omega} \times \langle \vec{v}_l \rangle^l \\ = -g_l \nabla p + \nabla \cdot (g_l \mu_l \nabla \langle \vec{v}_l \rangle^l) - K_d^p \langle \vec{v}_l \rangle^l \\ - \langle \vec{v}_s \rangle^s \Gamma_s + g_l \rho_l^b (\vec{g} - \vec{\omega} \times (\vec{\omega} \times \vec{x})) \end{aligned} \quad (4.14)$$

$$\langle \vec{v}_s \rangle^s = 0 \quad (4.15)$$

In this regime, K_d^p (superscript p denotes the porous flow regime) is:

$$K_d^p = \frac{g_l^2 \mu_l}{K} \quad (4.16)$$

Where K is the hydrodynamic permeability, which is modeled as stated by Eqn. 1.23.

The use of coefficients K_d^s and K_d^p allows to write the different momentum equations, for both convection regimes, in a similar way. The coefficient K_d^s , in the slurry flow regime, depends on the grain diameter, on the solid and envelope fractions and on the local hydrodynamic conditions (the magnitude of the relative velocity between the phases). On the other hand, in the porous flow regime, K_d^p , depends mostly on the characteristic length of the porous media and on the solid fraction. At the packing front, the interfacial drag coefficient in the porous region, K_d^p , is generally larger than the one in the slurry region, K_d^s . This difference can be even of various orders of magnitude depending on the local hydrodynamic conditions and grain size. Yet, along with the resolution of the momentum equations, the mass conservation condition must be

satisfied. The mass conservation equation closes the problem giving the missing information for solving the pressure field. Due to the use of the Boussinesq approximation, the mass conservation equation is simplified as:

$$\nabla \cdot (g_l \langle \vec{v}_l \rangle^l + g_s \langle \vec{v}_s \rangle^s) = 0 \quad (4.17)$$

4.1.3.2 Numerical implementation in *macroS3D*

The velocity-pressure coupling was implemented using an algorithm of the family PISO/SIMPLE but for multiphase flows. It is very similar to the IPSA algorithm used in the macroscopic solidification model of Heyvaert [101] but accounting for the use of collocated grids.

To perform the velocity-pressure coupling, the main numerical challenge lies on the transition between the slurry and porous convection regimes. During the development of *macroS3D* various approaches for imposing this transition were implemented and tested. Some of these approaches were:

- To impose large solid viscosity in the region where the equiaxed grains were packed. This approach led to ill conditioned linear systems and a non-physical equiaxed grain packing front.
- To use artificial source terms in the solid momentum equation such that, when $g_e \rightarrow g_e^{block}$; $\langle \vec{v}_s \rangle^s \rightarrow 0$. This approach also resulted in ill conditioned linear systems due to the introduction of non-physical forces.
- To use the *MULES* algorithm to limit the maximum amount of solid fraction. This approach performed a redistribution of solid phase when $g_e \geq g_e^{block}$, rather than fully blocking the solid fraction.

Finally, to overcome the problematic of the slurry/porous flow transition, this work proposes a modified velocity-pressure coupling algorithm, which is described below.

In order to define the regions in the domain where the slurry flow and porous flow regimes take place, the indicative function proposed by Založnik [77] and Nguyen [102] is used in *macroS3D*. This function is given by:

$$\alpha_t = 1.0 - 0.5 \left(1.0 - \tanh \left[\alpha \left(g_e^{block} - g_e \right) \right] \right) \quad (4.18)$$

where α is an arbitrary value. Figure 4.2 shows the shape of this function for different values of α and for $g_e^{block} = 0.3$. The function α_t is equal to unity in the slurry flow region, whereas it is equal to zero in the porous flow region. The transition between the two regimes is smooth and depends on the value of α : a sharper transition is produced using large values of α , while a smoother transition is produced using small values of α . The effect of α on the equiaxed grain packing will be discussed later on.

Note that in case of using a two-phase globular model, the packing criterion, g_e^{block} , represents the solid fraction at which the spherical grains pack. Therefore, the packing criterion may be

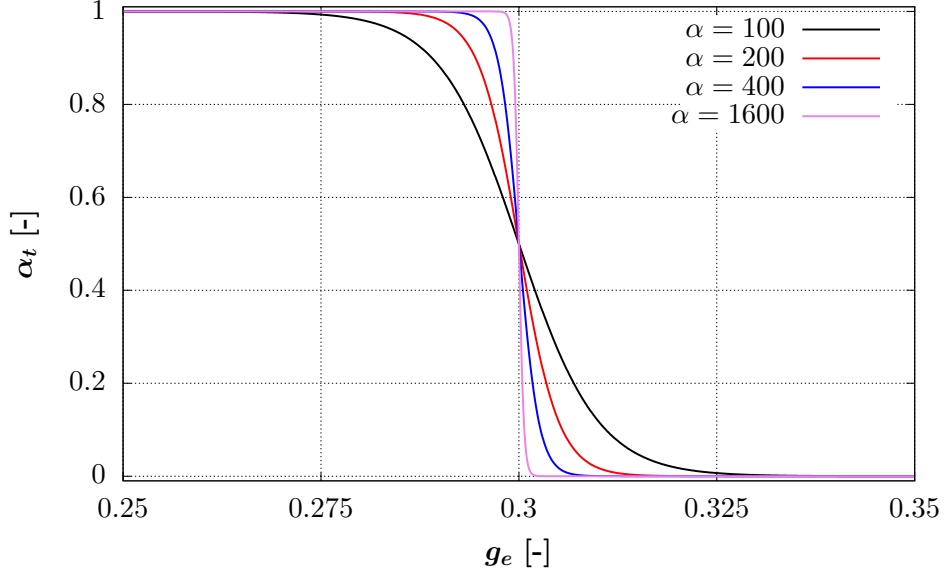


Figure 4.2 – Indicative function α_t for $g_e^{block} = 0.3$ and for various values of α , in the neighborhood of g_e^{block}

of the order of 0.5-0.6 in case of solidification of globular equiaxed grains. On the other hand, using a three-phase dendritic model, the packing criterion represents the envelope fraction at which the grains pack and its value is of the order or 0.3-0.4 [31].

Once the indicative function α_t is defined, the momentum equations can be written using a semi-discretized formulation following the finite-volume approach. For volume element p :

Solid momentum equation:

$$a_{s,p} \langle \vec{v}_s \rangle_p^s = \vec{H}_s - g_s \nabla p + g_s \rho_s^{ref} \vec{g}_{tot} + \alpha_t K_d^s \left(\langle \vec{v}_l \rangle_p^l - \langle \vec{v}_s \rangle_p^s \right) \quad (4.19)$$

Liquid momentum equation:

$$a_{l,p} \langle \vec{v}_l \rangle_p^l = \vec{H}_l - g_l \nabla p + g_l \rho_l^b \vec{g}_{tot} + \alpha_t K_d^s \left(\langle \vec{v}_l \rangle_p^l - \langle \vec{v}_s \rangle_p^s \right) + (1 - \alpha_t) K_d^p \langle \vec{v}_l \rangle_p^l \quad (4.20)$$

Where $a_{k,p}$ are accompanying coefficients that result from the discretization process. The vector \vec{H}_k is defined by:

$$\vec{H}_k = \vec{r}_k - \sum_n a_n \langle \vec{v}_k \rangle_n^k \quad (4.21)$$

Here the vector \vec{r}_k accounts for all source terms and a_n are accompanying coefficients of the neighboring cells that result from the discretization process. In particular, the term $\langle \vec{v}_s \rangle^s \Gamma_s$ in the liquid momentum equation is accounted for in \vec{r}_k since it can not be treated implicitly. Note that the pressure, drag and gravity contributions are not accounted for in \vec{H}_k .

To simplify the notation, the variable K_d is introduced:

$$K_d = \alpha_t K_d^s + (1 - \alpha_t) K_d^p \quad (4.22)$$

OpenFOAM uses a collocated grid formulation, so that all the physical quantities are defined and saved in the center of the mesh cells. In order to construct the phase fluxes on each cell face an interpolation is required. Note that $\{\bullet\}_f$ denotes the interpolated value from the cell center to the cell face. The solid and liquid fluxes on the cell faces, using Eqns. 4.19 and 4.20, are given by:

$$\begin{aligned} \phi_s = \langle \vec{v}_s \rangle^s \cdot \vec{S} = & \frac{\{\alpha_t\}_f}{\{a_{s,p}\}_f + \{K_d\}_f} \{\vec{H}_s\}_f \cdot \vec{S} - \frac{\{\alpha_t\}_f \{g_s\}_f}{\{a_{s,p}\}_f + \{K_d\}_f} |\vec{S}| \nabla^\perp p \\ & + \frac{\{\alpha_t\}_f \{g_s\}_f}{\{a_{s,p}\}_f + \{K_d\}_f} \{\vec{g}_{tot}\}_f \cdot \vec{S} + \frac{\{\alpha_t\}_f \{K_d\}_f}{\{a_{s,p}\}_f + \{K_d\}_f} \{\langle \vec{v}_l \rangle^l\}_f \cdot \vec{S} \end{aligned} \quad (4.23)$$

$$\begin{aligned} \phi_l = \langle \vec{v}_l \rangle^l \cdot \vec{S} = & \frac{1}{\{a_{l,p}\}_f + \{K_d\}_f} \{\vec{H}_l\}_f \cdot \vec{S} - \frac{\{g_l\}_f}{\{a_{l,p}\}_f + \{K_d\}_f} |\vec{S}| \nabla^\perp p \\ & + \frac{\{g_l\}_f}{\{a_{l,p}\}_f + \{K_d\}_f} \{\vec{g}_{tot}\}_f \cdot \vec{S} + \frac{\{K_d\}_f}{\{a_{l,p}\}_f + \{K_d\}_f} \{\langle \vec{v}_s \rangle^s\}_f \cdot \vec{S} \end{aligned} \quad (4.24)$$

Where \vec{S} is the vector normal to the cell face and its magnitude is equal to the face area. The interpolation of K_d to the cell faces is given by:

$$\{K_d\}_f = \{\alpha_t\}_f \{K_d^s\}_f + (1 - \{\alpha_t\}_f) \{K_d^p\}_f \quad (4.25)$$

In Eqns. 4.23 and 4.24, all terms are calculated explicitly, except for the pressure term. Note that all terms on the solid flux calculation (RHS of Eqn. 4.23) are multiplied by $\{\alpha_t\}_f$, such that the solid flux over a cell face in the porous flow region is equal to zero. Following, once the fluxes at the cell faces are written in terms of the pressure, the mass conservation is imposed:

$$\nabla \cdot (\{g_s\}_f \phi_s + \{g_l\}_f \phi_l) = 0 \quad (4.26)$$

Eqn. 4.26 is solved for the pressure. OpenFOAM discretizes the gradients considering an implicit orthogonal component and an explicit non-orthogonal component. If non-orthogonal meshes are used, two or more iterations of Eqn. 4.26 may be required to make the explicit component of the pressure gradient converge. Next, using the new calculated pressure, incomplete solid and liquid fluxes, ϕ_s^* and ϕ_l^* , are calculated. These fluxes do not account for the contribution of the interfacial drag term:

$$\begin{aligned} \phi_s^* &= \frac{\{\alpha_t\}_f}{\{a_{s,p}\}_f + \{K_d\}_f} \{\vec{H}_s\}_f \cdot \vec{S} - \frac{\{\alpha_t\}_f \{g_s\}_f}{\{a_{s,p}\}_f + \{K_d\}_f} |\vec{S}| \nabla^\perp p \\ &\quad + \frac{\{\alpha_t\}_f \{g_s\}_f}{\{a_{s,p}\}_f + \{K_d\}_f} \{\vec{g}_{tot}\}_f \cdot \vec{S} \end{aligned} \quad (4.27)$$

$$\begin{aligned} \phi_l^* &= \frac{1}{\{a_{l,p}\}_f + \{K_d\}_f} \{\vec{H}_l\}_f \cdot \vec{S} - \frac{\{g_l\}_f}{\{a_{l,p}\}_f + \{K_d\}_f} |\vec{S}| \nabla^\perp p \\ &\quad + \frac{\{g_l\}_f}{\{a_{l,p}\}_f + \{K_d\}_f} \{\vec{g}_{tot}\}_f \cdot \vec{S} \end{aligned} \quad (4.28)$$

Using Eqns. 4.27 and 4.28, the complete solid and liquid fluxes can be written as:

$$\phi_s = \phi_s^* + \frac{\{\alpha_t\}_f \{K_d\}_f}{\{a_{s,p}\}_f + \{K_d\}_f} \phi_l \quad (4.29)$$

$$\phi_l = \phi_l^* + \frac{\{K_d\}_f}{\{a_{l,p}\}_f + \{K_d\}_f} \phi_s \quad (4.30)$$

In case of the solid flux in Eqn. 4.29, the last term can be written implicitly using Eqn. 4.30, thus:

$$\phi_s = \phi_s^* + \frac{\{\alpha_t\}_f \{K_d\}_f}{\{a_{s,p}\}_f + \{K_d\}_f} \left(\phi_l^* + \frac{\{K_d\}_f}{\{a_{l,p}\}_f + \{K_d\}_f} \phi_s \right) \quad (4.31)$$

$$\phi_s = \left(1 - \frac{\{\alpha_t\}_f \{K_d\}_f^2}{(\{a_{s,p}\}_f + \{K_d\}_f)(\{a_{l,p}\}_f + \{K_d\}_f)} \right)^{-1} \left(\phi_s^* + \frac{\{\alpha_t\}_f \{K_d\}_f}{\{a_{s,p}\}_f + \{K_d\}_f} \phi_l^* \right) \quad (4.32)$$

Again, note that the solid flux is equal to zero in the porous flow region. Following the same procedure but this time for the liquid flux, it is obtained:

$$\phi_l = \left(1 - \frac{\{\alpha_t\}_f \{K_d\}_f^2}{(\{a_{s,p}\}_f + \{K_d\}_f)(\{a_{l,p}\}_f + \{K_d\}_f)} \right)^{-1} \left(\phi_l^* + \frac{\{K_d\}_f}{\{a_{l,p}\}_f + \{K_d\}_f} \phi_s^* \right) \quad (4.33)$$

Finally, the intrinsic velocities are reconstructed from the fluxes in the cell faces to the cell center as:

$$\langle \vec{v}_k \rangle^k = \left(\sum_f \frac{1}{|\vec{S}|} \vec{S} \vec{S} \right)^{-1} \cdot \left(\sum_f \frac{1}{|\vec{S}|} \vec{S} \phi_k \right) \quad (4.34)$$

4.1.4 Other macroscopic conservation equations

The macroscopic modeling of solidification also requires the resolution of conservation equations for the solute mass in solid and liquid phases, for grain density. In case of the use of a three-phase microscopic model a conservation equation for the envelope fraction is also required. These equations do not have any special treatment and therefore they are solved using the standard FVM method. Following, these equations are presented for a three-phase model approach, using the formulation as proposed by Tveito et al. [74]. A two-phase globular model approach can be recovered from the equations taking $g_s = g_e$, *i.e.* $g_l = g_l$. These equations are:

– **Solute mass balance in the liquid**

$$\frac{\partial}{\partial t} (g_l \rho_l \langle C_l \rangle^l) + \nabla \cdot (g_l \rho_l \langle \vec{v}_l \rangle^l \langle C_l \rangle^l) = -\Gamma_s C_l^* + \frac{\rho_l S_v^e D_l g_l}{g_l \delta_e} (C_l^* - \langle C_l \rangle^l) - \Phi_s k_p \langle C_l \rangle^l \quad (4.35)$$

Where the RHS, from left to right, corresponds to the interface solute exchanges due to growth, solute diffusion at microscopic scales and nucleation. These terms are discussed in the next section (Sect. 4.2).

– **Solute mass balance in the solid**

$$\frac{\partial}{\partial t} (g_s \rho_s \langle C_s \rangle^s) + \nabla \cdot (g_s \rho_s \langle \vec{v}_s \rangle^s \langle C_s \rangle^s) = k_p \Gamma_s C_l^* + \frac{\rho_s S_v^s D_s}{\delta_s} (k_p C_l^* - \langle C_s \rangle^s) + \Phi_s k_p \langle C_l \rangle^l \quad (4.36)$$

Again, the RHS of Eqn. 4.36, from left to right, correspond to the interface solute exchanges due to growth, solute diffusion at microscopic scales and nucleation.

– **Grain population balance**

$$\frac{\partial N_g}{\partial t} + \nabla \cdot (N_g \langle \vec{v}_s \rangle^s) = \dot{N} \quad (4.37)$$

where \dot{N} is the grain density nucleation rate. The solid mass generation due to nucleation is given by:

$$\Phi_s = \rho_s V_0 \dot{N} \quad (4.38)$$

with V_0 the initial grain volume.

– **Grain envelope balance**

$$\frac{\partial g_e}{\partial t} + \nabla \cdot (g_e \langle \vec{v}_s \rangle^s) = \frac{1}{\rho_s} (\Gamma_e + \Phi_s) \quad (4.39)$$

Where Γ_e represents the envelope growth rate. At a nucleation event, the envelopes are fully solid, therefore the nucleation source here is equal to Φ_s . Note that Eqn. 4.39 presents the same numerical challenge than the mass balance of solid phase (Eqn. 4.2),

which requires a bounded solution. An error on the calculation of the transport of envelope fraction will not have repercussions on the overall mass balance (Eqn. 4.17), therefore, the envelope fraction can be easily corrected by truncation. This truncation does not introduce a large error since the coupled system of partial differential equations is solved iteratively, which leads to a converged value of the envelope flux and hence, of envelope fraction. The same comment is valid for Eqn. 4.37 since the minimum density of equiaxed grains is bounded by zero.

4.1.5 Validation of the transport model in *macroS3D*

As the implementation of the model accounting for equiaxed grain movements is new, it needs to be validated using a simple study case. In order to perform the validation, the sedimentation column case proposed by Nguyen [102] is considered here. This validation case does not include solidification and consists on a two-dimensional column, 10 mm wide and 100 mm high, in which at $t = 0$ spherical particles of 288 μm radius are placed between $20\text{ mm} \leq y \leq 80\text{ mm}$, where y denotes the height measured from the base of the column, with a density of 10^9 particles per cubic meter. Following, the particles are allowed to settle until they pack forming a bed of packed particles. The packing fraction is assumed to be $g_e^{block} = 0.3$, which is a non-physical value for spherical particles. The intention here is to validate a new implementation by means of a numerical exercise. The thermophysical properties are assumed to be of a Sn-5 wt.%Pb alloy as reported in Appendix A.1.3.

To perform the numerical simulations, the domain of study was discretized using square shaped cells of 0.5 mm edge. This mesh is equivalent in size to the one used by Nguyen [102]. With regard to the simulations numerical set up, the *upwind* interpolation scheme was used for the discretization of all advective terms, while a *linear* interpolation scheme for all diffusion terms. In addition, an implicit Euler time-stepping scheme was used for the temporal discretization. On the boundaries of this study case, a no-slip condition is imposed for the liquid intrinsic velocity while a slip condition for the solid intrinsic velocity. For all the other quantities, a zero gradient condition is imposed. This implies that all the boundaries are adiabatic. At $t = 0$, a uniform temperature equal to 224.9°C is imposed. The intrinsic solute concentration in the liquid is set to 5.515 wt.% in the region populated by particles, whereas in the fully liquid region is set to 5 wt.%. For its part, the intrinsic solute concentration in the solid is set to 0.328 wt.% in the region populated by particles. These concentrations imply that the average solute concentration is uniform and equal to 5 wt.% throughout the domain. A null intrinsic velocity was imposed in both, solid and liquid phases, as initial condition.

On this numerical exercise, three aspects of the transport implementation in *macroS3D* were explored. The first one is related to the value of α , which represent the smoothness of the slurry/porous transition, the second one is related to the interpolation technique of the indicative function α_t and the third one is related to the influence of the time step chosen to depict the slurry/porous transition. For this, the sedimentation case was performed using two interpolation schemes for α_t : linear and downwind with respect to $\langle \vec{v}_s \rangle^s$ and, for each scheme, four values of α were considered arbitrarily: 100, 200, 400 and 1600. Furthermore, for each pair “scheme/ α

value” four time-step values, Δt , were used: 5×10^{-3} s, 1×10^{-3} s, 5×10^{-4} s and 1×10^{-4} s. In total, this benchmark case was performed with 32 different numerical configurations.

Figures 4.3, 4.4 and 4.5 show the characteristic evolution of solid fraction and, solid velocity and liquid velocity over time, respectively. During sedimentation, the particles settled at $4.9 \text{ mm} \cdot \text{s}^{-1}$ whereas the surrounding liquid flowed upwards at $0.54 \text{ mm} \cdot \text{s}^{-1}$, approximately. At $t = 1.3$ s, the first particles touch the base of the column and at $t = 15$ s the bed of packed particles was completely formed. This bed of particles presented a height of 20 mm and a solid fraction around 0.3, which is in correspondence to the mass conservation and to the imposed packing fraction. Although no vortex nor instabilities were observed on the velocity fields as reported by Nguyen [102], the other observations with respect the velocity magnitude and particle packing are in full agreement with the reference.

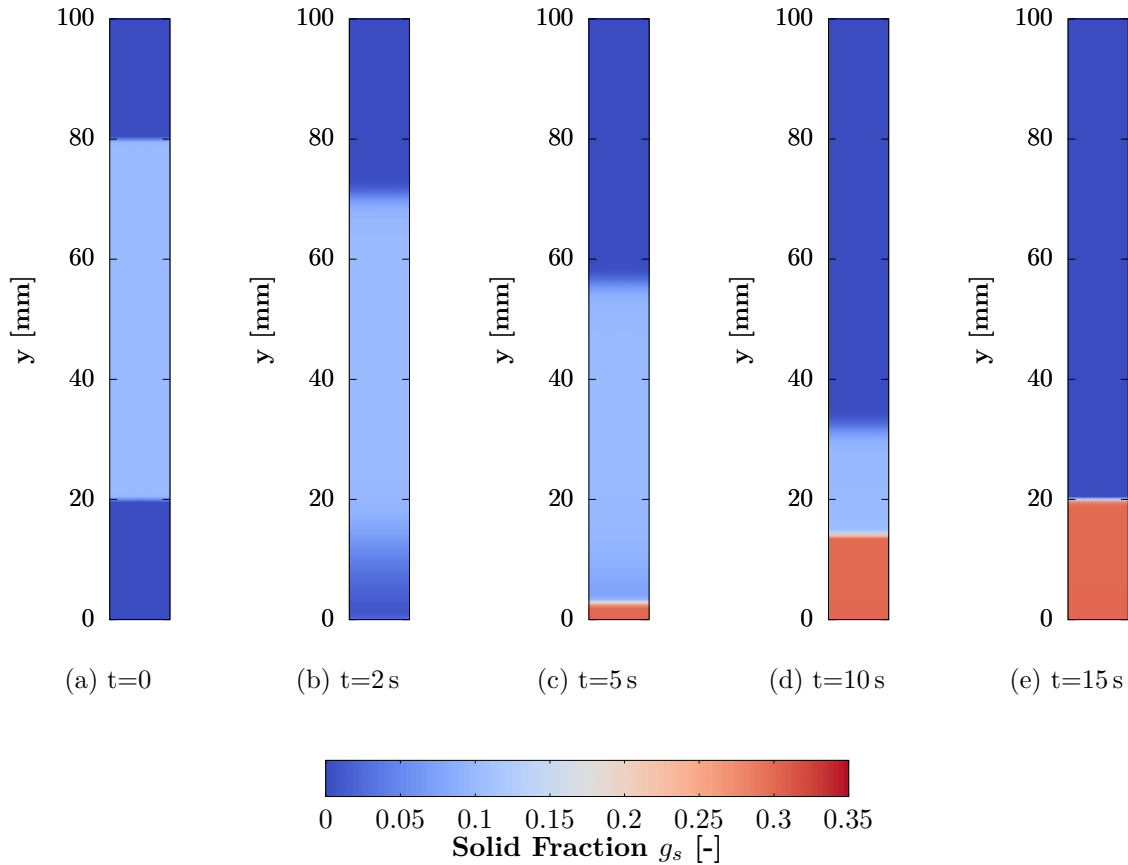


Figure 4.3 – Solid fraction field g_s over time obtained with *macroS3D* for the sedimentation column case proposed by Nguyen [102]. Numerical configuration: $\alpha = 1600$, $\Delta t = 1 \times 10^{-4}$ s and α_t was interpolated using a downwind scheme with respect to $\langle \vec{v}_s \rangle^s$.

In Figure 4.6 profiles for different scalar magnitudes over time are presented over time on the vertical centerline of the column. The region populated by particles is low in energy and in solute with respect to the fully liquid regions. This is explained since solid and liquid phases transport different amounts of those quantities. The grain density population follows the solid

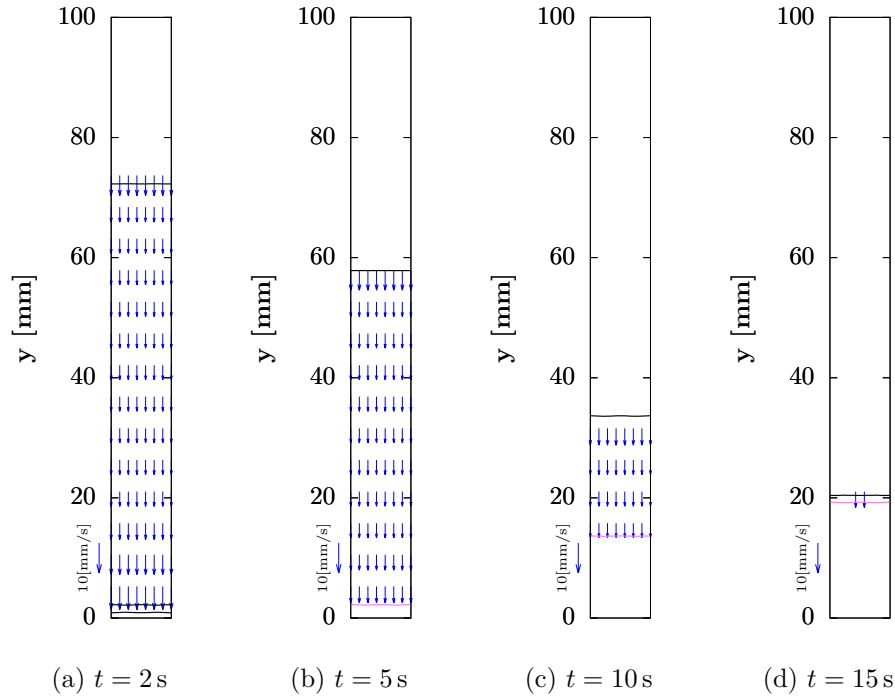


Figure 4.4 – Solid intrinsic velocity $\langle \vec{v}_s \rangle^s$ over time obtained with *macroS3D* for the sedimentation column case. Black contours represent $g_s = 0.01$ and violet contours represent $g_s = 0.29$. Numerical configuration: $\alpha = 1600$, $\Delta t = 1 \times 10^{-4}$ s and α_t was interpolated using a downwind scheme with respect to $\langle \vec{v}_s \rangle^s$.

fraction profile, which agrees to Eqn. 4.37. The temperature remained constant and uniform throughout the height, as expected according to the thermodynamic equilibrium imposed as initial condition.

In order to quantify the impact of the various numerical configurations used to simulate this case, the solid fraction profile over time, on the vertical centerline, is presented in Fig. 4.7 for relevant combinations of α_t interpolation scheme, α value and time-step. Yet, the figure also presents the solutions given by Nguyen (FEM) and SOLID[®] (FVM). From the figure, it is pointed out:

- During the particles free-fall, the different combinations of parameters do not have a large impact on the solution. However, important differences are visible during the formation of the bed of packed particles.
- When a small value of α is used, *e.g.* $\alpha = 100$, an accumulation of solid phase is produced in the base of the column, leading to solid fraction values greater than the imposed packing limit. This effect is explained because the slurry flow regime is still present for g_s beyond the packing fraction, *i.e.* until $g_s \sim 0.325$ (see Fig. 4.2). This allows the particles to continue settling and consequently to create this zone of high solid fraction. The accumulation effect disappears when the transition slurry/porous regime is sharpened by choosing a higher value of α (*e.g.* $\alpha = 1600$).

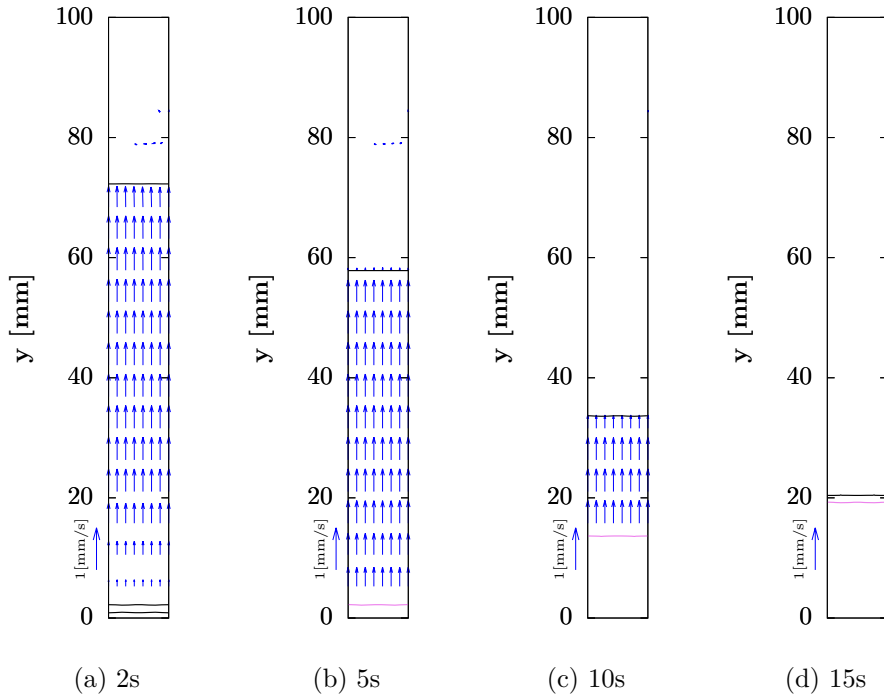


Figure 4.5 – Liquid intrinsic velocity $\langle \vec{v}_l \rangle^l$ over time obtained with *macroS3D* for the sedimentation column case. Black contours represent $g_s = 0.01$ and violet contours represent $g_s = 0.29$. Numerical configuration: $\alpha = 1600$, $\Delta t = 1 \times 10^{-4}$ s and α_t was interpolated using a downwind scheme with respect to $\langle \vec{v}_s \rangle^s$.

- When using a linear scheme to interpolate α_t from the cell centers to the cell faces, an accumulation of solid phase is produced in the interface between the bed of packed particles and the fully liquid region. A linear interpolation makes the cell faces, between a cell with excess of solid phase (*i.e.* $g_s \geq g_e^{block}$) and another near the fully liquid state $g_s \rightarrow 0$, allow a solid flux cross them. This is because the interpolated value of solid fraction on these faces is lower than the packing limit ($\{g_s\}_f \leq g_e^{block}$), implying that $\{\alpha_t\}_f > 0$. In this case, the interface is formed because no more solid phase remains above the front and not because a slurry/porous transition took place. Indeed, the transition takes place from the second cell below the interface.

This numerical issue is overcome using a downwind interpolation scheme with respect to $\langle \vec{v}_s \rangle^s$ for the indicative function α_t . With this type of scheme, the faces take the value of the cell in which a solid flux is attempting to enter. This scheme prevents having solid phase accumulation on the interface since it does not allow any solid flux to enter a cell that presents an excess of solid fraction *i.e.* $g_s \geq g_e^{block}$.

- When a smaller time-step is used, the representation of the slurry/porous regime transition is improved. The velocity-pressure coupling algorithm used by *macroS3D* does not re-distribute the solid phase when the packing criterion is reached. Therefore, there will be always an error associated to the excess of solid phase with respect to the

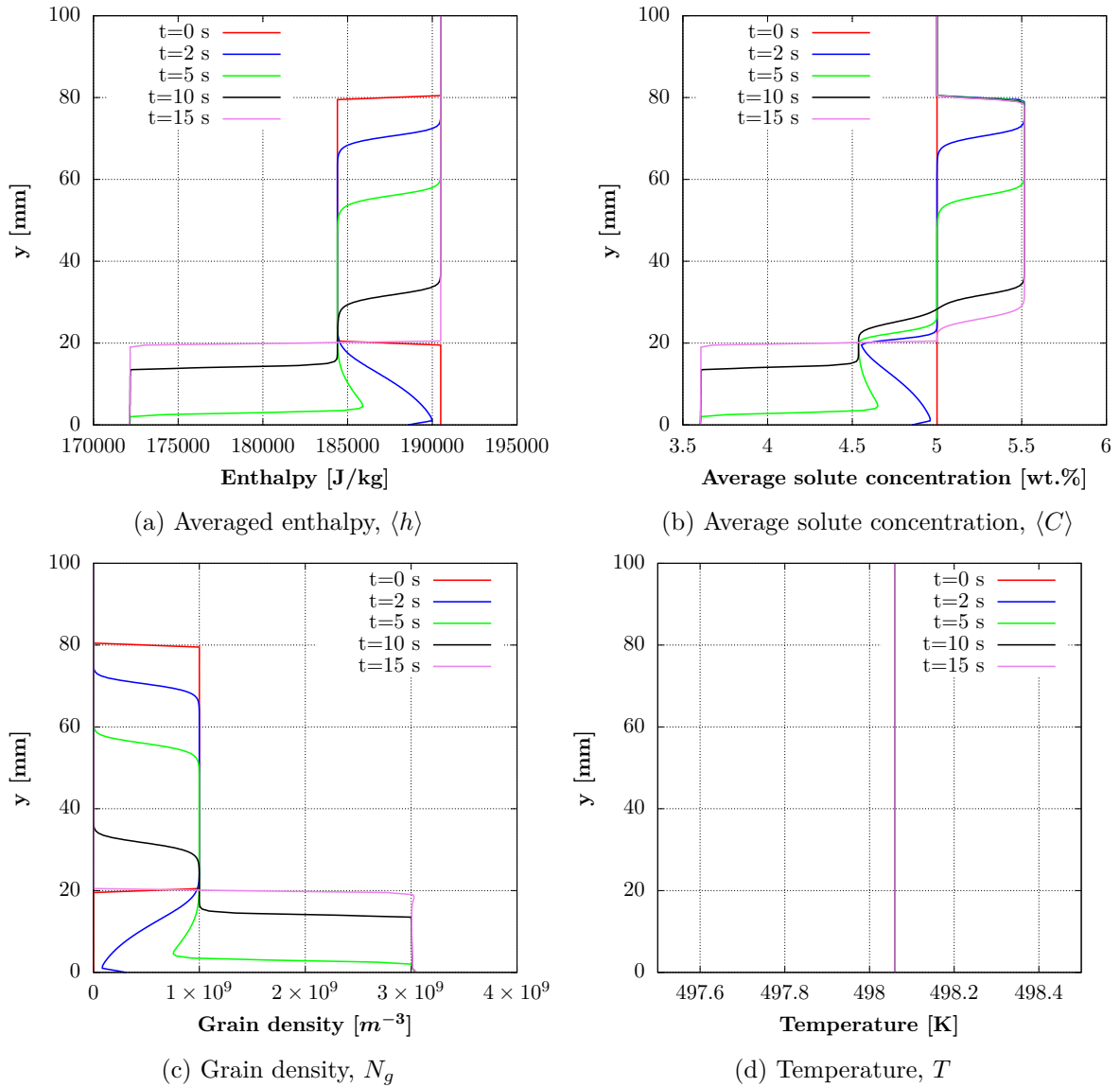


Figure 4.6 – Average enthalpy, average solute concentration, grain density and temperature on the vertical centerline over time obtained with *macroS3D* for the sedimentation column case. Numerical configuration: $\alpha = 1600$, $\Delta t = 1 \times 10^{-4}$ s and α_t was interpolated using a downwind scheme with respect to $\langle \vec{v}_s \rangle^s$.

packing limit, that can enter to a cell within one time-step.

Tables 4.1 and 4.2 present the maximum solid fraction, with respect to the value of α and time-step, produced when the indicative function, α_t , is interpolated using a *linear* or a *downwind* scheme, respectively. In case of the linear scheme, two zones of interest are reported: the interface between the fully liquid region and the bed of packed particles, and the base of the column. On the other hand, for the downwind scheme, only the base of the column is considered as zone of interest since no new maximum is reached in the interface. The tables clearly reveal that the use of a sharp transition, *i.e.* by using a high value of α , improves the representation

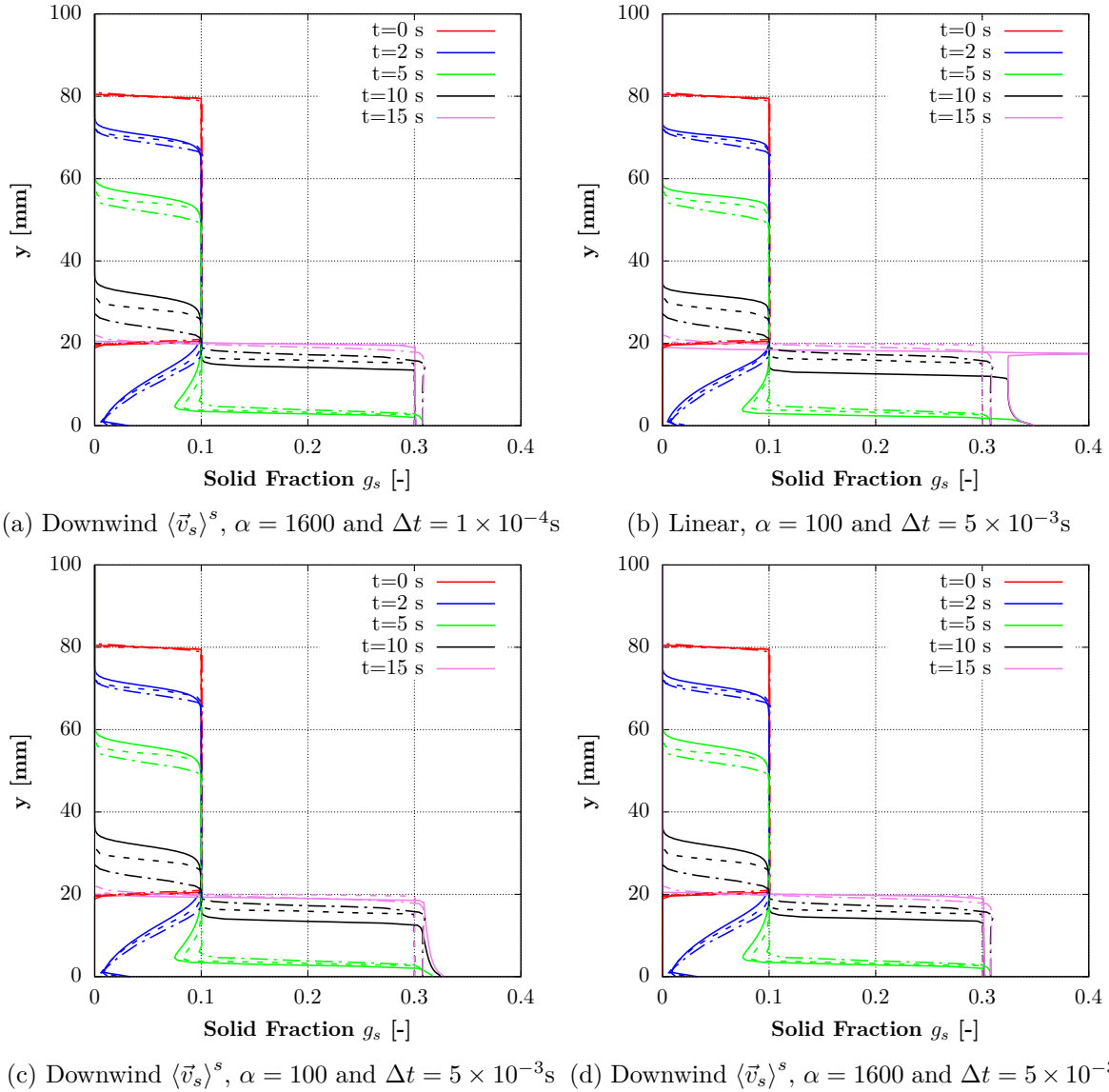


Figure 4.7 – Solid fraction on the vertical centerline over time for different numerical configurations on *macroS3D*. Solid line: *macroS3D* (FVM). Dashed line: *SOLID*[®] (FVM). Point-dash line: Nguyen (FEM) [102].

of the packing fraction criterion. In addition, the numerical aberrations in the interface are drastically reduced when a small time-step is used in case of the use of a linear scheme. Indeed, the most appropriate choice to perform numerical simulations may seem to be a high value of α , to sharpen the slurry/porous regime transition, a downwind interpolation scheme, to avoid issues in the interface, and a small time-step. However, the use of a sharp transition or a downwind scheme in more complex cases, may lead to ill conditioned linear systems solving the mass and momentum conservation equations. The sedimentation column case did not present any of these complications since it is simple benchmark case, with the sole purpose of validation. In solidification cases, the time-step is mostly limited by the temporal resolution required to solve

the microscopic model, rather than solving the macroscopic transport. A linear interpolation or a smooth transition cannot be discarded as valid options since they have an acceptable numerical accuracy when a small time-step is used.

Table 4.1 – Maximum solid fraction at $t = 15$ s in the interface between the fully liquid region and the bed of packed particles and in the base of the column when a linear interpolation scheme for α_t is used.

α \ Δt		5×10^{-3} s	1×10^{-3} s	5×10^{-4} s	1×10^{-4} s
		100	Interface	0.432591	0.333166
	Base	0.349184	0.326909	0.322507	0.314275
200	Interface	0.475281	0.358238	0.330431	0.305485
	Base	0.345226	0.31875	0.313819	0.30884
400	Interface	0.337005	0.374946	0.312403	0.307501
	Base	0.343227	0.316108	0.309981	0.305337
1600	Interface	0.361162	0.387857	0.320143	0.310506
	Base	0.341792	0.314343	0.3089	0.302264

Table 4.2 – Maximum solid fraction at $t = 15$ s in the base of the column when a downwind interpolation scheme with respect to $\langle \vec{v}_s \rangle^s$ is used.

α \ Δt	5×10^{-3} s	1×10^{-3} s	5×10^{-4} s	1×10^{-4} s
	100	0.327642	0.321814	0.318853
200	0.315459	0.312528	0.311038	0.307384
400	0.308565	0.307093	0.306342	0.304493
1600	0.302567	0.302197	0.302007	0.301536

macroS3D presented an excellent agreement to the solutions given by Nguyen [102] and to the solutions given by SOLID[®]. In view of the results, it is concluded that the velocity-pressure coupling algorithm proposed here and implemented in *macroS3D* is able to represent in a good way the different solidification convection regimes and their transition.

4.2 Microscopic modeling in *macroS3D*

4.2.1 Grain growth kinetics

This section is dedicated to describe the grain growth kinetics models implemented in *macroS3D*. To this point, *macroS3D* was able to represent the solid growth by means of an infinitely fast microscopic solute diffusion at the microscopic scales (Chapt. 3). This type of model cannot depict the thermal and solutal undercoolings, which are the main driving force for solid growth. Moreover, the model was not able to give information about the microstructure, such as grain size or grain morphology.

The new developments were focused in two types of grain growth descriptions: a two-phase globular model and a three-phase dendritic model. These kinetics models were already described in Chapter 1 but in the context of a review. Here the models will be fully described, along with their implementation in *macroS3D*.

4.2.1.1 Two-phase globular model

This type of model assumes a spherical grain morphology and limited diffusion in both phases at microscopic scales. Here, Eqn. 1.9 is re-written considering equilibrium at the solid-liquid interface, $C_s^* = k_p C_l^*$, and using the approximations for the solute concentration gradients at the solid-liquid interface given in Eqns. 1.10 and 1.11:

$$\Gamma_s C_l^* (1 - k_p) = \rho_l S_v D_l \frac{C_l^* - \langle C_l \rangle^l}{\delta_l} - \rho_s S_v D_s \frac{k_p C_l^* - \langle C_s \rangle^s}{\delta_s} \quad (4.40)$$

where the grain specific surface area for spherical grains is given by:

$$S_v = 4\pi R^2 N_g \quad (4.41)$$

with $R = \sqrt[3]{\frac{3g_s}{4\pi N_g}}$ the averaged grain radius.

In case of the diffusion lengths, both of them are modeled in the same way as in the software SOLID[®]. The diffusion length in solid is assumed to be proportional to the grain size, such that:

$$\delta_s = R/5 \quad (4.42)$$

The diffusion length in the liquid is modeled as proposed by Bedel [72] and it accounts for the simultaneous diffusion, interface motion and liquid convection effects:

$$\delta_l = d \left\{ \frac{d}{R} - \frac{f(R, \Delta) + g(R_f, R, \Delta)}{d \left[R + d - (R + \Delta + d) \exp\left(-\frac{\Delta}{d}\right) \right] - f(R, \Delta) + \left(\exp\left(-\frac{\Delta}{d}\right) - 1 \right) g(R_f, R, \Delta)} \right\}^{-1} \quad (4.43)$$

Where $R_f = \sqrt[3]{\frac{3}{\pi N_g}}$ is the final grain radius. The other required relations are:

$$f(R, \Delta) = \frac{(R + \Delta)^2 - R^2}{2} \quad (4.44) \quad g(R_f, R, \Delta) = \frac{R_f^3 - (R + \Delta)^3}{3(R + \Delta)} \quad (4.45)$$

$$d = \frac{D_l}{v_g} \quad (4.46) \quad \Delta = \min \left[(R_f - R), \frac{2R}{Sh_{conv}} \right] \quad (4.47)$$

$$Sh_{conv} = \frac{2Sc^{1/3} Re^{n(Re)}}{3(1 - g_s)} \quad (4.48) \quad Sc = \frac{\mu_l}{\rho D_l} \quad (4.49) \quad n(Re) = \frac{2Re^{0.28} + 4.65}{3(Re^{0.28} + 4.65)} \quad (4.50)$$

Where the Reynolds number, Re , is defined as in Eqn. 4.13.

These relations also need the velocity of the solid-liquid front V_g for a spherical shaped grain, which in a two-phase model can be easily calculated as (with R^0 denoting the last time-step averaged grain radius):

$$V_g = \frac{R - R^0}{\Delta t} \quad (4.51)$$

In *macro3D*, Eqn. 4.40 is solved along with a local energy balance using the temporal splitting-operator scheme proposed by Založnik [65]. The unknowns of this non-linear system are Γ_s and C_l^* . The local energy balance is given by:

$$\langle h \rangle = c_p (T_f + m_l C_l^*) + (1 - g_s^{gr}) L_f \quad (4.52)$$

In addition, Eqn. 4.52 requires a relation between g_s^{gr} and Γ_s which is given by the solid mass conservation, formulated within the splitting scheme:

$$\Gamma_s = \frac{\rho_s (g_s^{gr} - g_s^{nucl})}{\Delta t} \quad (4.53)$$

Where g_s^{gr} and g_s^{nucl} are the solid fractions at the nucleation and growth stage of the operator splitting scheme, respectively. The solving strategy is the same followed by Založnik [65], who proposes to linearise the system using the last known value of C_l^* and to iterate until the convergence of Γ_s and C_l^* . Once these values are updated, the algorithm proceeds to update the average solute concentrations in solid and liquid ($\langle C_s \rangle^s$ and $\langle C_l \rangle^l$, respectively) using the corresponding interface solute exchanges due to solid growth and solute diffusion at microscopic scales (see Eqns. 4.36 and 4.35).

Note that the solute interface balance of Eqn. 4.40 depends on the average solute concentration in both phases. Moreover, the diffusion lengths and specific surface areas require geometrical relations which depends on the solid fraction that is a priori not known. For this reason, the algorithm follows an iterative procedure until the values of g_s^{gr} , $\langle C_l \rangle^l$, $\langle C_s \rangle^s$, Γ_s and C_l^* are fully converged (see Fig. 4.14).

4.2.1.2 Three-phase dendritic model

As was previously mentioned in Chap. 1, this type of model uses the concept of “grain envelope”, which is a container of the solid grain and the intradendritic liquid that is directly in contact with the grain. Here, the envelope fraction is not necessarily equal to the solid fraction.

Unlike the globular model, that performs the solute balance on the solid-liquid interface, the three-phase model performs the solute balance on the intradendritic liquid (see Fig. 1.7). The balance is given by Eqn. 1.13. Both, SOLID[®] and *macroS3D*, use the approximation proposed by Tveito et al. [74], who showed that the contribution of $\frac{\partial C_l^*}{\partial t}$ can be neglected without introducing an important error in the calculation of the solute balance. As in the globular model, the solute balance is re-written considering equilibrium at the solid-liquid interface $C_s^* = k_p C_l^*$, and the approximations for the solute concentration gradients (Eqns. 1.10 and 1.11):

$$\Gamma_s C_l^* (1 - k_p) - \cancel{\rho_l g_l \frac{\partial C_l^*}{\partial t} \approx 0} = \rho_l S_v^E D_l \frac{g_l}{g_{le}} \frac{C_l^* - \langle C_l \rangle^l}{\delta_l} - \rho_s S_v^S D_s \frac{k_p C_l^* - \langle C_s \rangle^s}{\delta_s} \quad (4.54)$$

where $g_{li} = g_l - g_e$ is the intradendritic liquid fraction and $g_{le} = 1 - g_e$ the extradendritic liquid fraction. The envelope specific surface area, S_v^E , is mainly determined by the predefined envelope shape. *macroS3D* follows the same approach as SOLID[®] by considering the grain envelopes as octahedrons, thus:

$$S_v^E = 4\sqrt{3}R^2 N_g \quad (4.55)$$

where $R = \sqrt[3]{\frac{3}{4}g_e N_g}$ denotes the averaged grain arm length, $\lambda_2 = \frac{R_{env}}{5}$ the secondary arm spacing and $R_{env} = \sqrt[3]{3g_e 4\pi N_g}$ the equivalent envelope radius (if an equivalent spherical envelope is considered). The solid specific surface area, S_v^S , is modeled by the expression proposed by Appolaire [103]:

$$S_v^S = \frac{4}{\lambda_2} \sqrt{g_i g_e} (1 - g_i^m) + g_i^m S_v^E \quad (4.56)$$

where the coefficient m is equal to 6 according to Nielsen [104]. Following, the diffusion lengths, δ_l and δ_s , are calculated exactly in the same way as in the previous section (Sect. 4.2.1.1). The expressions given in Eqns. 4.42 and 4.43 are based on a solid-liquid spherical front, so that, they are incompatible with the predefined octahedral envelope morphology. In order to correct these expressions, they are calculated using R_{env} instead of R , and $V_g = \frac{1}{\pi} \left(\frac{R}{R_{env}}\right)^2 V_{tip}$, which is defined as the velocity of the “envelope/extradendritic liquid” front for a spherical shaped envelope.

The envelope growth rate, Γ_e , for an octahedral envelope morphology, is given by:

$$\Gamma_e = \frac{1}{\sqrt{3}} S_v^E V_{tip} \quad (4.57)$$

where V_{tip} is the grain tip velocity which has to be represented by an appropriate model.

macroS3D uses a paraboloidal tip velocity model, proposed originally by Lipton et al. [69, 70] and adapted by Ananth and Gill [71] to account for the effect of convection. The full set of equations that describes this model is:

Total tip undercooling:

$$T - T_f - m_l \langle C_l \rangle^{le} = \frac{L_f}{c_p} \Omega_T - m_l \langle C_l \rangle^{le} \left[1 - \frac{1}{1 - (1 - k_p) \Omega_C} \right] \quad (4.58)$$

Tip selection criterion:

$$R_{tip}^2 V_{tip} = \frac{\Gamma_{GT}}{\sigma^*} \left[\frac{m_l (k_p - 1) \langle C_l \rangle^{le}}{D_l (1 - (1 - k_p) \Omega_C)} + \frac{L_f}{2\alpha c_p} \right]^{-1} \quad (4.59)$$

where $\langle C_l \rangle^{le} = \frac{g_l \langle C_l \rangle^l - g_{li} C_l^*}{g_{le}}$ is the average solute concentration in the extradendritic liquid, Γ_{GT} the Gibbs-Thompson coefficient and σ^* the tip selection constant. The thermal and solutal dimensionless supersaturations are obtained as:

$$\Omega_T = F(Pe_T, Pu_T, Re_T) \quad (4.60) \quad \Omega_C = F(Pe_C, Pu_C, Re_C) \quad (4.61)$$

$$F(Pe, Pu, Re) = 2Pe \int_1^\infty \exp \left[-\ln(\eta) + (1 - \eta^2) - \frac{2Pu}{E_1(Re)} (1 - \eta^2 + \ln(\eta)(1 + \eta^2)) \right] d\eta \quad (4.62)$$

with $Pr = \frac{c_p \mu_l}{k}$ the Prandtl number, $Sc = \frac{\mu_l}{\rho_l D_l}$ the Schmidt number, Pe the tip Péclet numbers linked to tip growth, Pu the tip Péclet numbers linked to liquid convection, and Re the tip Reynolds numbers:

$$Pe_T = \frac{R_{tip} V_{tip}}{2\alpha} \quad Pe_C = \frac{R_{tip} V_{tip}}{2D_l}$$

$$Pu_T = \frac{R_{tip} |\langle \vec{v}_s \rangle^s - \langle \vec{v}_l \rangle^l|}{2\alpha} \quad Pu_C = \frac{R_{tip} |\langle \vec{v}_s \rangle^s - \langle \vec{v}_l \rangle^l|}{2D_l}$$

$$Re_T = \frac{Pe_T + Pu_T}{Pr} \quad Re_C = \frac{Pe_C + Pu_C}{Sc}$$

The unknowns that *macroS3D* solves for are the tip velocity, V_{tip} , and tip radius, R_{tip} . The non-linear system of equations, constituted by Eqns. 4.58 and 4.59, is solved using a Newton-Raphson method. The semi-infinite integral of Eqn. 4.62 is approximated by a 10-points Gaussian quadrature. Finally, the exponential integral function, denoted by E_1 , is calculated through the “boost” mathematical library.

Once the tip velocity model is fully resolved, it is required to calculate the value of the both diffusion lengths, δ_l and δ_s are calculated. The *macroS3D* algorithm for the three-phase model is structured in the same way as for two-phase globular model.

4.2.2 Grain nucleation and nuclei re-injection

The grain nucleation is handled in a simplified way in *macroS3D*. As initial condition, the study domain is configured to have a predefined amount of nuclei per unit of volume, N . A nucleus is a precursor or seed for the nucleation of a grain. The numerical implementation assumes that the grains nucleate when two conditions are met: the local undercooling is below a predefined nucleation undercooling, ΔT_{nucl} , and the local grain density is equal to zero. The local amount of grains to be nucleated corresponds to the local amount of available nuclei. The expression that describe the grain nucleation rate is given by:

$$\dot{N}^1 = N\delta(t) \quad \text{if} \quad (T_f + m_l \langle C_l \rangle^l) - T > \Delta T_{nucl} \quad \text{and} \quad N_g = 0 \quad (4.63)$$

where \dot{N}^1 is the amount of nucleated grains per cubic meter in one second.

When the microscopic model is coupled to the macroscopic model, the equiaxed grains can move. During solidification, due to equiaxed grain movement, regions with no remaining nuclei nor equiaxed grains and $(T_f + m_l \langle C_l \rangle^l) - T > \Delta T_{nucl}$ can take place. When this happens, the liquid in these regions can reach large undercoolings. This can triggers a equiaxed-to-columnar-transition (ECT), which is when columnar grains grow from the packing front of equiaxed grains. The representation of ECT is far from the scope of this work and, therefore, is not included in *macroS3D*. In addition, any equiaxed grain that enters this undercooled region may be submitted to a strong driving force to grow. This effect may lead to numerical problems if the temporal discretization is not able to describe the growth of grains submitted to strong undercoolings. Moreover, as the equiaxed grains move in the domain, at the end of solidification regions without any grain can appear if the ECT is not represented. In order to overcome this problem, the *macroS3D* model includes a re-injection of nuclei to avoid regions without nuclei. The re-injection is done locally and it occurs when the local density of equiaxed grains and the local density of nuclei is less than a predefined minimum, N_g^{min} . The mathematical expression that defines the nuclei re-injection rate is given by:

$$N = N^{inj} \quad \text{if} \quad N_g < N_g^{min} \quad \text{and} \quad N < N_g^{min} \quad (4.64)$$

Where N^{inj} is the number of nuclei per unit of volume which is locally set when the conditions are met.

Note that Eqn. 4.63 defines the source terms for the macroscopic grain population balance (Eqn. 4.37).

4.2.3 Validation of the microscopic modeling in *macroS3D*

The validation of the microscopic modeling in *macroS3D* was carried out considering the study case proposed by Bedel [72], which consists on the solidification of a Al-5 wt.%Si alloy in a unitary control volume at a constant cooling rate of $45 \text{ K} \cdot \text{s}^{-1}$, starting form a fully liquid state. Three different case configurations for the final grain size were considered: *Case A*: $R_f = 0.1 \text{ mm}$, *Case B*: $R_f = 1 \text{ mm}$ and *Case C*: $R_f = 10 \text{ mm}$. The final grain size is a key physical parameter since

it determines the distance between the growing grains and thus their level of solutal interaction. The simulations were carried out using the two-phase globular model and the three-phase model. The alloy thermophysical properties, used to perform the numerical simulations, are reported in Appendix A.1.4.

Figures 4.8, 4.9 and 4.10 present a comparison between the results obtained using SOLID[®] (ref. [72]) and *macro3D*. In case of using a two-phase globular model, only the temperature and solid fraction are reported for the interval $t < 1.5$ s. The figures show that when the grains are closer, *i.e.* small final grain size, they interact sooner than when the grains are distant. Indeed, the grain growth kinetic models are able to depict the recalescence, which is a direct consequence of the limited solute diffusion in solid and liquid phases at microscopic scales.

The comparison revealed an excellent agreement between the two solutions when a globular model is used. No differences can be noticed to the naked eye. On the other hand, when comparing the results for the three-phase model, small differences are noticed for both, envelope fraction, g_e , and internal solid fraction, g_i . In order to detect algorithmic problems, the overall implementation was intensively checked without finding the source of these small discrepancies. The most probable source is the resolution of the paraboloidal tip velocity model, which is a highly non-linear problem and requires a numerical integration. A numerical integration can be sensitive to the used numerical approach and to the convergence criterion.

Although the small discrepancies, the microscopic modeling in *macro3D* properly depicted the grain growth using different grain growth kinetics models and therefore, it is validated for use in macroscopic solidification simulations.

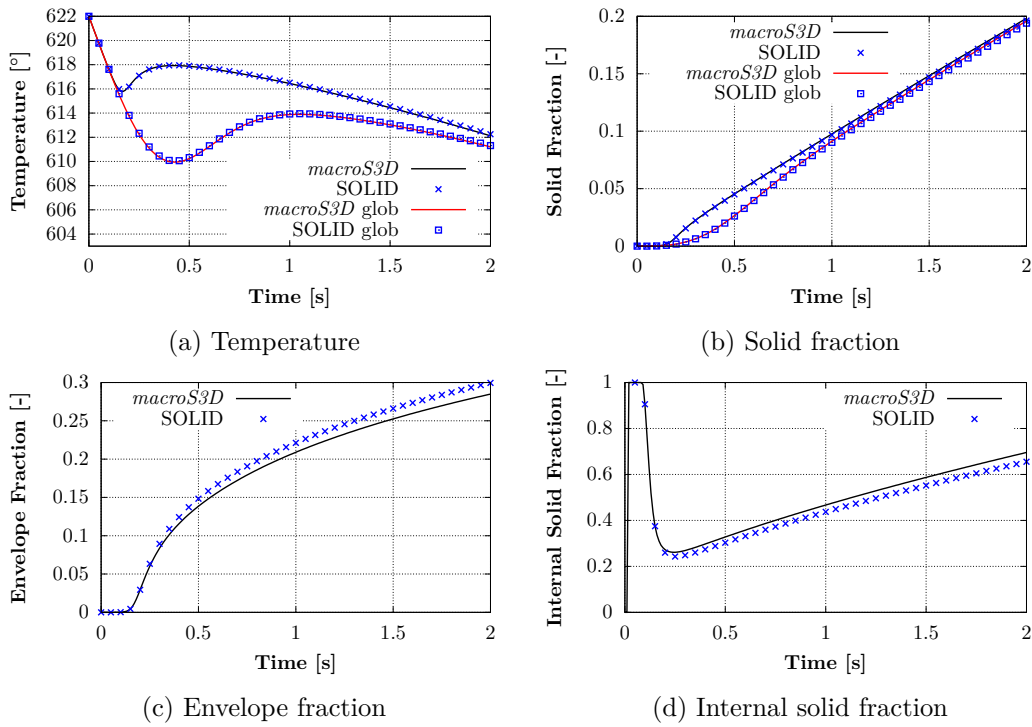


Figure 4.8 – Evolution of different magnitudes over time. Comparison between *SOLID*[®] and *macroS3D* for the *Case A*. “glob” denotes results obtained using a two-phase globular model.

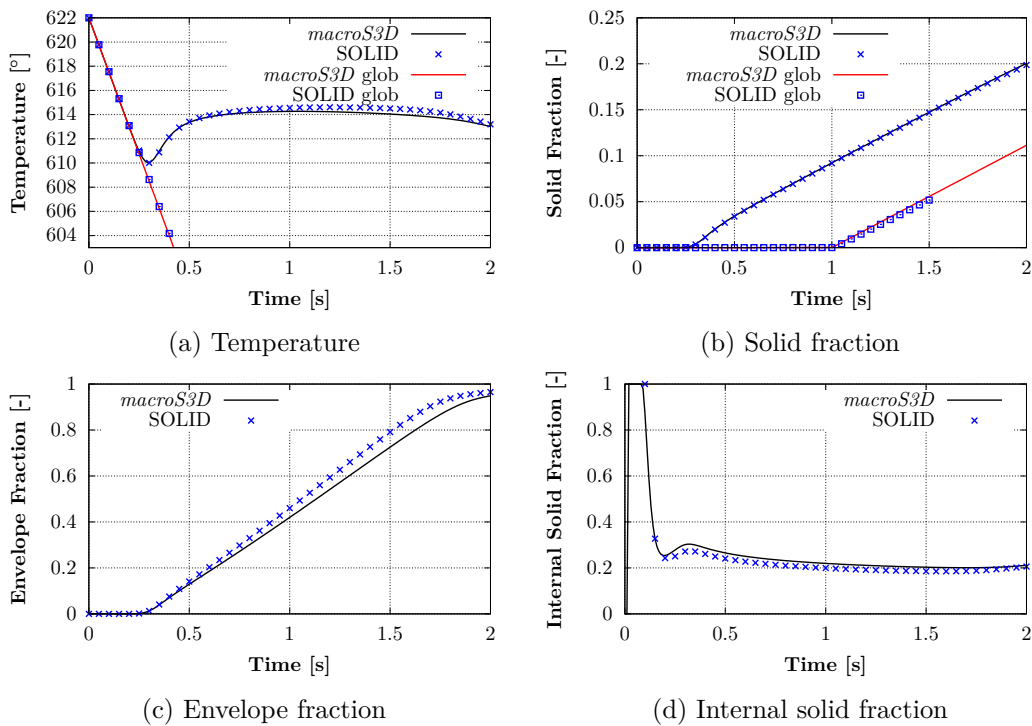


Figure 4.9 – Evolution of different magnitudes over time. Comparison between *SOLID*[®] and *macroS3D* for the *Case B*. “glob” denotes results obtained using a two-phase globular model.

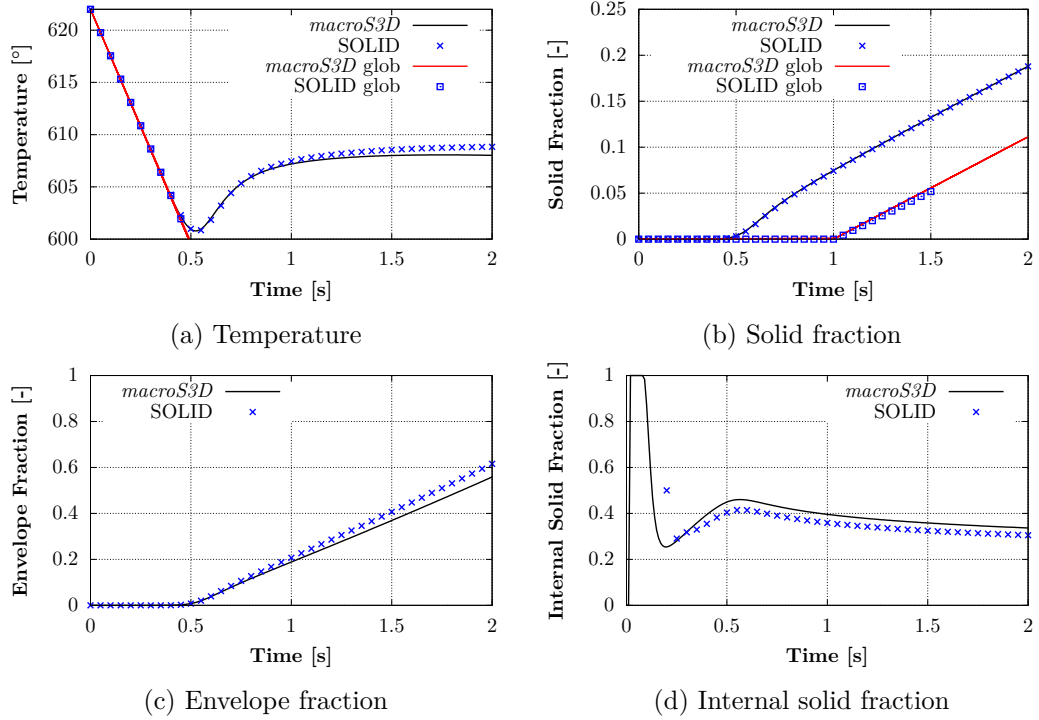


Figure 4.10 – Evolution of different magnitudes over time. Comparison between *SOLID*[®] and *macroS3D* for the *Case C*. “glob” denotes results obtained using a two-phase globular model.

4.3 Coupling of macroscopic conservation equations with microscopic modeling

The implementations of grain growth kinetic models and grain motion were carried out separately, so that, the next step is to couple both developments. For that, the operator splitting scheme algorithm for solidification proposed by Založnik and Combeau [65] was implemented in *macroS3D*. The operator splitting algorithm is based on scale separation (transport/growth) at the level of the numerical time integration and is a robust and flexible numerical framework for convection/diffusion multiscale models.

The original algorithm (in ref. [65]) includes only transport and growth stages. In order to include nucleation modeling, *macroS3D* follows an approach similar to the used by Heyvaert [101, 39] or Nguyen [34, 102] where a nucleation stage, between the transport and growth stages, is included in the coupling algorithm. The purpose of this section is to overview the implementation of the algorithm in *macroS3D*, rather than presenting all details. Schematics of the overall operator splitting (Fig. 4.11), transport stage (Fig. 4.12), nucleation stage (Fig. 4.13) and growth stage (Fig. 4.14) algorithms are presented with the corresponding procedure descriptions. In Figures 4.11 and 4.14 each “converged?” decision diamond is numbered. The convergence criteria for each decision is given in Table 4.3.

Table 4.3 – Convergence criteria for the different decisions in the algorithm *macroS3D*

Decision diamond	Criteria
(1)	$\max \left(\frac{n+1 T^{tr} - n T^{tr}}{n+1 T^{tr}} \right) < 10^{-8}$
(2)	$\max \left(\frac{m+1 g_s^{gr} - m g_s^{gr}}{m+1 g_s^{gr}} \right) < 10^{-2}$
(3)	$\max \left(\frac{C_l^* - prev C_l^*}{C_l^*} \right) < 10^{-10}$
(4)	$\max \left(\frac{p+1 g_s^{gr} - p g_s^{gr}}{p+1 g_s^{gr}} \right) < 10^{-6}$ and $\max \left(\frac{p+1 \langle C_l \rangle^{l(gr)} - p \langle C_l \rangle^{l(gr)}}{p+1 \langle C_l \rangle^{l(gr)}} \right) < 10^{-6}$

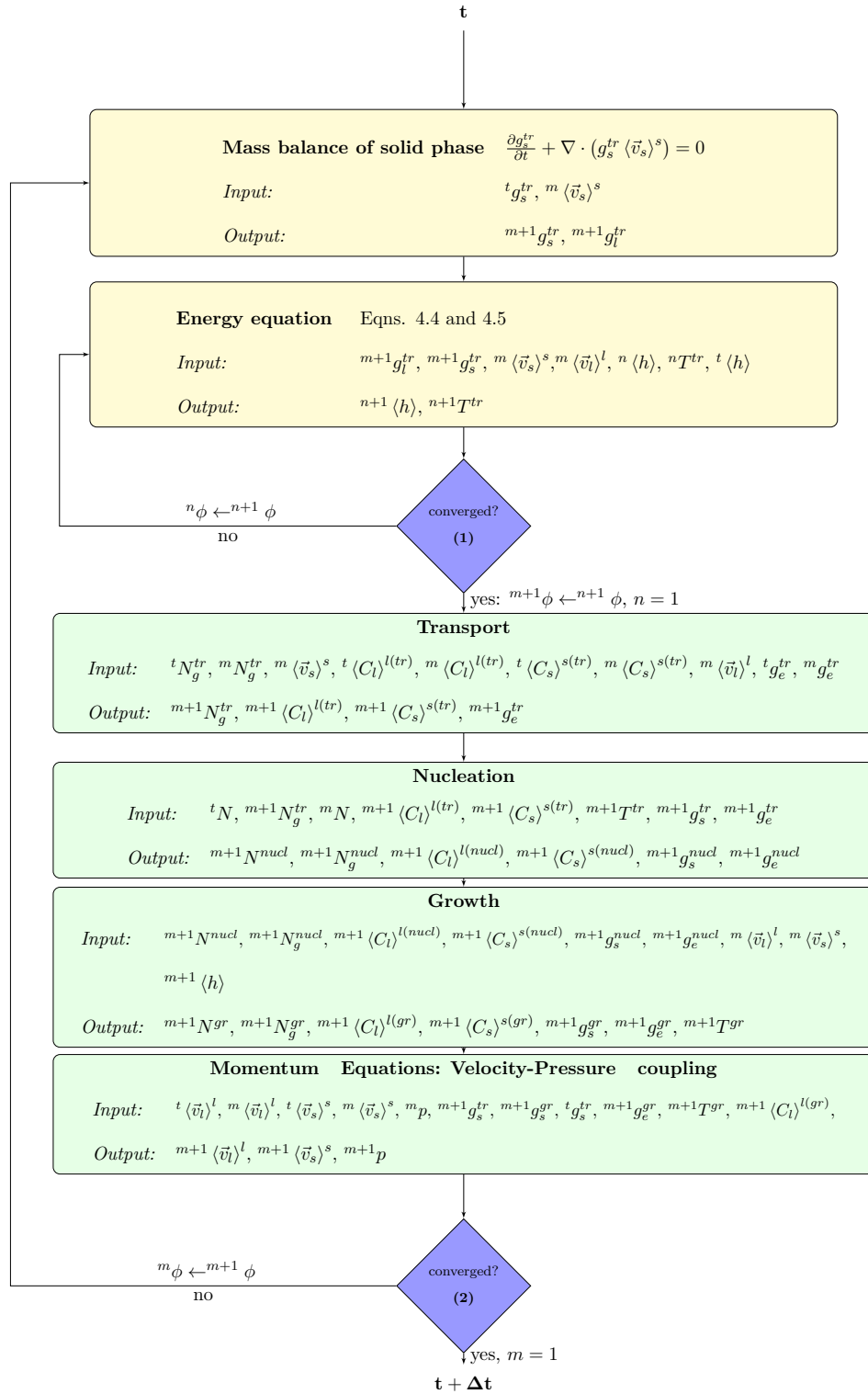


Figure 4.11 – The overall operator splitting algorithm for solidification implemented in *macroS3D*. The variable ϕ denotes an arbitrary field. The index m denotes the iteration “m” within a time-step. The index t denotes the old time-step (previous macro-timestep). The index n denotes the iterations for the energy equation.

Transport

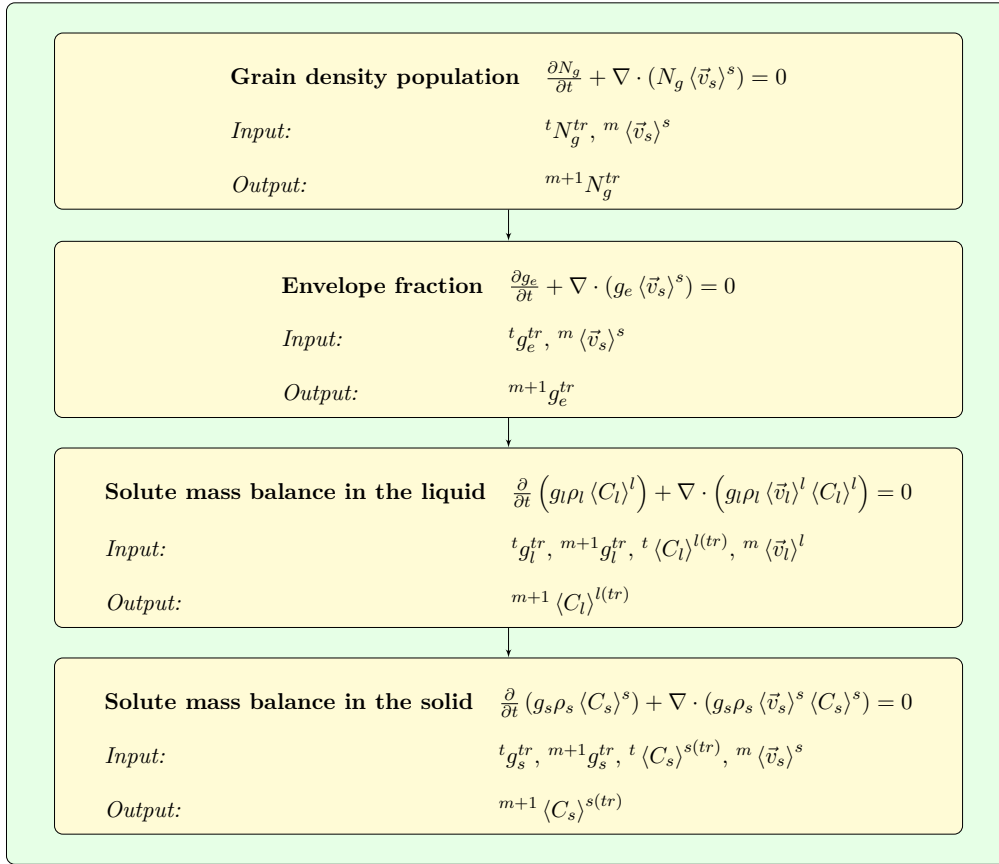


Figure 4.12 – Transport stage in *macroS3D*. The index m denotes the iteration “m” within a time-step. The index t denotes the old time-step (previous macro-timestep).

Nucleation

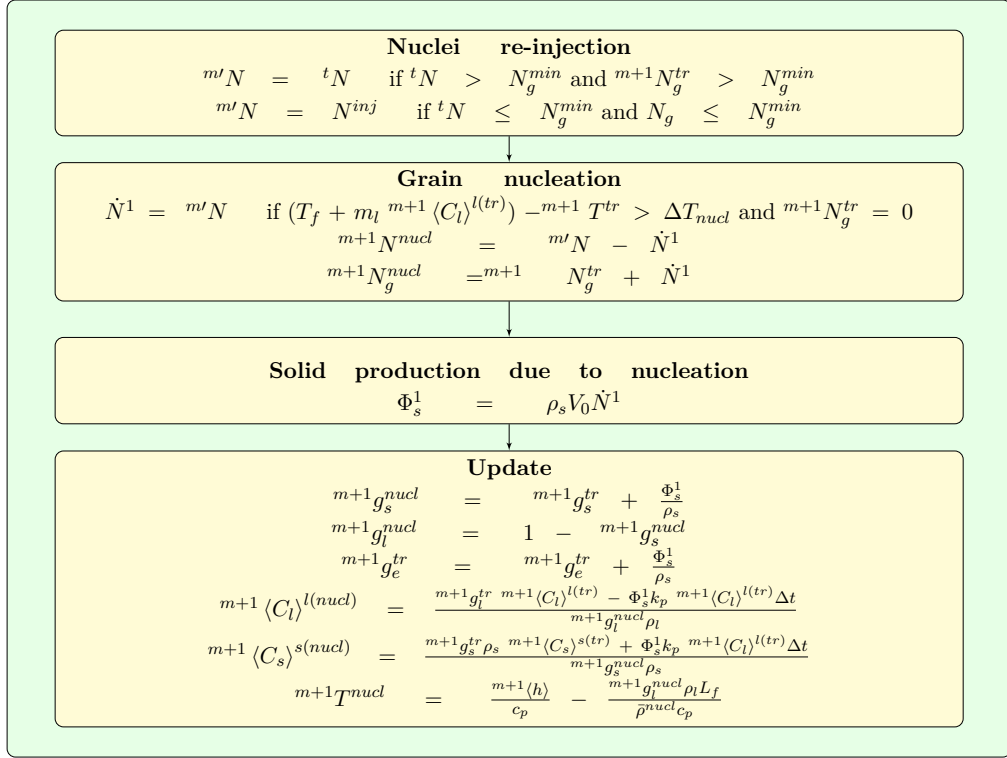


Figure 4.13 – Nucleation stage in *macroS3D*. The index m denotes the iteration “m” within a time-step. The index t denotes the old time-step (previous macro-timestep).

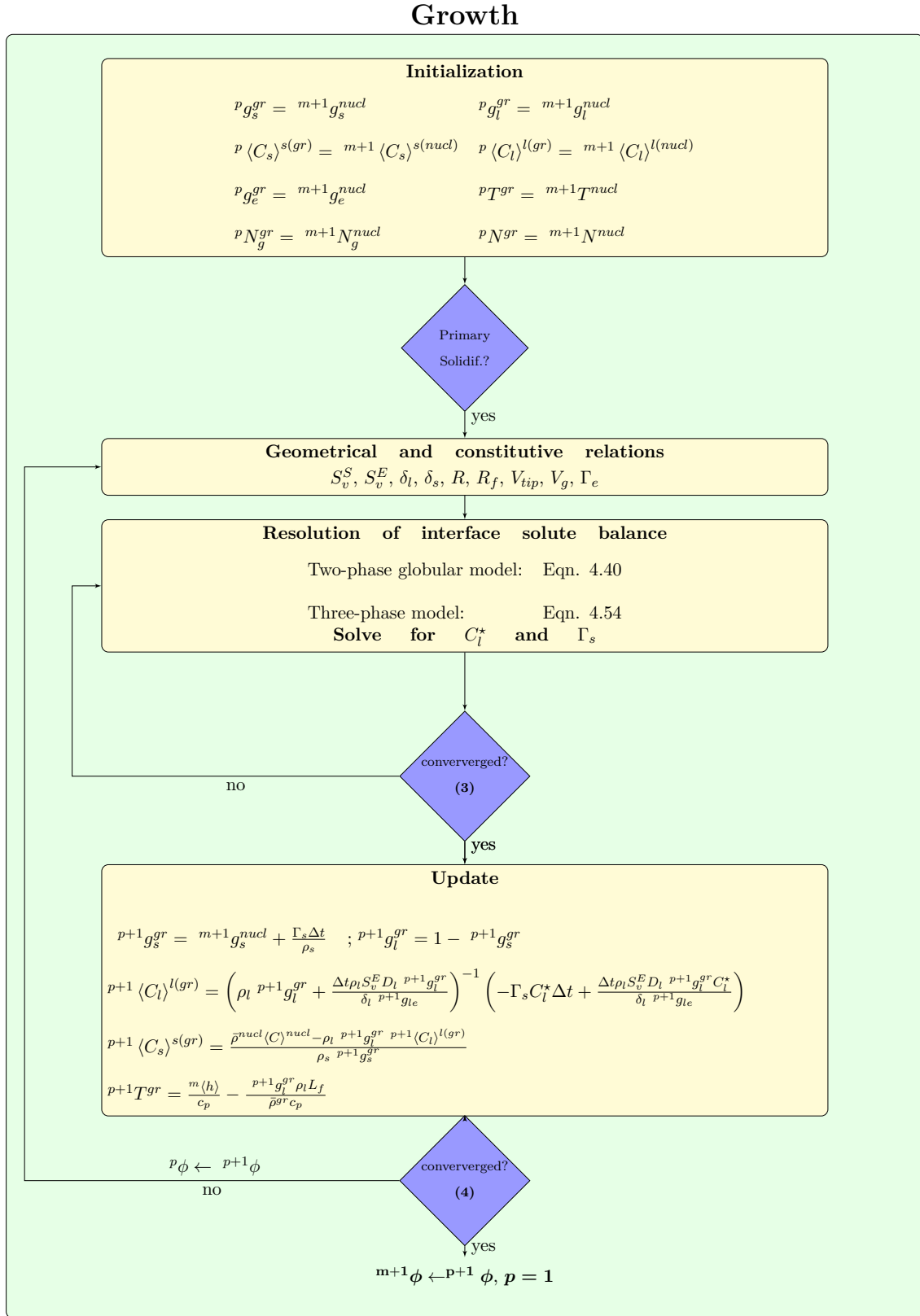


Figure 4.14 – Growth stage in *macroS3D*. The index m denotes the iteration “m” within a time-step. The variable ϕ denotes an arbitrary field. The index t denotes the old time-step (previous macro-timestep). The index p denotes the internal iterations of the grain growth algorithm

4.3.1 Validation of the multiscale modelling in *macroS3D*: The Hebditch and Hunt case

In order to validate the implementation of the coupling of macroscopic and microscopic modeling in *macroS3D*, the Hebditch and Hunt case [50] was considered to be simulated since it is one of the best known model cases for macroscopic solidification and macrosegregation with equiaxed grain motion in literature and has been widely used to validate and verify solidification models [79, 101, 34, 105]. The Hebditch and Hunt case consists of the solidification of a Sn-5 wt.%Pb alloy in a two-dimensional cavity, 100 mm wide and 60 mm high. The left wall of the cavity is cooled down whereas all the others walls are thermally insulated, as shown in Fig. 4.15. The thermophysical properties used to perform the simulation are reported in Appendix A.1.3. Only nucleation, equiaxed grain motion and equiaxed grain packing are described in this numerical exercise.

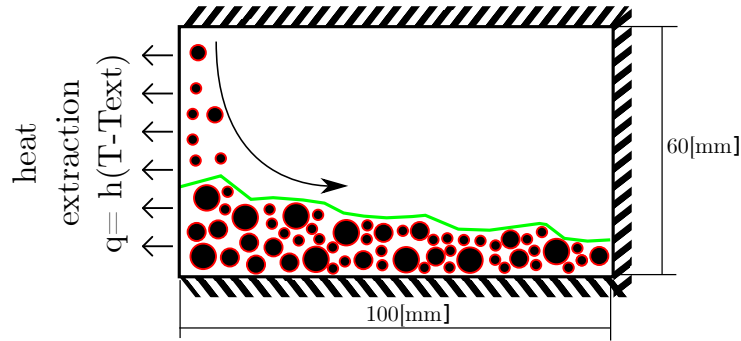


Figure 4.15 – Schematic of the solidification domain in the Hebditch and Hunt case. Chill heat transfer parameters: $h = 300 \text{ W}/(\text{m}^2\text{K})$ and $T_{ext} = 25 \text{ }^\circ\text{C}$. *macroS3D* only describes nucleation, equiaxed grain motion and equiaxed grain packing.

Besides validating the *macroS3D* implementation, the mesh size dependency and numerical scheme dependency are also investigated here. For that, the domain is discretized with rectangular shaped cells using three different mesh sizes: 80x60, 120x90 and 160x120 (*cells along the width x cells along the height*). For each mesh size the case was simulated using the *upwind* and *van Leer* interpolation schemes for all advection terms. In total, 6 numerical configurations were used to perform the simulations. All simulations also used a linear interpolation for both, diffusion terms and the α_t indicative function (with $\alpha = 100$). The time step was set to $\Delta t = 1 \times 10^{-3}\text{s}$, except for the cases whose mesh was 160x120, where the time step was set to $\Delta t = 4 \times 10^{-4}\text{s}$. As initial conditions, the temperature was adjusted to be uniform throughout the domain and equal to $T = 226 \text{ }^\circ\text{C}$ (0.43 $^\circ\text{C}$ above the *liquidus* temperature) and both, solid and liquid velocities, adjusted to be null. The nucleation undercooling, ΔT_{nucl} was considered to be zero. On the boundaries, a no-slip condition was used for the liquid intrinsic velocity while a slip condition for the solid intrinsic velocity. The packing criterion was set to $g_e^{block} = 0.3$ and only the two-phase globular model was used.

Figure 4.16 shows a comparison between the solutions obtained with SOLID[®], which is considered as reference, and *macroS3D* (*upwind* scheme). The comparison reports the liquid

intrinsic velocity, average solute concentration and solid fraction contours. The figure shows that with the onset of solidification, equiaxed grains nucleate near the chill. These grains sediment because their density is larger than that of the liquid, forming a consolidated bed of packed grains in the bottom of the domain. Simultaneously to the equiaxed grain growth, lead is rejected to the liquid, increasing its density. Particularly, in this case, thermal and solutal buoyancy effects act cooperatively since lead enriched liquid is heavier than the one at nominal composition. Due to the case configuration, an anticlockwise liquid circulation takes place in the fully liquid region. This is a direct consequence of the colder and enriched liquid located on the left boundary and of the equiaxed grains entraining the liquid. As solidification continues, a bed of packed grains begins to grow from the bottom in a tilted way due to the imposed packing fraction and to collisions between the grains. Through the bed of packed grains, solute enriched liquid flows towards the bottom. This flow produces such solute enrichment that grains begin to remelt and consequently a segregation channel is created in the bottom. Once all equiaxed grains are packed, the intradendritic liquid flow also creates a solute enriched zone near the top of the domain. The comparison reveals that **SOLID[®]** and *macroS3D* present a good agreement describing the macrosegregation pattern, the liquid velocity and the pile-up of equiaxed grains. The magnitude of the liquid thermosolutal convection and the velocity of equiaxed grains is in good correspondence as reported in the Tables 4.4 and 4.5. Nevertheless, the solutions are not exactly identical. It has been shown that due to the high non-linearity of solidification models, the solution is highly sensitive to spatial and time discretizations and to the selected numerical scheme [4].

Table 4.4 – Maximum liquid intrinsic velocity for different instants. In the cases name, the letter denotes *Upwind* or *Van Leer* interpolation schemes whereas the number the mesh size.

Case	t = 150 s	t = 200 s	t = 350 s
SOLID[®]	12.6213	11.1436	11.8157
U80x60	11.6359	10.1904	10.1904
U120x90	10.5546	10.0116	9.56236
U160x120	13.8169	14.2769	10.4557
V80x60	12.0913	12.2471	11.2533
V120x90	10.6883	10.3092	8.82196
V160x120	20.4775	14.9538	8.53169

Table 4.5 – Maximum solid intrinsic velocity for different instants. In the cases name, the letter denotes *Upwind* or *Van Leer* interpolation schemes whereas the number the mesh size.

Case	t = 150 s	t = 200 s	t = 350 s
SOLID[®]	15.1725	13.3923	11.7294
U80x60	21.0481	17.083	9.41262
U120x90	15.2353	15.2926	11.6865
U160x120	14.637	19.1106	11.4546
V80x60	17.8599	16.0879	13.3588
V120x90	15.6598	14.1216	12.1698
V160x120	22.2441	14.9436	8.7193

Continuing with the comparison, Fig. 4.17 presents the equiaxed grains density at the end of solidification for the different cases performed with *macroS3D* and the solution given by SOLID[®]. The figure shows a good agreement between the cases that use both meshes, 80x60 and 120x90. Moreover, these solutions are in correspondence to the solution given by SOLID[®]. However, for the cases performed with a 160x120 mesh, the grain density pattern is completely different. These numerical simulations were performed with a smaller time step with respect to the others. One of the possible source of discrepancies is the nuclei re-injection methodology. The nuclei re-injection in *macroS3D* takes place when different criteria are met. When using a smaller time step, more times it is checked if the criteria are met, so that, more nuclei re-injection events are likely to occur. This effect is observable for both interpolation schemes, *upwind* and *van Leer*, however with a more drastical effect when a *van Leer* scheme is used. This last observation requires to be confirmed performing more simulations with different numerical configurations. This task is away from the scope of this thesis.

In order to improve the understanding of the effect of the spatial discretization (mesh size) and the interpolation scheme for advection on the macrosegregation pattern, Fig. 4.18 presents a comparison between the two investigated interpolation schemes – *upwind* and *Van Leer*. From the figure it is noted that all numerical configurations depicts the solute enriched channel in the bottom of the domain. Moreover, the *upwind* scheme also depicts a secondary enriched zone near the top. The macrosegregation pattern given by the *upwind* scheme seems to converge to a single solution as the spatial discretization is smaller. Regarding the *van Leer* scheme, the position and intensity of the secondary enriched zone seems unclear. When the amount of mesh is increased, the segregation pattern notably changes. This effect can be explained since the *van Leer* interpolation depends on the gradients of the field in which it is operating, such that, the solution is better described near shocks or discontinuities. As the amount of mesh increases, discontinuities are better described and thus, the *van Leer* interpolation operates differently.

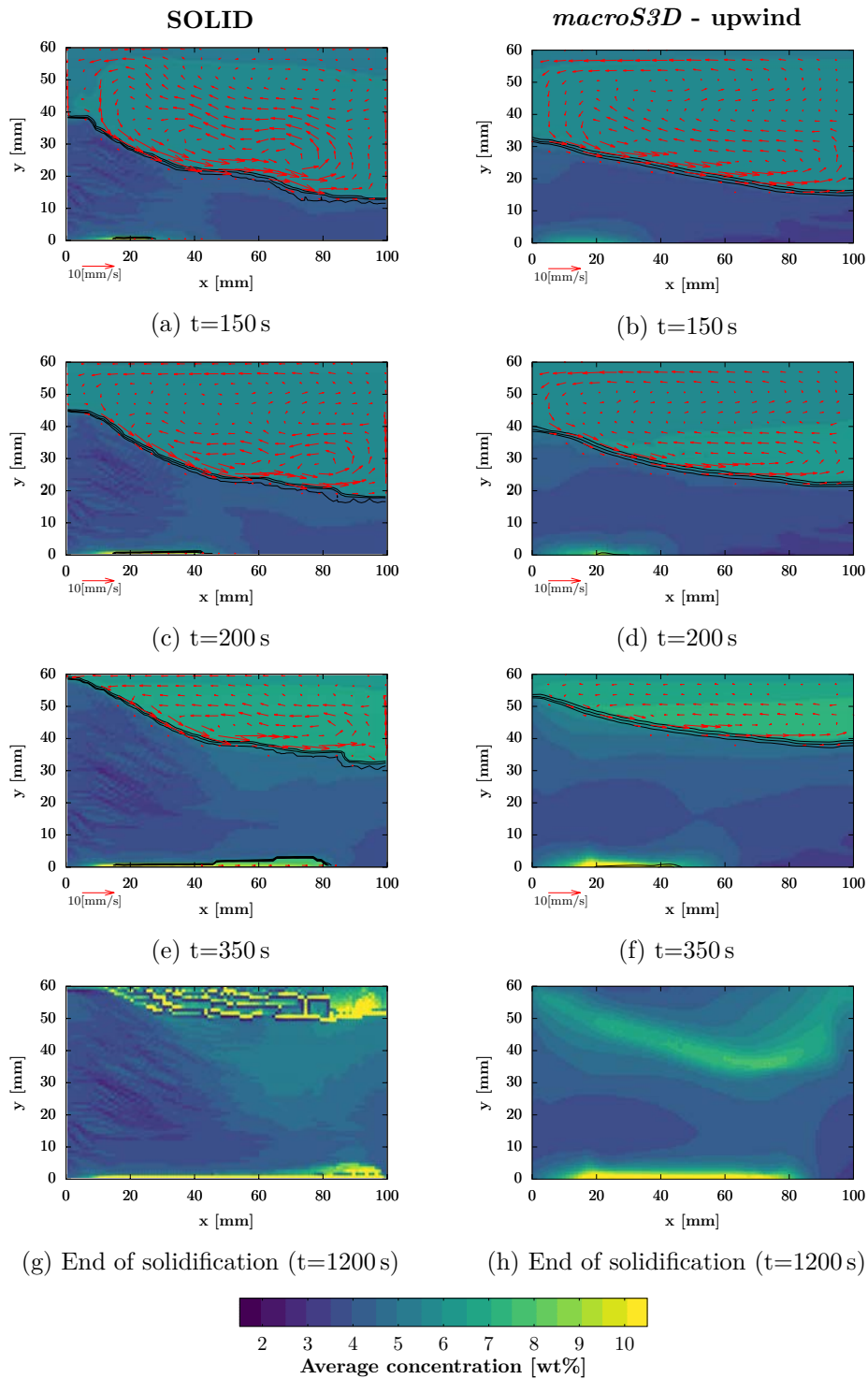


Figure 4.16 – Comparison between the solutions given by **SOLID**[®] and **macroS3D** (*upwind*, mesh 80x60) at various instants for the average solute concentration (color map), liquid intrinsic velocity (vectors) and formation of the bed of packed grains (black contours for solid fraction equals to 0.1, 0.2 and 0.3).

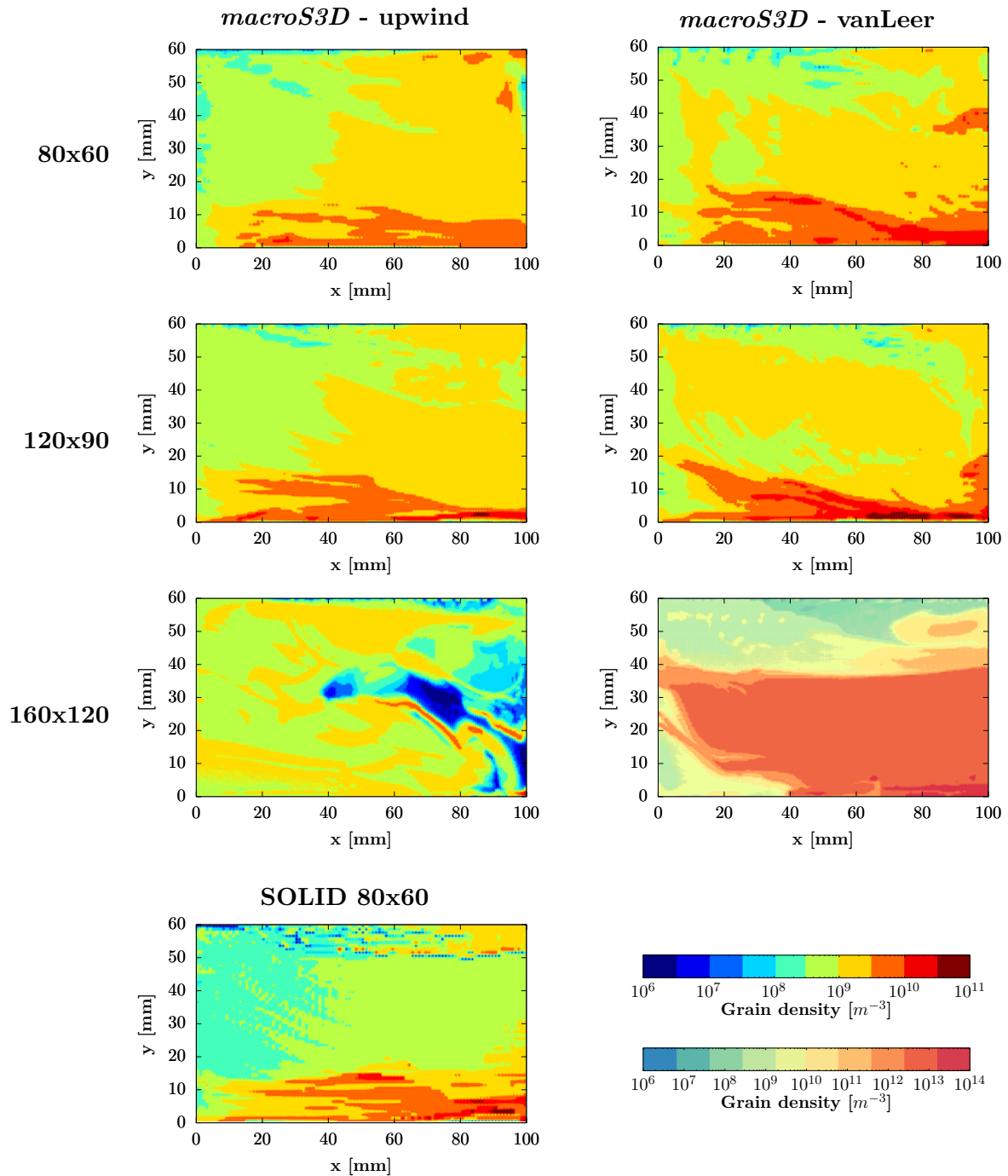


Figure 4.17 – Comparison between the solutions given by *SOLID*[®] and *macroS3D* for the equiaxed grain density (color map) at the end of solidification. Note the different color scales in case V160x120.

Since the model is highly non-linear, each mesh size will lead to a different solution, that is, a different prediction of solidification pattern.

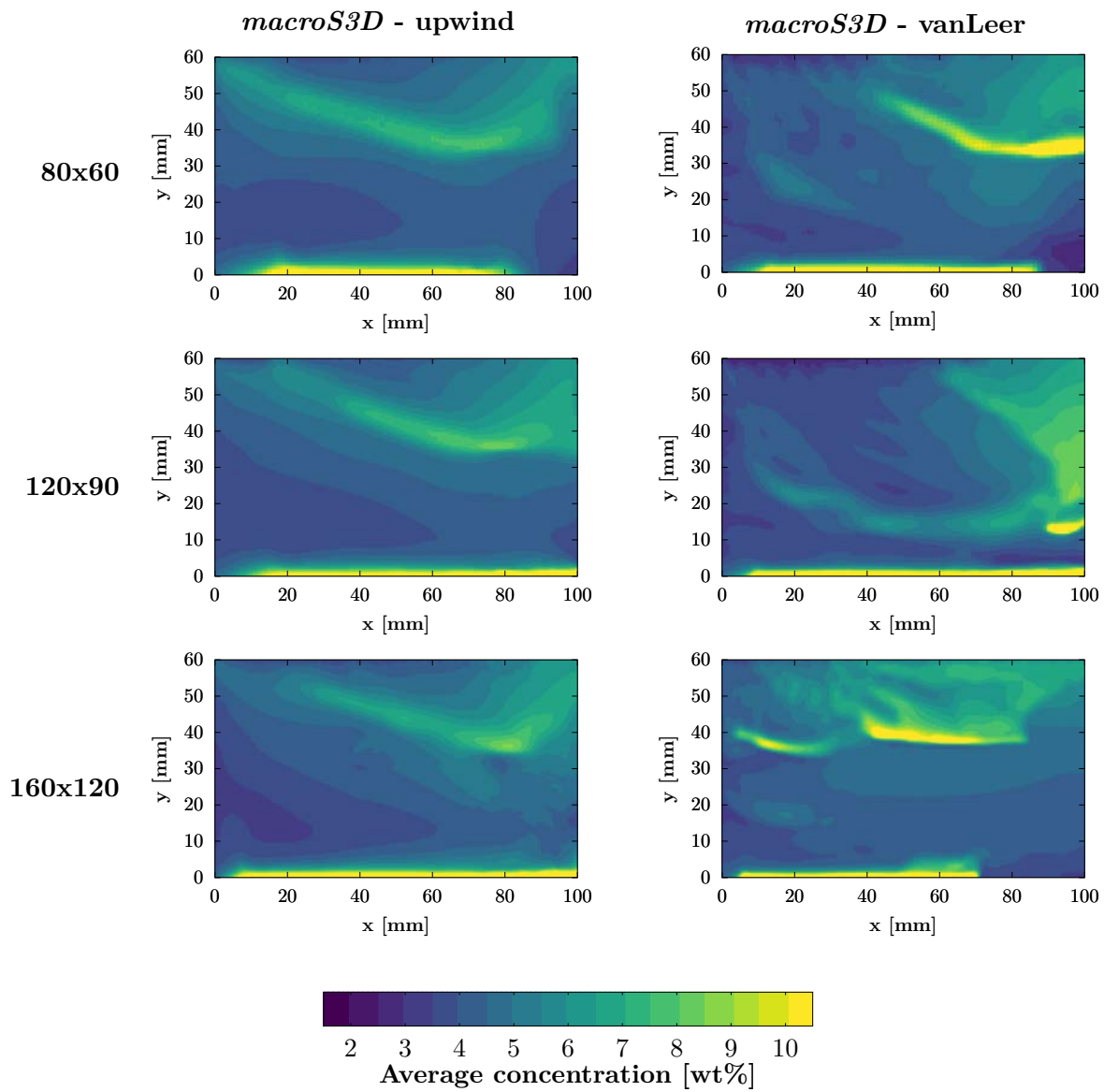


Figure 4.18 – Comparison between the solutions given by *macroS3D* for the macrosegregation pattern (color map) at the end of solidification using different mesh sizes and different numerical schemes.

4.4 Simulations of the GRADECET experiments

The new developments carried out in *macroS3D* enabled the numerical simulation of the GRADECET experiments considering grain growth kinetics and equiaxed grain movement. Recall that these experiments consisted of the directional solidification under centrifugal conditions of cylindrical TiAl samples. In this chapter, only the cases solidified under normal terrestrial gravity and an apparent gravity of $\vec{g}_{tot} = 5g$ (Case 1G and Case 5G in Chapt. 3, respectively) were simulated. The other levels of centrifugation were not considered due to the high cost of computing time and time limitations. A simulation takes about one month to be completed if equiaxed grain motion, a limited diffusion grain growth kinetics model and centrifugation (5g) is accounted for. Moreover, considering only two cases enabled the study of the influence of other process parameters, such as the grain packing fraction, g_e^{block} , and the nuclei density in the equiaxed region, which will be presented later.

The setup of the new numerical simulations was similar to the cases already presented in Chapt. 3. The boundary and initial conditions were identical. With respect to the solid intrinsic velocity, a slip condition was assumed in all the boundaries and a null velocity was imposed as initial condition (at $t = 0$). The geometry and mesh structuring were similar. Only the number of cells that constitute the mesh was changed to 1×10^5 in order to reduce the computing cost (200 cells along the cylinder length and 22.4 cells, in average, along the cylinder diameter). With this number of cells, the mesh presented a maximum non-orthogonality angle of 31.29° and a maximum skewness of 0.52, that is, the new mesh presented a good quality.

In order to represent the CET that takes place during solidification, the domain was separated in two different regions as shown in Fig. 4.19. The first region, $z \leq z_{CET}$, was adjusted to only present columnar growth, whereas the second region, $z > z_{CET}$, was adjusted to only present equiaxial growth. In the columnar region, the grains were allowed to grow but not to move. On the other hand, in the equiaxial region the grains were allowed to grow and to move. This two region configuration was achieved by imposing the porous flow regime throughout the columnar region and the slurry flow regime throughout the equiaxed region. The porous flow regime was also triggered in the equiaxed region where the predefined packing, g_e^{block} , limit was reached.

To define the length of the columnar region, the distance between the melting front and the CET was considered to be $\Delta z_{col} = 16.5$ mm, as reported by Reilly [1] for the case where $\vec{g}_{tot} = 5g$ (see Fig. 4.1). The position of the melting front in the numerical setup was adjusted to $z_{mel} = 18.34$ mm at $t = 0$. With this, the position of the CET was approximated as $z_{CET} = z_{mel} + \Delta z_{col} \sim 35$ mm

At $t = 0$, the density of nuclei was adjusted to be $N = 10^{11} \text{m}^{-3}$ in the columnar region, whereas two numerical configurations for the nuclei density in the equiaxed region were studied: $N = 10^9 \text{m}^{-3}$ and $N = 10^{11} \text{m}^{-3}$. The furnace thermal protocol imposes a second solidification front at around $t = 460$ s moving from the “hot” end of the sample parallel to the apparent gravity vector (see Fig. 3.13). In the model this leads to equiaxed grain nucleation in the “hot” end of the sample. According the experimental observations, the main source of nuclei are grain fragments from the columnar region [1], and therefore equiaxed grain nucleation in the “hot”

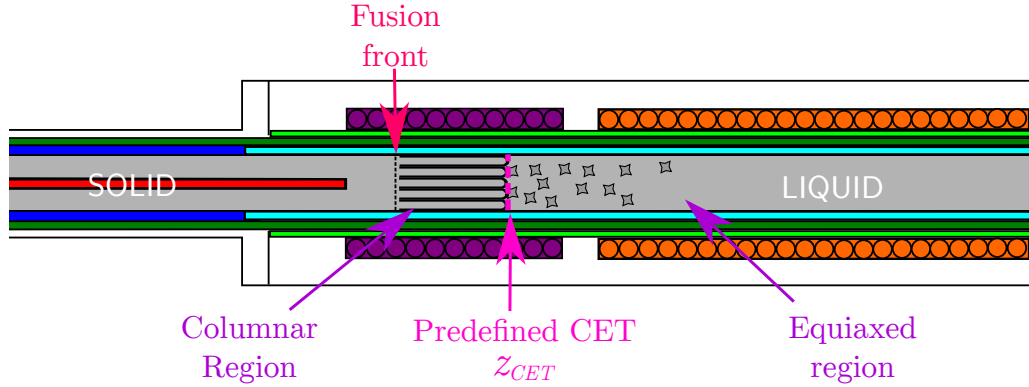


Figure 4.19 – Schematic of the columnar and equiaxed regions considered in the simulations. The predefined CET was adjusted to $z_{CET} = 35$ mm. The TiAl sample is shown in gray. The heaters are shown in purple and orange.

end of the sample, far from the columnar front, is not completely realistic. To avoid non physical response from the model, the equiaxed grain nucleation was not allowed for $z > 100$ mm. In addition to the nuclei configuration, two numerical configurations for the predefined equiaxed grains packing limit were also studied: $g_e^{block} = 0.1$ and $g_e^{block} = 0.3$. In total, eight different numerical configurations were simulated as reported in Table 4.6. All the numerical simulations were carried out using the interpolation scheme *upwind* for the advective terms and a linear interpolation scheme for the diffusion terms. A *downwind with respect to $\langle \vec{v}_s \rangle^s$* interpolation scheme was used for the slurry/porous indicative function α_t , with $\alpha = 10^4$. These parameters produce a sharp slurry/porous transition and they avoid phase accumulation issues near the packing front, as discussed in Sect. 4.1.5. For the discretization of the temporal terms, an implicit Euler scheme was used. The time step was set to $\Delta t = 10^{-3}$ s for the cases with normal terrestrial gravity, *i.e.* $\vec{g}_{tot} = 1g$, and to $\Delta t = 10^{-4}$ s for the cases in which $\vec{g}_{tot} = 5g$. All the simulations were performed using a two-phase globular model. Each simulation was performed using parallel computing over 32 cores, taking approximately 30 days to be finish for the cases in which $\vec{g}_{tot} = 5g$ and 4 days for the cases under terrestrial gravity. The thermophysical parameters used to perform these simulations are reported in Table 4.7.

Although the microstructure of the Case 1G did not present an equiaxed region, in this section it is considered that there is one. This assumption enables the study of the effect of centrifugation on the equiaxed grain motion by comparing the Case 1G to the Case 5G under the same numerical configuration.

4.4.1 Results and discussion

4.4.1.1 Liquid flow in the columnar region: comparison between the cases G1P3N9 and G5P3N9

Figures 4.20 and 4.21 present the liquid flow along with the liquid fraction for the cases G1P3N9 and G5P3N9 in the columnar region, respectively. These cases were chosen arbitrarily because the grain density in the columnar region is identical in all cases, and therefore, only the level of

Table 4.6 – Numerical configuration for the cases simulated considering grain growth kinetics and equiaxed grain movement. Note that the case name is related to the gravity level, packing fraction and nuclei density in the equiaxed region.

Case name	Gravity level	Packing fraction	Nuclei in equiaxed region
	G	P	N
	g_{tot}	g_e^{block}	$N[\text{m}^{-3}]$
G1P1N9	1g	0.1	10^9
G1P1N11	1g	0.1	10^{11}
G1P3N9	1g	0.3	10^9
G1P3N11	1g	0.3	10^{11}
G5P1N9	5g	0.1	10^9
G5P1N11	5g	0.1	10^{11}
G5P3N9	5g	0.3	10^9
G5P3N11	5g	0.3	10^{11}

apparent gravity plays a differentiating role between the cases. As it was previously analysed in Sect. 3.3.1, the cylinder center is colder than the cylinder sides along the cylinder at the beginning of solidification. Given this radial difference of temperature, the solidification starts first in the cylinder center rather than the cylinder sides (see temperature contours in Figs. 4.20 and 4.21). This triggers an aluminum enrichment and a density decrease in the liquid of the mushy zone, in the cylinder center.

For the case G1P3N9, the flow pattern is similar to the one described in Sect. 3.3.2.1 for the Case 1G, where the aluminum enriched liquid flows antiparallel to the apparent gravity in the cylinder center and parallel in the cylinder sides due to buoyancy forces. This current of solute enriched liquid in the cylinder center is deflected to the cylinder sides by the liquid flow in the fully liquid region before arriving to the fully liquid region, which means that solute enriched liquid does not escape from the mushy zone during the columnar growth. The liquid in the fully liquid region is parallel to the apparent gravity in the cylinder center and antiparallel in the cylinder sides. This flow pattern was previously described (Sect. 3.3.2.1) as a ring of three dimensional toroidal circulation.

In the case G5P3N9, the liquid pattern is similar to the case G1P3N9, however, solute enriched liquid is able to escape from the mushy zone with this level of apparent gravity. The interdendritic flow of solute enriched liquid, which is towards the fully liquid region, creates regions with a high liquid fraction in the cylinder center (see Fig. 4.21). In spite of this flow, segregation channels do not appear in the mushy zone with this level of apparent gravity. Liquid enters the mushy zone mainly by the cylinder sides to compensate the liquid that escapes from

Table 4.7 – Thermophysical properties used in the simulations considering grain growth kinetics and equiaxed grain movement

Property	Symbol	Units	Value
Nominal aluminum concentration	C_0	[wt%]	32.96
Partition coefficient	k_p	[–]	0.885
Melting point of the pure substance	T_f	[°C]	1975.66
Liquidus slope	m_l	[K/wt%]	-14.089
Pseudo-peritectic concentration	C_{inv}	[wt%]	35.2
Diffusion coefficient in liquid	D_l	[m ² /s]	3.0×10^{-9}
Diffusion coefficient in solid	D_s	[m ² /s]	1.0×10^{-11}
Reference density	ρ	[kg/m ³]	3877.8
Kinematic viscosity	ν_l	[m ² /s]	1.65×10^{-6}
Thermal conductivity in the liquid phase	k_l	[W/mK]	16.22
Thermal conductivity in the solid phase	k_s	[W/mK]	26.37
Solutal expansion coeff.	β_C	[wt% ⁻¹]	8.465×10^{-3}
Thermal expansion coeff.	β_T	[°C ⁻¹]	1.1785×10^{-4}
Latent heat	L_f	[J/kg]	3.62×10^5
Specific heat capacity	c_p	[J/(kgK)]	1100
Characteristic length for permeability	λ_2	[m]	6.50×10^{-5}
Initial volume of a equiaxed grain	V_0	[m]	5.24×10^{-9}
Nucleation undercooling	ΔT_{nucl}	[K]	1×10^{-3}

the mushy zone. The liquid is also able to enter the mushy zone by the cylinder center (*e.g.* see Fig. 4.21). This effect is a consequence of the instabilities created near the columnar front. The radial inversion of the temperature gradient does not play an important role determining flow features in the columnar region in both cases, G1P3N9 and G5P3N9, since the columnar front arrives to the predefined CET position, z_{CET} at $t = 305$ s, approximately. At this moment the radial inversion of temperature gradient is located at $z \sim 43$ mm. At $t = 485$ s, when the sample is quenched, the columnar region is not fully solid, as shown in Fig. 4.22 for case G1P3N9.

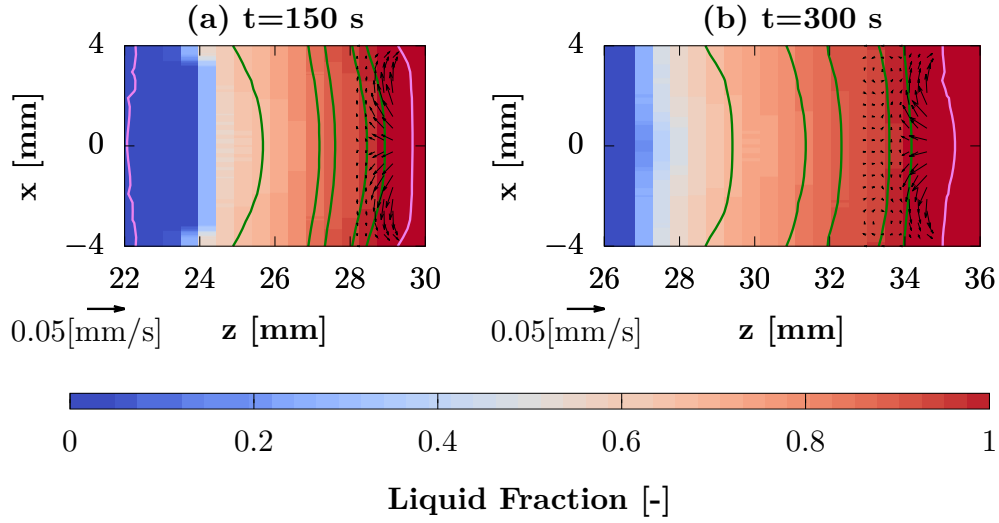


Figure 4.20 – Liquid velocity and liquid fraction in the main plane of study inside the columnar region for the case G1P3N9. Violet contours delimit the mushy zone. Temperature contours are in green for 1490, 1500, 1503, 1508, 1510 °C.

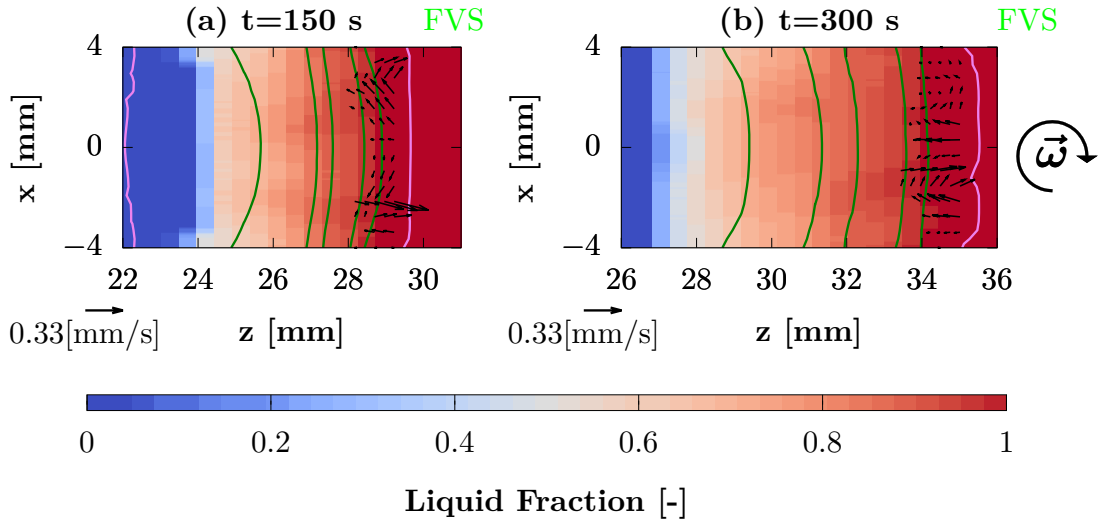


Figure 4.21 – Liquid velocity and liquid fraction in the main plane of study inside the columnar region for the case G5P3N9. Violet contours delimit the mushy zone. Temperature contours are in green for 1490, 1500, 1503, 1508, 1510 °C.

4.4.1.2 Liquid flow in the equiaxed region

Figures 4.22 and 4.24 present the liquid flow pattern in the equiaxed region along with the liquid fraction over time in the main plane of study for the cases G1P3N9 and G5P3N9, respectively. As it was previously explained, when $\vec{g}_{tot} = 1g$, solute enriched liquid is not able to escape from the mushy zone during the columnar growth and thus, the liquid convection in the equiaxed region is driven by thermal buoyancy forces. Indeed, in the case G1P3N9 (without centrifugation, see Fig. 4.22), at $t = 50$ s, the liquid flows parallel to the apparent gravity in the cylinder center and

antiparallel in the cylinder sides. This flow pattern is a consequence of the instantaneous radial temperature distribution: the cylinder center is colder than the cylinder sides. At $t = 250$ s, the inversion of radial temperature gradient takes place at $z \sim 50$ mm. For $z \gtrsim 50$ mm the liquid flows antiparallel to the apparent gravity in the cylinder center and parallel in the cylinder sides. Note that to this instant, only columnar growth has taken place. At $t = 400$ s, equiaxed grains appear in the domain for $z < 50$ mm, approximately. In the presence of equiaxed grains, the liquid flow is affected by three simultaneous processes: (1) the buoyancy effect driven by the solute and temperature radial distribution, (2) the settling of equiaxed grains (see Fig. 4.28), and (3) the expulsion of liquid from the packing front due to the packing of equiaxed grains. Regarding the buoyancy effect in the slurry zone (the zone populated by equiaxed grains), the inversion of the radial temperature gradient takes place at $z \sim 46$ mm, driving to a flow parallel to the apparent gravity in the cylinder center and antiparallel in the cylinder sides. This flow pattern is reinforced by the settling of equiaxed grains which entrains the liquid in the cylinder center. This effect notably increases the magnitude of the liquid velocity (note the different scale vectors in Fig. 4.22). The cylinder center is a preferential zone for the settling of equiaxed grains since the no-slip condition imposed to the liquid as boundary condition increases the drag on the settling equiaxed grains in the cylinder sides. At $t = 450$ s, a packed equiaxed region takes place in equiaxed region due to the settling of equiaxed grains, as shown in Fig. 4.23. The equiaxed grains continue to grow in the packed equiaxed region, enriching locally the interdendritic liquid. This leads to a density decrease in the intradendritic liquid of the packed region. Due to solutal buoyancy effects, this liquid tends to flow antiparallel to the apparent gravity. Indeed, part of this enriched liquid escapes from the packed region by the cylinder sides (see Fig. 4.23). This current of enriched liquid drives a flow pattern in the slurry region that is antiparallel to the apparent gravity in the cylinder sides and parallel in the cylinder center. At $t = 485$ s the inversion of radial temperature gradient takes place at $z \sim 49$ mm *i.e.* for $z < 49$ mm the cylinder center is colder than the cylinder sides. This means that from a thermal point of view, the liquid should flow parallel to the apparent gravity in the cylinder center and antiparallel in the cylinder sides, for $z < 49$ mm. However, the liquid flows antiparallel to the apparent gravity in the cylinder sides up to $z \sim 80$ mm due to solutal buoyancy effects triggered by the enriched liquid that escapes from the packed equiaxed region. Moreover, the magnitude of the liquid convection greatly increases over time, during the equiaxed growth. This is due to two simultaneous processes that occur as the cooling rate increases. The first is related to the faster aluminum rejection from the growing solid in the packed region. This leads to a stronger current of aluminum enriched liquid escaping from the packed region by the cylinder sides. The second process is related to a faster equiaxed grain growth rate in the slurry region as the cooling rate increases. This leads to a stronger liquid entrainment by the equiaxed grains as they settle. The cooling rate is controlled by the furnace thermal protocol.

In the case G5P3N9, at $t = 50$ s and $t = 200$ s aluminum enriched liquid escapes from the mushy zone during the columnar growth. This liquid is lighter than the one at nominal composition, so that, it flows antiparallel to the apparent gravity. The Coriolis acceleration pushes this current of enriched liquid towards the flight velocity side of the sample, creating the

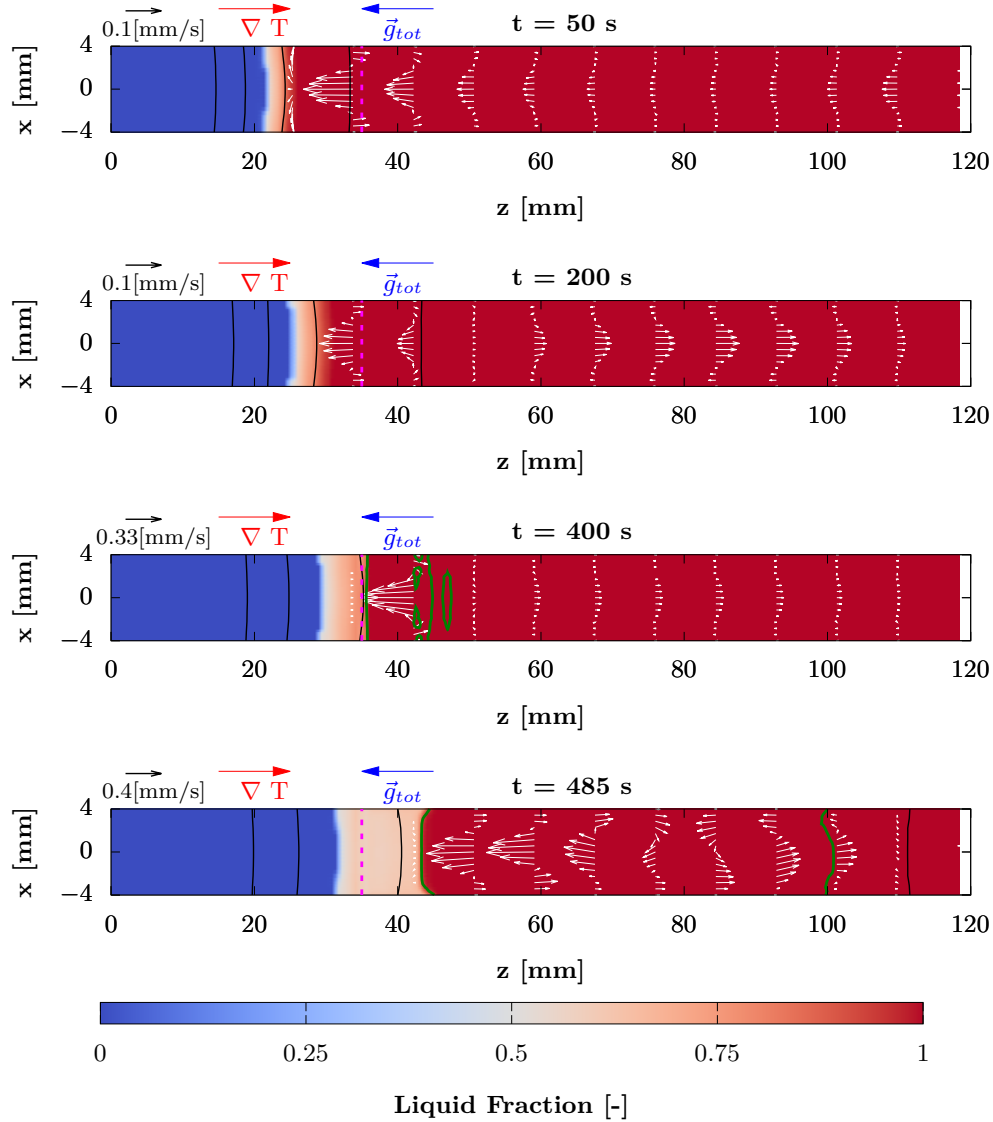


Figure 4.22 – Evolution of the liquid velocity pattern in the main plane of study in the equiaxed region for the case G1P3N9. Temperature contours in black: 1400,1450,1500 and 1550 °C. Violet dashed line delimits the columnar region. The green contours delimit the slurry region.

one-vortex fluid flow pattern that has been already described and analysed in Sect. 3.3.2.2. At $t = 400$ s and $t = 485$ s although equiaxed grains appear in the domain, the structure of the one-vortex liquid flow pattern does not change. This is mainly for two reasons. The first one is because aluminum enriched liquid escapes from the packed equiaxed region. This aluminum enriched current flows antiparallel to the apparent gravity, from the packed region to the slurry region, hence, it is deflected towards the flight velocity side, reinforcing the one-vortex fluid flow pattern. This process is very similar to what happens during columnar growth. The second reason is because the inertia or drag are relatively small compared to the Coriolis acceleration.

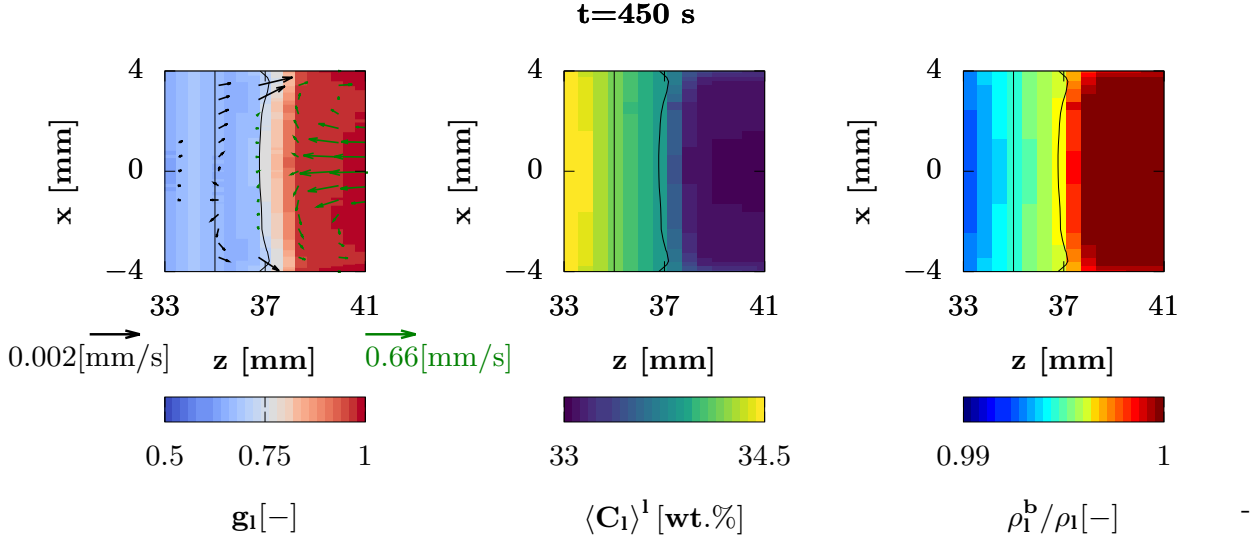


Figure 4.23 – Liquid intrinsic velocity and different fields in the packed equiaxed region for the case G1P3N9 at $t = 450$ s. Lines in black limit the packed equiaxed region. From left to right: liquid fraction, averaged solute concentration in liquid and buoyancy liquid density ($\frac{\rho_l^b}{\rho_l} = 1 - \beta_T (T - T_{ref}) - \beta_C (\langle C_l \rangle^l - C_{ref})$).

This can be demonstrated performing a scaling analysis. The Rossby number, $Ro = \frac{U_{ref}}{2\omega L_{ref}}$, is defined as the ratio between the inertia and the Coriolis accelerations. Here, the reference velocity, $U_{ref} = 4.57 \text{ mm} \cdot \text{s}^{-1}$, is considered to be the maximum liquid velocity at $t = 450$ s in the main plane of study. The centrifuge angular velocity is $\omega = 3.466 \text{ rad} \cdot \text{s}^{-1}$ and the characteristic length $L_{ref} \sim 100 \text{ mm}$ which corresponds to the length of the equiaxed region approximately. With this set of values, the Rossby number is equal to $Ro = 1.65 \times 10^{-3} \ll 1$, that is, the Coriolis acceleration plays a more important role than inertial accelerations on determining the fluid flow features. This was already concluded in the Sect. 3.3.2.2.

Following, a scaling analysis to compare the drag to the Coriolis accelerations is proposed. Consider the drag term of the momentum equation for the liquid (Eqn. 4.6):

$$K_d^s (\langle \vec{v}_l \rangle^l - \langle \vec{v}_s \rangle^s) = \frac{3g_e \rho_l C_d}{4d_g} U_{rel} (\langle \vec{v}_l \rangle^l - \langle \vec{v}_s \rangle^s) \quad (4.65)$$

where $U_{rel} = |\langle \vec{v}_l \rangle^l - \langle \vec{v}_s \rangle^s|$ is the magnitude of the relative velocity between the phases. This velocity is considered to be $U_{rel} \sim 12 \text{ mm}$, which corresponds to the maximum relative velocity in the slurry region at $t = 450$ s. In addition, the average solid fraction at this instant is $g_s = 1.4 \times 10^{-3}$ and the average grain diameter $d_g = 2.61 \times 10^{-4} \text{ m}$ in the slurry region of the main plane of study. With these values, the drag coefficient can be calculated as proposed by Ni and Beckermann [60] (from Eqn. 4.9 to Eqn. 4.13):

$$C_d = \frac{48C_{ke}g_s}{Re} + Cie = 13.627 \quad (4.66)$$

As the value of the solid fraction is small, $g_s \rightarrow 0$, the drag coefficient obtained here is similar to the obtained through the Stokes law, $C_d^{Stokes} = \frac{24\nu_l}{U_{rel}d_g} = 11.02$. Thus, considering that the radial component of the velocities is of the order of millimeters per second, the order of magnitude of the drag force can be estimated with Eqn. 4.65 as $2004 \left(\langle \vec{v}_l \rangle^l - \langle \vec{v}_s \rangle^s \right) \sim 2 \text{ kg}/(\text{m}^2\text{s}^2)$ for this set of values. On the other hand, the term of the Coriolis acceleration in the liquid momentum equation (Eqn. 4.6) is $2g_l\rho_l\vec{\omega} \times \langle \vec{v}_l \rangle^l$. Considering the maximum magnitude of the liquid velocity in the main plane of study at $t = 450 \text{ s}$, $\langle \vec{v}_l \rangle^l \sim 4.57 \text{ mm} \cdot \text{s}^{-1}$, the Coriolis term can be approximated as $114.85 \text{ kg}/(\text{m}^2\text{s}^2)$ for the same set of values as for the drag term. Comparing the two values shows the large influence that has the Coriolis acceleration on the radial direction of the liquid convection in comparison to other forces such as drag. All the cases with centrifugation presented the one-vortex fluid flow structure in the slurry region, which is in agreement to the scaling analysis.

4.4.1.3 Equiaxed grain motion in the equiaxed region

Before discussing the simulations results, a simplified analysis about the forces exerted on a single globulitic equiaxed grain is proposed. Firstly, consider a solidification case under normal terrestrial gravity conditions. Neglecting the forces related to grain collision, the main forces that drive the grain movement are the drag force, \vec{F}_{drag} , and the apparent weight, \vec{F}_{bp} (Principle of Archimedes), as schematized in Fig. 4.25a. The solid velocity, \vec{v}_s is assumed to be parallel to the apparent gravity and the liquid velocity, \vec{v}_l , to be antiparallel. The drag force is equivalent to $\vec{F}_{drag} = \frac{1}{2}C_d\rho_l U_{rel}(\vec{v}_l - \vec{v}_s)$, whereas, the apparent weight is equivalent to $\vec{F}_{bp} = \frac{4}{3}\pi \left(\frac{d_g}{2}\right)^3 (\rho_s^{ref} - \rho_l^b) \vec{g}_{tot}$. Assuming that only axial grain movement is produced, *i.e.* only along the cylinder, the force balance on the globulitic grain is given by:

$$\frac{4}{3}\pi \left(\frac{d_g}{2}\right)^3 \rho_s (2\vec{\omega} \times \vec{v}_s) + \frac{1}{2}C_d\rho_l U_{rel}(\vec{v}_l - \vec{v}_s) - \frac{4}{3}\pi \left(\frac{d_g}{2}\right)^3 (\rho_s^{ref} - \rho_l^b) \vec{g}_{tot} = m_p \vec{a}_p \quad (4.67)$$

Where m_p and a_p are the mass and the acceleration of the equiaxed grain, respectively. With Eqn. 4.67 is possible to estimate the solid velocity of an equiaxed grain of diameter d_g . For that, it is required to know the liquid velocity that surrounds the equiaxed grains and the drag coefficient. Figure 4.26 presents a comparison between the drag model of Ni and Beckermann [60], which is used in *macroS3D*, and the Stokes law, $C_d^{Stokes} = \frac{24\nu_l}{d_g U_{rel}}$. As Fig. 4.26 shows, the model of Ni and Beckermann [60] approaches to the Stokes law when the solid fraction approaches to zero. Given the low solid fraction in the slurry region of the studied cases ($g_s \sim 0.02$), the analysis will continue assuming the Stokes law, for sake of simplicity. Furthermore, the acceleration a_p will be considered null since the momentum response time $\tau_V = \frac{\rho_s d_g^2}{18\nu_l \rho_l}$ is of the order of $\tau_V \sim 10^{-4} \text{ s}$ for a grain diameter of $d_g = 0.5 \text{ mm}$. This means that the drag force balances the apparent weight almost instantaneously. Thus, the axial velocity of a grain is given by:

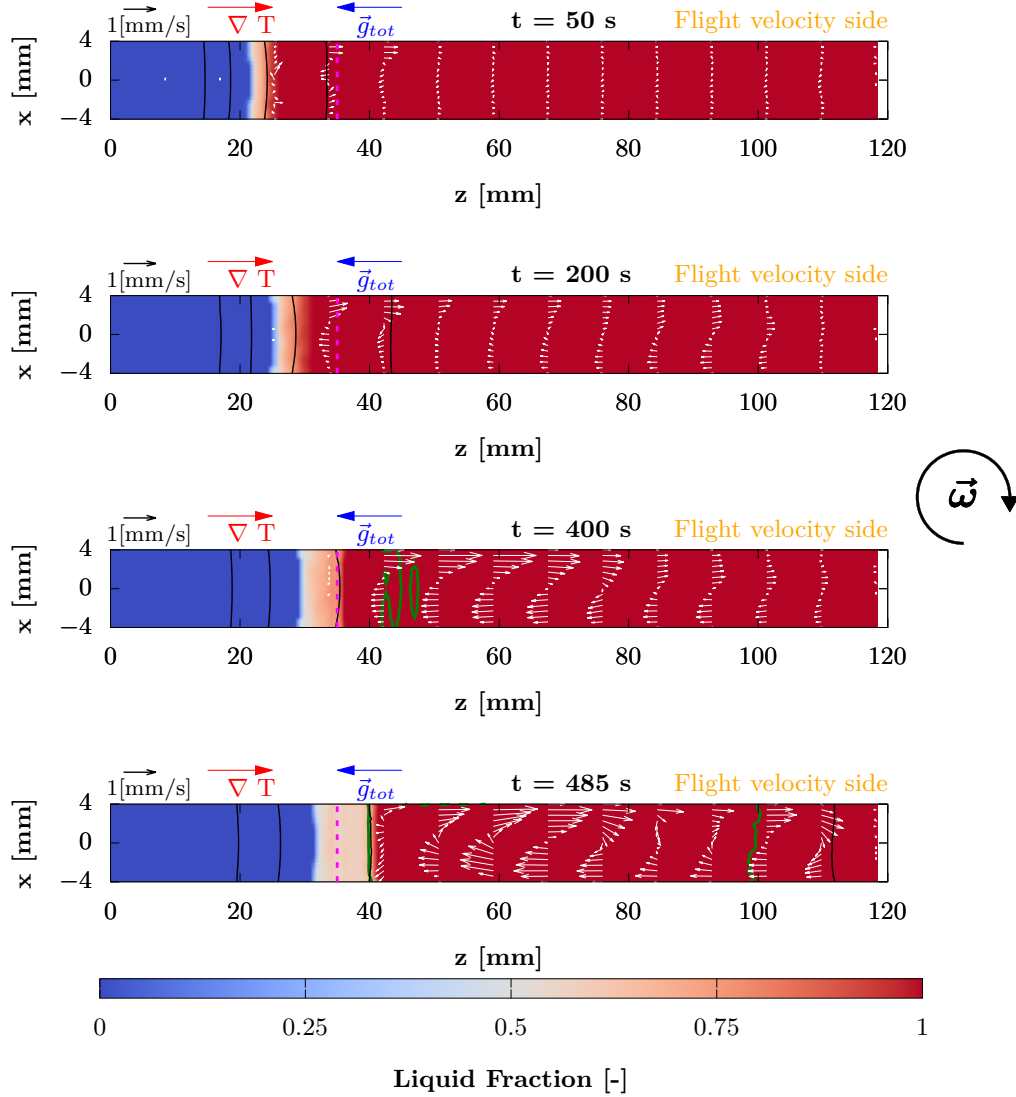


Figure 4.24 – Evolution of the liquid velocity pattern in the main plane of study in the equiaxed region for the case G5P3N9. Temperature contours in black: 1400,1450,1500 and 1550 °C. Violet dashed is the predefined CET position. The green contours delimit the slurry region.

$$\vec{v}_s^{axial} = -\frac{\vec{g}_{tot} d_g^2 (\rho_s^{ref} - \rho_l)}{18\nu_l \rho_l} + \vec{v}_l^{axial} \quad (4.68)$$

In Eqn. 4.68, the velocities are defined positive when they are antiparallel to the apparent gravity \vec{g}_{tot} .

Under centrifugal conditions, in addition to the drag force and the apparent weight, the Coriolis force is also exerted to the equiaxed grains, as is schematized in Fig. 4.25b. In the axial direction, the analysis performed before, where the drag force is balance to the apparent weight,



Figure 4.25 – Schematic of the forces exerted on a globulitic equiaxed grain. (a) Case under normal terrestrial gravity. (b) Case with centrifugation.

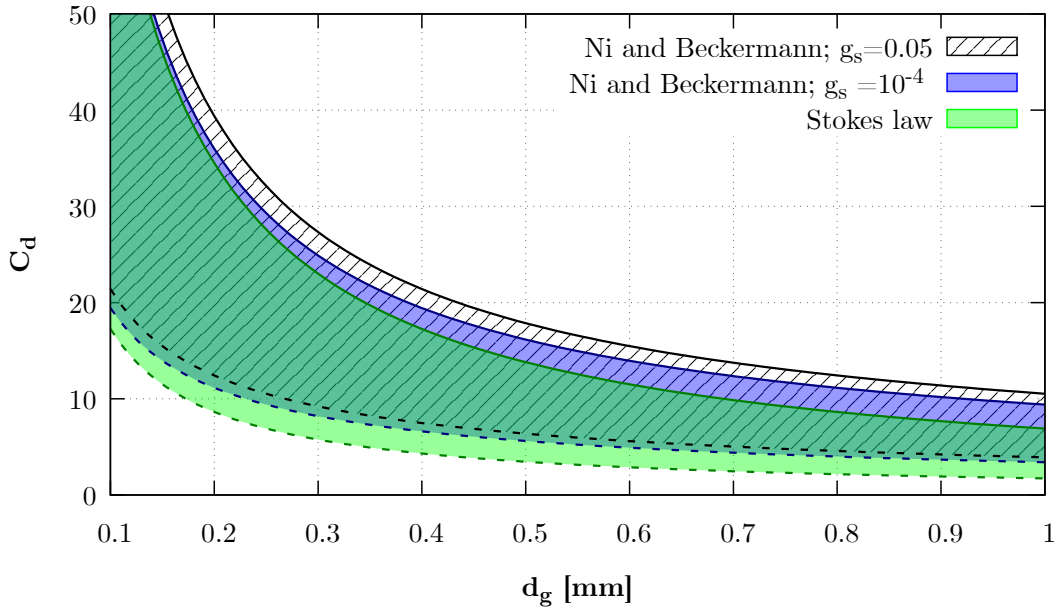


Figure 4.26 – Drag coefficient, C_d , vs grain diameter, d_g , between $U_{rel} = 20 \text{ mm} \cdot \text{s}^{-1}$ (dashed lines) and $U_{rel} = 5 \text{ mm} \cdot \text{s}^{-1}$ (solid lines). Green region corresponds to Stokes flow. Blue and black-dashed regions correspond to Ni and Beckermann [60] for $g_s = 10^{-4}$ and $g_s = 0.05$, respectively.

remains (Eqn. 4.68). However, in the radial direction, the Coriolis force is balanced to the drag force, such that the radial component of the solid velocity is given by:

$$\vec{v}_s^{radial} = \frac{4\omega g_{tot} d_g^4 \rho_s (\rho_s - \rho_l)}{18 (\nu_l \rho_l)^2} - \frac{2\omega \vec{v}_l^{axial} d_g^2 \rho_s}{18 \nu_l \rho_l} + \vec{v}_l^{radial} \quad (4.69)$$

Note that a Stokes flow regime was assumed in Eqn. 4.68 and Eqn. 4.69, thus, they do not describe the exact same model used in this work, but they describe the drag effect in a simplified manner. With Eqn. 4.69 it is possible to estimate the radial component of the velocity of the

equiaxed grains knowing the velocity of the liquid, \vec{v}_l . For that, consider a characteristic grain diameter in the study cases, $d_g \sim 5 \times 10^{-4} \text{m}$, and a null liquid velocity. Assuming the case in which $\vec{g}_{tot} = 5g$, the axial component of the solid velocity is $\vec{v}_s^{axial} = 26 \text{mm} \cdot \text{s}^{-1}$ and the radial component is $\vec{v}_s^{radial} = 1.8 \text{mm} \cdot \text{s}^{-1}$. This shows that the radial component of the solid velocity is very small in comparison to the axial component for the given parameters. Therefore, it is possible to conclude that the Coriolis force does not play a major role in the movement of equiaxed grains for the conditions given in the slurry region of the study cases.

In order to make this analysis independent of process parameters, a dimensionless number that relates the characteristic time of drag response and the characteristic time of the system rotation is proposed:

$$R_{CD} = \frac{\frac{\rho_s d_g^2}{18\nu_l \rho_l}}{\frac{1}{\omega}} = \frac{\omega \rho_s d_g^2}{18\nu_l \rho_l} = \frac{\text{Characteristic time of drag response}}{\text{Characteristic time of rotation}} \quad (4.70)$$

The number R_{CD} is smaller than one ($R_{CD} \ll 1$) when the movement of the particles – in this case equiaxed grains – is controlled by the drag force because they “react” faster to the drag than to the system rotation. On the other hand, when this number is greater than one ($R_{CD} \gg 1$) the time of the rotation of the system is smaller than the drag response time, which means that the Coriolis force controls the movement of the equiaxed grains in comparison to the drag force. Figure 4.27 presents the value of R_{CD} for the cases that have been studied in this thesis. Indeed, for the study case where $\vec{g}_{tot} = 5g$, the figure shows that for equiaxed grains whose diameter is $d_g < 0.8 \text{mm}$ the value of R_{CD} is less than 0.1. This means that for the case where $\vec{g}_{tot} = 5g$, a large influence of the Coriolis force on the movement of equiaxed grains is not expected.

Figure 4.28 presents the solid intrinsic velocity along with the equiaxed grain diameter over time in the slurry region of the main plane of study for the case G1P3N9. At $t = 400 \text{s}$ and $t = 415 \text{s}$ the inversion of the radial temperature gradient is produced around $z \sim 46 \text{mm}$ which means that for $z < 46 \text{mm}$ the cylinder center is colder than the cylinder sides, whereas for $z > 46 \text{mm}$ is in the other way around. Indeed, the first equiaxed grains appear in the cylinder center, to appear later in the cylinder sides, in the radial direction.

These equiaxed grains settle towards the columnar front at the same time they grow. The settling velocity of the equiaxed grains is larger in the cylinder center than in the cylinder sides, which is explained by two reasons: (1) The liquid convection reinforces the settling velocities in the cylinder center, whereas reduces it in the cylinder sides, and (2) the equiaxed grains grow faster in the cylinder center due to the temperature radial distribution, making them to settle faster than the ones located in the cylinder sides. At $t = 450 \text{s}$ equiaxed grains populate all the region where nucleation was allowed to take place ($z < 100 \text{mm}$). At this moment, the inversion of the radial temperature gradient takes place at $z \sim 37 \text{mm}$, so that, the cylinder sides are colder than the cylinder center in throughout the slurry region. This leads to a faster growth in the cylinder sides, therefore, a faster settling velocity, as seen in Fig. 4.28 for $z \sim 60 \text{mm}$. However, in the cylinder sides the non-slip condition imposed for the liquid increases the drag exerted over the equiaxed grains, leading to a faster settling in the cylinder center, with respect

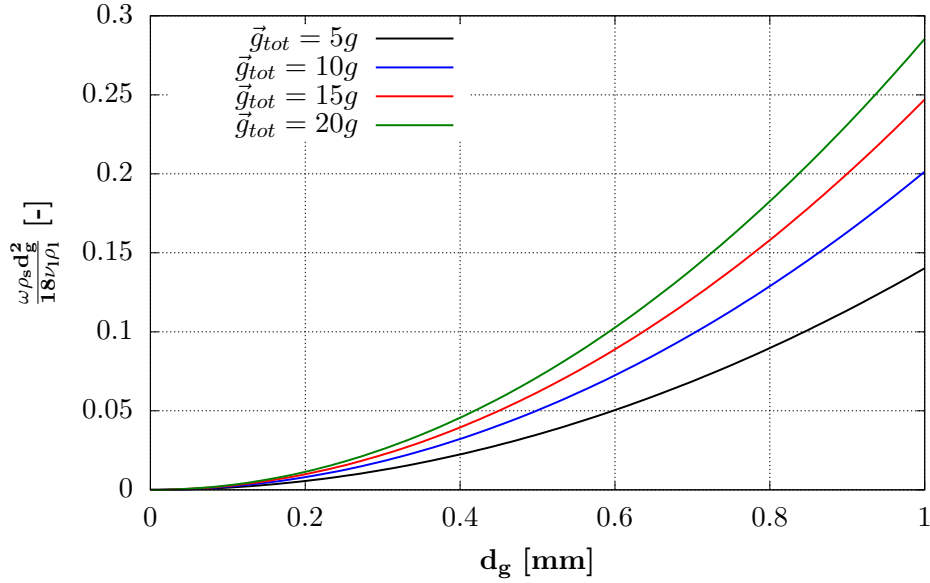


Figure 4.27 – Ratio between the characteristic time of drag response and the characteristic time of rotation vs the grain diameter for different levels of apparent gravity (centrifuge arm is assumed 4 m).

to the cylinder sides. Moreover, the equiaxed grains increase their velocity towards the packing front as they grow. The increase of settling velocity is mainly controlled by the grain diameter since the balance between the drag force and the apparent weight occurs almost instantaneously (recall the response time τ_V). At $t = 485$ s the equiaxed grain growth rate increases driven by the cooling rate imposed by the furnace protocol. This implies that the equiaxed grains grow faster and thus, they settle faster. The final position of the packing front is $z \sim 43$ mm.

Figure 4.29 shows the solid intrinsic velocity along with the equiaxed grain diameter over time for the case G5P3N9. Again, the figure presents the results in the slurry region of the main plane of study. At $t = 400$ s and $t = 415$ s the equiaxed grains that appeared in the domain settle faster in the opposite to flight velocity side. This is due to the effect of the liquid convection that is antiparallel to the apparent gravity in flight velocity side and parallel in the opposite to flight velocity side. At $t = 450$ s the equiaxed grains settle faster in the opposite to flight velocity side of the sample, again due to the effect of the liquid convection. At this moment, the packing front is located around $z \sim 39$ mm and it is not fully symmetric. The packing front is slightly higher in the opposite to flight direction side because the grains pack faster as they settle faster in this side. As in the case G1P3N9, the equiaxed grains increase their velocity as they settle since they grow. At $t = 485$ s the equiaxed grains continue settling towards the packing front, which is finally located at $z \sim 40$ mm. The velocity profile of the equiaxed grains is mainly controlled by the level of apparent gravity, the grain size and the liquid convection. As expected, the Coriolis acceleration does not play a major role determining the features of settling of equiaxed grains.

It is worth to mention that in the cases studied here, the liquid thermosolutal convection

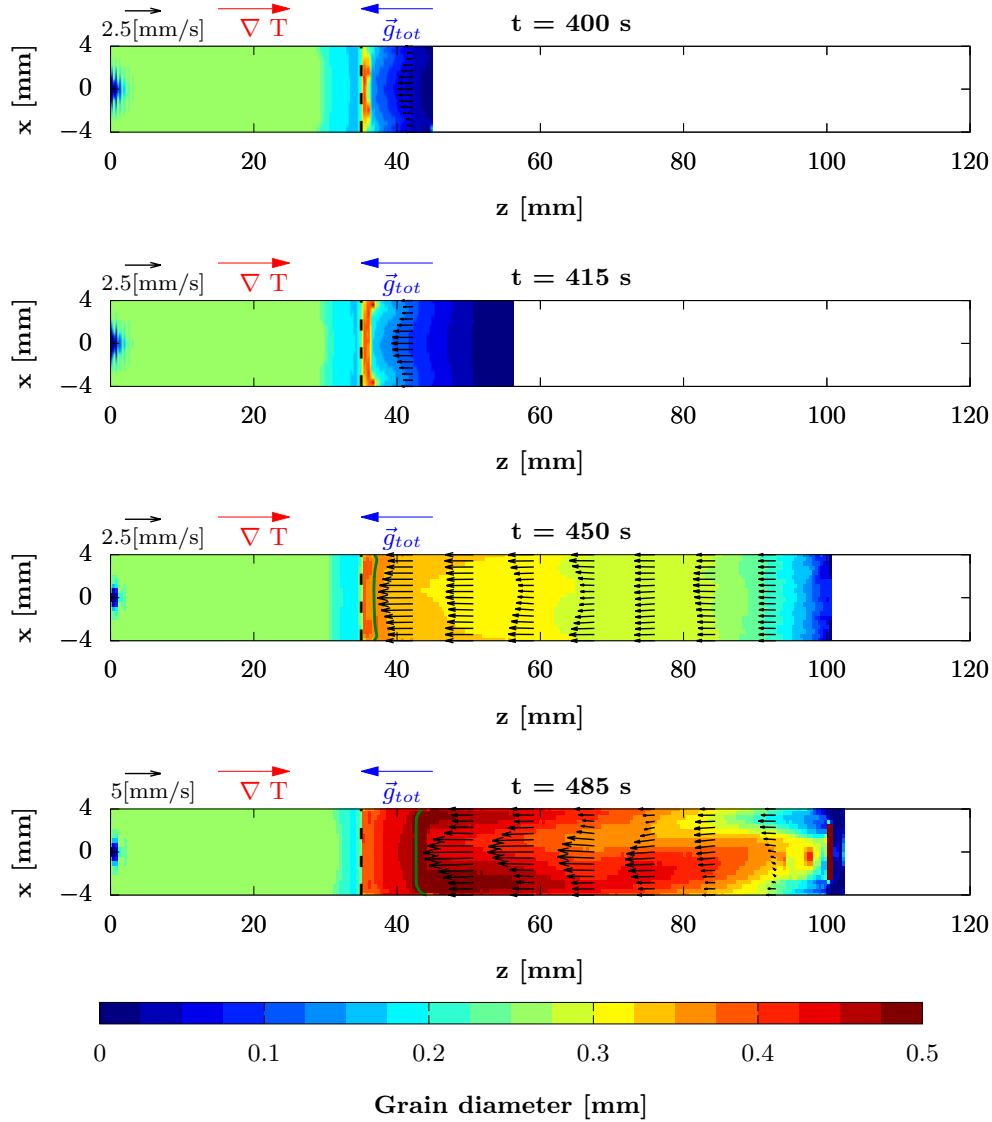


Figure 4.28 – Evolution of the equiaxed grain velocity in the slurry region for the case G1P3N9, along with the distribution of grain diameter. Black dashed line is the position of the predefined CET. Green line denotes the equiaxed grains packing front. The blank space in the plot is because the absence of equiaxed grains (they have not nucleated yet).

and the equiaxed grain motion seem to be not as tightly coupled: the grains settle almost independently to the liquid flow and the liquid flow is virtually independent of the settling of solid grains. This is because the solid fraction in the slurry zone is extremely small.

4.4.1.4 Grain growth in the equiaxed region

Figure 4.30, presents the undercooling, $T - (T_f + m_l \langle C_l \rangle^l)$, for different case configurations in the main plane of study at $t = 450$ s. The figure shows that in the columnar and in the packed

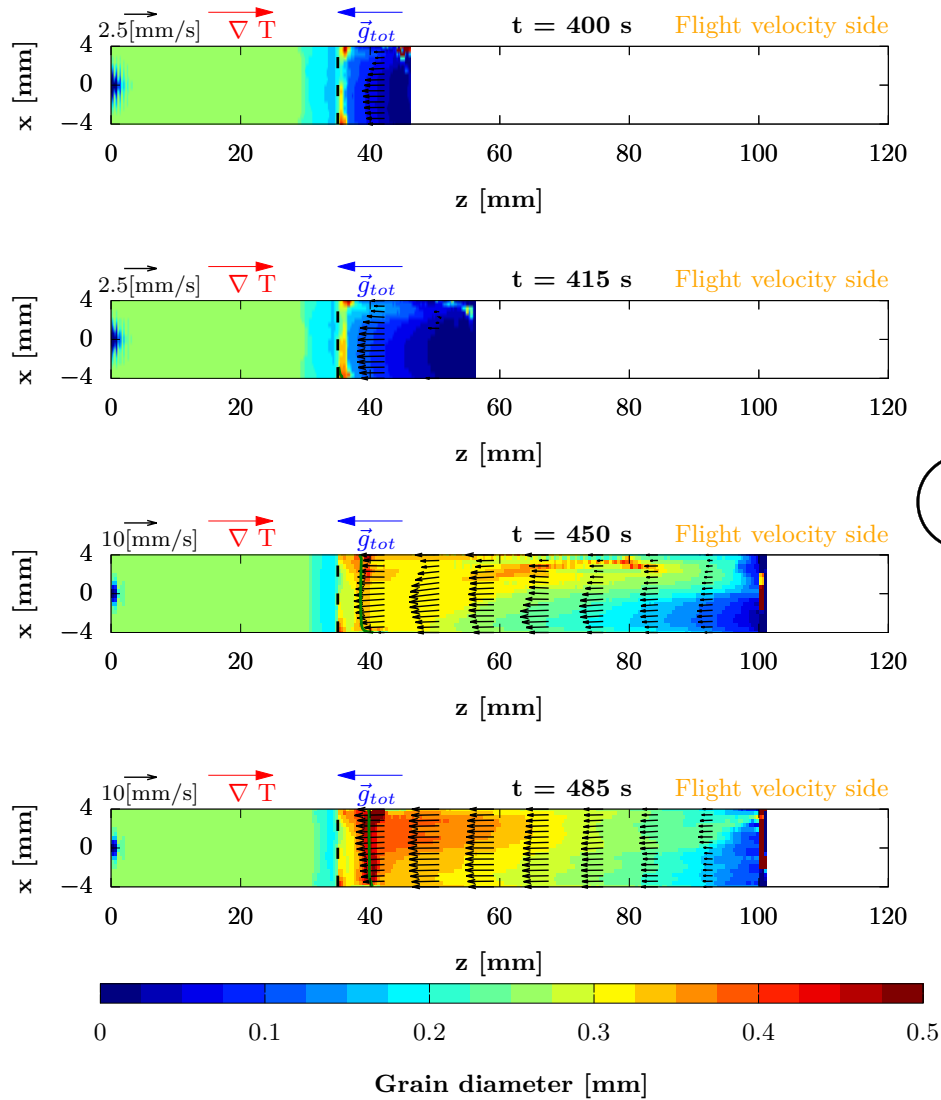


Figure 4.29 – Evolution of the equiaxed grain velocity in the slurry region for the case G5P3N9, along with the distribution of grain diameter. Black dashed line is the position of the predefined CET. Green line denotes the equiaxed grains packing front.

equiaxed regions, the undercooling is close to zero, which means that the solidification takes place almost at full equilibrium. This is because as the equiaxed grains in these regions are close to each other, making their solute interactions much faster.

On the other hand, the figure shows that the equiaxed grains grow from a liquid that presents undercoolings of the order of -6°C in the slurry region. These undercooling levels may lead to dendritic equiaxed grains, *i.e.* equiaxed grains with large and elongated primary arms. Unfortunately, the two-phase globular model is unable to depict the expected dendritic morphology. Moreover, the equiaxed grain motion strongly depends on the grain diameter, as it was already

discussed in Sect. 4.4.1.3. A dendritic grain has a larger cross sectional area in comparison to a globular grain at equivalent mass. This means that the dendritic grains are more likely to be entrained by the liquid than the globular grains. Therefore, given the high levels of undercooling in the slurry region and the limitations of the two-phase globular model to depict realistic equiaxed grain morphologies, the overall pattern of settling of equiaxed grains requires to be confirmed by further analysis and numerical simulations. Unfortunately, due to time limitations this task will remain as a perspective work.

4.4.1.5 Aluminum macrosegregation

Figure 4.31 presents the relative aluminum segregation for several case configurations at the end of the solidification protocol, that is, just before the sample is fully quenched, in the main plane of study. In the figure, three regions are identified: (1) the columnar region, where $z < z_{CET} = 35$ mm, (2) the packed equiaxed region and (3) the slurry region. For each one of these regions, the aluminum segregation pattern is described below.

In the columnar region, a positive segregation is present in the cylinder center, whereas a negative segregation is present in the cylinder sides. The positive segregation is explained because the interdendritic liquid flow is antiparallel to the apparent gravity in the cylinder center, bringing solute enriched liquid from deep in the mushy zone to the columnar front. On the other hand, the negative segregation is explained because the interdendritic liquid flow is parallel to the apparent gravity in the cylinder sides. This flow takes liquid impoverished in aluminum from the columnar front to the depths of the mushy zone. This pattern is similar to the one already found in the fully columnar cases of Chapt. 3 and present in both apparent gravity configurations, *i.e.* under normal terrestrial gravity ($\vec{g}_{tot} = g$), and under centrifugation ($\vec{g}_{tot} = 5g$). Furthermore, the magnitude of the aluminum segregation in cases under centrifugation is larger than in cases under terrestrial gravity. This is due to the magnitude of the liquid convection that is stronger as the level of apparent gravity increases.

Regarding the packed equiaxed region, it is initially built-up as the equiaxed grains settle towards the columnar front. Once the first equiaxed grains are packed, the packed equiaxed region continues to grow as the equiaxed grains settle towards the packing front. As the equiaxed grains settle, they also grow. During their growth, aluminum is rejected to the surrounding liquid. This implies that the equiaxed grains are constituted with less aluminum than the liquid from which they grow. As the equiaxed grains pack, they create a region strongly depleted in aluminum, as seen in the packed equiaxed region of Fig. 4.31. Aluminum continues to be rejected in the packed region as the packed equiaxed grains grow. This growth enriches in aluminum the liquid of the packed equiaxed region decreasing its density. An interdendritic flow of aluminum enriched liquid, antiparallel to the apparent gravity, takes place within the packed equiaxed region (see Fig. 4.23). This current of enriched liquid flows through the packed equiaxed region into the slurry region, depleting packed region even more. A particular segregation pattern is found in the case G1P1N11, which present a gradient of aluminum concentration from the columnar front to the packing front: the packed zone gets enriched in aluminum. This gradient is explained by two reasons. The first one is due to the interdendritic flow in the packed region that

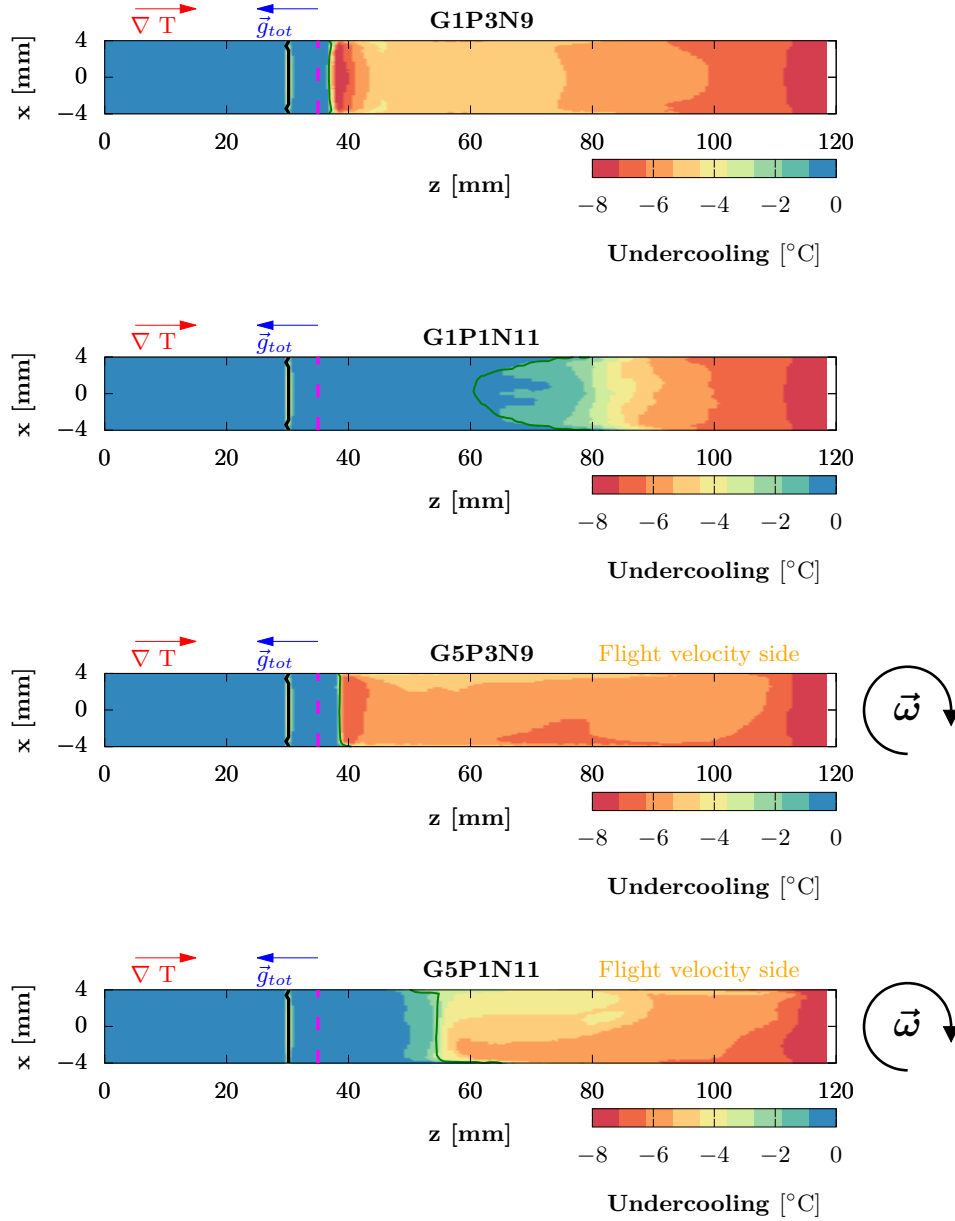


Figure 4.30 – Undercooling, $T - (T_f + m_l \langle C_l \rangle^l)$, for different case configurations in the main plane of study at $t = 450$ s. Black line limits the fully solid region and the solidifying region. Magenta dashed line is the predefined CET position. Green line is the equiaxed packing front.

flows antiparallel to the apparent gravity, bringing aluminum enriched liquid from the depths of the packed region towards the packing front. The second reason is because new equiaxed grains nucleate and grow from a more enriched liquid in the slurry region. The slurry region gets aluminum enriched over time due to the enriched liquid that escapes from the packed equiaxed region.

Table 4.8 presents the length of the packed region for all studied cases. The length of this

region mainly depends on the predefined packing criterion, g_e^{block} , and the initial number of nuclei in the slurry region. In cases under centrifugation, this length is between 20% and 40% smaller with respect to the cases solidified under normal terrestrial gravity. This difference is explained since the equiaxed grains settle faster in the cases under centrifugation, and thus, they have less time to grow before they pack. This observation can be corroborated by comparing the grain diameter maps of Figures 4.28 and 4.29. These figures show that in cases under normal terrestrial gravity, the grain diameter is larger in comparison to the cases under centrifugation in the packed equiaxed region, for the same configuration of initial nuclei density and of packing criterion.

Table 4.8 – Length of the region of packed grains for all the studied cases. Cases under normal terrestrial gravity on the two columns of the left. Cases under centrifugation on the two columns of the right.

Case name	Packed length	Case name	Packed length
G1P1N9	20.2	G5P1N9	12.07
G1P1N11	42.4	G5P1N11	33.99
G1P3N9	8.12	G5P3N9	5.05
G1P3N11	18.84	G5P3N11	13.032

At the time the sample is quenched, the slurry region is still present in much of the length of the sample. In the cases solidified under normal terrestrial gravity, the cylinder sides presents an enrichment that corresponds to the liquid that escapes from the packed zone as shown in Sect. 4.4.1.2. On the other hand, in cases under centrifugation, the flight velocity side of the sample presents is aluminum enriched. This corresponds to the enriched liquid that escapes from the packed region. This liquid flows antiparallel to the apparent gravity, and therefore, is deflected by the Coriolis acceleration towards the flight velocity side.

4.5 Summary

The main results obtained in this Chapter can be resumed as follow:

- New developments were carried out in *macroS3D*. This developments were focused in the implementation of equiaxed grain movement and grain growth kinetics.
- A modified PISO/SIMPLE velocity-pressure coupling algorithm was proposed to account for the slurry/porous regime transition. This new algorithm was validated using a sedimentation column case as proposed by Nguyen [102].
- In order to improve the representation of grain growth kinetics, a two-phase globular model and a three-phase model were implemented in *macroS3D*. These implementations

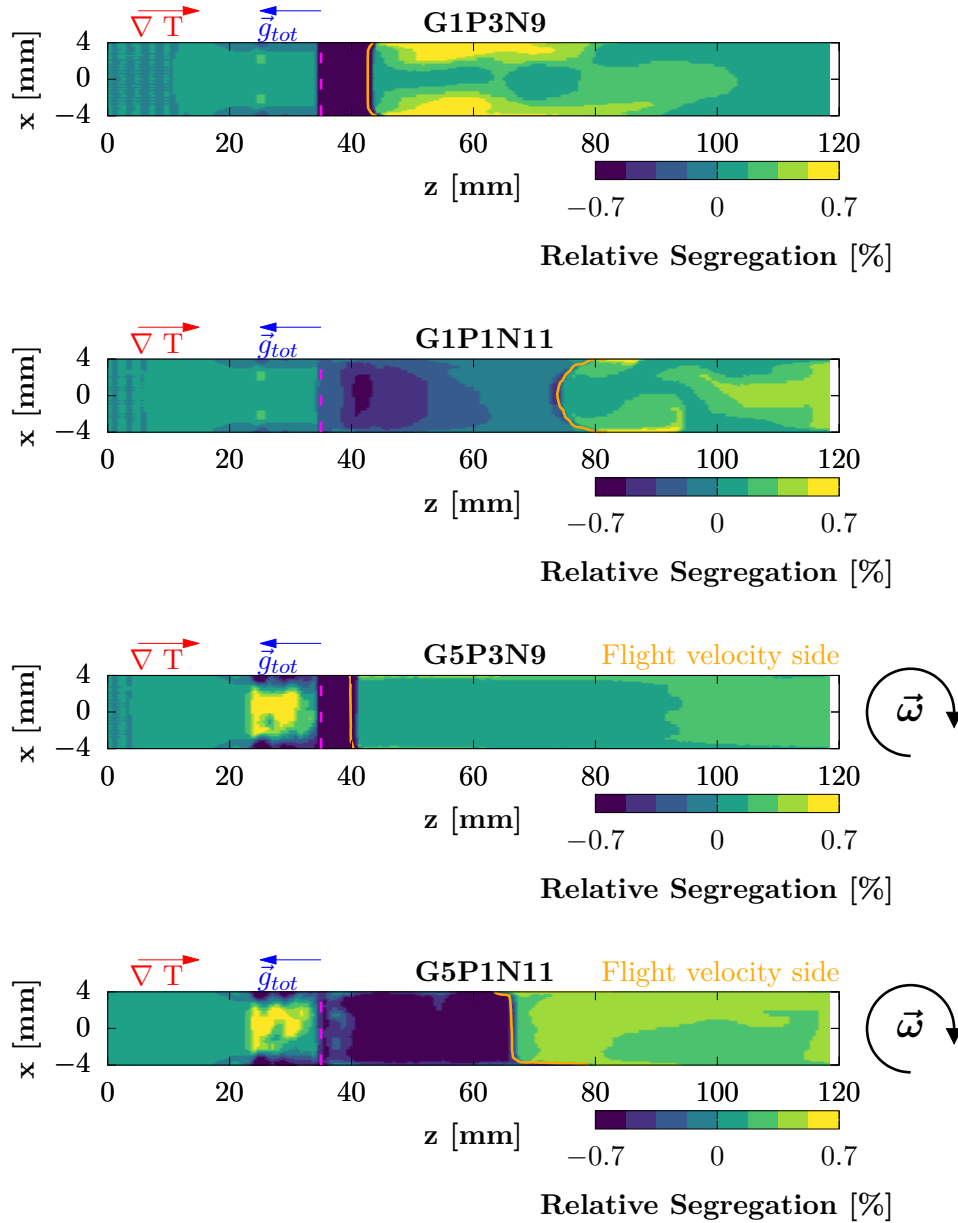


Figure 4.31 – Relative aluminum segregation $\frac{\langle C \rangle - C_0}{C_0} \times 100\%$ in the main plane of study at the end of the solidification protocol for different case configurations. Magenta dashed line is the position of the predefined CET. Orange line denotes the equiaxed grains packing front.

were validated using the solidification of an unitary control volume as proposed by Bedel [72].

- The macroscopic modeling (transport) and the microscopic modeling (nucleation and growth) were coupled using the operator splitting algorithm as proposed by Založnik [79]. This implementation was validated using the Hebditch and Hunt case [50], which has been widely used to verify macroscopic solidification models.

- Once the new implementations were validated, *macroS3D* was used to simulate the GRADECET experiments of TiAl directional solidification under centrifugal conditions. For that different numerical configurations were considered.
- The simulations showed that, in spite of the presence of equiaxed grains, a one single vortex fluid flow pattern takes place in the slurry region of the cases under centrifugal conditions due to the Coriolis acceleration.
- The simulations also showed that the influence of the Coriolis force on the motion of equiaxed grains for the studied cases is weak. This is because the equiaxed grains responds faster to the drag force than to the Coriolis force, and thus, their movement is governed by the balance between the drag force and the apparent weight.
- The aluminum segregation pattern obtained with a two-phase globular model was characterized.

General conclusions and perspectives

Throughout the development of this work, several numerical simulations of the GRADECET project experiments have been carried out. These experiments consisted in the directed solidification of cylindrical samples of TiAl under normal conditions of terrestrial gravity and under different levels of centrifugation. The main objective of the simulations was to improve the understanding the effect of centrifugation on the liquid thermosolutal convection, the equiaxed grain motion and the aluminum macrosegregation. The results contained in this work can be broken down into three main axes: (1) the formulation of a macroscopic solidification model in a rotating coordinate system, (2) the development of a new numerical tool to enable three-dimensional numerical simulations of solidification and (3) the preliminary explanations of the effect of centrifugation in the aforementioned experiments.

The first axis consisted, in a first instance, in the study of the numerical modeling of solidification at macroscopic scales. Here, the focus was mostly put on the models developed in our team, particularly on the model used by Heyvaert et al. [39]. This model presents the latest advances in relation to the multiscale modeling of solidification. In a second instance, this solidification model was considered as reference to be written in rotating coordinates such that, the effect of centrifugation could be depicted. Indeed, it was demonstrated that the non-inertial accelerations – centrifugal and Coriolis – appear in the momentum equation for the liquid, as well as, in the momentum equation for the solid in an averaged form. These accelerations add important three-dimensional aspects to the original model, making it impossible to use two-dimensional axisymmetric formulations, such as the one already implemented in the SOLID[®] software. These circumstances led to the second axes of this work.

The second axis of this work consisted of the implementation of the macroscopic solidification model, including the centrifugal and Coriolis accelerations, in a new computational tool. This new tool was called *macroS3D* and was based on the finite-volume open-source OpenFOAM platform. At first, a simplified solidification model was implemented as reported in Chapt. 3. This simplified model assumes columnar growth and an infinitely fast solute diffusion model at the microscopic scales, that is, solidification always occurs under full thermodynamic equilibrium conditions. In a second stage, the model initially implemented in *macroS3D* was extended to account for advanced models of grain growth kinetics and for the motion of equiaxed grains. For that, a modified PISO/SIMPLE velocity-pressure coupling algorithm was proposed and implemented. This modified algorithm enables the proper representation of the transition between the slurry and porous convection regimes. The second axis of this work produced a new nu-

merical tool which enables the three-dimensional macroscopic simulation of solidification. In addition, this tool also enables parallel computing which dramatically reduces the time required to perform simulations.

The third and last axis is related to the explanations obtained by means of numerical simulations of the liquid thermosolutal convection and equiaxed grain motion under centrifugal conditions. The explanations can be broken down according to the case configurations studied in this work.

When a fully columnar solidification was considered, the main results can be summarized as:

- In the case solidified under normal terrestrial gravity, the flow in the columnar region is controlled by solutal buoyancy forces. On the other hand, the flow in the fully liquid region is controlled by thermal buoyancy forces. This is because the aluminum enriched liquid is not able to escape from the mushy zone due to the restriction imposed by the flow in the fully liquid region.
- In cases with centrifugation, aluminum enriched liquid is able to escape from the mushy zone. This leads to a current flow of aluminum enriched liquid antiparallel to the apparent gravity. The Coriolis accelerations rapidly deflects this flow towards the flight velocity side of the sample, generating a one-vortex liquid flow pattern in the fully liquid region.
- An non-axisymmetric aluminum segregation pattern takes place in the cases solidified under centrifugal conditions. Moreover, an aluminum enrichment takes place in the flight velocity side of the sample. This is a consequence of the one-vortex liquid flow pattern.
- Post-mortem measurements of aluminum concentration were conducted on the sample in which $\vec{g}_{tot} = 15g$. These measurements revealed an aluminum enrichment in the flight velocity side of the sample. This finding confirms the observations of the one-vortex liquid flow pattern.

When a columnar and equiaxed regions were considered by a predefined CET position, the main results can be summarized as:

- The liquid flow in the slurry region is controlled by the Coriolis acceleration in the centrifugally solidified cases. Again, the one-vortex liquid flow pattern takes place.
- The equiaxed grain motion is weakly affected by the Coriolis acceleration. Indeed, the grain motion is mainly governed by the balance between the drag force and the grain apparent weight. This is mainly due to the extremely small solid fraction in the slurry region.
- The thermosolutal liquid convection and equiaxed motion on the cases solidified under centrifugation seem to be independent of each other. This is because the small volume fraction of the globulitic equiaxed grains in the slurry region is not able to affect the

liquid thermosolutal convection that is governed by the Coriolis acceleration. On the other hand, the force balance on a grain shows that the equiaxed grain motion is governed primarily by the apparent gravity and drag and that the entrainment by the liquid has a very weak effect at high gravity.

- The predicted packed region in the centrifugally solidified cases is smaller than in the cases solidified under normal terrestrial gravity. This is because the equiaxed grains have less time to grow before they pack in cases under centrifugation.

4.6 Perspectives

Although the efforts made to carry out numerical simulations as much as similar to the experimental protocol, special considerations had to be made regarding the case configuration and the alloy solidification path. In this respect, the improvement of the thermal boundary conditions and the modeling of the full alloy, considering explicitly all the components, are steps forward to better represent the physics during the experiments. Following, the use of a three-phase microscopic model, which is currently available in *macroS3D*, can enable a better description of the grain morphology, and thus, a better description of the equiaxed grain motion and aluminum macrosegregation. This could not be done within the frame of this thesis due to time limitations.

Finally, it is worth to mention that *macroS3D* will be a fundamental part of a new project led by our team, which is called *OpenSOLID*. This project intends to bring state-of-the-art software for casting simulation to the metallurgical industry.

Appendix A : Thermophysical properties

Contents

A.1	Validation	154
A.1.1	Thermophysical properties: Pb-18wt.%Sn alloy	154
A.1.2	Thermophysical properties: water/glycerol mixture for the rotating annulus case	154
A.1.3	Thermophysical properties: Sedimentation column and Hebditch-Hunt benchmark cases (Sn-5wt.%Pb)	156
A.1.4	Thermophysical properties: cases of solidification of an unitary control volume (Al-5wt.%Si)	157

A.1 Validation

A.1.1 Thermophysical properties: Pb-18wt.%Sn alloy

Table A.1 – Thermophysical properties of Pb-18wt.%Sn used in the simulation case of Sect. 3.1.1.1.

Property	Symbol	Units	Value
Nominal concentration	C_0	[wt%]	18.0
Partition coefficient	k_p	[–]	0.310
Melting point of the pure substance	T_f	[°C]	327.5
Liquidus slope	m_l	[K/wt%]	-2.334
Eutectic concentration	C_{eut}	[%wt]	61.911
Reference density	ρ	[kg/m ³]	9250
Kinematic viscosity	ν_l	[m ² /s]	1.19×10^{-7}
Thermal conductivity	k	[W/mK]	17.9
Solutal expansion coeff.	β_C	[wt% ⁻¹]	4.90×10^{-3}
Thermal expansion coeff.	β_T	[K ⁻¹]	1.16×10^{-4}
Reference temperature	T_{ref}	[°C]	285.488
Reference concentration	C_{ref}	[wt%]	18
Latent heat	L_f	[J/kg]	3.76×10^4
Specific heat capacity	c_p	[J/(kgK)]	176
Secondary arm spacing	λ_2	[m]	1.85×10^{-4}

A.1.2 Thermophysical properties: water/glycerol mixture for the rotating annulus case

– *Buoyancy liquid density* ρ_l^b [kg/m³]:

$$\rho_l^b = -0.00739(T - T_{ref})^2 - 0.3202(T - T_{ref}) + 1043$$

– *Kinematic viscosity* ν_l [m²/s]:

$$\nu_l = 1.0903 \times 10^{-9}(T - T_{ref})^2 - 4.5198 \times 10^{-8}(T - T_{ref}) + 1.62 \times 10^{-6}$$

– *Thermal diffusivity* $\alpha[m^2/s]$:

$$\alpha = 3.0057 \times 10^{-10}(T - T_{ref}) + 1.29 \times 10^{-7}$$

Table A.2 – Thermophysical properties of the water/glycerol mixture used in the simulation case of Sect. 3.1.1.2.

Property	Symbol	Units	Value
Specific heat capacity	c_p	[J/(kgK)]	3880
Reference temperature	T_{ref}	[°C]	22
Fluid density at 20[°C]	ρ	[kg/m ³]	1044

A.1.3 Thermophysical properties: Sedimentation column and Hebditch-Hunt benchmark cases (Sn-5wt.%Pb)

Table A.3 – Thermophysical properties of Sn-5wt.%Pb alloy used in the sedimentation column (Sect. 4.1.5) and the Hebditch-Hunt benchmark cases (Sect. 4.3.1)

Property	Symbol	Units	Value
Nominal concentration	C_0	[wt%]	5.0
Partition coefficient	k_p	[–]	0.0656
Melting point of the pure substance	T_f	[°C]	232.0
Liquidus slope	m_l	[K/wt%]	-1.286
Eutectic concentration	C_{eut}	[wt%]	38.10264
Liquid reference density	ρ_l	[kg/m ³]	7000.0
Solid density for grain buoyancy	ρ_s	[kg/m ³]	7142.9
Kinematic viscosity	ν_l	[m ² /s]	1.428571×10^{-7}
Thermal conductivity	k	[W/mK]	55.0
Solutal expansion coeff.	β_C	[wt% ⁻¹]	-5.3×10^{-3}
Thermal expansion coeff.	β_T	[K ⁻¹]	6.0×10^{-5}
Reference temperature	T_{ref}	[°C]	226.0
Reference concentration	C_{ref}	[wt%]	5.0
Latent heat	L_f	[J/kg]	6.1×10^4
Specific heat capacity	c_p	[J/(kgK)]	260.0
Characteristic length for permeability	d_p	[m]	200.0×10^{-6}
Packing limit grain volume fraction	g_e^{pack}	[–]	0.3
Tortuosity	τ	[–]	$6/\pi$
Kozeny constant	K_k	[–]	5.0

A.1.4 Thermophysical properties: cases of solidification of an unitary control volume (Al-5wt.%Si)

Table A.4 – Thermophysical properties of Al-5wt.%Si alloy used in the cases of solidification in an unitary control volume (Sect. 4.2.3)

Property	Symbol	Units	Value
Nominal concentration	C_0	[wt%]	5.0
Partition coefficient	k_p	[-]	0.117
Melting point of the pure substance	T_f	[°C]	660
Liquidus slope	m_l	[K/wt%]	-7.7
Liquid reference density	ρ_l	[kg/m ³]	2500.0
Solid density for grain buoyancy	ρ_s	[kg/m ³]	2500.0
Thermal conductivity	k	[W/mK]	50.0
Latent heat	L_f	[J/kg]	3.8×10^5
Specific heat capacity	c_p	[J/(kgK)]	940
Gibbs-Thomson coefficient	Γ_{GT}	[mK]	0.9×10^{-7}
Tip selection constant	σ^*	[-]	0.02533029

List of Tables

2.1	Scalar conservation equations for solidification modeling written in terms of the rotating reference frame.	50
3.1	Thermophysical properties used in the simulations.	72
3.2	Total apparent gravity (g is the normal terrestrial gravity), centrifuge angular velocity, ω , reference velocity, U_{ref} and Rossby number, $Ro = \frac{U_{ref}}{2\omega L}$ for all the studied cases. The reference velocity is considered to be the average of the maximum velocity in the main plane of study at the instants $t = 50$ s $t = 200$ s and $t = 400$ s.	80
4.1	Maximum solid fraction at $t = 15$ s in the interface between the fully liquid region and the bed of packed particles and in the base of the column when a linear interpolation scheme for α_t is used.	109
4.2	Maximum solid fraction at $t = 15$ s in the base of the column when a downwind interpolation scheme with respect to $\langle \vec{v}_s \rangle^s$ is used.	109
4.3	Convergence criteria for the different decisions in the algorithm <i>macroS3D</i>	118
4.4	Maximum liquid intrinsic velocity for different instants. In the cases name, the letter denotes <i>Upwind</i> or <i>Van Leer</i> interpolation schemes whereas the number the mesh size.	124
4.5	Maximum solid intrinsic velocity for different instants. In the cases name, the letter denotes <i>Upwind</i> or <i>Van Leer</i> interpolation schemes whereas the number the mesh size.	125
4.6	Numerical configuration for the cases simulated considering grain growth kinetics and equiaxed grain movement. Note that the case name is related to the gravity level, packing fraction and nuclei density in the equiaxed region.	131
4.7	Thermophysical properties used in the simulations considering grain growth kinetics and equiaxed grain movemen	132
4.8	Length of the region of packed grains for all the studied cases. Cases under normal terrestrial gravity on the two columns of the left. Cases under centrifugation on the two columns of the right.	146
A.1	Thermophysical properties of Pb-18wt.%Sn used in the simulation case of Sect. 3.1.1.1.	154

A.2	Thermophysical properties of the water/glycerol mixture used in the simulation case of Sect. 3.1.1.2.	155
A.3	Thermophysical properties of Sn-5wt.%Pb alloy used in the sedimentation column (Sect. 4.1.5) and the Hebditch-Hunt benchmark cases (Sect. 4.3.1)	156
A.4	Thermophysical properties of Al-5wt.%Si alloy used in the cases of solidification in an unitary control volume (Sect. 4.2.3)	157

List of Figures

RE-1	Schéma du four et de l'échantillon de TiAl dans la centrifugeuse. L'échantillon est représenté en gris et les éléments chauffants en orange et jaune. L'angle d'inclinaison du four est indiqué par l'angle α , la vitesse de vol du four par \vec{V}_{flight} (en bleu), la gravité apparente totale par \vec{g}_{tot} (en orange) et le gradient de température principal de ∇T (en rouge). Le plan d'étude principal est défini comme celui formé par le vecteur de vitesse de vol \vec{V}_{flight} et la gravité apparente totale, \vec{g}_{tot} . Quatre gravités apparentes différentes ont été étudiées sous centrifugation: $\vec{g}_{tot} = 5g, 10g, 15g$ et $20g$	iv
RE-2	Evolution du schéma de vitesse des liquides dans le plan d'étude principal dans la région entièrement liquide pour le cas 1G. Contours de température en noir: 1400, 1450, 1500 et 1550 °C.	vii
RE-3	Evolution du champ de vitesse du liquide dans le plan d'étude principal dans la région entièrement liquide pour le cas 20G. Contours de température en noir: 1400, 1450, 1500 et 1550 °C.	viii
RE-4	Segregation relative de l'aluminium $\frac{\langle C \rangle - C_0}{C_0} \times 100\%$ dans le plan principal d'étude en fin de solidification pour différents niveaux de centrifugation. Contours à $\langle C \rangle = C_0$ (ligne noire).	xi
1	Binary phase diagram Ti-Al [20] along with the range in which α_2 and γ phases coexist.	8
1.1	Scales of solidification [42]	14
1.2	Effect of the grain movement on macrosegregation in a case of Pb-Sn. A stainless steel mesh was placed at the half-height of the mold (de Groh [48]).	16
1.3	Two 1D illustrative cases with different orientation between thermal gradient \vec{G} and gravity \vec{g} . Each case has a solid (black), mush (gray) and liquid (white) regions. No solutal buoyancy effects considered.	18
1.4	Segregation maps reported by Hebditch and Hunt [50]. Red circle shows the main sense of the liquid flow.	19
1.5	Representative elementary volume (REV) for the representation of columnar and equiaxed grains (adapted from [7])	20
1.6	Schematic of solute diffusion at solid-liquid interface in the two-phase approach for microscopic modeling.	22

1.7	Schematic of the intradendritic liquid solute balance in the three-phase approach where g_e denotes the envelope fraction, g_{li} the intradendritic liquid and g_{le} the extradendritic liquid. The intradendritic liquid is considered to be perfectly mixed.	24
1.8	Complete algorithm proposed by Založnik and Combeau [65] for solidification modeling. Note that the numerical time integration of the respective operators is separated.	31
1.9	Example of semi-industrial centrifugal casting of TiAl cylindrical ingots. Note the “seagull wing” shape of the radial columnar growth. g_{cent} denotes the direction of the centrifugal acceleration. Vector \vec{g} denotes the direction of the normal terrestrial gravity.	35
1.10	Fixed reference frame (black) and rotating reference frame (red) which is dependent in time. The center of rotation in the fixed coordinate system is (0,0)	36
2.1	Fixed reference frame (black) and a moving reference frame (blue) at constant velocity \vec{V}^f . The axes of both reference frames are aligned.	43
2.2	Schematic representation of how the same velocity vector is <i>observed from</i> a fixed reference frame $\vec{u}^f(\vec{x}^f, t)$ and a rotating reference frame $\vec{u}(\vec{x}, t)$	44
3.1	Schematic and instantaneous result of the Pb-18wt%Sn solidification case proposed by Bellet et al. [51]	60
3.2	Comparison between “castFoam” and <i>macroS3D</i> : Instantaneous intrinsic liquid velocity magnitude and liquid fraction at $t = 120$ s along the H_2 line (see Fig. 3.1a)	61
3.3	Comparison between “castFoam” and <i>macroS3D</i> : Averaged solute concentration of tin at the end of solidification in H_1 and H_2 lines (See Fig. 3.1a)	62
3.4	Tin segregation map at the end of solidification. Comparison between <i>macroS3D</i> and “castFoam” [4] (re-plotted).	63
3.5	Schematic of the rotating annulus case along with the three-dimensional mesh used to perform the numerical simulations.	64
3.6	Instantaneous liquid velocity fields projected into the corresponding horizontal plane of height 12.4 cm. Comparison between results obtained with <i>macroS3D</i> and experimental measurements. The inner side (blue line) is 4 °C colder than the outer side (red line).	65
3.7	Comparison between <i>macroS3D</i> numerical results, experimental measurements and numerical results from [91]: Mean azimuthal velocity vs radial position for horizontal lines at 12.4, 9.7, 7.0, 4.3 and 1.6 cm from the annulus base	66
3.8	Schematic of the sample, heaters and thermocouples. The thermocouples are represented by the red wires and the heaters by purple (“H3”) and orange (“H1” and “H2”) circles. At $t = 0$, the heaters temperatures are $T_{H1} = 1623$ °C , $T_{H2} = 1623$ °C and $T_{H3} = 1543$ °C.	67
3.9	Temperature measured by the thermocouples in the three stages of the furnace protocol. Time $t = 0$ is adjusted the beginning of the solidification stage.	68

3.10	Schematic of the furnace and the TiAl sample in the centrifuge. The sample is represented in grey and the heaters in orange and yellow. The furnace tilting angle is denoted by α , the furnace flight velocity by \vec{V}_{flight} (in blue), the total apparent gravity by \vec{g}_{tot} (in orange) and the main temperature gradient by ∇T (in red). The main plane of study is defined as the one formed by the flight velocity vector, \vec{V}_{flight} and the total apparent gravity, \vec{g}_{tot} . Four different apparent gravities were investigated under centrifugation: $\vec{g}_{tot} = 5g, 10g, 15g$ and $20g$	68
3.11	Results of the solidification path simulation using Thermo-Calc Software along with the approximations used in the this work.	69
3.12	Schematic of the three-dimensional mesh	70
3.13	Temperature boundary condition imposed along the cylindrical sample for four different times. These temperature profiles are the result of the dedicated thermal furnace model. The thermal protocol does not depend on the apparent gravity level. The gray shaded area represents the alloy solidification range.	71
3.14	Contribution of radial heat diffusion, $\mathbf{R}(t, z) = \frac{k}{\rho c_p} \left(\frac{1}{r} \frac{\partial}{\partial r} r \frac{\partial T}{\partial r} \right)$, calculated using information of the boundary conditions. The mushy zone is located between 21 mm and 26 mm at $t = 50$ s between 24 mm and 31 mm at $t = 200$ s and between 28 mm and 45 mm at $t = 400$ s approximately.	74
3.15	Evolution of the liquid density, in terms of ρ_l^b/ρ_l in the main plane of study inside the mushy zone for the case 1G. White contours delimit the mushy zone ($g_l = 0.01, g_l = 0.99$). For (a) and (b), temperature contours in black: 1500, 1510 °C. For (c) temperature contours 1506,1508 and 1510 °C. It is shown the sign of coefficient $\mathbf{R}(t, z)$ depending on the shape of the temperature contours.	76
3.16	Evolution of the liquid velocity and liquid fraction in the main plane of study inside the mushy zone for the case 20G. <i>FVS</i> denotes the flight velocity side of the sample. White contours delimit the mushy zone ($g_l = 0.01, g_l = 0.99$). For (a) and (b), temperature contours in black: 1500 and 1510 °C. For (c) temperature contours 1508 and 1510 °C.	77
3.17	Evolution of the liquid velocity and liquid fraction in the main plane of study inside the mushy zone for the case 1G. White contours delimit the mushy zone ($g_l = 0.01, g_l = 0.99$). For (a) and (b), temperature contours in green: 1490, 1500 and 1510 °C. For (c) temperature contours 1490,1500,1503,1506,1508 and 1510 °C.	78
3.18	Evolution of the liquid velocity and liquid fraction in the main plane of study in the mushy zone for the case 20G. <i>FVS</i> denotes the flight velocity side of the sample. White contours delimit the mushy zone ($g_l = 0.01, g_l = 0.99$). For (a) and (b), temperature contours in green: 1490, 1500 and 1510 °C. For (c) temperature contours 1490,1500,1503,1505.2,1508 and 1510 °C.	79
3.19	Evolution of the liquid velocity pattern in the main plane of study in the fully liquid region for the 1G case. Temperature contours in black: 1400, 1450, 1500, and 1550 °C.	81

3.20	Evolution of the liquid velocity pattern in the main plane of study in the fully liquid region for the 20G case. Temperature contours in black: 1400, 1450, 1500, and 1550 °C.	82
3.21	Temperature, average concentration in the liquid and liquid density (in terms of ρ_l^b/ρ_l) in the main plane of study at $t = 200$ s for the case 1G. Violet contours delimit the mushy zone. Temperature contours in black: 1400, 1450, 1500, and 1550 °C.	83
3.22	Temperature, average concentration in the liquid and liquid density (in terms of ρ_l^b/ρ_l) in the main plane of study at $t = 200$ s for the case 20G. Violet contours delimit the mushy zone. Temperature contours in black: 1400, 1450, 1500, and 1550 °C.	84
3.23	3D views of the domain at $t = 150$ s for the case 20G. (a) Relative segregation $\frac{\langle C \rangle - C_0}{C_0} \times 100\%$. (b) Axial intrinsic liquid velocity magnitude (negative magnitude in the direction parallel to the apparent gravity).	85
3.24	Relative aluminum segregation $\frac{\langle C \rangle - C_0}{C_0} \times 100\%$ in the main plane of study at the end of solidification for different centrifugation levels. Contours at $\langle C \rangle = C_0$ (black line).	86
3.25	Relative segregation $\frac{\langle C \rangle - C_0}{C_0} \times 100\%$ for the case 15G in transversal planes at the end of solidification.	87
3.26	Comparison of aluminum concentration between EDX measurements and numerical simulations in the Case 15G. Line-point: Measurements (3-point moving averaging). Solid Line: Numerical results. Dashed line: Numerical results displaced 0.5 mm and -0.5 mm in the y -axis direction (normal to the main plane of study).	88
4.1	Microstructure of the experiments of directional solidification under centrifugal conditions carried out within the framework of the GRADECET project. The full analysis of the microstructure is reported in ref. [1]. The violet line is the melting front at $t = 0$. The white line is the onset of columnar growth. The red line delimits the columnar region to the equiaxed region. The black lines are recognizable differences in the microstructure. The light blue line delimits the equiaxed region to the quenched liquid region. In Case 1G, the yellow line delimits the columnar region to the quenched liquid region (there is no CET).	92
4.2	Indicative function α_t for $g_e^{block} = 0.3$ and for various values of α , in the neighborhood of g_e^{block}	99
4.3	Solid fraction field g_s over time obtained with <i>macroS3D</i> for the sedimentation column case proposed by Nguyen [102]. Numerical configuration: $\alpha = 1600$, $\Delta t = 1 \times 10^{-4}$ s and α_t was interpolated using a downwind scheme with respect to $\langle \vec{v}_s \rangle^s$	104

4.4	Solid intrinsic velocity $\langle \vec{v}_s \rangle^s$ over time obtained with <i>macroS3D</i> for the sedimentation column case. Black contours represent $g_s = 0.01$ and violet contours represent $g_s = 0.29$. Numerical configuration: $\alpha = 1600$, $\Delta t = 1 \times 10^{-4}$ s and α_t was interpolated using a downwind scheme with respect to $\langle \vec{v}_s \rangle^s$	105
4.5	Liquid intrinsic velocity $\langle \vec{v}_l \rangle^l$ over time obtained with <i>macroS3D</i> for the sedimentation column case. Black contours represent $g_s = 0.01$ and violet contours represent $g_s = 0.29$. Numerical configuration: $\alpha = 1600$, $\Delta t = 1 \times 10^{-4}$ s and α_t was interpolated using a downwind scheme with respect to $\langle \vec{v}_s \rangle^s$	106
4.6	Average enthalpy, average solute concentration, grain density and temperature on the vertical centerline over time obtained with <i>macroS3D</i> for the sedimentation column case. Numerical configuration: $\alpha = 1600$, $\Delta t = 1 \times 10^{-4}$ s and α_t was interpolated using a downwind scheme with respect to $\langle \vec{v}_s \rangle^s$	107
4.7	Solid fraction on the vertical centerline over time for different numerical configurations on <i>macroS3D</i> . Solid line: <i>macroS3D</i> (FVM). Dashed line: SOLID [®] (FVM). Point-dash line: Nguyen (FEM) [102].	108
4.8	Evolution of different magnitudes over time. Comparison between SOLID [®] and <i>macroS3D</i> for the <i>Case A</i> . “glob” denotes results obtained using a two-phase globular model.	116
4.9	Evolution of different magnitudes over time. Comparison between SOLID [®] and <i>macroS3D</i> for the <i>Case B</i> . “glob” denotes results obtained using a two-phase globular model.	116
4.10	Evolution of different magnitudes over time. Comparison between SOLID [®] and <i>macroS3D</i> for the <i>Case C</i> . “glob” denotes results obtained using a two-phase globular model.	117
4.11	The overall operator splitting algorithm for solidification implemented in <i>macroS3D</i> . The variable ϕ denotes an arbitrary field. The index m denotes the iteration “m” within a time-step. The index t denotes the old time-step (previous macro-timestep). The index n denotes the iterations for the energy equation.	119
4.12	Transport stage in <i>macroS3D</i> . The index m denotes the iteration “m” within a time-step. The index t denotes the old time-step (previous macro-timestep). . . .	120
4.13	Nucleation stage in <i>macroS3D</i> . The index m denotes the iteration “m” within a time-step. The index t denotes the old time-step (previous macro-timestep). . . .	121
4.14	Growth stage in <i>macroS3D</i> . The index m denotes the iteration “m” within a time-step. The variable ϕ denotes an arbitrary field. The index t denotes the old time-step (previous macro-timestep). The index p denotes the internal iterations of the grain growth algorithm	122
4.15	Schematic of the solidification domain in the Hebditch and Hunt case. Chill heat transfer parameters: $h = 300$ W/(m ² K) and $T_{ext} = 25$ °C. <i>macroS3D</i> only describes nucleation, equiaxed grain motion and equiaxed grain packing.	123

4.16	Comparison between the solutions given by SOLID [®] and <i>macroS3D</i> (<i>upwind</i> , mesh 80x60) at various instants for the average solute concentration (color map), liquid intrinsic velocity (vectors) and formation of the bed of packed grains (black contours for solid fraction equals to 0.1, 0.2 and 0.3).	126
4.17	Comparison between the solutions given by SOLID [®] and <i>macroS3D</i> for the equiaxed grain density (color map) at the end of solidification. Note the different color scales in case V160x120.	127
4.18	Comparison between the solutions given by <i>macroS3D</i> for the macrosegregation pattern (color map) at the end of solidification using different mesh sizes and different numerical schemes.	128
4.19	Schematic of the columnar and equiaxed regions considered in the simulations. The predefined CET was adjusted to $z_{CET} = 35$ mm. The TiAl sample is shown in gray. The heaters are shown in purple and orange.	130
4.20	Liquid velocity and liquid fraction in the main plane of study inside the columnar region for the case G1P3N9. Violet contours delimit the mushy zone. Temperature contours are in green for 1490, 1500, 1503, 1508, 1510 °C.	133
4.21	Liquid velocity and liquid fraction in the main plane of study inside the columnar region for the case G5P3N9. Violet contours delimit the mushy zone. Temperature contours are in green for 1490, 1500, 1503, 1508, 1510 °C.	133
4.22	Evolution of the liquid velocity pattern in the main plane of study in the equiaxed region for the case G1P3N9. Temperature contours in black: 1400,1450,1500 and 1550 °C. Violet dashed line delimits the columnar region. The green contours delimit the slurry region.	135
4.23	Liquid intrinsic velocity and different fields in the packed equiaxed region for the case G1P3N9 at $t = 450$ s. Lines in black limit the packed equiaxed region. From left to right: liquid fraction, averaged solute concentration in liquid and buoyancy liquid density ($\frac{\rho_l^b}{\rho_l} = 1 - \beta_T (T - T_{ref}) - \beta_C (\langle C_l \rangle^l - C_{ref})$).	136
4.24	Evolution of the liquid velocity pattern in the main plane of study in the equiaxed region for the case G5P3N9. Temperature contours in black: 1400,1450,1500 and 1550 °C. Violet dashed is the predefined CET position. The green contours delimit the slurry region.	138
4.25	Schematic of the forces exerted on a globulitic equiaxed grain. (a) Case under normal terrestrial gravity. (b) Case with centrifugation.	139
4.26	Drag coefficient, C_d , vs grain diameter, d_g , between $U_{rel} = 20$ mm · s ⁻¹ (dashed lines) and $U_{rel} = 5$ mm · s ⁻¹ (solid lines). Green region corresponds to Stokes flow. Blue and black-dashed regions correspond to Ni and Beckermann [60] for $g_s = 10^{-4}$ and $g_s = 0.05$, respectively.	139
4.27	Ratio between the characteristic time of drag response and the characteristic time of rotation vs the grain diameter for different levels of apparent gravity (centrifuge arm is assumed 4 m).	141

4.28	Evolution of the equiaxed grain velocity in the slurry region for the case G1P3N9, along with the distribution of grain diameter. Black dashed line is the position of the predefined CET. Green line denotes the equiaxed grains packing front. The blank space in the plot is because the absence of equiaxed grains (they have not nucleated yet).	142
4.29	Evolution of the equiaxed grain velocity in the slurry region for the case G5P3N9, along with the distribution of grain diameter. Black dashed line is the position of the predefined CET. Green line denotes the equiaxed grains packing front. . .	143
4.30	Undercooling, $T - (T_f + m_l \langle C_l \rangle^l)$, for different case configurations in the main plane of study at $t = 450$ s. Black line limits the fully solid region and the solidifying region. Magenta dashed line is the predefined CET position. Green line is the equiaxed packing front.	145
4.31	Relative aluminum segregation $\frac{\langle C \rangle - C_0}{C_0} \times 100\%$ in the main plane of study at the end of the solidification protocol for different case configurations. Magenta dashed line is the position of the predefined CET. Orange line denotes the equiaxed grains packing front.	147

Bibliography

- [1] N. Reilly. *Hétérogénéités de fabrication des aluminures de titane: caractérisation et maîtrise de leurs formations en coulée centrifuge*. PhD thesis, Institut Jean Lamour, Université de Lorraine, Nancy, France, 2016.
- [2] N. Ramachandran, J.P. Downey, P.A. Curreri, and J.C. Jones. Numerical modeling of crystal growth on a centrifuge for unstable natural convection configurations. *Journal of crystal growth*, 126(4):655–674, 1993.
- [3] G. Müller, G. Neumann, and W. Weber. The growth of homogeneous semiconductor crystals in a centrifuge by the stabilizing influence of the coriolis force. *Journal of crystal growth*, 119(1-2):8–23, 1992.
- [4] H. Combeau, M. Bellet, Y. Fautrelle, D. Gobin, E. Arquis, O. Budenkova, B. Dussoubs, Y. Du Terrail, A. Kumar, Ch.-A. Gandin, et al. Analysis of a numerical benchmark for columnar solidification of binary alloys. In *IOP Conference Series: Materials Science and Engineering*, volume 33, page 012086. IOP Publishing, 2012.
- [5] C. Beckermann and R. Viskanta. Double-diffusive convection during dendritic solidification of a binary mixture. *PhysicoChemical Hydrodynamics*, 10(2):195–213, 1988.
- [6] S. Ganesan and D.R. Poirier. Conservation of mass and momentum for the flow of interdendritic liquid during solidification. *Metallurgical Transactions B*, 21(1):173, 1990.
- [7] J. Ni and C. Beckermann. A volume-averaged two-phase model for transport phenomena during solidification. *Metallurgical Transactions B*, 22(3):349, 1991.
- [8] F.H. Froes, C. Suryanarayana, and D. Eliezer. Synthesis, properties and applications of titanium aluminides. *Journal of materials science*, 27(19):5113–5140, 1992.
- [9] K. Kothari, R. Radhakrishnan, and N. Wereley. Advances in gamma titanium aluminides and their manufacturing techniques. *Progress in Aerospace Sciences*, 55:1–16, 2012.
- [10] B.P. Bewlay, S. Nag, A. Suzuki, and M.J. Weimer. TiAl alloys in commercial aircraft engines. *Materials at High Temperatures*, 33(4-5):549–559, 2016.
- [11] H. Clemens and W. Smarsly. Light-weight intermetallic titanium aluminides—status of research and development. In *Advanced materials research*, volume 278, pages 551–556. Trans Tech Publ, 2011.

- [12] T. Tetsui. Gamma Ti aluminides for non-aerospace applications. *Current opinion in solid state and materials science*, 4(3):243–248, 1999.
- [13] S.-W. Kim, J.K. Hong, Y.-S. Na, J.-T. Yeom, and S. E. Kim. Development of tial alloys with excellent mechanical properties and oxidation resistance. *Materials & Design (1980-2015)*, 54:814–819, 2014.
- [14] E.A. Loria. Quo vadis gamma titanium aluminide. *Intermetallics*, 9(12):997–1001, 2001.
- [15] T. Tetsui. Application of TiAl in a turbocharger for passenger vehicles. *Advanced Engineering Materials*, 3(5):307–310, 2001.
- [16] M.T. Jovanović, B. Dimčić, I. Bobić, S. Zec, and V. Maksimović. Microstructure and mechanical properties of precision cast tial turbocharger wheel. *Journal of Materials Processing Technology*, 167(1):14–21, 2005.
- [17] H. Clemens and S. Mayer. Intermetallic titanium aluminides in aerospace applications—processing, microstructure and properties. *Materials at High Temperatures*, 33(4-5):560–570, 2016.
- [18] A. Denquin. *Etude des transformations de phase et approche du comportement mécanique des alliages biphasés à base de TiAl: une contribution au développement de nouveaux alliages intermétalliques*. PhD thesis, Université de Lille 1, Lille, France, 1994.
- [19] J. Aguilar, A. Schievenbusch, and O. Kättlitz. Investment casting technology for production of tial low pressure turbine blades—process engineering and parameter analysis. *Intermetallics*, 19(6):757–761, 2011.
- [20] V.T. Witusiewicz, A.A. Bondar, U. Hecht, S. Rex, and T. Velikanova. The Al–B–Nb–Ti system: III. thermodynamic re-evaluation of the constituent binary system Al–Ti. *Journal of alloys and compounds*, 465(1-2):64–77, 2008.
- [21] T. Tetsui, T. Kobayashi, T. Mori, T. Kishimoto, and H. Harada. Evaluation of yttria applicability as a crucible for induction melting of TiAl alloy. *Materials transactions*, 51(9):1656–1662, 2010.
- [22] V. Güther, M. Allen, J. Klose, and H. Clemens. Metallurgical processing of titanium aluminides on industrial scale. *Intermetallics*, 103:12–22, 2018.
- [23] J. Gussone, Y.-C. Hagedorn, H. Gherekhloo, G. Kasperovich, T. Merzouk, and J. Hausmann. Microstructure of γ -titanium aluminide processed by selective laser melting at elevated temperatures. *Intermetallics*, 66:133–140, 2015.
- [24] S. Biamino, A. Penna, U. Ackelid, S. Sabbadini, O. Tassa, P. Fino, M. Pavese, P. Gennaro, and C. Badini. Electron beam melting of Ti–48Al–2Cr–2Nb alloy: Microstructure and mechanical properties investigation. *Intermetallics*, 19(6):776–781, 2011.

- [25] J. Schwerdtfeger and C. Körner. Selective electron beam melting of Ti-48Al-2Nb-2Cr: Microstructure and aluminium loss. *Intermetallics*, 49:29–35, 2014.
- [26] T. Tetsui, K. Shindo, S. Kaji, S. Kobayashi, and M. Takeyama. Fabrication of TiAl components by means of hot forging and machining. *Intermetallics*, 13(9):971–978, 2005.
- [27] T. Voisin, J.-P. Monchoux, M. Hantcherli, S. Mayer, H. Clemens, and A. Couret. Microstructures and mechanical properties of a multi-phase β -solidifying tial alloy densified by spark plasma sintering. *Acta Materialia*, 73:107–115, 2014.
- [28] N. Reilly, B. Rouat, G. Martin, D. Daloz, and J. Zollinger. Enhanced dendrite fragmentation through the peritectic reaction in tial-based alloys. *Intermetallics*, 86:126–133, 2017.
- [29] Y. Souhar, V.F. De Felice, C. Beckermann, H. Combeau, and M. Založnik. Three-dimensional mesoscopic modeling of equiaxed dendritic solidification of a binary alloy. *Computational Materials Science*, 112:304–317, 2016.
- [30] A. Viardin, M. Založnik, Y. Souhar, M. Apel, and H. Combeau. Mesoscopic modeling of spacing and grain selection in columnar dendritic solidification: Envelope versus phase-field model. *Acta Materialia*, 122:386–399, 2017.
- [31] A. Olmedilla, M. Založnik, B. Rouat, and H. Combeau. Packing of sedimenting equiaxed dendrites. *Physical Review E*, 97(1):012910, 2018.
- [32] A. Olmedilla, M. Založnik, T. Messmer, B. Rouat, and H. Combeau. Packing dynamics of spherical and nonconvex grains sedimenting at low stokes number. *Physical Review E*, 99(1):012907, 2019.
- [33] A. Ludwig and M. Wu. Modeling of globular equiaxed solidification with a two-phase approach. *Metallurgical and Materials Transactions A*, 33(12):3673–3683, 2002.
- [34] T. Nguyen, Ch.-A Gandin, H. Combeau, M. Založnik, and M. Bellet. Finite element multi-scale modeling of chemical segregation in steel solidification taking into account the transport of equiaxed grains. *Metallurgical and Materials Transactions A*, 49(5):1725–1748, 2018.
- [35] A. Pakanati, M. M’Hamdi, H. Combeau, and M. Založnik. Investigation of macrosegregation formation in aluminium dc casting for different alloy systems. *Metallurgical and Materials Transactions A*, 49(10):4710–4721, 2018.
- [36] I. Vannier. *Modélisation de la solidification des lingots d’acier*. PhD thesis, Institut National Polytechnique de Lorraine, Vandoeuvre-les-Nancy, France, 1995.
- [37] I. Vannier, H. Combeau, and G. Lesoult. Numerical model for prediction of the final segregation pattern of bearing steel ingots. *Materials Science and Engineering: A*, 173(1-2):317–321, 1993.

- [38] H. Combeau, M. Založnik, S. Hans, and P.E. Richy. Prediction of macrosegregation in steel ingots: influence of the motion and the morphology of equiaxed grains. *Metallurgical and materials transactions B*, 40(3):289–304, 2009.
- [39] L. Heyvaert, M. Bedel, M. Založnik, and H. Combeau. Modeling of the coupling of microstructure and macrosegregation in a direct chill cast al-cu billet. *Metallurgical and Materials Transactions A*, 48(10):4713–4734, 2017.
- [40] R. Mooney. *A Bridgman Furnace Front Tracking Model*. PhD thesis, Trinity College, Dublin, Ireland, 2015.
- [41] S. Battaglioli. *Numerical modelling of directional solidification in metal alloys*. PhD thesis, Trinity College, Dublin, Ireland, 2018.
- [42] J. Dantzig and M. Rappaz. *Solidification: -Revised & Expanded*. EPFL press, 2016.
- [43] J. Szekely and A.S. Jassal. An experimental and analytical study of the solidification of a binary dendritic system. *Metallurgical Transactions B*, 9(3):389–398, Sep 1978.
- [44] M. Worster. Natural convection in a mushy layer. *Journal of fluid mechanics*, 224:335–359, 1991.
- [45] W.D. Bennon and F.P. Incropera. A continuum model for momentum, heat and species transport in binary solid-liquid phase change systems— I. model formulation. *International Journal of Heat and Mass Transfer*, 30(10):2161–2170, 1987.
- [46] P. Bousquet-Melou, B. Goyeau, M. Quintard, F. Fichot, and D. Gobin. Average momentum equation for interdendritic flow in a solidifying columnar mushy zone. *International journal of heat and mass transfer*, 45(17):3651–3665, 2002.
- [47] C. Beckermann. Modelling of macrosegregation: applications and future needs. *International Materials Reviews*, 47(5):243–261, 2002.
- [48] H.C. Degroh III. Macroscopic segregation and nucleation in undercooled Pb-Sn alloys. Technical report, NASA Lewis Research Center, Cleveland, OH, United States, 1989.
- [49] J. Boussinesq. *Theorie Analytique de la Chaleur vol 2* (Paris: Gauthier-Villars). 1903.
- [50] D.J. Hebditch and J.D. Hunt. Observations of ingot macrosegregation on model systems. *Metallurgical transactions*, 5(7):1557–1564, 1974.
- [51] M. Bellet, H. Combeau, Y. Fautrelle, D. Gobin, M. Rady, E. Arquis, O. Budenkova, B. Dussoubs, Y. Duterrail, A. Kumar, et al. Call for contributions to a numerical benchmark problem for 2d columnar solidification of binary alloys. *International Journal of Thermal Sciences*, 48(11):2013–2016, 2009.
- [52] D. A. Drew. Mathematical modeling of two-phase flow. *Annual review of fluid mechanics*, 15(1):261–291, 1983.

- [53] M. Ishii and T. Hibiki. *Thermo-fluid dynamics of two-phase flow*. Springer Science & Business Media, 2010.
- [54] C.Y. Wang and C. Beckermann. A unified solute diffusion model for columnar and equiaxed dendritic alloy solidification. *Materials Science and Engineering: A*, 171(1-2):199–211, 1993.
- [55] C.Y. Wang and C. Beckermann. Equiaxed dendritic solidification with convection: Part i. multiscale/multiphase modeling. *Metallurgical and materials transactions A*, 27(9):2754–2764, 1996.
- [56] C.Y. Wang and C. Beckermann. A multiphase solute diffusion model for dendritic alloy solidification. *Metallurgical and Materials Transactions A*, 24(12):2787–2802, 1993.
- [57] J. Dantzig and M. Rappaz. *Solidification: Revised & Expanded*, chapter 10, pages 445–480. EPFL press, 2016.
- [58] C. Prakash. Two-phase model for binary solid-liquid phase change, Part I: Governing equations. *Numerical Heat Transfer, Part B Fundamentals*, 18(2):131–145, 1990.
- [59] C. Prakash. Two-phase model for binary solid-liquid phase change, part ii: Some illustrative examples. *Numerical Heat Transfer, Part B: Fundamentals*, 18(2):147–167, 1990.
- [60] J. Ni and C. Beckermann. Modeling of globulitic alloy solidification with convection. *Journal of Materials Processing and Manufacturing Science*, 2:217–231, 1993.
- [61] M. Wu and A. Ludwig. A three-phase model for mixed columnar-equiaxed solidification. *Metallurgical and Materials Transactions A*, 37(5):1613–1631, 2006.
- [62] M. Wu and A. Ludwig. Using a three-phase deterministic model for the columnar-to-equiaxed transition. *Metallurgical and Materials Transactions A*, 38(7):1465–1475, 2007.
- [63] M. Wu, J. Li, A. Ludwig, and A. Kharicha. Modeling diffusion-governed solidification of ternary alloys—part 1: Coupling solidification kinetics with thermodynamics. *Computational materials science*, 79:830–840, 2013.
- [64] W. Kurz, B. Giovanola, and R. Trivedi. Theory of microstructural development during rapid solidification. *Acta metallurgica*, 34(5):823–830, 1986.
- [65] M. Založnik and H. Combeau. An operator splitting scheme for coupling macroscopic transport and grain growth in a two-phase multiscale solidification model: Part i—model and solution scheme. *Computational Materials Science*, 48(1):1–10, 2010.
- [66] M. Rappaz and Ph. Thevoz. Solute diffusion model for equiaxed dendritic growth. *Acta Metallurgica*, 35(7):1487–1497, 1987.

- [67] B. Appolaire, H. Combeau, and G. Lesoult. Modeling of equiaxed growth in multicomponent alloys accounting for convection and for the globular/dendritic morphological transition. *Materials Science and Engineering: A*, 487(1-2):33–45, 2008.
- [68] W. Kurz and D.J. Fisher. *Fundamentals of solidification*, volume 1. trans tech publications Aedermannsdorf, Switzerland, 1986.
- [69] J. Lipton, M.E. Glicksman, and W. Kurz. Dendritic growth into undercooled alloy metals. *Materials Science and Engineering*, 65(1):57–63, 1984.
- [70] J. Lipton, M. Glicksman, and W. Kurz. Equiaxed dendrite growth in alloys at small supercooling. *Metallurgical and Materials Transactions A*, 18(2):341–345, 1987.
- [71] R. Ananth and W.N. Gill. Self-consistent theory of dendritic growth with convection. *Journal of Crystal Growth*, 108(1-2):173–189, 1991.
- [72] M. Bedel. *Étude de la formation des structures de solidification et des macroségrégations en coulée semi-continue d'aluminium*. PhD thesis, Institut Jean Lamour, Université de Lorraine, Nancy, France, 2014.
- [73] N. Leriche, H. Combeau, Ch.-A. Gandin, and M. Založnik. Modelling of columnar-to-equiaxed and equiaxed-to-columnar transitions in ingots using a multiphase model. In *IOP Conference Series: Materials Science and Engineering*, volume 84, page 012087. IOP Publishing, 2015.
- [74] K. Tveito, A. Pakanati, M. M’Hamdi, H. Combeau, and M. Založnik. A simplified three-phase model of equiaxed solidification for the prediction of microstructure and macrosegregation in castings. *Metallurgical and Materials Transactions A*, 49(7):2778–2794, 2018.
- [75] A. Pakanati, M. M’Hamdi, H. Combeau, and M. Založnik. Investigation of macrosegregation formation in aluminium dc casting for different alloy systems. *Metallurgical and Materials Transactions A*, 49(10):4710–4721, Oct 2018.
- [76] M. Ishii. One-dimensional drift-flux model and constitutive equations for relative motion between phases in various two-phase flow regimes. Technical report, Argonne National Lab., Ill.(USA), 1977.
- [77] M. Založnik. *Modeling of macrosegregation in direct chill casting*. PhD thesis, Univerza v Novi Gorici, Fakulteta za podiplomski študij, Slovenia, 2006.
- [78] M. Bedel, L. Heyvaert, M. Založnik, H. Combeau, D. Daloz, and G. Lesoult. Process-scale modelling of microstructure in direct chill casting of aluminium alloys. In *IOP Conference Series: Materials Science and Engineering*, volume 84, page 012100. IOP Publishing, 2015.
- [79] M. Založnik, H. Combeau, and A. Kumar. An operator splitting scheme for coupling macroscopic transport and grain growth in a two-phase multiscale solidification model: Part II - Application of the model. *Computational Materials Science*, 48(1):11–21, 2010.

- [80] H. Rodot, L.L. Regel, and A.M. Turtchaninov. Crystal growth of IV-VI semiconductors in a centrifuge. *Journal of Crystal Growth*, 104(2):280–284, 1990.
- [81] A. Sample and A. Hellowell. The effect of mold precession on channel and macro-segregation in ammonium chloride-water analog castings. *Metallurgical Transactions B*, 13(3):495–501, 1982.
- [82] A. Sample and A. Hellowell. The mechanisms of formation and prevention of channel segregation during alloy solidification. *Metallurgical Transactions A*, 15(12):2163–2173, 1984.
- [83] G. Zimmermann, M. Hamacher, and L. Sturz. Effect of zero, normal and hyper-gravity on columnar dendritic solidification and the columnar-to-equiaxed transition in neopentylglycol-(d) camphor alloy. *Journal of Crystal Growth*, 2019.
- [84] L. Yang, L.H. Chai, Y.F. Liang, Y.W. Zhang, C.L. Bao, S.B. Liu, and J.P. Lin. Numerical simulation and experimental verification of gravity and centrifugal investment casting low pressure turbine blades for high Nb-TiAl alloy. *Intermetallics*, 66:149–155, 2015.
- [85] D. Olbers, J. Willebrand, and C. Eden. *Ocean dynamics*. Springer Science & Business Media, 2012.
- [86] D.J. Tritton. *Physical fluid dynamics*. Springer Science & Business Media, 2012.
- [87] G.K. Batchelor. *An introduction to fluid dynamics*. Cambridge university press, 1967.
- [88] A. Kageyama and M. Hyodo. Eulerian derivation of the coriolis force. *Geochemistry, Geophysics, Geosystems*, 7(2), 2006.
- [89] M.L. Combrinck and L.N. Dala. Eulerian derivations of non-inertial navier-stokes equations. *29th Congr. Int. Counc. Aeronaut. Sci*, 577, 2014.
- [90] Official OpenFOAM Repository. <https://github.com/OpenFOAM>. Accessed: 20/05/2019.
- [91] P. Hignett, A.A. White, R.D. Carter, W.D. Jackson, and R.M. Small. A comparison of laboratory measurements and numerical simulations of baroclinic wave flows in a rotating cylindrical annulus. *Quarterly Journal of the Royal Meteorological Society*, 111(467):131–154, 1985.
- [92] R. Young, P.L. Read, W.-G. Früh, D. Smith, and S.H. Risch. The thermally-driven rotating annulus: horizontal velocities in regular and weakly chaotic flow regimes. University of Oxford, <https://doi.org/10.5287/bodleian:dr26xx49n>, 2015. Dataset.
- [93] S. Battaglioli, A.J. Robinson, and S. McFadden. Influence of natural and forced gravity conditions during directional columnar solidification. *International Journal of Heat and Mass Transfer*, 126:66–80, 2018.

- [94] P.K. Sung, D.R. Poirier, and S.D. Felicelli. Simulating the initiation of a channel during directional solidification of a superalloy. *Metallurgical and Materials Transactions A*, 32(1):202–207, 2001.
- [95] A. Harten. High resolution schemes for hyperbolic conservation laws. *Journal of computational physics*, 49(3):357–393, 1983.
- [96] B.P. Leonard. The ultimate conservative difference scheme applied to unsteady one-dimensional advection. *Computer methods in applied mechanics and engineering*, 88(1):17–74, 1991.
- [97] J.P. Boris and D.L. Book. Flux-corrected transport. i. shasta, a fluid transport algorithm that works. *Journal of computational physics*, 11(1):38–69, 1973.
- [98] S.T. Zalesak. Fully multidimensional flux-corrected transport algorithms for fluids. *Journal of computational physics*, 31(3):335–362, 1979.
- [99] S. Márquez. *An extended mixture model for the simultaneous treatment of short and long scale interfaces*. PhD thesis, Universidad Nacional del Litoral, Santa Fe, Argentina, 2013.
- [100] P.K. Agarwal and B.K. O’Neill. Transport phenomena in multi-particle systems—i. pressure drop and friction factors: unifying the hydraulic-radius and submerged-object approaches. *Chemical Engineering Science*, 43(9):2487–2499, 1988.
- [101] L. Heyvaert. *Modélisation de la formation des structures et des microporosités durant la solidification d’alliages d’aluminium*. PhD thesis, Institut Jean Lamour, Université de Lorraine, Nancy, France, 2015.
- [102] T. Nguyen. *Multiscale finite element modeling of macrosegregation and grain transport*. PhD thesis, École nationale supérieure des mines de Paris, Sophia Antipolis, France, 2015.
- [103] B. Appolaire. *Prise en compte du mouvement des cristaux equiaxes dans la modélisation de la solidification des lingots d’acier coulés en fonderie*. PhD thesis, Institut National Polytechnique de Lorraine, Vandoeuvre-les-Nancy, France, 1999.
- [104] Ø. Nielsen, A. Mo, B. Appolaire, and H. Combeau. Measurements and modeling of the microstructural morphology during equiaxed solidification of Al-Cu alloys. *Metallurgical and Materials Transactions A*, 32(8):2049–2060, 2001.
- [105] T. Wang, O. Budenkova, Y. Delannoy, Y. Fautrelle, and E. Wang. A 3-phase equiaxed solidification numerical model for binary alloy coupling macroscopic transport and grain growth. In *Solidification and Gravity 2018*, pages 179–184. Hungarian Academy of Sciences - University of Miskolc, Materials Science Research Group, 2018.

Abstract

TiAl alloys are an important material for automotive and aerospace industries due to their low density and high strength at high temperatures. However, due to their high reactivity in liquid state, low superheat must be used in casting in order to limit contamination. Centrifugal casting is an option to enhance mold filling at low superheat. In centrifugal casting the buoyancy driven flow is intensified and the flow structure is modified by the combined effect of the non-inertial accelerations – centrifugal and Coriolis – which appear in the rotating system. The consequence are particular patterns of macrosegregation and of distribution of microstructures in the solidified part. These patterns are not well understood. The objective of this thesis is to explain the flow structure, as well as the transport of solid grains and of chemical species during solidification of TiAl alloys in centrifuged systems. In the framework of this thesis a 3D finite-volume implementation of a multiscale solidification model was developed, which was required due to the inherently three-dimensional nature of the flow. The model was then used to simulate dedicated experiments of directional solidification of cylindrical samples of the TiAl GE alloy (Ti-47Al-2Cr-2Nb) that were previously conducted in the frame of the ESA GRADECET project. These experiments were carried out in the ESA “Large Diameter Centrifuge” at centrifugation levels between 5g and 20g, where g is the normal terrestrial gravity acceleration. The results of the simulations show that the Coriolis acceleration entirely modifies the liquid flow structure during solidification and lead to a one-vortex fluid flow pattern in the domain. On the contrary, it is shown that the Coriolis acceleration has only a weak impact on the motion of equiaxed grains. At high gravity level the grain motion is mainly controlled by the balance between the apparent gravity and the drag force. It is also shown that the final aluminum macrosegregation pattern show a strong enrichment on the flight velocity side of the sample due to the asymmetry of the liquid flow induced by the Coriolis force.

Keywords: Solidification, centrifugal casting, TiAl alloys, numerical modeling

Résumé

Les alliages TiAl sont un groupe de matériaux important pour les industries automobile et aérospatiale, de par leur faible densité et bonne tenue mécanique à haute température. Cependant, à cause de leur forte réactivité à l'état liquide, au moment de couler ces alliages, il faut utiliser une faible surchauffe pour limiter la contamination. La coulée centrifuge est une option pour améliorer le remplissage du moule à faible surchauffe. En coulée centrifuge, l'effet de la poussée d'Archimède sur le mouvement du liquide est renforcé, ce qui modifie l'écoulement par l'effet combiné de la force centrifuge et de force de Coriolis qui apparaissent dans le système en rotation. Ceci fait que des motifs particuliers de macroségrégation et de distribution de microstructures se forment dans la pièce solidifiée, et l'origine de ces motifs n'est pas très bien comprise. L'objectif de cette thèse est d'expliquer l'écoulement du liquide ainsi que le transport des grains solides et des espèces chimiques pendant la solidification d'alliages TiAl en coulée centrifuge. Un modèle 3D volume finis de solidification multi-échelle a d'abord été développé dans le cadre de cette thèse. Un tel modèle était nécessaire à cause de la nature tridimensionnelle des écoulements. Le modèle a ensuite été utilisé pour simuler des essais expérimentaux de solidification dirigée d'échantillons cylindriques en alliage TiAl GE (Ti-47Al-2Cr-2Nb), précédemment réalisés dans le cadre du projet ESA GRADECET. Ces essais ont été réalisés dans la “Large Diameter Centrifuge” de l'ESA, à des intensités de centrifugation entre 5g et 20g, où g est l'accélération standard de la gravité terrestre. Les résultats des simulations montrent que la force de Coriolis modifie complètement l'écoulement du liquide pendant la solidification, résultant en une unique boucle de convection dans le bain liquide. Inversement, la force de Coriolis n'a qu'un faible effet sur le mouvement des grains équiaxes. A forte centrifugation, le mouvement des grains est surtout gouverné par l'équilibre entre la gravité apparente et la force de trainée. Les résultats montrent aussi que la macroségrégation finale de l'aluminium n'est pas symétrique et présente un fort enrichissement le long du bord d'attaque de l'échantillon. Ceci est dû à l'asymétrie de l'écoulement induite par la force de Coriolis.

Mots-clés: Solidification, coulée centrifuge, alliage TiAl, modélisation numérique